

**Data-Driven HTS Strategies for Selection of Drug Combinations and 3D Models for  
Physiologically Relevant Drug Discovery**

by

**Stanton Joseph Kochanek**

Bachelor's of Science, John Carroll University, 2013

Submitted to the Graduate Faculty of

The University of Pittsburgh, School of Pharmacy

of the requirements for the degree of

Doctor of Philosophy

University of Pittsburgh

2019

UNIVERSITY OF PITTSBURGH

SCHOOL OF PHARMACY

This thesis/dissertation was presented

by

**Stanton Joseph Kochanek**

**PhD**

It was defended on

July 8, 2019

and approved by

Jan Beumer PharmD and PhD, Professor, Pharmaceutical Sciences

Philip Empey PharmD and PhD, Assistant Professor, Pharmacy and Therapeutics

Edwin Jackson PhD, Professor, Pharmacology and Chemical Biology

Barry Gold PhD, Professor, Pharmaceutical Sciences

Samuel Poloyac PharmD and PhD, Associate Dean for Graduate and Postdoctoral  
Programs, Pharmaceutical Sciences

Paul A. Johnston PhD: Associate Professor, Pharmaceutical Sciences

Copyright © by Stanton Joseph Kochanek

2019

## **Data-Driven HTS Strategies for Selection of Drug Combinations and 3D Models for Physiologically Relevant Drug Discovery**

Stanton Joseph Kochanek, PhD, University of Pittsburgh, 2019

Currently, the approval rate for cancer drugs is dismal, where only ~ 5% of candidates that enter phase I clinical trials become therapies. To address this, it is necessary to improve our preclinical strategies. In particular, the leading clinical observation for patient treatment is that drug combinations more consistently provide better therapeutic outcomes and reduce or delay the emergence of drug resistance as opposed to monotherapy alone. What's more, models that better recapitulate tumor biology are more likely to be predictive of therapeutic success. Therefore, it was necessary for our laboratory to use data-driven high-throughput / content screening strategies to confirm synergistic drug-drug interactions and optimize cell culture conditions in 3D for drug discovery, to address these preclinical limitations. Specifically, we developed a strategy to confirm and evaluate the synergistic interaction between DCs identified in a pilot screen of 20 drugs performed in pairwise combinations. We were able to both confirm synergism across 4 DCs and develop a mechanism of synergistic action. We also characterized 11 head and neck squamous cell carcinoma cell lines as multicellular tumor spheroids (MCTSs) looking at changes in cellular viability and spheroid diameter over time as well as other microenvironmental characteristics of a solid tumor. Lastly, we applied our MCTSs to screen 19 FDA approved drugs to determine drug sensitivity in both 2D and 3D models. We observed that 2D was consistently more sensitive than 3D and that it was necessary to implement several metrics to adequately evaluate drug effect in 3D.

## Table of Contents

<b>Abbreviations</b> .....	xv
<b>1.0 Drug Combinations in Cancer Therapy: An Overview of the History, Methods for Identification, and Current Advances</b> .....	1
<b>1.1 A History of Drug Combinations in Cancer Pharmacology</b> .....	1
<b>1.2 Development of Screening Methods for Antineoplastic Agents in Cancer</b>	5
<b>1.3 Prioritizing Drug Combinations for Cancer Treatment</b> .....	7
<b>1.4 Where Do We Go Now: Data-driven Approaches for Drug Discovery</b> .....	11
<b>2.0 Confirmation of Selected Synergistic Cancer Drug Combinations Identified in an HTS Campaign and Exploration of Drug Efflux Transporter Contributions to the Mode of Synergy</b> .....	15
<b>2.1 NCI ALMANAC and its Influence on Drug Combination Screening</b> .....	15
<b>2.2 HTS Campaign to Identify Synergistic Drug-Drug Interactions for Confirmation</b> .....	16
<b>2.3 Materials and Methods</b> .....	24
<b>2.4 Confirmation of Selected Synergistic Drug Combinations Flagged in the Pilot Phase of the NCI-60 DC-HTS Campaign</b> .....	31
<b>2.5 Analysis and Confirmation of Drug Combination 1</b> .....	32
<b>2.6 Analysis and Confirmation of Drug Combination 2</b> .....	35
<b>2.7 Analysis of Drug Confirmation 3</b> .....	37
<b>2.8 Analysis and Confirmation of Drug Combination 4</b> .....	40

2.9 Development and Validation of the High Content Imaging ABCG2 Drug Efflux Transporter Hoechst Accumulation Assay .....	42
2.10 Do Gefitinib and Raloxifene Inhibit ABCG2 Transporter Substrate Efflux?	
52	
2.11 Discussion .....	61
<b>3.0 Multicellular Tumor Spheroids: Physiological Relevance and Application in Cancer Drug Discovery.....</b>	<b>70</b>
3.1 MCTSs An Improvement to 2D Cell Culture .....	70
3.2 Comparison of Methods for Generating 3D Cell Culture Conditions .....	73
3.2.1 Anchorage-dependent Models .....	73
3.2.2 Anchorage-Independent Methods for 3D .....	74
3.2.3 Introduction to Spheroid Generating Methods for 3D.....	74
3.3 Overview of Spontaneous Aggregation Methods of 3D.....	76
3.3.1 Rotative / Rotary Cell Culture .....	76
3.3.2 Hanging Drop Method .....	76
3.3.3 Liquid Overlay Technique.....	77
3.3.4 Magnetic Levitation .....	77
3.4 Overview of ULA for Production of 3D Cell Culture .....	78
3.5 Beyond MCTS Models, a Vision of the Future .....	80
3.6 3D Conclusions and Future .....	83
<b>4.0 High Content Screening Characterization of Head and Neck Squamous Cell Carcinoma Multicellular Tumor Spheroid Cultures Generated in 384-well Ultra-low Attachment Plates to Screen for Better Cancer Drug Leads .....</b>	<b>85</b>

<b>4.1 Challenges and Unmet Needs in Head and Neck Drug Discovery .....</b>	<b>85</b>
<b>4.1.1 Necessity of Physiologically Relevant Models for Improved Clinical Translation .....</b>	<b>86</b>
<b>4.1.2 HNSCC MCTS Production using Ultra-low Attachment Technology</b>	<b>87</b>
<b>4.2 Materials and Methods .....</b>	<b>88</b>
<b>4.3 Results .....</b>	<b>96</b>
<b>4.3.1 Morphology and viability of HNSCC Multicellular Tumor Spheroids formed in 384-well U-bottomed Ultra Low Attachment Microtiter Plates.</b>	<b>96</b>
<b>4.3.2 HNSCC Multicellular Tumor Spheroid Growth Phenotypes in ULA-plates</b>	<b>98</b>
<b>4.3.3 HNSCC Multicellular Tumor Spheroid Cell Proliferation .....</b>	<b>107</b>
<b>4.3.4 HNSCC Multicellular Tumor Spheroid Mitochondrial Mass and Membrane Potential.....</b>	<b>110</b>
<b>4.3.5 Doxorubicin Penetration and Cytotoxicity in HNSCC Multicellular Tumor Spheroid Cultures.....</b>	<b>114</b>
<b>4.4 Discussion .....</b>	<b>121</b>
<b>5.0 Determination of Drug Sensitivity in Head and Neck Squamous Cell Carcinoma using Multicellular Tumor Spheroids and 2D Cell Culture Models .....</b>	<b>129</b>
<b>5.1 Overview of Head and Neck Squamous Cell Carcinoma .....</b>	<b>129</b>
<b>5.1.1 MCTS as Physiological Relevant In Vitro Models for Screening Drug Candidates .....</b>	<b>130</b>

5.1.2 Overview and Review of MCTS Characterization .....	131
5.2 Materials and Methods .....	132
5.3 Results and Discussion .....	138
5.3.1 3D and 2D Drug Screen Assay Development and Performance ....	138
5.3.2 Drug Sensitivity in 2D and 3D HNSCC Cell Culture .....	142
5.3.3 Determination of Overall Drug Impact Across All Five Cell Lines.	146
5.3.4 FDA Approved Drugs for Head and Neck Cancer .....	150
5.3.5 HNSCC Sensitivity to Cisplatin .....	151
5.3.6 HNSCC Sensitivity to Docetaxel .....	154
5.3.7 HNSCC Sensitivity to Methotrexate .....	159
5.3.8 HNSCC Sensitivity to Bleomycin .....	162
5.3.9 HNSCC Sensitivity to 5'FU.....	165
5.3.10 HNSCC Sensitivity to Gefitinib as a Proxy of Cetuximab .....	169
5.3.11 HNSCC Sensitivity to Sunitinib.....	172
5.3.12 HNSCC Sensitivity to Everolimus.....	176
5.4 Discussion: The Necessity of Assessing Drug Impact on Multiple Fronts: Compound Sensitivity and Insensitivity in both 3D and 2D HNSCC Cell Lines	180
5.4.1 Challenges of HNSCC Treatment in Patients and the Necessity of Physiologically Relevant Preclinical Models.....	182
5.4.2 Clinical Translation with MCTS: Relationship of In Vitro Drug Concentrations to Patient Treatment.....	186
6.0 Implications, Limitations, and Future Directions .....	188

<b>6.1 Data-Driven Strategies for Drug Discovery and Screening</b> .....	<b>188</b>
<b>6.1.1 3D Application of Data-Driven Strategies</b> .....	<b>190</b>
<b>6.2 Limitations</b> .....	<b>192</b>
<b>6.2.1 Challenges in Cancer Drug Screening</b> .....	<b>192</b>
<b>6.2.2 Challenges with MCTS</b> .....	<b>193</b>
<b>6.3 Future Directions</b> .....	<b>195</b>
<b>Bibliography</b> .....	<b>197</b>

## List of Tables

<b>Table 1 Selected Drug Combinations, NCI-60 Cell Lines, Tumor Histology's, Individual Drug GI50s, and Drug Interaction Analysis Summary .....</b>	<b>23</b>
<b>Table 2 Selected Drug Combinations, NCI-60 Cell Lines, Drug Efflux Transporter mRNA Expression Levels and Compound Functional Activities .....</b>	<b>65</b>
<b>Table 3 CellTiter Blue Drug GI50 Comparison HNSCC 2D Monolayers Vs MCTS Cultures .....</b>	<b>137</b>
<b>Table 4 Screening Statistics for QC Evaluation of Assay Performance .....</b>	<b>145</b>
<b>Table 5 Drug Mediated Effects on HNSCC MCTS Morphology.....</b>	<b>147</b>
<b>Table 6 Drug Mediated Effects on HNSCC MCTS Live/Dead Staining.....</b>	<b>148</b>
<b>Table 7 Ranked Scores of Drug Impact on HNSCC MCTS By Compound .....</b>	<b>149</b>
<b>Table 8 Representative Example of Drug Impact Scoring in UM-22B Cell Line....</b>	<b>150</b>

## List of Figures

<b>Figure 1 Hierarchical Clustering Analysis of the Individual GI50 data for the Pilot HTS Screen .....</b>	<b>18</b>
<b>Figure 2 4 x 4 Drug Combination Matrices.....</b>	<b>19</b>
<b>Figure 3 Confirmation of Gefitinib-Vinorelbine Flagged Synergy .....</b>	<b>21</b>
<b>Figure 4 10 X 10 Drug Combination Matrix for Confirmation of the Synergy between Gefitinib and Mitoxantrone in OVCAR-5 Ovarian Cancer Cell Line.....</b>	<b>33</b>
<b>Figure 5 Confirmation of Drug Combination 1 between Gefitinib and Mitoxantrone in OVCAR-5 Ovarian Cancer Cell Line .....</b>	<b>34</b>
<b>Figure 6 Confirmation of Drug Combination 2 between Raloxifene and Mitoxantrone in the KM12 Colon Cancer Cell Line .....</b>	<b>36</b>
<b>Figure 7 Confirmation of Drug Combination 3 between Raloxifene and Daunorubicin in the NCI-H23 Non-Small Cell Lung Cancer Cell Line.....</b>	<b>39</b>
<b>Figure 8 Confirmation of Drug Combination 4 between Gefitinib and Vinorelbine in the MDA-MB-485 Melanoma Cell Line .....</b>	<b>41</b>
<b>Figure 9 High Content Imaging Assay to measure the Accumulation of the ABCG2 Substrate Hoechst 33342 in MDCKII-EV and MDCKII-ABCG2 Cell Lines .....</b>	<b>44</b>
<b>Figure 10 Effects of Exposure to the ABCG2 Inhibitor Ko143 on Hoechst 33342 Accumulation in MDCKII-EV and MDCKII-ABCG2 Cell Lines.....</b>	<b>48</b>
<b>Figure 11 Effects of Exposure to Ko143, Gefitinib or Raloxifene on Hoechst 33342 Accumulation in MDCKII-EV and MDCKII-ABCG2 Cell Lines.....</b>	<b>54</b>

<b>Figure 12 Effects of Exposure to Raloxifene on Hoechst 33342 Accumulation in MDCKII-EV and MDCKII-ABCG2 Cell Lines.....</b>	<b>59</b>
<b>Figure 13 Characterization of HNSCC multicellular tumor spheroid morphology and viability in Ultra-low Attachment Plates.....</b>	<b>97</b>
<b>Figure 14 Growth phenotypes of multicellular tumor spheroids produced by five representative HNSCC cell lines seeded and maintained in Ultra-low Attachment Plates.....</b>	<b>100</b>
<b>Figure 15 Correlation between FaDu cell seeding density multicellular tumor spheroid diameter and Cell Titer Blue ® RFU Signals.....</b>	<b>103</b>
<b>Figure 16 Development of a necrotic core in multicellular tumor spheroids formed by the FaDu and OSC19 HNSCC cell lines seeded and maintained in Ultra-low Attachment Plates.....</b>	<b>105</b>
<b>Figure 17 Distribution of the fluorescence in multicellular tumor spheroids formed from HNSCC cell lines pre-labeled with Celltracker Orange® prior to cell seeding into Ultra-low Attachment plates .....</b>	<b>108</b>
<b>Figure 18 Cell proliferation in HNSCC multicellular tumor spheroids produced and cultured in Ultra-low Attachment Plates.....</b>	<b>109</b>
<b>Figure 19 Mitochondrial mass and Membrane potential in HNSCC multicellular tumor spheroids produced in Ultra-low Attachment Plates.....</b>	<b>111</b>
<b>Figure 20 Doxorubicin Drug Distribution in multicellular tumor spheroids formed in Ultra-low Attachment Plates .....</b>	<b>115</b>
<b>Figure 21 MCTS Morphological Effects by Doxorubicin Treatment Over Time ....</b>	<b>118</b>

<b>Figure 22 Doxorubicin-induced cytotoxicity in multicellular tumor spheroids formed in Ultra-low Attachment Plates .....</b>	<b>119</b>
<b>Figure 23 Assay work flow and representative images and quantitative data of HNSCC multicellular tumor spheroids.....</b>	<b>140</b>
<b>Figure 24 QC values of maximum and minimum controls in both 3D and 2D culture conditions .....</b>	<b>143</b>
<b>Figure 25 Cisplatin sensitivity in HNSCC 3D multicellular tumor spheroids and 2D cell culture conditions .....</b>	<b>152</b>
<b>Figure 26 Docetaxel sensitivity in HNSCC 3D multicellular tumor spheroids and 2D cell culture conditions .....</b>	<b>157</b>
<b>Figure 27 Methotrexate sensitivity in HNSCC 3D multicellular tumor spheroids and 2D cell culture conditions.....</b>	<b>160</b>
<b>Figure 28 Bleomycin sensitivity in HNSCC 3D multicellular tumor spheroids and 2D cell culture conditions .....</b>	<b>163</b>
<b>Figure 29 5'FU sensitivity in HNSCC 3D multicellular tumor spheroids and 2D cell culture conditions.....</b>	<b>167</b>
<b>Figure 30 Gefitinib sensitivity in HNSCC 3D multicellular tumor spheroids and 2D cell culture conditions .....</b>	<b>170</b>
<b>Figure 31 Sunitinib sensitivity in HNSCC 3D multicellular tumor spheroids and 2D cell culture conditions .....</b>	<b>174</b>
<b>Figure 32 Everolimus sensitivity in HNSCC 3D multicellular tumor spheroids and 2D cell culture conditions.....</b>	<b>178</b>

## Abbreviations

HTS – High Throughput Screening

DCs – Drug Combinations

DCM – Drug Combination Matrix

BCRP – Breast Cancer Resistance Protein

Pgp/MDR1 – P-glycoprotein 1 / Multidrug resistance 1

ALMANAC – A Large Matrix of Anti-Neoplastic Agent Combinations

MOAs – Mechanisms of action

ABC – ATP binding cassette

TKI – tyrosine kinase inhibitor

EGF-R – Epidermal growth factor-receptor

EGF – Epidermal growth factor

DMSO – Dimethylsulfoxide

PBS – Phosphate buffered saline

MEM – Minimum essential medium

DMEM – Dulbecco's modified Eagle's medium

RPMI – Roswell park Memorial Institute

FBS – Fetal bovine serum

P/S – Penicillin and Streptomycin

NCI – National Cancer Institute

DTP – Developmental Therapeutics Program

MDCKII – Madin-Darby Canine Kidney II cell line

CTG – CellTiter-Glo

CTB – CellTiter-Blue

RLU – Relative Light Units

RFU – Relative Fluorescent units

GI<sub>50</sub> – Growth Inhibition 50

DCMs – Drug Combination Matrices

PDI – Pharmacodynamic drug interaction model

%GI – Percent Growth Inhibition

CLF – Cell Loss Fraction

EV – Empty Vector

IXM – Image Express Micro

MWCS – Multi-wavelength cell scoring

CI – Combination Index

MIFI – Mean integrated fluorescent intensity

CML – Chronic myelogenous leukemia

FDA – Food and Drug Administration

NCI–National Cancer Institute

MXR – Multi-xenobiotic resistance transporter

HNC – Head and Neck Cancer

HNSCC – Head and Neck squamous cell carcinoma

MCTS – Multicellular Tumor Spheroid

ECM – Extracellular Matrix

2D – two dimensional

3D – three dimensional

CAM – Calcein AM

ETHD – Ethidium Homodimer

TMRM – Tetra-methyl-rhodamine methyl ester

PD-1 – anti-programmed death-ligand 1

EDU – 5-ethynyl-2'-deoxyuridine

CTO – CellTracker Orange

MTO – MitoTracker Orange

VAMP – vincristine, amethopterin, 6-mercaptopurine, and prednisone

CNS – Central Nervous System

SRB – sulphorhodamine B

MTA – Molecularly targeting agents

GBM – Glioblastoma multiforme

TCGA – The Cancer Genome Atlas

CCLE – Cancer Cell Line Encyclopedia

COSMIC – Catalogue of Somatic Mutations in Cancer

APE-1 – apurinic/aprimidinic endonuclease-1/redox effector factor-1

ULA – Ultra-low attachment

STAT – Signal transducer and activator of transcription

PI3K – Phosphoinositide 3-Kinase pathway

SRC-TKI – src family kinase, tyrosine kinase inhibitor

mTOR – Mammalian target of rapamycin

S:B – Signal to background

## **1.0 Drug Combinations in Cancer Therapy: An Overview of the History, Methods for Identification, and Current Advances**

### **1.1 A History of Drug Combinations in Cancer Pharmacology**

Drug combinations in cancer therapy represent an improvement on standard monotherapy treatment modalities, especially when the combination performs in an additive or synergistic way, thereby augmenting the overall therapeutic effect.<sup>1, 2</sup> In early oncology (1900-1940s), few therapeutic options existed save for surgery and radiation, and even then, most surgical options were limited to the treatment of localized tumors. It wasn't until the 1940's when Charles Huggins and Sidney Farber both demonstrated the ability of chemical compounds to successfully target susceptibilities within specific cancers; the use of estrogens to cause regression of prostatic tumors in humans and the use of aminopterin, a folic acid derivative, to induce partial remission in childhood leukemia, respectively.<sup>3, 4</sup> Following these milestones in cancer therapy, nitrogen mustard (1949) and other chemotherapeutics were identified as being capable of cytotoxicity and became included in the standard regimen for the treatment of oncological malignancies.<sup>5 6</sup>

Many of the early clinical studies introducing single chemotherapeutic agents for treatment of cancers elicited partial regression or remission rather than full removal of tumor burden. Because of this roadblock it became necessary for others in the field of oncology and cancer pharmacology to propose new strategies, specifically, the use of two or more agents to block different enzymes within the same metabolic pathway to

produce potentiation of antiproliferative effects.<sup>7</sup> Several laboratories demonstrated the improved effects of dual therapy in mice through the use of antimetabolites and antileukemic drugs.<sup>8-10</sup> However, it wasn't until Emil Frei, Emil Freireich, and James Holland that the clinical efficacy of drug combinations was demonstrated when they used combination therapy to treat patients with acute myelocytic and lymphocytic leukemia.<sup>11</sup> This group determined that the combined effects of methotrexate and 6-mercaptopurine in patients with acute leukemia, by either continuous or intermittent treatment schedules, was able to produce remission in 42 of the 65 patients (either partial or complete). Within the study only 17 deaths were reported, of which, only 5 were shown to be caused by marrow hypoplasia associated with antimetabolite drug toxicity. This study did not provide a direct comparison to monotherapy alone but does demonstrate that in order for combination therapy to be maximally effective, both drugs must be able to produce an antineoplastic effect. Despite limitations outlined by the authors, this was the first study to illustrate the therapeutic utility of drug combinations. Furthermore, this study provided a springboard for the selection of chemotherapeutic agents to be used in combination with a biological rationale generated from information gathered in both animal studies and clinical use, and for the selection of 6-mercaptopurine instead of 8-azaguanine.<sup>6, 8, 10</sup>

One of the major challenges to adequately treat cancer especially in the selection and prioritization of drugs for use in combinations, is to minimize toxicity while maximizing efficacy in patients. A publication by Sartorelli in 1969, less than a decade after Frei, outlines the primary goal and rationale of using combination therapies, which is to capitalize on the metabolic susceptibilities of cancer by “rational modification” of a current chemotherapeutic to improve efficacy or to achieve a greater level of disruption / alteration

of metabolic processes by using drugs in combination.<sup>12</sup> Furthermore, Satorelli's review illustrates the utility of selecting drugs of differing toxicities to be more effective in a tumor population while sparing the healthy normal cellular population. Attempts at minimizing toxicity provided a major challenge during the 1950-1970s, when few documented biological differences existed between malignant and normal cells in terms of potential exploitable susceptibilities, save for differences in cellular proliferation.<sup>12, 13</sup> DeVita *et. al* 1975 highlighted the importance of providing a sufficient level of effect with monotherapies to cause a "lethal blockade" of metabolic pathways but that given the complexity of such pathways, alteration or inhibition of a single biological site may not be sufficient.<sup>2</sup> This article also presents a potential hazard of using drugs in combination, mainly, that without sufficient biological rationale or clinical evidence of antineoplastic effect, empirically pairing drugs may cause interference and antagonism, thereby, limiting efficacious effects and producing greater associated toxicity.<sup>2</sup>

To test if a combination of four drugs could be more efficacious with prolonged therapeutic impact in patients than monotherapies, Freireich and colleagues used a combination known as VAMP (vincristine, amethopterin, 6-mercaptopurine, and prednisone) for the treatment of acute lymphoblastic leukemia.<sup>14, 15</sup> They noticed a marked increase in remission within the patient population with the application of VAMP treatment upwards of ~ 60% and with an increase in the duration of remission better than the currently available treatment modalities at the time.<sup>14, 15</sup> The rationale for the use of the combination was that each compound was capable of an inhibitory effect individually, in both murine models and patients. The empirical prediction for using the drugs in combination was that a when used together, these antineoplastic agents would provide

greater patient responses and prolonged remission. Each drug's individual mechanism of action is as follows: vincristine is a vinca alkaloid capable of blocking  $\beta$ -tubulin from polymerizing during microtubule formation, and causes mitotic arrest; amethopterin is an antimetabolite of folic acid that is capable of disrupting the metabolic conversion of folic acid into tetrahydrofolate, which is required for addition of methyl groups to purine ribonucleotides and thereby inhibits DNA replication; 6-mercaptopurine is an analog of the natural purine hypoxanthine, and gets incorporated into DNA which causes strand breaks pending a functioning mismatch repair system; and prednisone is a glucocorticoid found to be capable of lympholytic effects which suppress mitosis of lymphocytic cells. Following in Freireich's footsteps, DeVita *et. al* 1970 also demonstrated the utility of using drugs in combination for the treatment of Hodgkin's disease, whereby vincristine, nitrogen mustard or cyclophosphamide, procarbazine hydrochloride, and prednisone were used to provide complete remission in 81% of their patients, and prolonged the median survival within the responding group to greater than 42 months.<sup>16</sup> Furthermore, the authors were able to demonstrate that through the use of this combination 47% of the remitted patients were disease free at 4 years post treatment and 77% remained alive.<sup>16</sup> Additionally, Einhorn and Donohue (1977) demonstrated the success of a three-drug combination consisting of cis-platinum, vinblastine, and bleomycin in patients suffering from disseminated testicular cancer, and reported complete remission in 74% and partial remission in 26% of patients (55 patients total), with 32 remaining disease-free 6 to 30 months after the study.<sup>17</sup>

Given the success of these drug combinations, the components of which are still vital regimens in the treatment of many cancers, it has been important to develop better

methods to select and prioritize drugs given both the complexities of cancers and the potential drug-drug interactions that might exist.

## **1.2 Development of Screening Methods for Antineoplastic Agents in Cancer**

In 1949 several murine models of solid tumors were developed, in particular the L1210 murine leukemia model. The introduction of this model provided an invaluable tool for screening therapeutics pre-clinically and became the standard for screening compounds for efficacy in leukemias.<sup>10, 18, 19</sup> Through the use of the L1210 and P388 leukemias, B16 melanoma and Lewis lung carcinoma mouse models, more than 45 compounds were identified as having antineoplastic activity.<sup>20</sup> In a review by Shoemaker, the author illustrated the utility of the many mouse models and also their limitations, mainly, the inability to efficiently screen for compounds with a sufficient amount of throughput. In an attempt to better screen for antineoplastic compounds within a broader spectrum of tumors, specifically, solid tumors, a panel of 60 cell lines was developed by the National Cancer Institute (NCI) across 9 tumor types: leukemia, colon, lung, brain (CNS), renal, melanoma, ovarian, breast, and prostate.<sup>21</sup>

With the use of the new panel, aptly named the “NCI-60”, several projects spanning decades provided an abundance of information that was previously absent in the research community. In particular, the creation of practical microtiter plate cytotoxicity assays during the 1980’s to 1990’s allowed for more robust assays and enabled the determination of cell sensitivity against putative antineoplastic compounds.<sup>22</sup> Both MTT and XTT assays allowed for the measurement of cell viability through the reduction of

tetrazolium salts to formazan and the proceeding conversion can be measured via a colorimeter. For their purposes, the NCI wanted a non-tetrazolium method to improve both the throughput and ease of use of their viability reagent so a method using sulphorhodamine B (SRB) was developed which met the necessary requirements, needing only a chemical fixation step, and allowed for differentiation between cell kill and growth inhibition.<sup>22-24</sup> In addition, a T<sub>0</sub> plate was included to allow a comparison point between early cell viability and at the assay endpoint.<sup>22-25</sup> Through the use of the NCI-60 and growth inhibition assays, more antineoplastic compounds could be assessed. However, during the 1980s and 1990s the demand for the NCI was 10,000 compounds per year and presented a logistical challenge that required assay miniaturization and optimization.<sup>25</sup> In particular, duration in culture and cell seeding density had to be optimized in an attempt to produce minimal spurious results, specifically, compounds that required many cell cycles were not overlooked and also so that cell lines with fast doubling times don't seem suspiciously hypersensitive to particular compounds. In an effort to accommodate this during optimization, the NCI used a high initial cell inoculum (e.g., 20,000cells/well) and a brief preincubation and treatment period (e.g., 1-2 days).<sup>25</sup>

For their preliminary screens the NCI decided to implement seeding densities between 5000-40,000 cells per well within a 96-well microtiter plate, where plates were preincubated 24hrs, followed by drug treatment for an additional 48hrs and culminating with SRB as the endpoint assay.<sup>25</sup> Several natural products / crude extracts were prescreened at a single concentration before being included in the full screen, where all compounds and extracts were tested with five log<sub>10</sub>-spaced concentrations, starting in the majority of compounds at 100μM, and natural product extracts starting at 100μg/mL.<sup>25</sup>

Through their optimized screening protocol, the NCI was able to identify 9-methoxy-N<sup>2</sup>-methylellipticinium acetate, which demonstrated higher sensitivity in the CNS / brain tumor cell line subpanel than in any other cell lines.<sup>26, 27</sup> In addition, the NCI also identified cephalostatin 1 as a lead with broad activity across several solid tumor derived cell lines, with an “undefined” mechanisms of action and as such merited follow-up.<sup>28, 29</sup> Overall, during the 5yr period of time from 1990 to 1995, over 100,000 materials, both pure compounds and natural products, were tested against the 60 cell line panel and provided a basis for assay miniaturization for high-throughput screening of antineoplastic drugs, many aspects of which are still used today.

### **1.3 Prioritizing Drug Combinations for Cancer Treatment**

Traditionally, the selection of compounds for combination therapy in patients was done empirically, often without a specific rationale. Drug combinations were selected on the basis of experimentation and observation, because more in-depth information was unavailable, such as tumor genetic / mutational information. An early example of an empirically selected drug combination was with the combination VAMP, which consisted of vincristine, amethopterin, 6-mercaptopurine, and prednisone. This combination was utilized in leukemias because the compounds had displayed effectiveness individually in both murine models and patients.<sup>14, 30</sup> In addition, the drugs did not have overlapping mechanisms of action, and as such were combined with the goal of producing a greater more durable effect than was experienced with monotherapy.<sup>14, 30</sup>

Through the glimmer of hope provided to patients by this combination and many others, we observed an impetus within the NCI and the research community to develop more sophisticated screening strategies from the early leukemia mouse models to the NCI60 cell line panel, with the goal to prioritize preclinical compounds and natural products for clinical translation. Given the development of an established screening methodology by the NCI in the 1990s, the next logical research step was to develop strategies for identifying drugs that could be used in combination, especially those that were capable of favorable drug-drug interactions vis-à-vis supra-additive effectiveness. The use of combination therapy is rationalized by both the vast molecular complexity of and the vast intra- & inter-tumoral genetic diversity seen in all cancers. There is overwhelming evidence, that in order to effectively treat cancers, the use of at least two or more anti-neoplastic agents in combination is required. The rationale being, to target different molecular susceptibilities within individual patients' tumors and with the hope to use these therapies to reduce the emergence of drug resistance or at-least to prolong its development.

Importantly, with the advent of molecularly targeting agents (MTAs), molecular vulnerabilities within cancer types / patient tumors are able to be targeted with more specificity and less toxic side effects.<sup>31</sup> The utility of MTAs was demonstrated by the drug imatinib (Gleeve/Glivec; Novartis) capable of inhibiting an oncogenic fusion of BCR-ABL. Fusion of ABL to BCR was caused by a chromosomal translocation via the breakage of chromosome 9 at the ABL gene and fusion to chromosome 22 at the BCR gene, which produced a tyrosine kinase with constitutive activity present in cases of both chronic myeloid leukemia and gastrointestinal stromal tumors; patients treated with imatinib in

both conditions responded extremely well, superior to the standard chemotherapeutic regimens with minimal side-effects.<sup>32-34</sup> Despite the overwhelming success of the introduction of MTAs, such as imatinib, using a monotherapy for treatment of a heterogenous cancer population has the potential to select for unresponsive clonal populations of tumor cells or create selective pressure against cells within the population influencing the development of drug resistance and thereby, causing reemergence of the disease.<sup>35, 36</sup>

In a review by Dancey and Chen, the authors illustrate that “with few exceptions” drug regimens that have proven curative in cancer treatment have been a combination of individually potent agents, with non-overlapping toxicity, at ideal doses and on a schedule adapted to coincide with normal cell recovery.<sup>31</sup> To demonstrate this the authors have included several successful drug combinations in patients containing both a molecularly targeted agent in conjunction with a standard chemotherapeutic drug regimen in the treatment of breast (trastuzumab), colorectal (bevacizumab) and non-small lung (bevacizumab) cancers.<sup>37-39</sup> Furthermore, drugs when used in combination have the possibility to produce synergistic effects either through overlapping mechanisms of action or by off-target effects that enhance and augment the overall pharmacological impact of the drugs beyond their individual effect levels. By identifying these drug-drug interactions through screening we can provide preclinical combinations earlier for potential clinical translation.

To better prioritize the potential of a prospective drug combination we must first identify whether the pharmacological interactions of the drugs are favorable or otherwise. Drugs are capable of interacting pharmacologically to produce an additive, antagonistic,

or synergistic response. Additivity occurs when the effect of two or more drugs is summative, where the sum of the effects of drug A or drug B individually is equivalent to the effects of the same concentrations of A and B together. Antagonism occurs when the effect of two or more drugs is negative, where the combination of drug A plus drug B is less effective than the sum of the effects of the individual drugs. Synergism occurs when the effect of two or more drugs in combination is greater than the additive effects of the individual drugs. In order to identify such pharmacological relationships, different analytical models and methodologies have been created and utilized in high throughput screening, such as Bliss and Loewe additivity models, isobologram analysis, Chou-Talalay median effect models and population-based lifetime modeling.<sup>40-44</sup>

In addition to qualifying a potential drug-drug interaction, we can use different “omics” (genomics, proteomics, metabolomics...etc) approaches to provide a more feasible biological rationale and testable hypothesis when attempting to advance a drug combination from *in vitro* to *in vivo*.<sup>45</sup> In particular, by sequencing and analyzing the whole transcriptome of different cancers, mutational “hotspots” can be identified that allude to susceptible oncogenic drivers and alterations in tumor suppressors. A study by Wood and colleagues in 2007 performed whole exome analysis with the DNA extracted from 11 breast and colorectal tumors, and illustrated commonality in several receptor tyrosine kinases (RTK) as well as the PI3K pathway, as well as some less common differences for example, in pathways responsible for cell adhesion.<sup>46</sup> Proteomic analysis of several RTKs within the PI3K pathway by Stommel et. al 2007 revealed downstream activation and contribution by coactivators of PI3K in a multitude of glioblastoma multiforme (GBM) cell lines, and that in order to provide sufficient inhibition of downstream signaling within

the PI3K pathway, it was necessary to target at least two components within the PI3K pathway as demonstrated by the authors.<sup>47</sup>

Altogether, these different methodologies provide a more analytical and precise manner of targeting specific susceptibilities at the tumor-level in patients, but effectively facilitating such treatment in patients has some limitations. Specifically, the tumor population is not just a single homogeneous population of cells but rather several smaller heterogenous populations of tumor cell subclones, tumor stem cells, and tumor-associated cells, that will each respond differently to stimuli or applied pressures.<sup>45</sup> Given this information, it is easy to see that a true representation of the total population by genomic, proteomic, and /or metabolomic analysis may be skewed towards expression from the larger cellular population. Another limitation that can restrict the proper implementation of “omics” approaches in treatment, is the presence of parallel contributors to downstream activation in major oncogenic pathways. For instance, several reports have illustrated how mutations in K-RAS and PI3K contribute to a poor overall response to compounds that target RTKs.<sup>48, 49</sup>

#### **1.4 Where Do We Go Now: Data-driven Approaches for Drug Discovery**

While the rationale for combining antineoplastic agents seems logical, the practicality and feasibility of ensuring the success of these drug combinations is another challenge entirely. A review by Dancey and Chen on combining targeted agents with standard chemotherapeutic modalities outline several contributing factors that have either resulted in success or failure in the clinic. Namely, the authors outline three key factors:

the nature of how the drug exerts its effects individually or in combination, the functionality and presence of the target in question, and any cellular factors that affect the drug's function and/or biological consequences of modulating the specific target.<sup>31</sup> One of our greatest challenges as researchers is to use the resources we have available to interpret the information from data generation to create research questions, and advance our knowledge for clinical applications. For instance, given the sophistication of more modern techniques and technologies, the scientific community has been able to incorporate data accumulated from cancer patients, tumors, and cancer cell lines into various databases. These resources include the cancer genome atlas (TCGA), the cancer cell line encyclopedia (CCLE), and catalogue of somatic mutations in cancer (COSMIC) databases, which have all been utilized to advance the quality of cancer research.<sup>50-52</sup> It is through the use of these resources in conjunction with solid experimentation and innovation that we can push the bounds of cancer research and increase our reach to the clinic.

#### Dissertation Overview:

In chapter 2 of this document, I will review the efforts of our laboratory to confirm the identified synergistic drug-drug interactions identified in an unbiased drug combination high throughput screening campaign contracted by the NCI. In particular, our goal was to design a strategy using isobologram plot analysis, the Chou-Talalay median effect model and the pharmacodynamic drug interaction model to generate data for identifying, confirming, and prioritizing drug combinations that display synergistic growth inhibitory effect towards cancer cell population of the NCI-60 panel.<sup>53, 54</sup> It is through our data-driven

methodologies that we were able to develop a mechanistic hypothesis to posit the potential mechanism of synergistic action for several drug combinations, and to design an imaging assay to follow up with this hypothesis.

Chapter 3 is a review and introduction to the use of 3D cell culture as a more physiologically relevant model for drug discovery. In addition, this chapter outlines the advantages and disadvantages within several 3D methodologies as well as advances that provide elements of physiological relevance and clinical translation within an *in vitro* 3D model. Lastly, chapter 3 outlines some of our laboratory's previous use with ultra-low attachment (ULA) conditions to lead into our use of ULA for the characterization of multicellular tumor spheroids (MCTS) of head and neck squamous cell carcinoma (HNSCC) cell lines.

Chapter 4 represents characterization studies for HNSCC where our goals were to determine changes in diameter, viability, and tumor microenvironmental characteristics over time in culture in ULA conditions. Furthermore, we wanted to optimize MCTS cell culture conditions for the purpose of drug screening.

Chapter 5 outlines the use of our optimized HNSCC MCTSs to determine drug sensitivity across 19 FDA approved compounds with 2D as a comparator. Our goal was to determine any changes in sensitivity between 2D and 3D and highlight effective drugs in 3D alone or both 2D and 3D. In addition, we designed a metric to evaluate the overall effect that drugs have across several parameters including morphology, diameter, and changes in cellular viability as imaging alone or CTB alone seemed to be insufficient to evaluate drug effect.

Chapter 6 is an overview of the implications, limitations, and future directions of the accumulated work from this dissertation. In particular, this chapter seeks to explore the major conclusions and rationalize the significance of this body of work as it pertains to cancer drug discovery.

## **2.0 Confirmation of Selected Synergistic Cancer Drug Combinations Identified in an HTS Campaign and Exploration of Drug Efflux Transporter Contributions to the Mode of Synergy.**

### **2.1 NCI ALMANAC and its Influence on Drug Combination Screening**

The NCI has previously published their analysis of data generated by our laboratory and a second contracted laboratory to screen drugs in pairwise drug combinations as an HTS of 100 FDA-approved compounds. The goal of generating such a large amount of data was for the production of a database to be used as a resource for the scientific community, in order to prioritize or categorize favorable (greater than additive) drug-drug interactions and otherwise, dubbed the ALMANAC (A Large Matrix of Anti-Neoplastic Agent Combinations).<sup>55</sup> The NCI established their own method of activity scoring amongst drug combinations and named their method “ComboScore”, the authors were able to analyze the combined activity of approximately 5,232 drug pairs tested against the NCI-60 cell line panel composed of 9 different tumor types: Breast, CNS, Colon, Leukemia, Melanoma, NSC Lung, Ovarian, Prostate, and Renal.<sup>55</sup> Through these efforts, the authors identified twenty combinations that merited a follow-up *in vivo* using mouse xenografts of tumor cells from the NCI-60 cell line panel, and two that went on to phase I clinical trials: clofarabine (antimetabolite) & bortezomib (proteasome inhibitor), and nilotinib (tyrosine kinase receptor inhibitor) & paclitaxel (mitotic inhibitor).<sup>55</sup> Overall, the authors were able to develop a database resource where there was a great unmet need, and the possibility for translation through logical progression by performing

experiments from contracted *in vitro* screening, to their own *in vivo* animal studies, and finally, culminating in clinical trials.

## **2.2 HTS Campaign to Identify Synergistic Drug-Drug Interactions for Confirmation**

As mentioned above, our laboratory was one of the contracted groups, tasked with the development and implementation of a screening strategy to identify greater than additive drug-drug interactions across the NCI-60 cell line panel and across 100 FDA approved drugs.<sup>56</sup> With such a screening effort comes challenges, in particular, being able to create a strategy that could: scale up in throughput; ensure that a robust and reproducible signal window with adequate performance statistics above passable for each assay existed; analyze the pharmacological relationship between two drugs in combination, and avoid compound handling & tracking errors.<sup>56</sup> In order to efficiently screen 100 compounds in pairwise combinations, we had to revise the traditional NCI 60 assay paradigm of 96-well plate format, 48hr compound exposure, in 5% fetal bovine serum (FBS), with endpoint measurements from fixing and staining with sulforhodamine B to 384-well plate format, 72hr compound exposure, 10% FBS, and endpoint measurements with CellTiter-Glo homogenous viability detection reagent.<sup>56</sup>

Given the changes implemented to the traditional NCI screening campaign, it was also necessary for the selection of seeding density across the 60 cell line panel to represent a cellular density that allowed for active proliferation over the 96hr period of incubation, and as such, conditions were optimized through two independent seeding density experiments to allow for such observations of active cellular proliferation during

compound exposure.<sup>56</sup> Through the selection of optimal seeding densities, we were also able to observe the assay performance statistics which both aided in our selection of seeding densities and allowed us to identify potential poor performers for the future growth inhibition assays for selection of concentrations for the screening campaign. To appropriately select concentrations for each individual compound prior to the screen, 5-point, 10-fold serial dilution growth inhibition assays were performed across each cell line, with GI<sub>50</sub> curves representing the % growth response observed with each compound.<sup>56</sup> With the pilot screen of 20 compounds, we were able to observe clusters of response linked to drug mechanisms of action and their effect across the panel of cell lines as seen in figure 1 (Figure 1).

To determine the effects of drugs in pairwise combination, we determined individual growth inhibition 50 (GI<sub>50</sub>) values of each compound, and selected concentrations for pairwise combinations within a 4x4 matrix configuration (Figure 2); all growth inhibitory effects produced in combination were scored and categorized vs individual GI<sub>50</sub>'s using a novel drug interaction score (DI) which takes into account the observed growth inhibitory effect for each drug combination and the measured replicates within the drug combination matrix as a modification of the Bliss independence model, and uses the pooled variance of the sample means between drugs A and B, to provide a score representative of the number of standard deviations away from the sample mean the observed drug effect is for each combination.<sup>56</sup> The DI score represents the Bliss independence formula divided by the square root of pooled variance between replicate measurements of individual drug effect from each drug matrix. The end result is a value representative of a number of standard deviations away from the drug effect mean. A DI

score of  $>3$  indicates synergy,  $< -3$  indicates antagonism, and a score between  $-3$  and  $3$  indicates an additive relationship. This score allowed us to prioritize putative synergistic drug-drug interactions for follow up.<sup>56</sup> We performed initial confirmation studies with a single combination between a drug designed and created at the University of Pittsburgh's

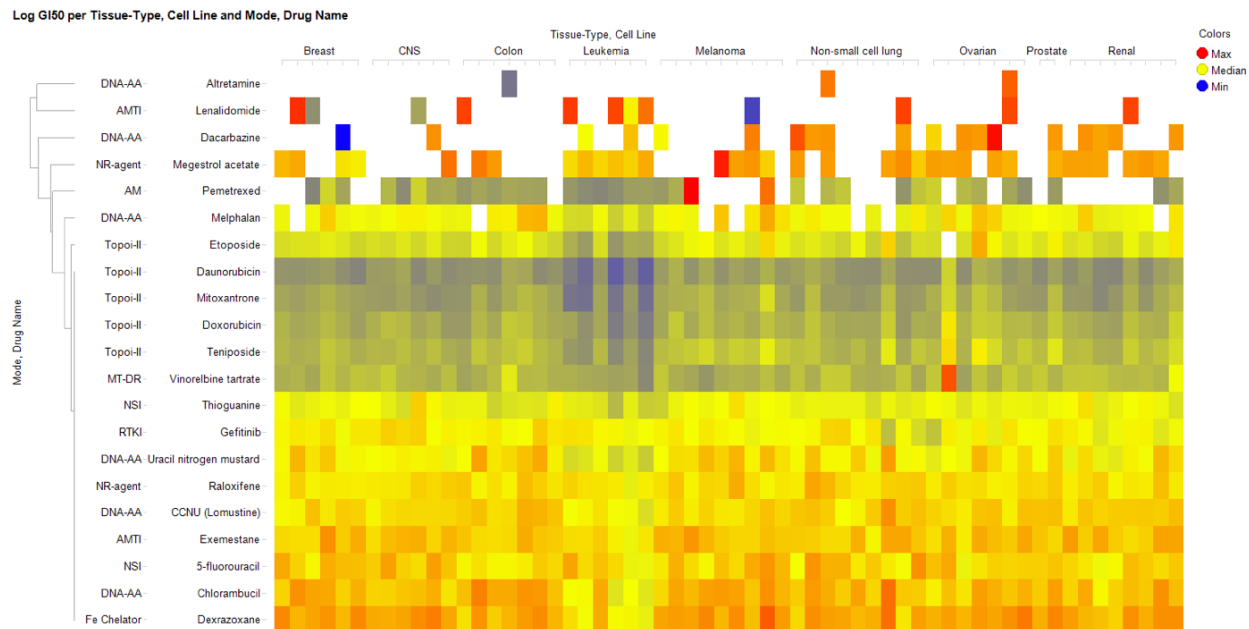


**Figure 1 Hierarchical Clustering Analysis of the Individual GI50 data for the Pilot HTS Screen**

A two-way hierarchical clustering analysis of the individual GI<sub>50</sub>s for the 20 pilot drugs and doxorubicin against the 60 cell lines grouped by tumor type shows drug clusters that respond with similar growth response patterns across tissue types and cell lines.

20 x Drug Combination  
Matrices (4 x 4)/Plate

16 wells: 1 x DMSO control well;  
3 x individual drug concentration wells per drug;  
and 9 x drug combination (3 x 3) wells

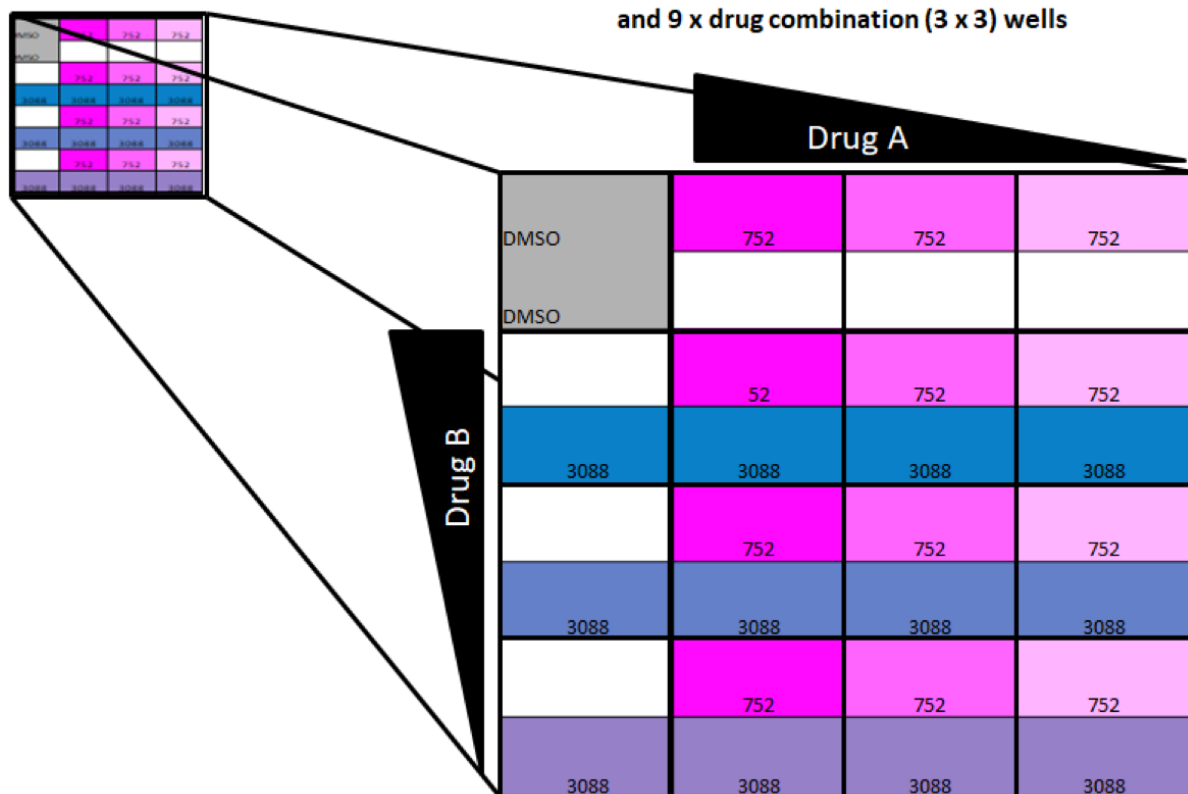


**Figure 2 4 x 4 Drug Combination Matrices**

Each individual Drug Combination Matrix included 3 x 3 DC wells (9 total) together with three wells (6 total) containing each of the corresponding individual drug concentrations, and one DMSO control well.

School of Pharmacy in collaboration with Dr. Barry Gold's laboratory, an apurinic/aprimidinic endonuclease-1/redox effector factor-1 (APE-1) inhibitor called AJAY-4 and the BRAF V600E kinase inhibitor vemurafenib, using the combination index (CI) plot analysis.<sup>53</sup> Through our efforts we decided to expand our analysis in the pilot screen to include two additional drug-drug interaction analysis methods in following up with prioritized combinations flagged as synergistic, to be discussed later in this chapter.

In the pilot phase of the NCI-60 DC HTS campaign, 190 individual 4 x 4 drug combination matrices (DCMs) of all possible pairwise combinations of 20 cancer drugs were screened against all NCI 60 tumor cell lines.<sup>56</sup> Although there was no obvious tissue type or cell line bias in the distribution of synergistic DI scores (DI scores >3) from the pilot HTS, eleven (5.8%) DCMs formed between six drugs accounted for 54% of DI scores >3 with each of the individual drugs participating in 3-4 DCMs; megestrol acetate, mitoxantrone, vinorelbine tartrate, raloxifene, gefitinib and daunorubicin.<sup>56</sup> It is standard practice in any screening campaign to confirm primary HTS actives as qualified hits before they progress into follow up assays and MOA studies. We previously reported the confirmation *in vitro* of the synergistic drug interaction between the vinca-alkaloid microtubule assembly inhibitor vinorelbine (Navelbine®) tartrate and epidermal growth factor-receptor (EGF-R) tyrosine kinase inhibitor (TKI) gefitinib (Iressa®) in the SK-MEL-5 melanoma cell line (Figure 3A-D).<sup>56</sup> In the studies presented herein, we applied the following criteria to select additional DCs flagged in the pilot DC HTS with DI scores >3 for confirmation of synergy *in vitro*: 1) DCs that exhibited DI scores >3 against multiple tumor cell lines; 2) DCs where more than one well in the DCM produced DI scores >3; 3) DCs that were cytotoxic rather than growth inhibitory or cytostatic; and 4) DCs where the individual drugs in the DC exhibited concentration dependent growth inhibition in the selected tumor cell lines. Four DCs from the pilot DC HTS met these criteria (Table 1).

Through searching the available scientific literature to determine a potential MOA that could explain the observed synergism, we discovered that a publication by Szakacs and colleagues (2004) established efflux transporter expression across the NCI60 cell line panel, and implicated several of the cell lines within our confirmation studies as

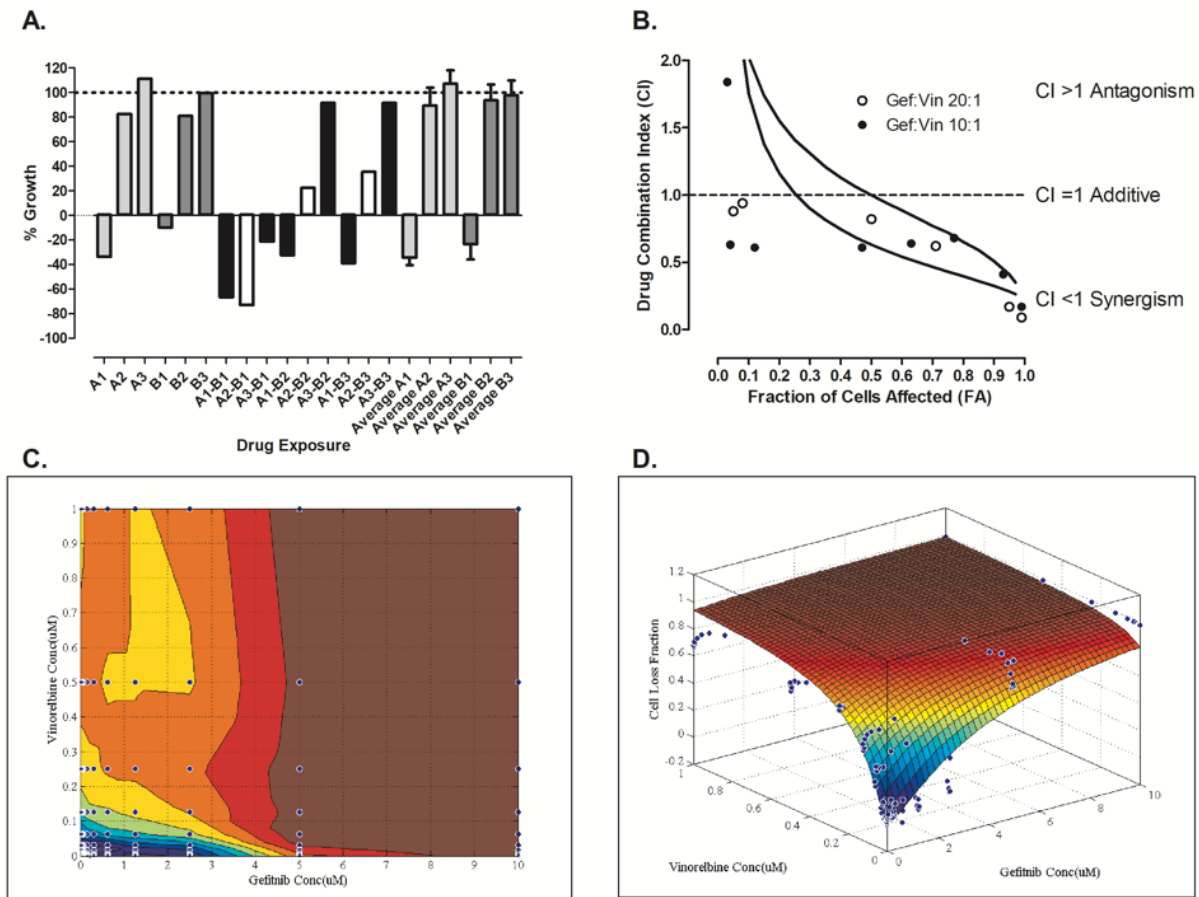


**Figure 3 Confirmation of Gefitinib-Vinorelbine Flagged Synergy**

**A) Pilot HTS Drug Combination Matrix Data** Vinorelbine (Drug A) was screened individually and in DC wells at concentrations of 1.0 (A1), 0.1 (A2), and 0.01  $\mu\text{M}$  (A3), while the gefitinib (Drug B) concentrations were 10.0 (B1), 1.0 (B2), and 0.1 (B3)  $\mu\text{M}$ . The % growth indicated on the Y axis for the 3 individual drug concentrations of vinorelbine (light grey bars) and gefitinib (dark grey bars) together with the 9 DC wells (black and white bars) from the 4 x 4 DCM are presented along with the means  $\pm$  SD (n=19) of the replicate data from the 3 individual drug concentrations screened in other DCMs. The 3 DC wells with DI scores >3 are indicated by the white bars (A2-B1, A2-B2, and A2-B3). Whether the bar represents an individual drug concentration of A or B or drug combination (A-B) well from the DCM, or the average of 19 replicates of the individual drug concentrations is indicated on the X axis. **B) Combination Index Analysis** The growth inhibition/fraction of SK-MEL-5 cells affected data from a more extensive 10 x 10

vinorelbine and gefitinib DCM was analyzed in the Chou-Talalay median effects model using the COMPUSYN software to calculate combination index (CI) scores and fit curves for the 20:1 and 10:1 fixed ratios of gefitinib and vinorelbine. CI scores <1.0 indicate that two drugs interact synergistically. **C) Isobologram Plot** The data from the 10 x 10 vinorelbine and gefitinib DCM was plotted as an isobologram contour graph. The concave contour lines of the isobologram plot indicate that vinorelbine and gefitinib interacted synergistically. **D) Drug-Drug Interaction Surface Response** The data from the 10 x 10 vinorelbine and gefitinib DCM was analyzed using the pharmacodynamic drug-drug interaction model to fit the experimental data and construct a three-dimensional graph of the data. The fitted  $\alpha$  parameter of the pharmacodynamic drug-drug interaction model was 0.77, which is >0 and indicates that vinorelbine and gefitinib interacted synergistically.

overexpressing ATP binding cassette transporters (ABC) ABCB1, ABCC1, and/or ABCG2, which have been implicated as playing a role in cancer drug resistance.<sup>57</sup> Furthermore, within each combination was the presence of an ABC transporter substrate and inhibitor as indicated in Table 2. This chapter describes the process used to confirm that the DCs interacted synergistically to inhibit selected tumor cell line growth *in vitro*, and our exploration of drug interactions with ABC transporters as a plausible MOA for the observed synergies.

**Table 1 Selected Drug Combinations, NCI-60 Cell Lines, Tumor Histology's, Individual Drug GI50s, and Drug Interaction Analysis Summary**

DC	NCI-60	Tumor	Drug-A GI50 $\mu$ M			Drug-B GI50 $\mu$ M			DC	CI	CMPYSYN	ISBG	PDI	PDI
#	Cell Line	Histology	Drug	Mean	SD	Drug	Mean	SD	Ratio	Score	DIC	DIC	$\alpha$ -Param.	DIC
1	KM12	Colon	Gefitinib	4.26	2.37	Mitoxantrone	0.22	0.1	50:1	CI <1	Synergy	Synergy	5.76	Synergy
1	MDA-MB-468	Breast	Gefitinib	0.77	0.43	Mitoxantrone	0.05	0.01	50:1	CI <1	Synergy	Synergy	37.4	Synergy
1	OVCAR-5	Ovarian	Gefitinib	0.99	0.87	Mitoxantrone	0.13	0.06	50:1	CI <1	Synergy	Synergy	74.5	Synergy
1	PC-3	Prostate	Gefitinib	5.67	4.1	Mitoxantrone	0.18	0.08	50:1	CI <1	Synergy	Synergy	1.4	Synergy
2	HCT-116	Colon	Raloxifene	11.45	4.05	Mitoxantrone	0.02	0.01	100:1	CI <1	Synergy	Synergy	1	Synergy
2	HCT-15	Colon	Raloxifene	17.5	5.95	Mitoxantrone	0.06	0.04	100:1	CI <1	Synergy	Synergy	0.92	Synergy
2	KM12	Colon	Raloxifene	23.7	2	Mitoxantrone	0.21	0.18	100:1	CI <1	Synergy	Synergy	1.2	Synergy
2	SW-620	Colon	Raloxifene	22.3	5.61	Mitoxantrone	0.03	0.02	100:1	CI <1	Synergy	Synergy	0.06	Synergy
3	DU-145	Prostate	Raloxifene	0.28	0.14	Daunorubicin	75	NA	100:1	CI <1	Synergy	Synergy	41	Synergy
3	NCI-H23	NSC lung	Raloxifene	0.15	0.04	Daunorubicin	34.4	NA	100:1	CI <1	Synergy	Synergy	4.8	Synergy
3	NCI-H522	NSC lung	Raloxifene	0.24	0.04	Daunorubicin	15.4	NA	100:1	CI <1	Synergy	Synergy	1	Synergy
4	SK-MEL-5	Melanoma	Gefitinib	4.63	0.15	Vinorelbine	0.22	0.04	10:1	CI <1	Synergy	Synergy	0.76	Synergy
4	MDA-MB-435	Melanoma	Gefitinib	11.4	0.61	Vinorelbine	0.19	0.12	10:1	CI <1	Synergy	Synergy	3.19	Synergy
4	HL-60	Leukemia	Gefitinib	10.1	2.56	Vinorelbine	0.06	0.01	10:1	CI <1	Synergy	Synergy	1.53	Synergy
4	MOLT-4	Leukemia	Gefitinib	6.43	2.1	Vinorelbine	0.06	0.01	10:1	CI <1	Synergy	Synergy	3.98	Synergy
4	RPMI-8226	Leukemia	Gefitinib	5.18	0.45	Vinorelbine	0.09	0.04	10:1	CI <1	Synergy	Synergy	0.82	Synergy

DC = drug combination

# = DC number

NCI-60 = National Cancer Institute 60 tumor cell line panel.

GI<sub>50</sub> = drug concentration at which cell growth was inhibited by 50%.

DC Ratio = fixed concentration ratio of drug A:drug B.

CI = combination index score

CMPYSUN = COMUSYN freeware online software program

DIC = drug interaction classification

Synergy = synergistic drug interaction

Pot. = potentiation.

ISBG = Isobologram contour graph

PDI = Pharmacodynamic Drug Interaction model

$\alpha$ -Param. = fitted  $\alpha$  parameter of the pharmacodynamic drug interaction model

Mean = average of replicate independent IC<sub>50</sub> determinations, n = 2-4.

SD = standard deviation of the mean

## **2.3 Materials and Methods**

### **Reagents**

Formaldehyde 37% was purchased from Sigma-Aldrich (St. Louis, MO). Hoechst 33342 was purchased from Life Technologies (Thermo Fisher Scientific, Waltham, MA). Dimethyl sulfoxide (DMSO) 99.9% high-performance liquid chromatography grade was obtained from Alfa Aesar (Ward Hill, MA). Dulbecco's Mg<sup>2+</sup>- and Ca<sup>2+</sup>-free phosphate-buffered saline (PBS), Minimum Essential Medium (MEM) supplemented with both GlutaMax™ and Earle's salts, and Geneticin® was purchased from Gibco (Grand Island, NY). Dulbecco's modified Eagle's medium (DMEM) and Roswell Park Memorial Institute Medium (RPMI-1640) were purchased from Corning (Manassas, VA). Fetal bovine serum (FBS), L-glutamine, penicillin and streptomycin (P/S) were purchased from Thermo Fisher Scientific. FDA approved anticancer compounds were obtained from commercial sources and shipped to the University of Pittsburgh by the National Cancer Institute (NCI) Developmental Therapeutics Program (DTP), as previously reported. The ABCG2 inhibitor KO-143 was kindly provided by Lisa C. Rohan PhD (University of Pittsburgh, School of Pharmacy).

### **Cells and Cell Culture Methods**

The NCI-60 cell lines were obtained from the NCI DTP Tumor Repository which performed Applied Biosystems AmpFLSTR® Identifiler® testing with PCR amplification to confirm consistency with the published Identifiler® STR profile for each of the NCI-60 cell lines and tested them for mycoplasma contamination. NCI-60 cell lines were maintained as previously described and cultured at 37°C in 5 % CO<sub>2</sub> and 95% humidity in either RPMI-1640 or DMEM supplemented with 10% FBS, 1% 2mM L-glutamine, and

100 U/mL penicillin and streptomycin.<sup>56</sup> NCI-60 cell line 384-well growth inhibition assays were conducted as described previously. Madin-Darby Canine Kidney II (MDCKII) cell lines stably expressing human ABCG2 (MDCKII-ABCG2) or transfected with empty vector (MDCKII-EV) were kindly provided by Dr. Patrick McNamara (University of Kentucky, College of Pharmacy) and were cultured in MEM supplemented with 5% FBS, 1% P/S, and 800µg/mL Geneticin® as described previously.<sup>58, 59</sup>

### **NCI-60 Cell Line Growth Inhibition Assays.**

The 384-well NCI-60 cell line growth inhibition assays using the Cell Titer Glo® (CTG) (Promega Corporation, Madison, WI) homogeneous cellular ATP detection reagent have been described previously.<sup>56</sup> On day 1 of the assay the NCI-60 cell lines were harvested by trypsinization, centrifugation, and viable trypan blue excluding cells were counted using a hemocytometer. 45 µL of cells at the appropriate cell density were seeded into the wells of white opaque clear bottomed 384-well barcoded assay plates (Greiner BioOne, Cat # 781098) using a Matrix™ multichannel pipettor (ThermoFisher, Waltham, MA) or a Microflo (BioTek, Winooski, VT) bulk reagent dispenser. Assay plates were then incubated at 37 °C in 5% CO<sub>2</sub> and 95% humidity for 24 h. On day 2 GI<sub>50</sub> replica daughter plates containing 2 µL of each compound concentration in 100% DMSO were thawed at 37 °C and the compounds were diluted in 98 µL of serum free RPMI-1640 media to an intermediate drug concentration (2 % DMSO), and then 5 µL were transferred into the test wells of the assay plate (0.2% DMSO final) using the 384-well transfer head on a Janus MDT Mini (Perkin Elmer, Waltham, MA) robotic liquid handling platform, plates were centrifuged at 100 x g for 1 minute and returned to an incubator at 37 °C in 5% CO<sub>2</sub> and 95% humidity for 72 h. On day 5, compound treated assay plates were removed from

the incubator, 25  $\mu$ L of CTG was added to the wells using a Microflo bulk reagent dispenser and after 15 min the relative light units (RLUs) were read on the SpectraMax M5e (Molecular Devices, LLC, Sunnyvale, CA). To analyze the growth inhibition data, we normalized the growth of compound-treated wells relative to the corresponding mean growth of our DMSO (0.2%) assay plate control wells (n= 64) and used GraphPad Prism 5 software to plot and fit data to curves using the sigmoidal dose response variable slope equation  $Y = \text{Bottom} + [\text{Top}-\text{Bottom}]/[1+10^{(\text{LogGI50}-X)*\text{HillSlope}}]$ . Where bottom is the Y value at the bottom plateau, top is the Y value at the top plateau, Log GI50 is the X value when the response is halfway between the bottom and top and the HillSlope describes the steepness of the curve. The growth inhibition 50 (GI<sub>50</sub>) value represents the concentration at which cell growth was inhibited by 50%.

### **Confirmation of Drug Combinations Scored Synergistic in the Pilot DC HTS**

We arrayed 10 x 10 drug combination matrices (DCMs) onto 384-well master plates (Chapter 2 Figure 4). Each DCM included 9 x 9 DC wells (81 total) together with nine wells (18 total) containing each of the corresponding individual drug concentrations, and one DMSO control well. Two 10 x 10 DCMs were matrices were arrayed in columns 3 to 22 of the 384-well plates, together with DMSO (0.2%) controls in columns 1, 2, 23, and 24 (n=64). We used three distinct methods to analyze the interactions between the two drugs in the DCMs as described previously.<sup>56</sup>

The Chou-Talalay Median-Effect model accounts for the dose responses of the two interacting drugs to determine the combination effect.<sup>60, 61</sup> The combination index (CI) score  $CI = (D_1/D_{X1}) + (D_2/D_{X2})$ , where  $D_1$  and  $D_2$  denote the doses of compound 1 and compound 2 required to reach an effect of X% as individual drug treatments, while

$D_{X1}$  and  $D_{X2}$  are the doses needed in combination to inhibit X% respectively. DCs with  $CI > 1$  exhibit antagonistic interactions, DCs with  $CI = 1$  exhibit additivity, and DCs with  $CI < 1$  exhibit synergistic interactions. The COMPUSYN freeware program was utilized to calculate CI values and evaluate DC synergy as described previously.<sup>53, 56</sup>

Isobologram plots can be used to determine whether drug interactions are additive.<sup>62</sup> In a plot of equally effective dose pairs termed isoboles for a single effect, when a specific effect level such as 50% of maximum is selected, the doses of drug A and drug B alone that produce this effect are plotted as axial points in a Cartesian plot. When a combination of drugs is additive, then the locus of points (dose pairs) that produce this effect form a straight-line connecting A to B. If the line connecting the actual dose pairs that produces the selected effect level experimentally significantly diverges from a straight line between A and B, then the drug combination is not additive. Isobologram plots were constructed in MATLAB® as described previously.<sup>56</sup>

The pharmacodynamic drug interaction (PDI) model has been used to describe the relation between drug effects such as % growth inhibition (%GI) or cell loss fraction (CLF).<sup>63</sup> The drug interaction effect  $F = F_{max} \times (C_A/IC_{50A} + C_B/IC_{50B} + \alpha \times C_A/IC_{50A} \times C_B/IC_{50B})^n / (C_A/IC_{50A} + C_B/IC_{50B} + \alpha \times C_A/IC_{50A} \times C_B/IC_{50B})^n + 1$ . Where  $F_{max}$  is the maximal effect of drug A and drug B,  $C_A$  and  $C_B$  are the concentration of drug A and drug B,  $IC_{50A}$  and  $IC_{50B}$  are the individual drug concentrations that induce 50% of the max growth inhibition or cell loss,  $n$  is the slope of the response surface, and  $\alpha$  is a parameter which characterizes the synergistic status of drug interaction. When  $\alpha = 0$  the drug interaction is additive, for  $\alpha > 0$  the drug interaction is synergistic, and for  $\alpha < 0$  the drug interaction is

antagonistic. The PDI analysis and plots were produced in MATLAB® as described previously.<sup>56</sup>

### **High Content Imaging Hoechst Accumulation Assays**

MDCKII-ABCG2 and MDCKII-EV cells were harvested, counted and seeded at 20,000 cells per well in 384-well black walled clear bottom microtiter plates (Greiner BioOne, # 781091) and were cultured at 37°C in 5 % CO<sub>2</sub> and 95% humidity overnight to allow cells adhere and form monolayers. After 8-12 h in culture, MDCKII-ABCG2 and MDCKII-EV adherent monolayers were exposed to the ABCG2 substrate Hoechst 33342 at 8µg/mL for 60 minutes at 37°C in 5 % CO<sub>2</sub> and 95% humidity before being fixed with 3.7% formaldehyde for 30 minutes, washed 3 times with 80µL PBS, and then two fluorescent images were acquired per well in the DAPI channel using a 10x Plan Fluor 0.3 NA objective the ImageXpress Micro (IXM) (Molecular Devices LLC, Sunnyvale, CA) imaging platform. The IXM is an automated wide field high content imaging platform integrated with the MetaXpress Imaging and Analysis software (Molecular Devices LLC). The IXM optical drive includes a 300 W Xenon lamp broad spectrum white light source and a 1.4-megapixel 2/3" chip Cooled CCD Camera and optical train for standard fluorescence imaging and a transmitted light module with phase contrast. The IXM has the following Zero Pixel Shift filter sets; DAPI, FITC/ALEXA 488, CY3/TRITC, CY5, and Texas Red. To acquire images of Hoechst-stained nuclei in MDCKII-ABCG2 and MDCKII-EV cells we used the IXM automated image-based focus algorithm to acquire both a coarse focus (large µm steps) set of images of Hoechst stained objects in the DAPI channel in the first well to be imaged, followed by a fine (small µm steps) set of images

to select the best focus image. In all subsequent wells, only the fine focus set of images were acquired to select the best focus Z-plane.

The IXM is integrated with the MetaXpress Imaging and Analysis software (Molecular Devices LLC, Sunnyvale, CA) and we used the multi-wavelength cell scoring (MWCS) image analysis module to quantify the integrated fluorescent intensities of the Hoechst-stained nuclei in digital images acquired on the IXM. The MWCS module image segmentation identified and classified Hoechst 33342 stained fluorescent objects in the DAPI channel that exhibited appropriate fluorescent intensities above background and morphology (size, width, length, and area) characteristics of MDCKII nuclei and used these objects to create nuclear masks for each cell. For MDCKII-ABCG2 and MDCKII-EV monolayers we defined the approximate minimum width of Hoechst stained nuclei to be 8  $\mu\text{m}$  and the approximate maximum width to be 15  $\mu\text{m}$ , and the threshold intensity above local background to be  $>50$ . The nuclear mask from in the DAPI channel was then used to quantify the mean integrated and mean average fluorescence intensity of Hoechst within the nuclear regions of MDCKII-ABCG2 or MDCKII-EV cells, and to count the number of cells per image. We utilized the well averaged mean integrated fluorescence intensity data from replicate wells to quantify and compare Hoechst accumulation in MDCKII-ABCG2 and MDCKII-EV cells. We exported the mean integrated and mean average fluorescence intensity data on a per cell basis and analyzed the frequency distributions of the MDCKII-ABCG2 and MDCKII-EV populations using the Spotfire® analytics software (TIBECO, Somerville, MA).

To investigate the effects of known and presumed ABCG2 drug efflux inhibitors on Hoechst accumulation in MDCKII-ABCG2 and MDCKII-EV monolayers, compounds were

added simultaneously with Hoechst and incubated for 60 minutes at 37°C in 5 % CO<sub>2</sub> and 95% humidity. Test compounds included the ABCG2 inhibitor KO-143 in the 0.02 to 10 μM range, and either Gefitinib or Raloxifene at 10 μM.

### **Imaging Data Visualizations**

Pseudo-color fluorescence intensity data visualizations were used to illustrate Hoechst 33342 uptake and accumulation in MDCKII-EV and MDCKII-ABCG2 monolayer cultures. Pseudo-color fluorescence intensity data visualizations present the relative fluorescent intensities in the image indicated as distinct colors with the “hotter” and “brighter” colors (low to high, yellow, red, white) representing higher intensity signals and cooler colors (low to high, purple, cyan, green) representing lower intensity signals.<sup>64</sup>

### **Statistical Analysis of Hoechst Accumulation Experiments**

Hoechst accumulation experiments were performed in triplicate with at least 3 independent experiments where either ABCG2 overexpressing MDCKII cells or EV expressing cells were used to determine a baseline for fluorescent substrate accumulation. Statistically significance differences in Hoechst accumulation between the two populations was determined via a Student’s t-test performed on GraphPad Prism 8 software. Statistical significance in MDCKII cell lines after DMSO, KO-143, Gefitinib, or Raloxifene exposure was determined between treatments using a one-way ANOVA with Tukey’s multiple comparisons as a post hoc test performed on GraphPad Prism 8 software.

## 2.4 Confirmation of Selected Synergistic Drug Combinations Flagged in the Pilot Phase of the NCI-60 DC-HTS Campaign

Table 1 in Chapter 2 lists four DCs identified in the pilot DC HTS campaign that were chosen for follow up confirmation of synergistic growth inhibition interactions in selected tumor cell lines. DC-1 between the EGF-R TKI gefitinib and the topoisomerase inhibitor mitoxantrone met our selection criteria in four cell lines representing different tumor histologies; colon, breast, ovarian and prostate. In contrast, DC-2 between the selective estrogen receptor modifier (SERM) raloxifene in combination with mitoxantrone met the criteria in four colon cancer cell lines. DC-3 between raloxifene and the topoisomerase inhibitor daunorubicin satisfied the criteria in one prostate cancer cell line and two non-small cell lung cancer cell lines. Finally, DC-4 between gefitinib and the microtubule assembly inhibitor vinorelbine fulfilled the criteria in two melanoma and three leukemia cell lines.

To determine whether the pharmacological interactions between two drugs are antagonistic, additive or synergistic involves the testing of a matrix of both drugs over a broad range of concentrations and fixed DC ratios to provide a pairwise interaction surface that is compared to the individual agent responses.<sup>43, 60, 62, 63</sup> To confirm the synergistic interactions between the DCs 1-4 (Table 1) we prepared 10 x 10 DCMs (Figure 4) and analyzed the fraction of cells affected by fixed DC

ratios to calculate CI values, plotted the data in isobologram contour graphs, and applied the PDI model to create three-dimensional (3D) graphs of the data and calculate the fitted  $\alpha$  parameter (Figures 5-8 and Table 1).<sup>56</sup> A 10 x 10 DCM provides a 9 x 9 drug interaction surface with multiple fixed DC ratios for CI analysis (Figure 4).<sup>53, 56</sup> We

selected maximal drug concentrations for the DCMs based on the individual drug  $GI_{50}$ s in the NCI-60 cell lines previously determined in the DC HTS campaign.<sup>56</sup> Figures 5-8 in chapter 2 illustrate a representative example of each of the drug combination confirmation analyses. Figure 5 represents DC-1 of gefitinib plus mitoxantrone in the OVCAR-5 cell line, Figure 6 represents DC-2 of raloxifene plus mitoxantrone in the KM12 colon cancer cell line, Figure 7 represents DC-3 of raloxifene plus daunorubicin in the NCI-H23 non-small cell lung cancer cell line, and Figure 8 represents DC-4 of gefitinib plus vinorelbine in the MDA-MB-435 melanoma cell line (Figures 5-8 and Table 1).

## **2.5 Analysis and Confirmation of Drug Combination 1**

We used maximal drug concentrations of 50 $\mu$ M and 1  $\mu$ M for gefitinib and mitoxantrone respectively (Figure 4), because individually these concentrations inhibited OVCAR-5, KM12, MDA-MB-468, and PC-3 growth by >50% and they were within the range of concentrations used in the DCM of the pilot DC HTS that produced DI scores >3. The central diagonal wells of the 10 x 10 DCM for DC-1 represents a fixed ratio of gefitinib to mitoxantrone of 50:1 (Figure 4), and when the fraction of OVCAR-5 cells that were affected at this fixed DC ratio were analyzed using the COMUSYN software the CI values were <1 and the drug interaction was classified as synergistic (Figure 5A and Table 1). The isobologram contour map of the DC-1 data in OVCAR-5 cells displayed characteristic non-linear contours bending towards the lower left corner of the graph also indicating that the interactions of DC-1 were synergistic (Figure 5B). Finally, the 3D plot of the DC-1 data produced by the PDI model exhibited a sail that projected outward together with a positive

fitted  $\alpha$ -parameter of 74.4 which both indicated that the interactions in DC-1 were synergistic. All three models classified the interactions between gefitinib and mitoxantrone in the OVCAR-5 cell line as synergistic. (Figure 5 and Table 1).

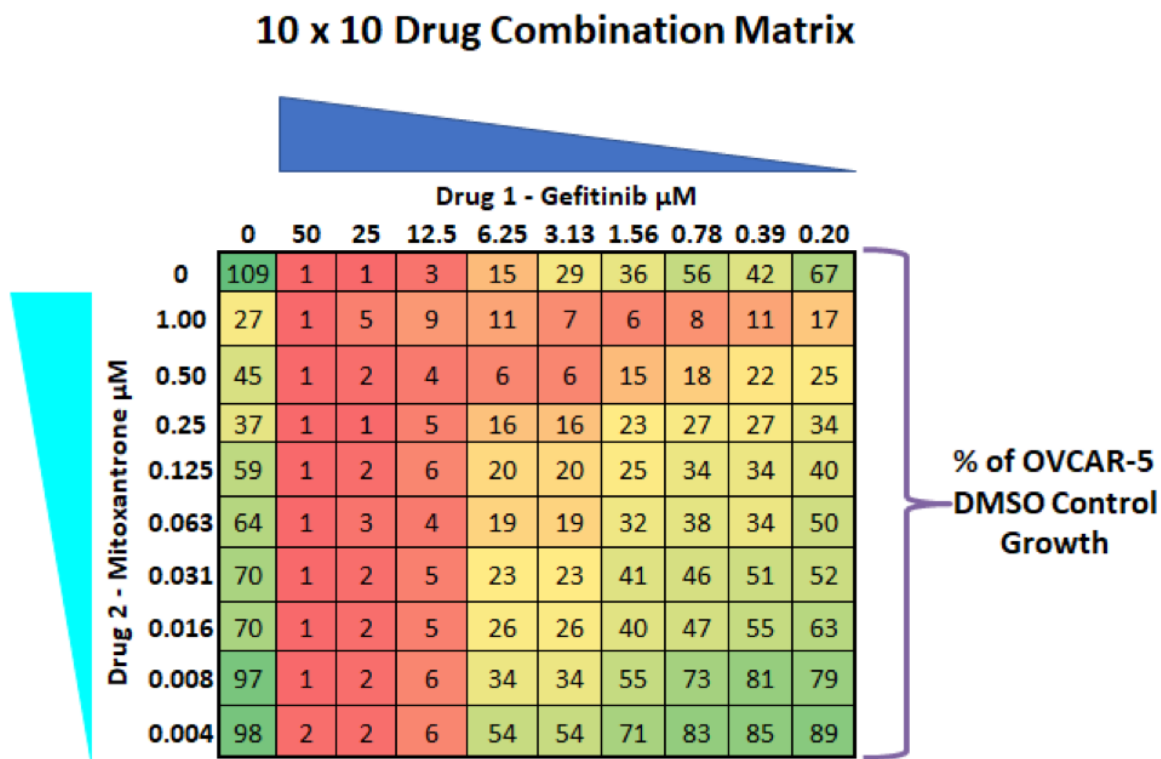
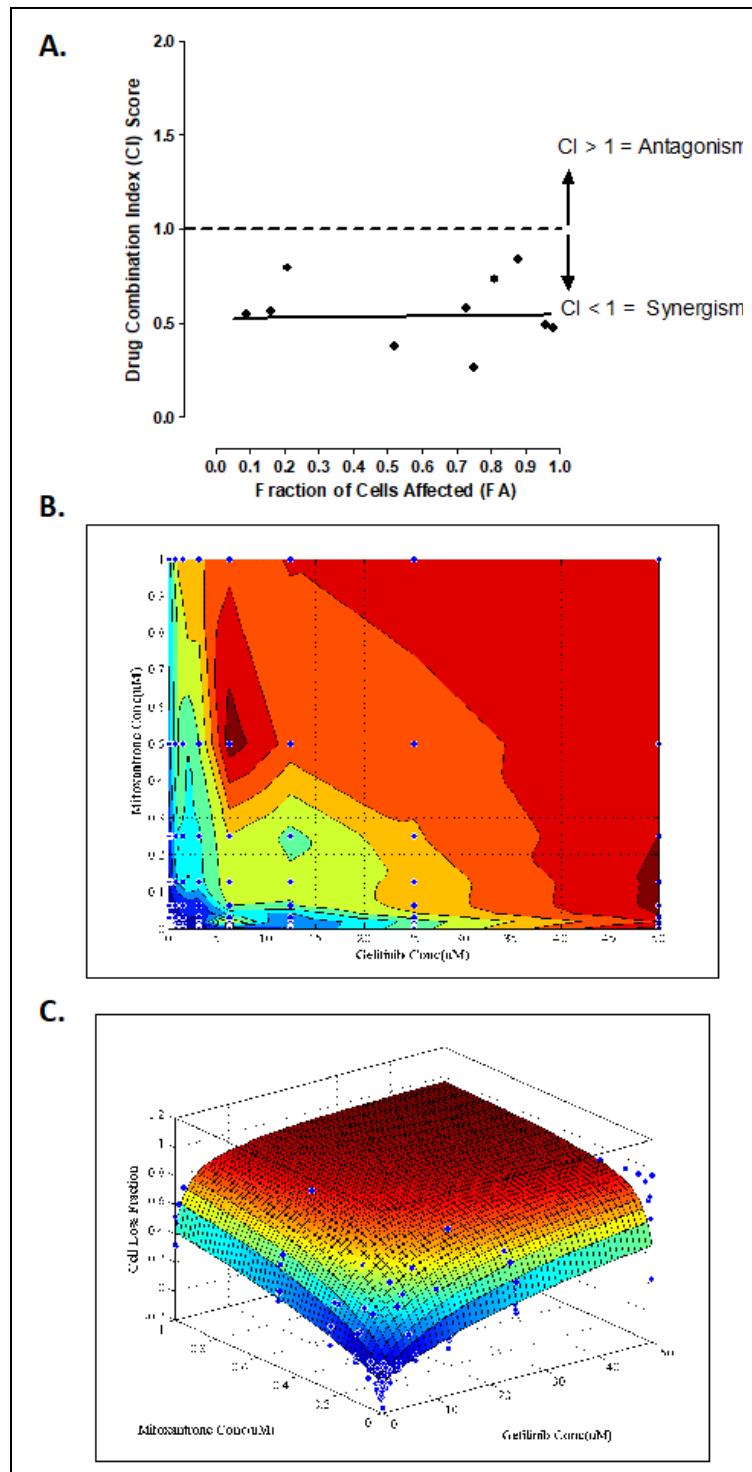


**Figure 4. 10 X 10 Drug Combination Matrix for Confirmation of the Synergy between Gefitinib and Mitoxantrone in OVCAR-5 Ovarian Cancer Cell Line**

Each individual DCM included 9 x 9 DC wells (81 total) together with nine wells (18 total) containing each of the corresponding individual drug concentrations, and one DMSO control well. The relative growth of the OVCAR-5 cells in each DCM well was normalized (%) relative to the mean growth of the DMSO control wells on the assay plate (=64). The % of growth was colored by conditional formatting using a red to green gradient representing low to high growth relative to the mean DMSO controls.

**Figure 5. Confirmation of Drug Combination 1 between Gefitinib and Mitoxantrone in OVCAR-5 Ovarian Cancer Cell Line**



**A) Combination Index Analysis**

The growth inhibition fraction of OVCAR-5 cells affected by a 10 x 10 gefitinib and mitoxantrone DCM was analyzed in the Chou-Talalay median effects model using the COMPUSYN software to calculate combination index (CI) scores (●) and fit the data for the 50:1 gefitinib to mitoxantrone fixed drug ratio. CI scores <1.0 indicate that the two drugs interacted synergistically.

**B) Isobologram Plot**

The data from the 10 x 10 gefitinib and mitoxantrone DCM in OVCAR-5 cells was plotted as an isobologram contour graph. The non-linear concave contour lines of the isobologram plot indicate that gefitinib and mitoxantrone interacted synergistically in OVCAR-5 cells.

**C) Drug-Drug Interaction Surface Response**

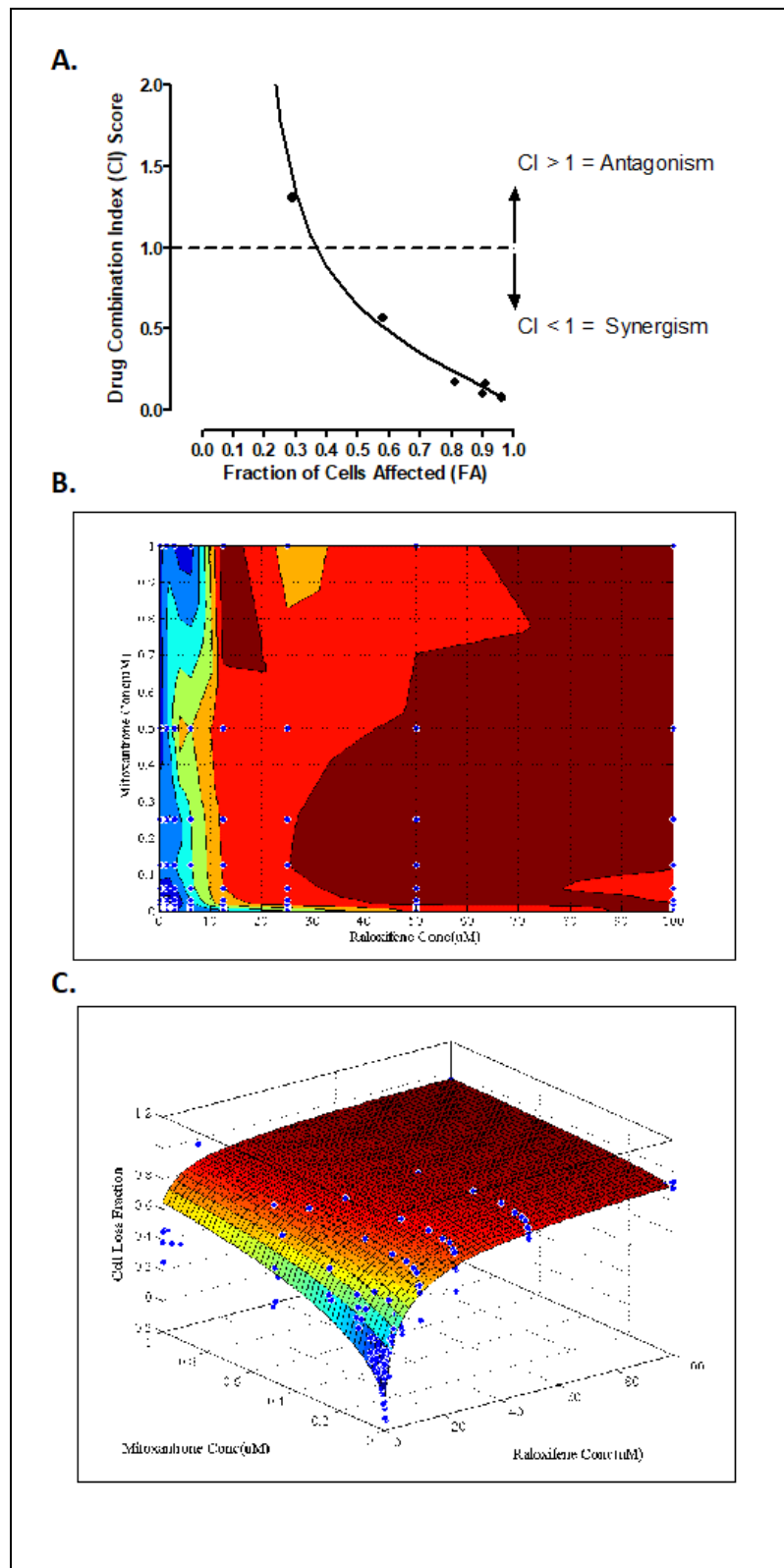
The data from the 10 x 10 gefitinib and mitoxantrone DCM in OVCAR-5 cells was analyzed

construct a three-dimensional graph of the data. The fitted  $\alpha$  parameter of the pharmacodynamic drug-drug interaction model was 0.77, which is  $>0$  and indicates that gefitinib and mitoxantrone interacted synergistically.

## 2.6 Analysis and Confirmation of Drug Combination 2

We used maximal drug concentrations of 100  $\mu\text{M}$  and 1  $\mu\text{M}$  for raloxifene and mitoxantrone respectively, because these concentrations were capable of  $>50\%$  growth inhibition across the selected cell lines HCT-116, HCT-15, KM12, and SW-620 (see  $\text{GI}_{50}$  values in Table 1) and they were also within the range of concentrations used in the DCM of the pilot DC HTS that produced DI scores  $>3$ . When the fraction of KM-12 cells affected at this 100:1 fixed DC ratio were analyzed using the COMUSYN software the CI values were  $<1$  and the drug interaction was classified as synergistic (Figure 6A, and Table 1). In addition, isobologram analysis of the raloxifene and mitoxantrone DC revealed non-linear contours bending towards the lower left corner of the graph indicating that the interactions were synergistic (Figure 6B, and Table 1). Lastly, with our PDI model, we were able to identify a drug-drug interaction relationship that demonstrated a sail that projected outward, in conjunction with a positive fitted  $\alpha$ -parameter of 1.20, 1, 0.92, 0.06 in KM12, HCT-116, HCT-15, and SW-620 respectively, all of which are indicative of a synergistic relationship between the two compounds (Figure 6C, and Table 1).

**Figure 6 Confirmation of Drug Combination 2 between Raloxifene and Mitoxantrone in the KM12 Colon Cancer Cell Line. A) Combination Index Analysis** The growth



inhibition fraction of KM12 cells affected data by a 10 x 10 raloxifene and mitoxantrone DCM was analyzed in the Chou-Talalay median effects model using the COMPUSYN software to calculate combination index (CI) scores (●) and to fit the data for the 100:1 raloxifene to mitoxantrone fixed drug ratio. CI scores <1.0 indicate that the two drugs interacted synergistically. **B)**

**Isobologram Plot** The data from the 10 x 10 raloxifene and mitoxantrone DCM in KM12 cells was plotted as an isobologram contour graph. The non-linear concave contour lines of the

isobologram plot indicate that raloxifene and mitoxantrone interacted synergistically. **C)**

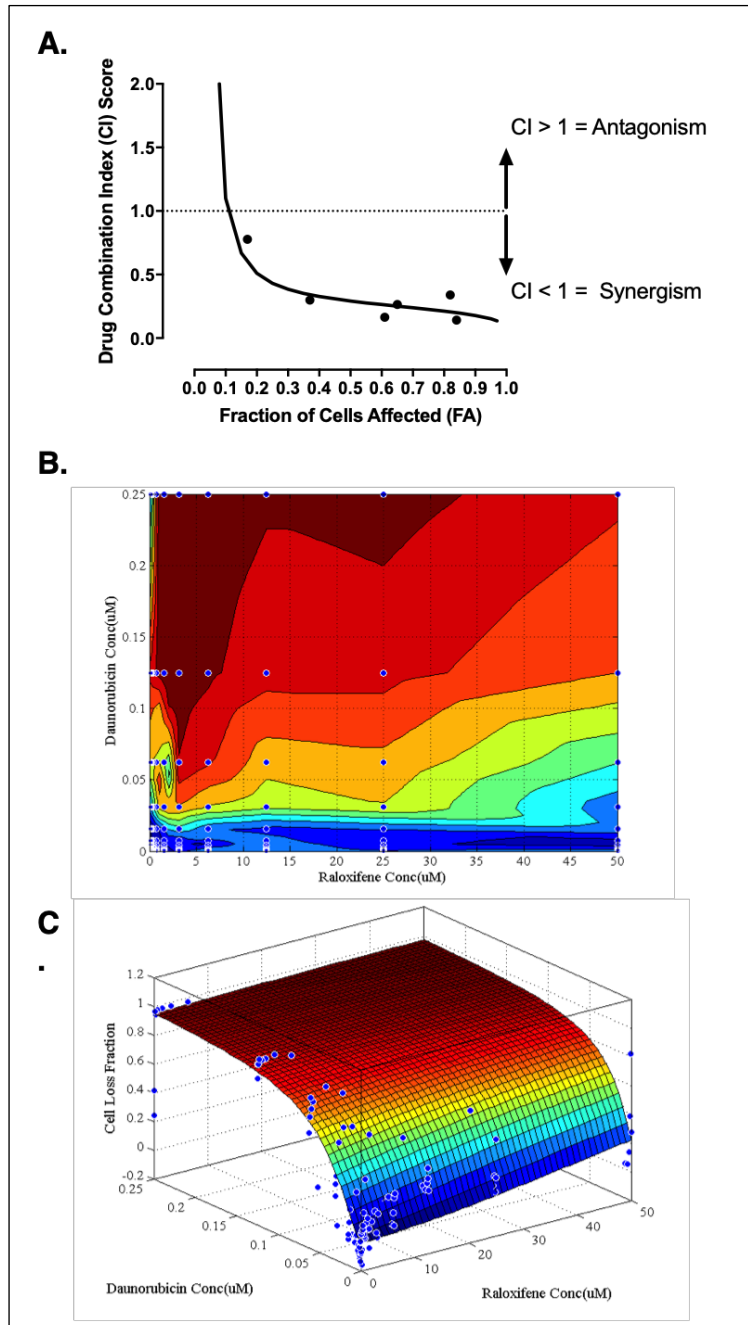
**Drug-Drug Interaction Surface Response** The data from the 10 x 10 raloxifene and mitoxantrone DCM in KM12 cells was analyzed using the pharmacodynamic drug-drug interaction model to fit the experimental data and construct a three-dimensional graph of the data. The fitted  $\alpha$  parameter of the pharmacodynamic drug-drug interaction model was 1.2, which is  $>0$  and indicates that raloxifene and mitoxantrone interacted synergistically.

## 2.7 Analysis of Drug Confirmation 3

We used maximal drug concentrations of 200  $\mu\text{M}$  and 1  $\mu\text{M}$  for raloxifene and daunorubicin respectively, as these concentrations were capable of  $>50\%$  growth inhibition across the selected cell lines DU-145, NCI-H23, and NCI-H522, as indicated by their mean  $\text{GI}_{50}$  values in Table 1. Additionally, the selection of these compounds was in following with the results obtained from the pilot screen as each combination produced a DI score  $>3$ . Using the combination index plot we observed a trend that produced a curve fitted to our data points where the greater the fraction of cells affected beyond  $\sim 0.1$  FA, produced a CI values less than one for the NCI-H23, and an overall synergistic relationship was observed across all other cell lines tested with this combination (Figure 7A, and Table 1). In isobologram plots, the plots arced towards the lower left corner of the graph in a concave downward fashion consistent with a synergistic interaction (Figure 7B, and Table 1). Lastly, using the PDI model we observed a positive fitted  $\alpha$ -parameters of 4.80 in NCI-H23, with an outwardly projected sail that indicated a synergistic

relationship, even with only modest inhibitory activity observed in raloxifene as indicated by the cooler blue and dark blue colors (Figure 7C, and Table 1). For the other cell lines, we observed positive fitted  $\alpha$ -parameters of 41.0 and 1 in DU-145 and NCI-H522 cell lines respectively, confirming the synergistic relationship between raloxifene and daunorubicin. (Table 1).

**Figure 7 Confirmation of Drug Combination 3 between Raloxifene and Daunorubicin in the NCI-H23 Non-Small Cell Lung Cancer Cell Line**



**A) Combination Index Analysis**

The growth inhibition fraction of NCI-H23 cells affected data by a 10 x 10 raloxifene and daunorubicin DCM was analyzed in the Chou-Talalay median effects model using the COMPUSYN software to calculate combination index (CI) scores (●) and to fit the data for the 100:1 raloxifene to daunorubicin fixed drug ratio. CI scores <1.0 indicate that the two drugs interacted synergistically.

**B) Isobologram Plot**

The data from the 10 x 10 raloxifene and daunorubicin DCM in NCI-H23 cells was plotted as an isobologram contour graph. The non-linear concave contour lines of the isobologram plot indicate that raloxifene and daunorubicin interacted synergistically in NCI-H23 cells.

**C) Drug-Drug**

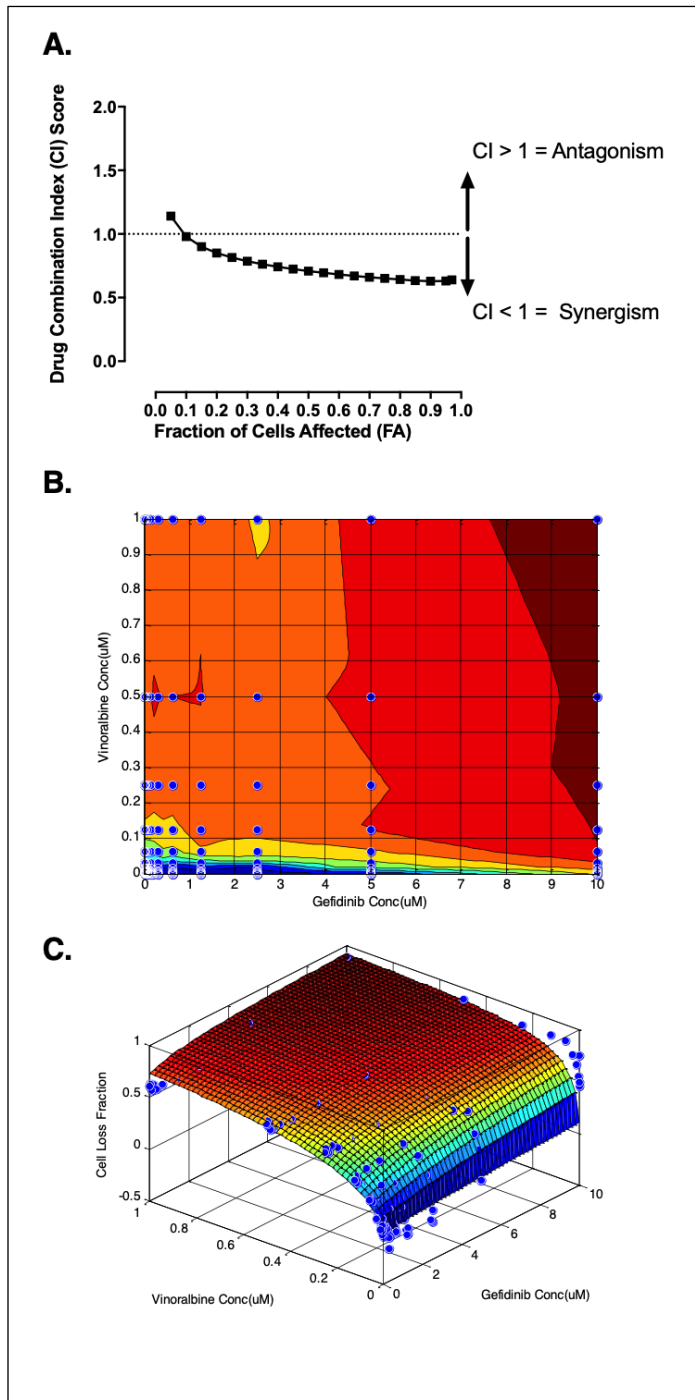
**Interaction Surface Response** The data from the 10 x 10 raloxifene and daunorubicin DCM in NCI-H23 cells was analyzed using the pharmacodynamic drug-drug interaction model to fit the experimental data and construct a three-dimensional graph of the data.

The fitted  $\alpha$  parameter of the pharmacodynamic drug-drug interaction model was 4.8, which is  $>0$  and indicates that raloxifene and daunorubicin interacted synergistically.

## 2.8 Analysis and Confirmation of Drug Combination 4

As previously described in Close et. al, the drug combination between gefitinib and vinorelbine was confirmed synergistic in the OVCAR-5 cell line using all three analytical methods (Figure 3A-D).<sup>56</sup> In Figure 8, we illustrate the confirmation of synergy between vinorelbine and gefitinib in the MDA-MB-435 melanoma cell line.. In the CI plot, we observed that the majority of data points produced a CI scores below 1 and the drug interaction was classified as synergistic (Figure 8A). As indicated in Table 1, all cell lines exposed to this combination of gefitinib and vinorelbine displayed CI score  $<1$ , indicating synergism. Additionally, our isobologram plot illustrated similar trends, whereby a synergistic effect was present across all effect levels with moderate effect levels (orange) displaying the deepest arc bending towards the southwest corner of the graph (Figure 8B). This would indicate that a more potent synergistic effect was achieved when drugs were used at a concentration that was not so high as to achieve high kill on its own. Lastly, using our PDI model, we observed that an outward inflated sail with a positive fitted  $\alpha$ -parameter of 3.19, and all other cell lines displayed a similar positive value which confirmed the synergistic relationship between gefitinib and vinorelbine in both melanoma and leukemia cell lines (Figure 8C, Table 1).

**Figure 8 Confirmation of Drug Combination 4 between Gefitinib and Vinorelbine in the MDA-MB-485 Melanoma Cell Line**



**A) Combination Index Analysis**

The growth inhibition fraction of MDA-MB-435 cells affected data by a 10 x 10 gefitinib and vinorelbine DCM was analyzed in the Chou-Talalay median effects model using the COMPUSYN software to calculate combination index (CI) scores (●) and fit the data for the 10:1 gefitinib to vinorelbine fixed drug ratio. CI scores <1.0 indicate that the two drugs interacted synergistically in MDA-MB-435 cells.

**B) Isobologram Plot** The data from the 10 x 10 gefitinib and vinorelbine DCM in MDA-MB-435 cells was plotted as an isobologram contour graph. The non-linear concave contour lines of the isobologram plot indicate that gefitinib and vinorelbine interacted synergistically in MDA-MB-435 cells.

**C) Drug-Drug Interaction Surface Response** The data from the 10 x 10 gefitinib and vinorelbine

DCM in MDA-MB-435 cells was analyzed using the pharmacodynamic drug-drug interaction model to fit the experimental data and construct a three-dimensional graph of

the data. The fitted  $\alpha$  parameter of the pharmacodynamic drug-drug interaction model was 3.19, which is  $>0$  and indicates that gefitinib and vinorelbine interacted synergistically.

## **2.9 Development and Validation of the High Content Imaging ABCG2 Drug Efflux Transporter Hoechst Accumulation Assay**

Various assay formats have been developed to measure and compare ABC transporter drug efflux activity in control and ABC transporter expressing cell lines. They include the use of flow cytometry to measure and compare the accumulation of fluorescent ABC transporter substrates in cells, or Transwell™ assays that measure the permeability and bi-directional, apical to basolateral and *vice versa*, passage of substrates through monolayer cultures separating substrate donor and acceptor chambers.<sup>58, 59, 65, 66</sup> We developed an imaging assay to measure the accumulation of the ABCG2 substrate Hoechst 33342 in MDCKII-EV and MDCKII-ABCG2 cell lines that have previously been used in both Transwell™ and flow cytometry assay formats.<sup>58, 59</sup> Assay development experiments established the following optimal 384-well assay conditions for the imaging based Hoechst accumulation assay: a cell seeding density of 20,000 MDCKII-EV or MDCKII-ABCG2 cells per well; a Hoechst 33342 concentration of 8  $\mu\text{g}/\text{mL}$ ; a dye accumulation period of 60 minutes at 37°C in 5 % CO<sub>2</sub> and 95% humidity; acquisition of two fluorescent images per well in the DAPI channel using a 10x Plan Fluor 0.3 NA objective on the IXM HCS platform; and image analysis using the MWCS module. Figure 9A shows representative grayscale 10x images of the Hoechst-stained nuclei acquired in the DAPI channel and the corresponding pseudo-color fluorescent pixel

intensity visualizations of MDCKII-EV and MDCKII-ABCG2 cells exposed to Hoechst using these assay conditions. Images of the Hoechst-stained nuclei of MDCKII-EV cells were brighter and more intense than those of MDCKII-ABCG2 cells, which was corroborated by the “hotter” and “brighter” colors (yellow, red, white) representing higher intensity signals in the pseudo-color pixel intensity visualizations of MDCKII-EV cells compared to the cooler colors (purple, cyan, green) representing the lower intensity signals observed in MDCKII-ABCG2 cells. We used the mean integrated fluorescent intensity (MIFI) data output of the MWCS image analysis module to quantify and compare Hoechst accumulation in MDCKII-ABCG2 and MDCKII-EV cell populations (Figure 9B), and on a well-averaged basis (Figure 9C). The results frequency distribution of the binned cellular MIFI data for the MDCKII-ABCG2 and MDCKII-EV populations exhibited different profiles that were substantially shifted in MIFI values relative to each other (Figure 9B). The MDCKII-ABCG2 population MIFI values were distributed in a single non-symmetrical peak around a median of ~100,000 that exhibited an extended tail towards higher MIFI values. The MDCKII-EV population MIFI values were distributed between two conjoined peaks with medians of ~200,000 and ~400,000, that would be consistent with 1n (Go/G1) and 2n (G2/M) DNA peaks characteristic of the normal cell cycle. Although there was some overlap between the MIFI values in the MDCKII-ABCG2 and MDCKII-EV populations, the MDCKII-ABCG2 population was substantially shifted to lower MIFI values relative to the majority of the MDCKII-EV population. At the well averaged level, the Hoechst MIFI values observed in MDCKII-ABCG2 wells were significantly (Student's t-test,  $p < 0.05$ ) lower than those detected in MDCKII-EV wells (Figure 9C). Collectively these data indicated that the expression of the ABCG2 drug efflux transporter in MDCKII

cells significantly reduced Hoechst accumulation levels compared to control cells (Figure 9).

Ko143 is a potent and less toxic analog of the fungal toxin fumitremorgin C which is a selective inhibitor of the ABCG2 efflux transporter.

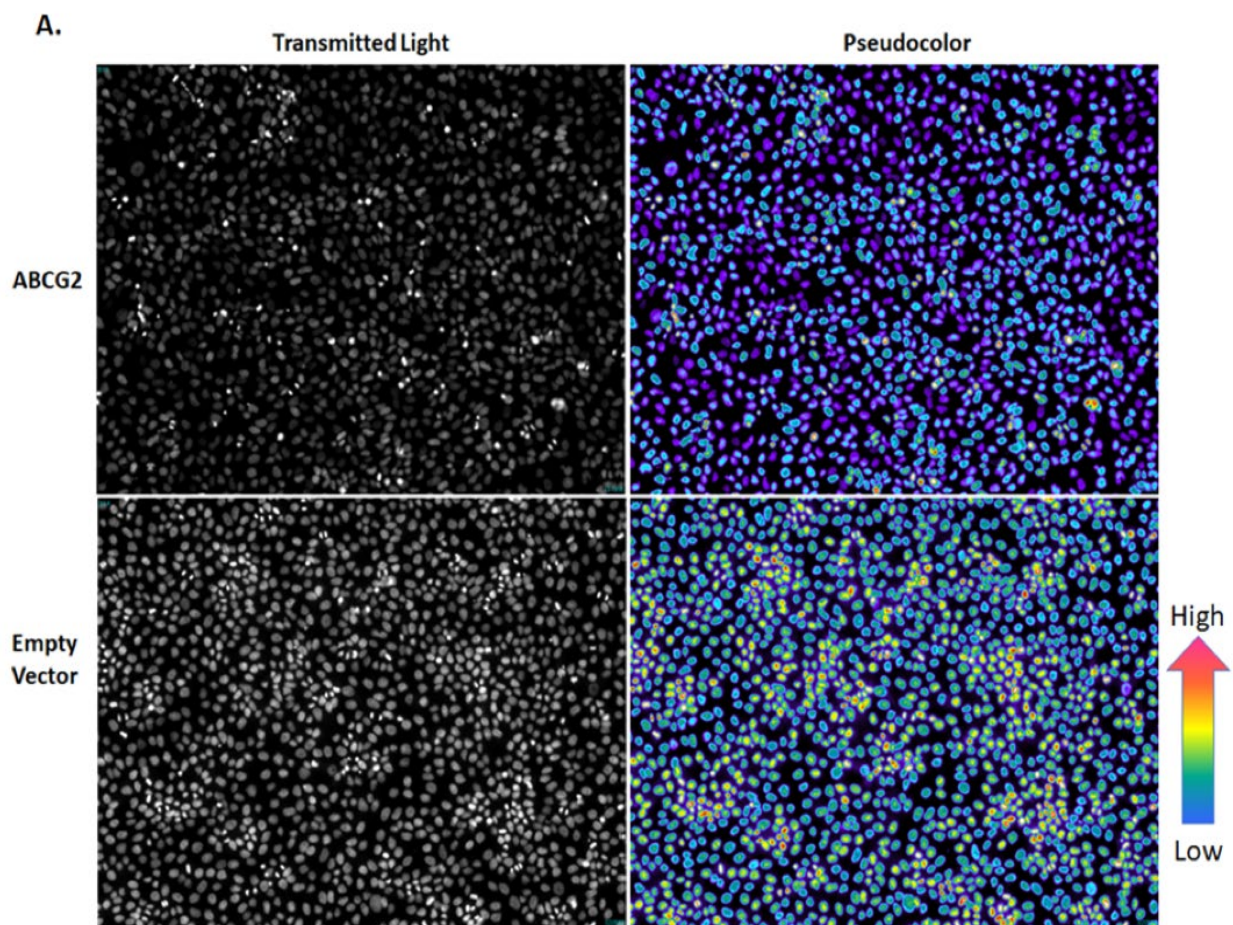
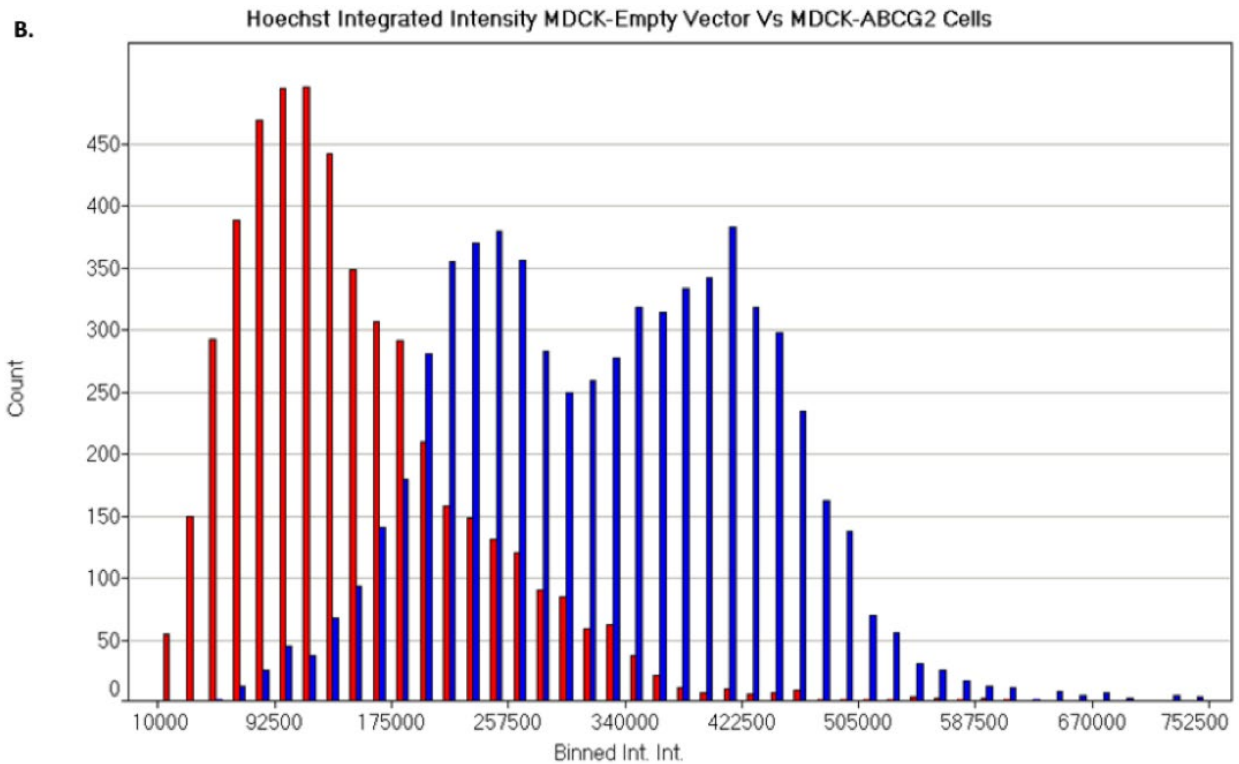


**Figure 9 High Content Imaging Assay to measure the Accumulation of the ABCG2 Substrate Hoechst 33342 in MDCKII-EV and MDCKII-ABCG2 Cell Lines**

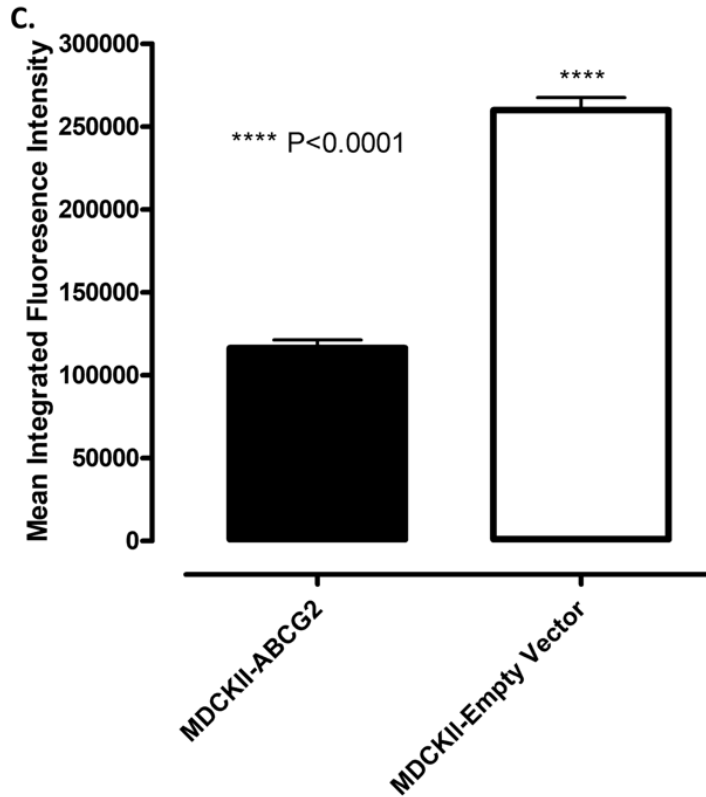
**A) Grayscale Images of Hoechst-stained Nuclei and Pseudo-color Fluorescent Pixel Intensity Visualizations of MDCKII-EV and MDCKII-ABCG2 Cells.** Representative 10x grayscale fluorescent images and the corresponding pseudo-color fluorescent pixel intensity visualizations of the Hoechst stained nuclei of MDCKII-EV and MDCKII-ABCG2 cells seeded into 384-well plates at 20,000 cell per well and exposed to 8  $\mu\text{g}/\text{mL}$  Hoechst 33342 for 60 minutes at 37°C in 5 % CO<sub>2</sub> and 95% humidity. Images

were acquired on the ImageXpress Micro HCS platform using a 10x Plan Fluor 0.3 NA objective. The corresponding pseudo-color fluorescence pixel intensity data visualizations present the relative fluorescent intensities as distinct colors with the “hotter” and “brighter” colors (low to high, yellow, red, white) representing higher intensity pixels and cooler colors (low to high, purple, cyan, green) representing lower intensity pixels.



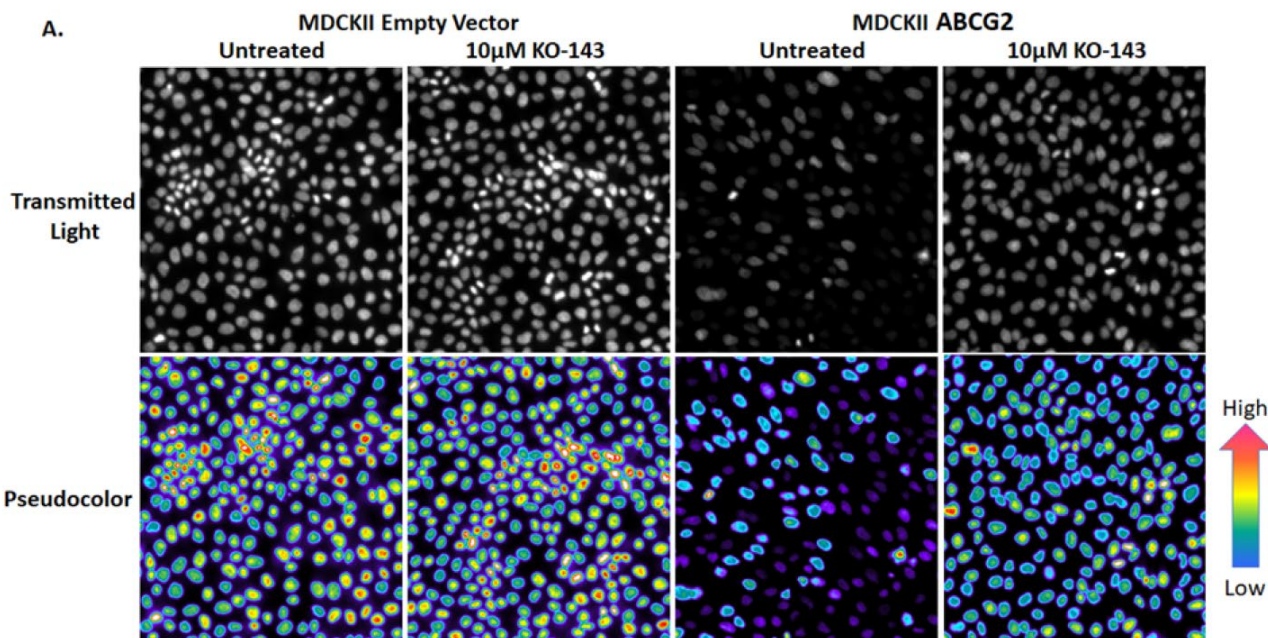
**B) Results Frequency Distribution of the Mean Integrated Fluorescent Intensities of the Hoechst-stained Nuclei in MDCKII-EV and MDCKII-ABCG2 Cell Populations.**

The binned cellular mean integrated Hoechst fluorescent intensity (MIFI) data output of the multiwavelength cell scoring (MWCS) image analysis module was plotted to quantify and compare the profiles of Hoechst accumulation in MDCKII-ABCG2 (■) and MDCKII-EV (■) cell populations. The Y-axis represents the number of cells detected in each MIFI bin plotted on the X-axis.



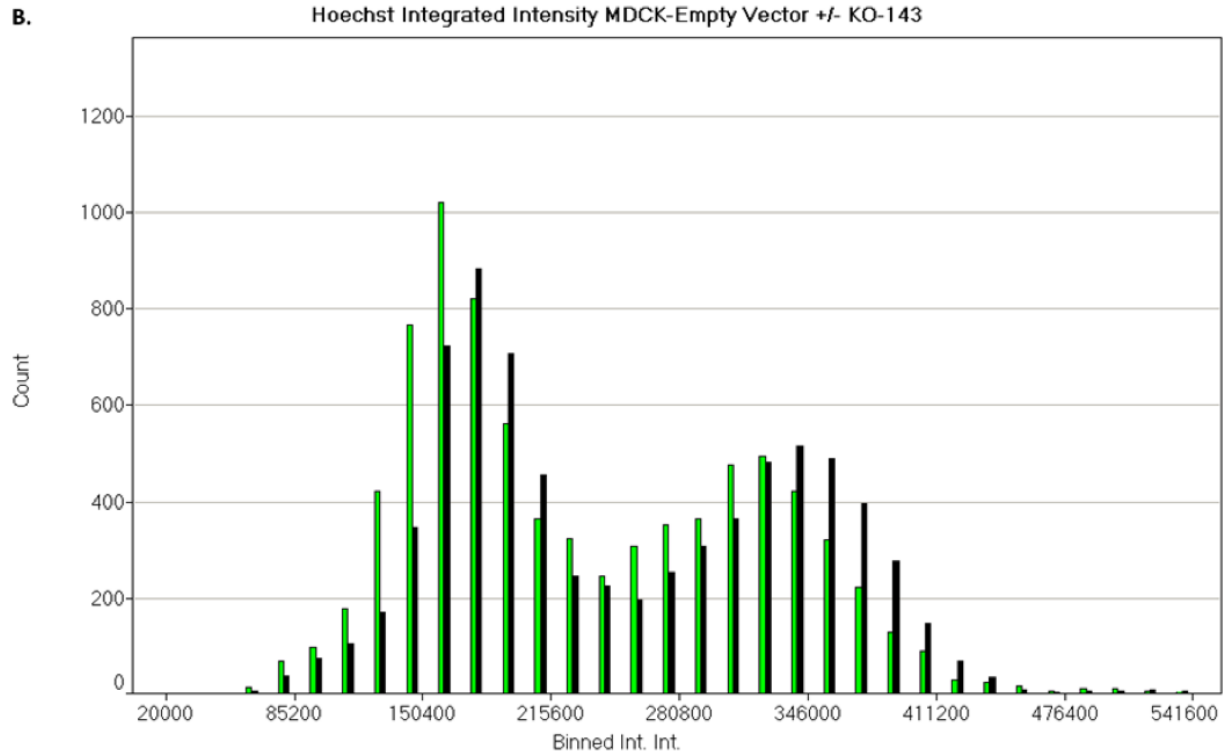
**C) Well-averaged Mean Integrated Fluorescent Intensities of the Hoechst-stained Nuclei in MDCKII-EV and MDCKII-ABCG2 Cell Populations** The well-based Hoechst average MIFI data for the MDCKII-ABCG2 and MDCKII-EV populations seeded in 384-well microtiter plates are presented as the mean MIFI values  $\pm$  SD (n = 5) of replicate wells. A Student's t-test was performed to determine whether there was a statistically significant difference in Hoechst accumulation between MDCKII-ABCG2 and MDCKII-EV cell lines,  $p < 0.05$ . Representative data from one of at least 3 independent experiments each performed in 5 replicate wells are shown.

Figure 10 shows the effects of co-administration of 10  $\mu$ M Ko143 on the accumulation of Hoechst 33342 in MDCKII-EV and MDCKII-ABCG2 cells. Relative to DMSO controls, exposure of MDCKII-EV cells to 10  $\mu$ M Ko143 had no discernable effect on the brightness and intensity of the Hoechst stained nuclei apparent in the grayscale images and corresponding pseudo-color pixel intensity visualizations (Figure 10A). In marked contrast, 10  $\mu$ M Ko143 increased the brightness and intensity of the Hoechst stained nuclei in the images and pseudo-color pixel intensity visualizations of MDCKII-ABCG2 cells relative to DMSO control cells. The images and pseudo-color pixel intensity visualizations of MDCKII-ABCG2 cells treated with Ko143 were very similar to those of MDCKII-EV cells  $\pm$  Ko143. The results frequency distribution of the binned cellular MIFI data for MDCKII-EV cell populations  $\pm$  Ko143 exposure exhibited overlapping profiles with two conjoined peaks with median MIFI values  $\sim$ 160,000 and  $\sim$ 340,000 (Figure 10B). In MDCKII-ABCG2 cells treated with DMSO, the binned cellular MIFI data were distributed in a single non-symmetrical peak around a median MIFI value  $\sim$ 80,000 with an extended tail towards higher MIFI values (Figure 10C). However, exposure of MDCKII-ABCG2 cells to Ko143 altered the MIFI distribution profile and shifted the MIFI values higher (Figure 10C). In MDCKII-ABCG2 cells exposed to Ko143, the binned cellular MIFI data were distributed between two conjoined peaks with median MIFI values  $\sim$  180,000 and  $\sim$ 360,000 (Figure 10C), very similar to the profiles of MDCKII-EV cells  $\pm$  Ko143 (Figure 10B). Figure 10D shows the time dependent change in well averaged Hoechst accumulation MIFI values in MDCKII-EV or MDCKII-ABCG2 cells  $\pm$  exposure to 10  $\mu$ M Ko143. In MDCKII-EV and MDCKII-ABCG2 cells treated with DMSO there was a gradual linear increase in Hoechst accumulation in both populations over time,



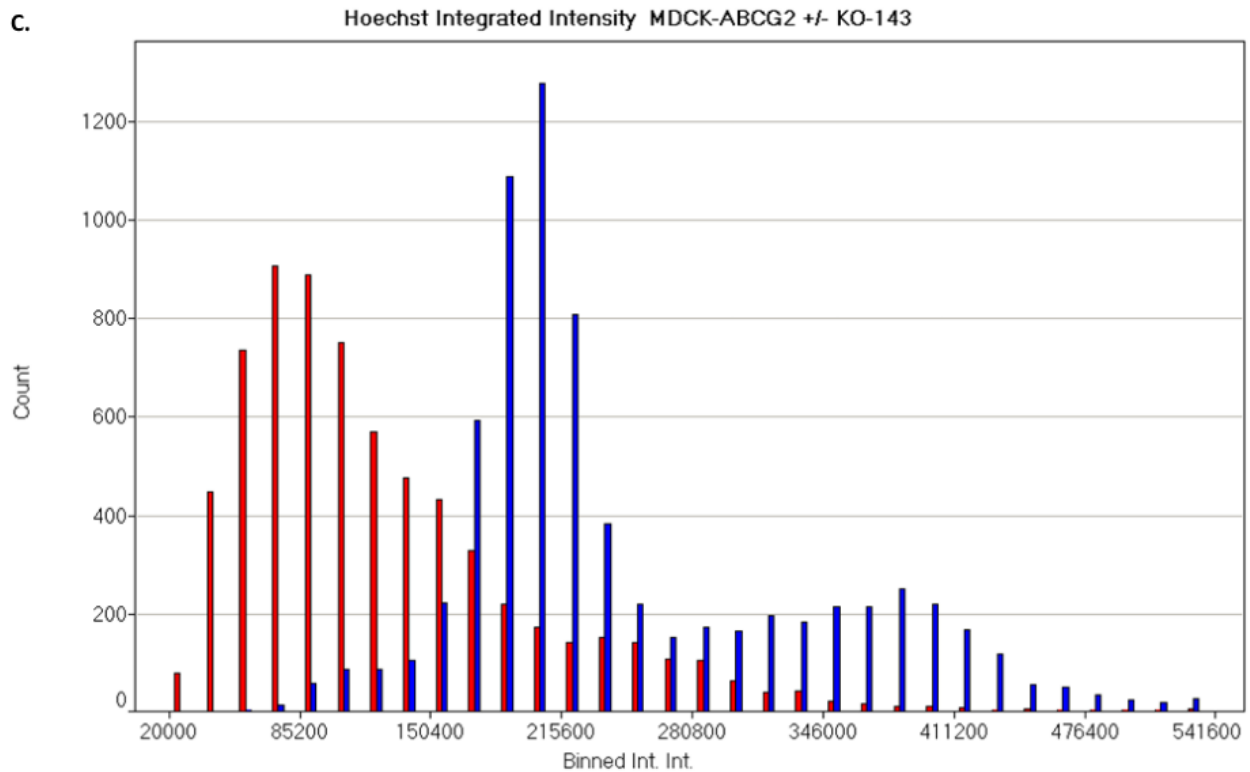
**Figure 10 Effects of Exposure to the ABCG2 Inhibitor Ko143 on Hoechst 33342 Accumulation in MDCKII-EV and MDCKII-ABCG2 Cell Lines**

**A) Grayscale Images of Hoechst-stained Nuclei and Pseudo-color Fluorescent Pixel Intensity Visualizations of MDCKII-EV and MDCKII-ABCG2 Cells  $\pm$  Ko143.** Representative 10x grayscale fluorescent images and the corresponding pseudo-color fluorescent pixel intensity visualizations of the Hoechst stained nuclei of MDCKII-EV and MDCKII-ABCG2 cells seeded into 384-well plates at 20,000 cell per well and exposed to 8  $\mu$ g/mL Hoechst 33342  $\pm$  10  $\mu$ M Ko143 for 60 minutes at 37°C in 5 % CO<sub>2</sub> and 95% humidity. Images were acquired on the ImageXpress Micro HCS platform using a 10x Plan Fluor 0.3 NA objective. The corresponding pseudo-color fluorescence pixel intensity data visualizations present the relative fluorescent intensities as distinct colors with the “hotter” and “brighter” colors (low to high, yellow, red, white) representing higher intensity pixels and cooler colors (low to high, purple, cyan, green) representing lower intensity pixels.



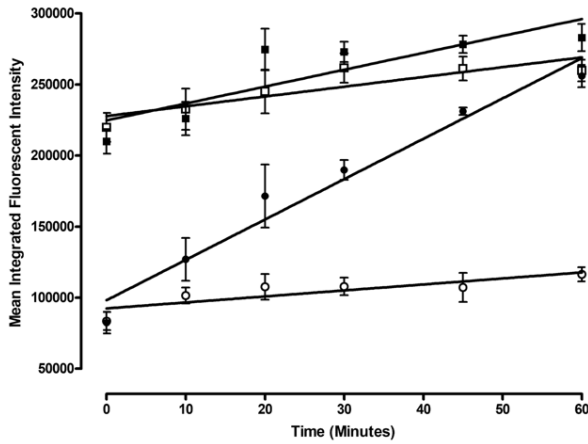
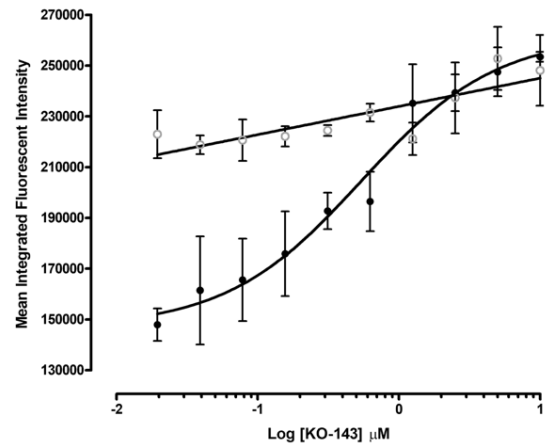
**B) Results Frequency Distribution of the Mean Integrated Fluorescent Intensities of the Hoechst-stained Nuclei in MDCKII-EV Cell Populations  $\pm$  10  $\mu$ M Ko143.** The binned cellular mean integrated Hoechst fluorescent intensity (MIFI) data output of the multiwavelength cell scoring (MWCS) image analysis module was plotted to quantify and compare the profiles of Hoechst accumulation in MDCKII-EV cell populations in the presence (■) or absence (■) of 10  $\mu$ M Ko143 for 60 minutes at 37°C in 5 % CO<sub>2</sub> and 95% humidity. The Y-axis represents the number of cells detected in each MIFI bin plotted on the X-axis.

C.



**C) Results Frequency Distribution of the Mean Integrated Fluorescent Intensities of the Hoechst-stained Nuclei in MDCKII-ABCG2 Cell Populations  $\pm$  10  $\mu$ M Ko143.**

The binned cellular mean integrated Hoechst fluorescent intensity (MIFI) data output of the multiwavelength cell scoring (MWCS) image analysis module was plotted to quantify and compare the profiles of Hoechst accumulation in MDCKII-ABCG2 cell populations in the presence (■) or absence (■) of 10  $\mu$ M Ko143 for 60 minutes at 37°C in 5 % CO<sub>2</sub> and 95% humidity. The Y-axis represents the number of cells detected in each MIFI bin plotted on the X-axis.

**D.****E.**

**D) Time Course of Hoechst Accumulation in MDCKII-EV and MDCKII-ABCG2 Cells  $\pm$  10  $\mu$ M Ko143.** The time dependent changes in well-averaged Hoechst MIFI values for MDCKII-ABCG2 and MDCKII-EV cells in the presence or absence of 10  $\mu$ M Ko143 throughout a 60-minute incubation period at 37°C in 5 % CO<sub>2</sub> and 95% humidity are presented as the mean MIFI values  $\pm$  SD (n = 3) of triplicate wells versus time in minutes. MDCKII-EV cells in the presence (■) or absence (□) of 10  $\mu$ M Ko143, and MDCKII-ABCG2 cells in the presence (●) or absence (○) of 10  $\mu$ M Ko143. Representative data from one of 3 independent experiments each performed in triplicate wells are shown. **E) Concentration Dependent Effects of Ko143 Exposure on Hoechst Accumulation in MDCKII-EV and MDCKII-ABCG2 Cells.** The well-averaged Hoechst MIFI values of MDCKII-ABCG2 and MDCKII-EV cells exposed to the indicated concentrations of Ko143 for 60-minutes at 37°C in 5 % CO<sub>2</sub> and 95% humidity are presented as the mean MIFI values  $\pm$  SD (n = 3) of triplicate wells versus Ko143 concentration in  $\mu$ M. MDCKII-EV cells (○) versus MDCKII-ABCG2 cells (●). The data represent one of 3 independent experiments each performed in triplicate wells.

with MDCKII-ABCG2 cells consistently exhibiting > 2-fold lower Hoechst accumulation MIFI values than MDCKII-EV cells. In MDCKII-EV cells co-administered Ko143, the linear rate of accumulation of Hoechst appeared to be marginally higher than in DMSO control wells. In MDCKII-ABCG2 cells however, exposure to Ko143 dramatically increased the linear rate of accumulation of Hoechst such that after 60 min, Hoechst accumulation MIFI values approached those observed in MDCKII-EV cells  $\pm$  Ko143 (Figure 10D). In MDCKII-EV cells, Hoechst accumulation increased in a roughly linear fashion as Ko143 concentrations were increased (Figure 10E). In MDCKII-ABCG2 cells however, the concentration dependent increase in Hoechst accumulation produced by Ko143 exposure could be fit to a sigmoidal curve ( $r^2 = 0.9$ ) and exhibited an  $IC_{50}$  of 0.54  $\mu$ M for inhibition of ABCG2-mediated Hoechst efflux (Figure 10E). Collectively these data demonstrated that exposure to Ko143 inhibited ABCG2-mediated Hoechst efflux in a concentration and time dependent manner in MDCKII-ABCG2 cells but not MDCKII-EV cells (Figure 10), thereby validating the ABCG2 efflux transporter HCS assay.

## **2.10 Do Gefitinib and Raloxifene Inhibit ABCG2 Transporter Substrate Efflux?**

Figure 11 shows the effects of co-administration of 10  $\mu$ M of either Ko143, gefitinib or raloxifene on the accumulation of Hoechst 33342 in MDCKII-EV and MDCKII-ABCG2 cells. Relative to DMSO controls, exposure of MDCKII-EV cells to 10  $\mu$ M Ko143, gefitinib or raloxifene had no discernable effect on the brightness and intensity of the Hoechst stained nuclei apparent in the grayscale images and corresponding pseudo-color pixel intensity visualizations (Figure 11A). In MDCKII-ABCG2 cells however, treatment with 10

$\mu\text{M}$  Ko143, gefitinib or raloxifene all enhanced the brightness and intensity of the Hoechst stained nuclei in the images and pseudo-color pixel intensity visualizations relative to cells exposed to DMSO (Figure 11B). Exposure of MDCKII-EV cells to 10  $\mu\text{M}$  gefitinib or raloxifene produced no discernable effects on the results frequency distribution profiles of the binned cellular MIFI population data which exhibited two conjoined peaks with median MIFI values  $\sim 200,000$  and  $\sim 400,000$  (Figure 11C, and Figure 12A). As expected, in MDCKII-ABCG2 cells treated with DMSO the binned cellular MIFI data were distributed in a single non-symmetrical peak around a median MIFI value  $\sim 60,000$  with an extended tail towards higher MIFI values (Figure 11D, and Figure 12B). Exposure of MDCKII-ABCG2 cells to 10  $\mu\text{M}$  gefitinib or raloxifene altered the MIFI distribution profile and shifted the MIFI values higher (Figure 11D and Figure 12B). Although the changes in the MIFI distribution profiles and the extent to which the MIFI values were shifted higher in MDCKII-ABCG2 cells by gefitinib or raloxifene were less dramatic than with Ko143 (Figure 10C), both drugs enhanced Hoechst accumulation (Figure 11D, and Figure 12B). At the well averaged level, exposure of MDCKII-EV cells to 10  $\mu\text{M}$  Ko143, gefitinib or raloxifene had no apparent effect on the Hoechst accumulation MIFI values (Figure 11E). In MDCKII-ABCG2 cells however, Hoechst accumulation MIFI values were significantly higher in wells that were treated with Ko-143 or gefitinib relative to DMSO controls (one-way ANOVA with multiple comparisons,  $p < 0.001$ ) (Figure 11F). Although the well averaged Hoechst accumulation MIFI

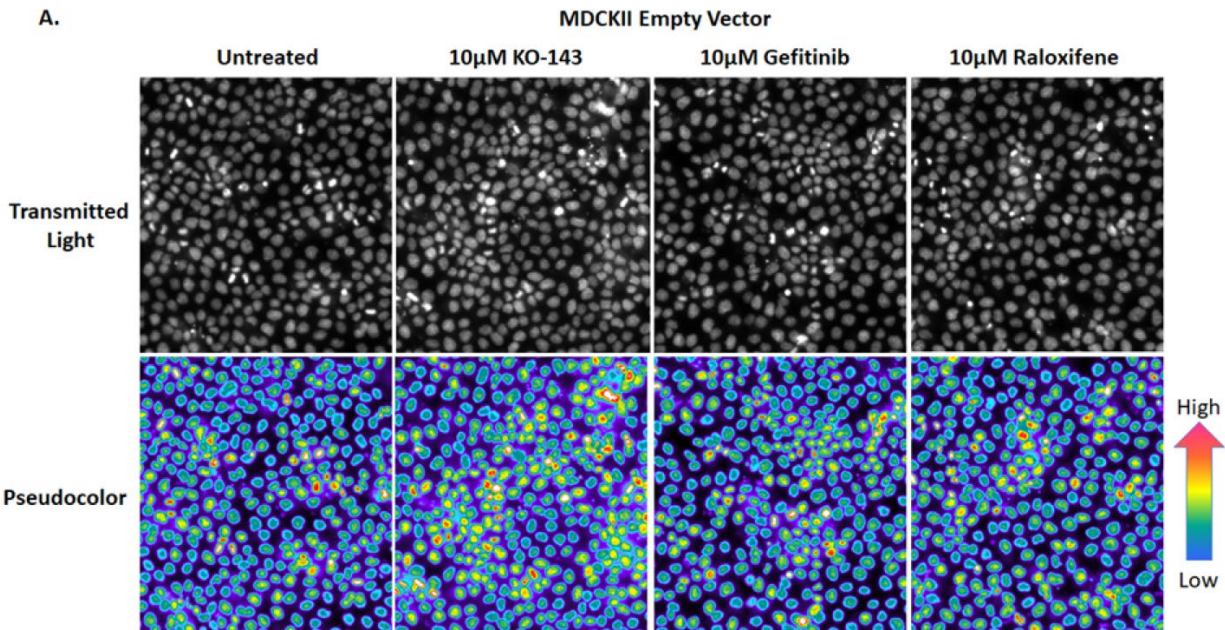
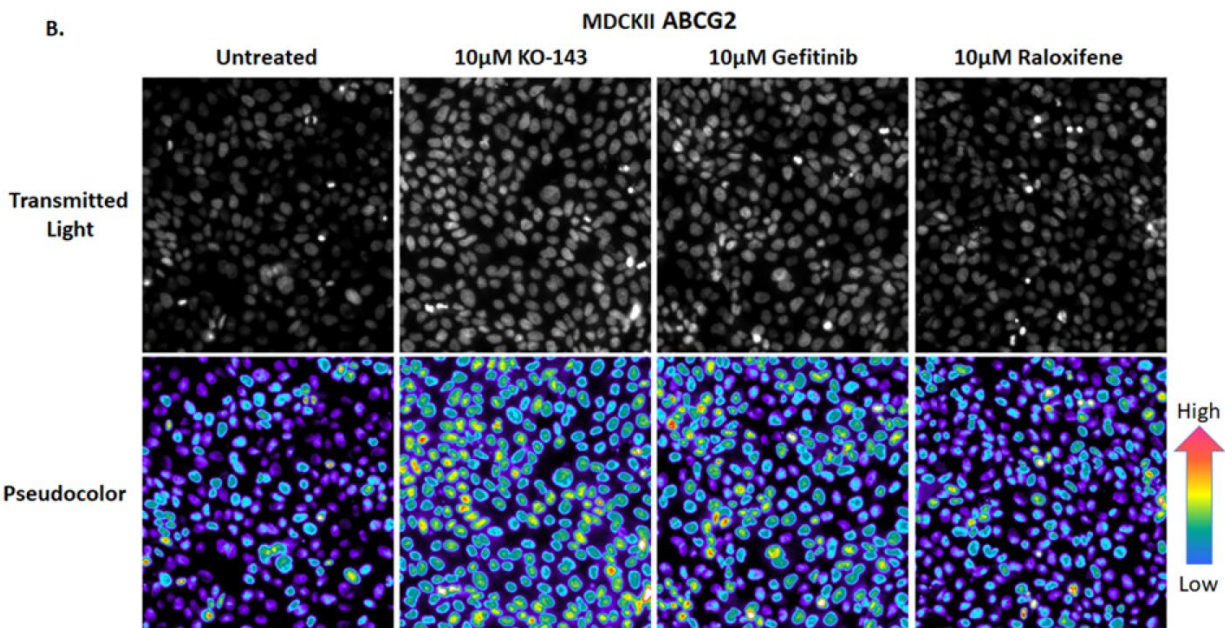
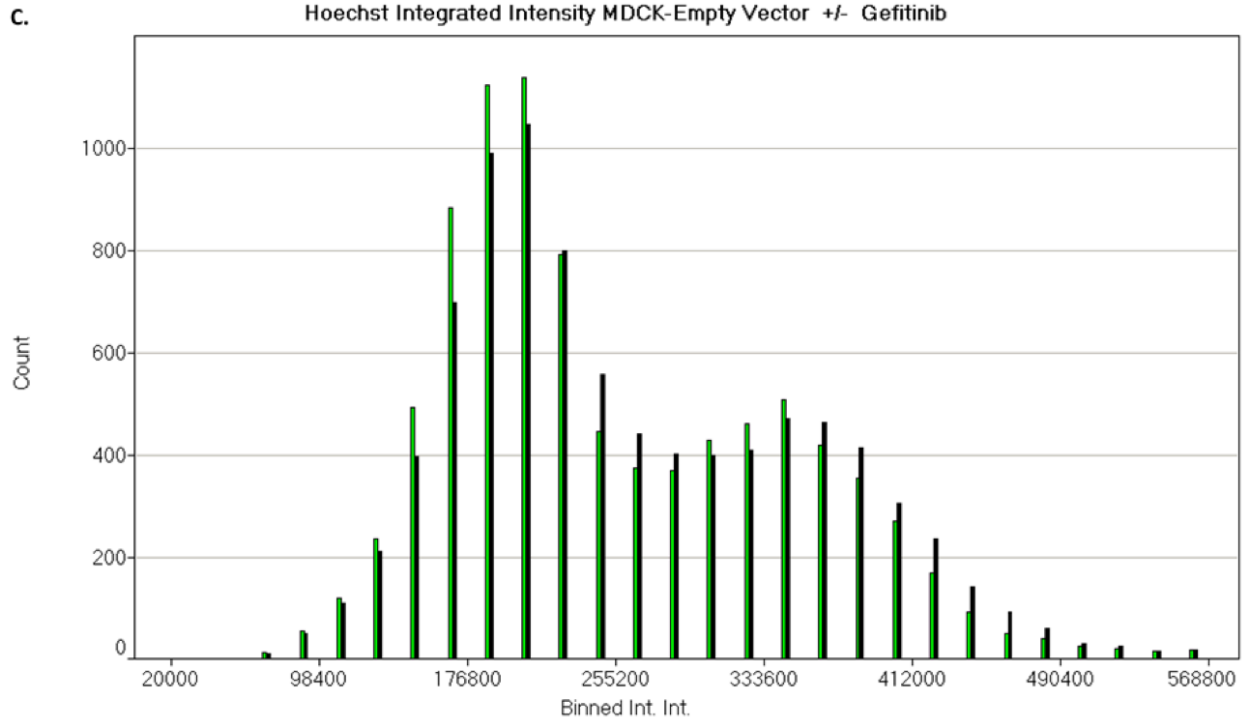


**Figure 11 Effects of Exposure to Ko143, Gefitinib or Raloxifene on Hoechst 33342 Accumulation in MDCKII-EV and MDCKII-ABCG2 Cell Lines**

**A) Grayscale Images of Hoechst-stained Nuclei and Pseudo-color Fluorescent Pixel Intensity Visualizations of MDCKII-EV Cells Exposed to Ko143, Gefitinib or Raloxifene.** Representative 10x greyscale fluorescent images and the corresponding pseudo-color fluorescent pixel intensity visualizations of the Hoechst stained nuclei of MDCKII-EV cells seeded into 384-well plates at 20,000 cell per well and exposed to 8  $\mu$ g/mL Hoechst 33342  $\pm$  10  $\mu$ M Ko143, Gefitinib or Raloxifene for 60 minutes at 37°C in 5 % CO<sub>2</sub> and 95% humidity. Images were acquired on the ImageXpress Micro HCS platform using a 10x Plan Fluor 0.3 NA objective. The corresponding pseudo-color fluorescence pixel intensity data visualizations present the relative fluorescent intensities as distinct colors with the “hotter” and “brighter” colors (low to high, yellow, red, white) representing higher intensity pixels and cooler colors (low to high, purple, cyan, green) representing lower intensity pixels.

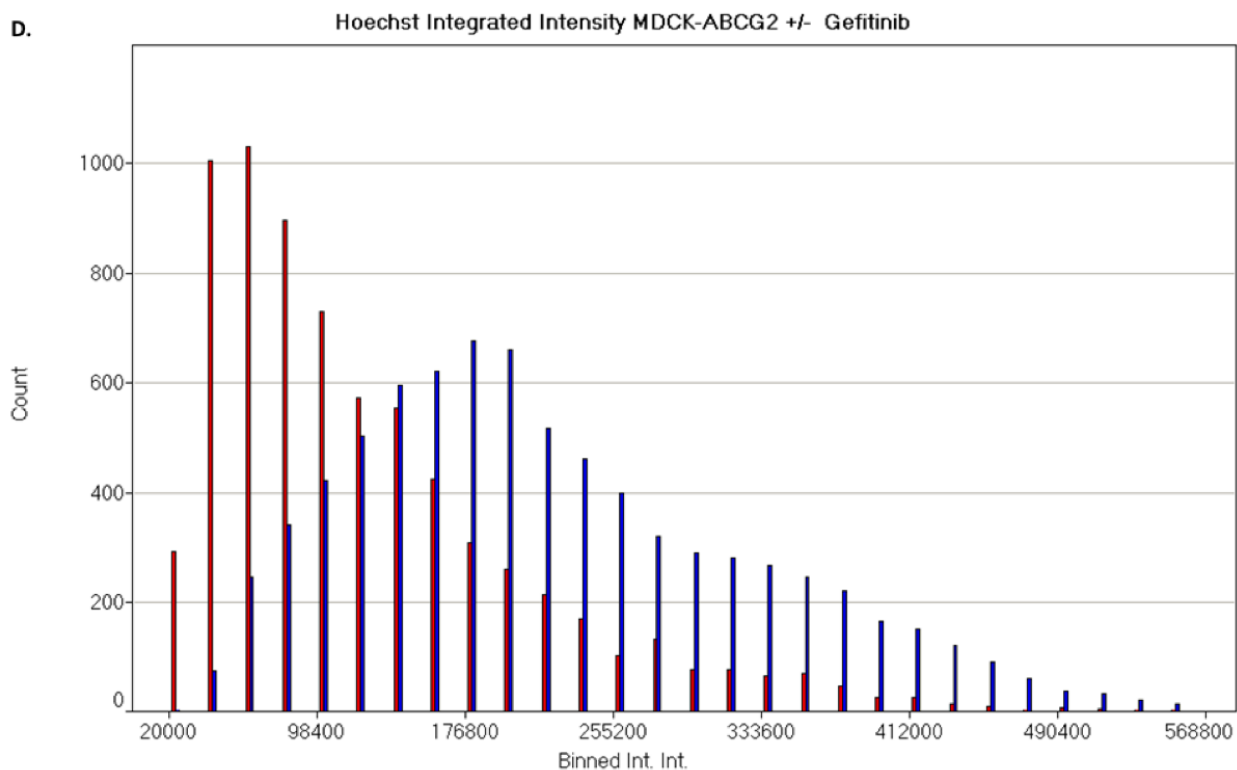


**B) Grayscale Images of Hoechst-stained Nuclei and Pseudo-color Fluorescent Pixel Intensity Visualizations of MDCKII-ABCG2 Cells Exposed to Ko143, Gefitinib or Raloxifene.** Representative 10x grayscale fluorescent images and the corresponding pseudo-color fluorescent pixel intensity visualizations of the Hoechst stained nuclei of MDCKII-ABCG2 cells seeded into 384-well plates at 20,000 cell per well and exposed to 8  $\mu$ g/mL Hoechst 33342  $\pm$  10  $\mu$ M Ko143, Gefitinib or Raloxifene for 60 minutes at 37°C in 5 % CO<sub>2</sub> and 95% humidity. Images were acquired on the ImageXpress Micro HCS platform using a 10x Plan Fluor 0.3 NA objective. The corresponding pseudo-color fluorescence pixel intensity data visualizations present the relative fluorescent intensities as distinct colors with the “hotter” and “brighter” colors (low to high, yellow, red, white) representing higher intensity pixels and cooler colors (low to high, purple, cyan, green) representing lower intensity pixels.



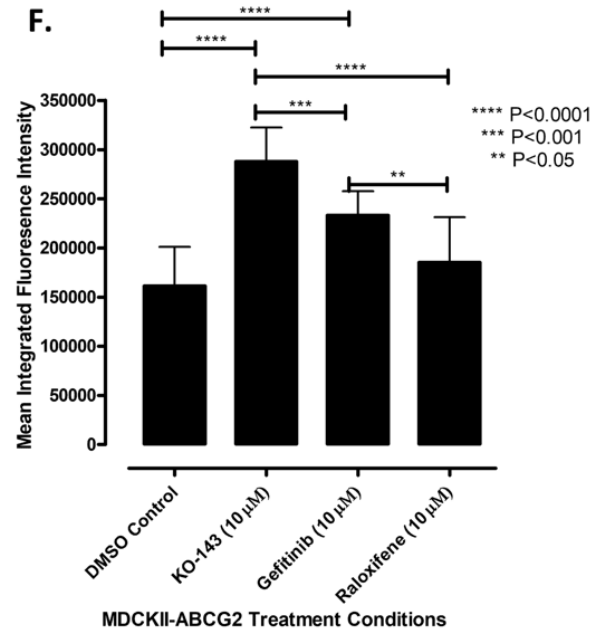
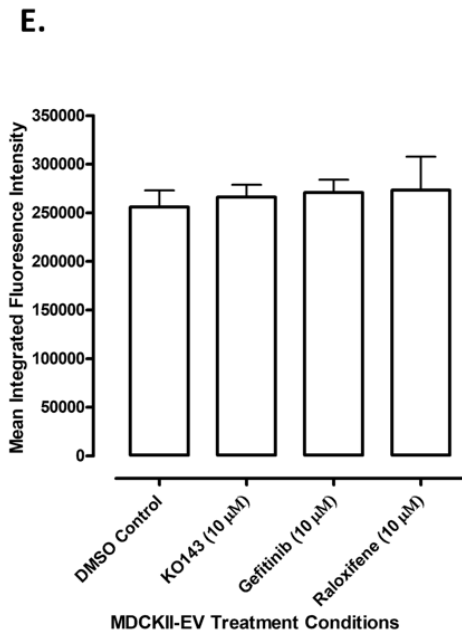
**C) Results Frequency Distribution of the Mean Integrated Fluorescent Intensities of the Hoechst-stained Nuclei in MDCKII-EV Cell Populations  $\pm$  10  $\mu$ M Gefitinib.** The binned cellular mean integrated Hoechst fluorescent intensity (MIFI) data output of the multiwavelength cell scoring (MWCS) image analysis module was plotted to quantify and compare the profiles of Hoechst accumulation in MDCKII-EV cell populations in the presence (■) or absence (■) of 10  $\mu$ M Gefitinib for 60 minutes at 37°C in 5 % CO<sub>2</sub> and 95% humidity. The Y-axis represents the number of cells detected in each MIFI bin plotted on the X-axis.

D.



**D) Results Frequency Distribution of the Mean Integrated Fluorescent Intensities of the Hoechst-stained Nuclei in MDCKII-ABCG2 Cell Populations  $\pm$  10  $\mu$ M Gefitinib.**

The binned cellular mean integrated Hoechst fluorescent intensity (MIFI) data output of the multiwavelength cell scoring (MWCS) image analysis module was plotted to quantify and compare the profiles of Hoechst accumulation in MDCKII-ABCG2 cell populations in the presence (■) or absence (■) of 10  $\mu$ M Gefitinib for 60 minutes at 37°C in 5 % CO<sub>2</sub> and 95% humidity. The Y-axis represents the number of cells detected in each MIFI bin plotted on the X-axis.



**E) Hoechst Accumulation in MDCKII-EV Cells  $\pm$  10  $\mu$ M Ko143, Gefitinib or Raloxifene.** The well-averaged Hoechst MIFI values ( $\square$ ) for MDCKII-EV cells incubated in the presence or absence of 10  $\mu$ M Ko143, Gefitinib or Raloxifene for 60 minutes at 37°C in 5 % CO<sub>2</sub> and 95% humidity are presented as the mean MIFI values  $\pm$  SD (n = 3) of triplicate wells versus time in minutes. **F) Hoechst Accumulation in MDCKII-ABCG2 Cells  $\pm$  10  $\mu$ M Ko143, Gefitinib or Raloxifene.** The well-averaged Hoechst MIFI values ( $\blacksquare$ ) for MDCKII-ABCG2 cells incubated in the presence or absence of 10  $\mu$ M Ko143, Gefitinib or Raloxifene for 60 minutes at 37°C in 5 % CO<sub>2</sub> and 95% humidity are presented as the mean MIFI values  $\pm$  SD (n = 3) of triplicate wells versus time in minutes. We performed one-way ANOVA with Tukey’s multiple comparisons as a post hoc test to determine whether there was a statistically significant difference in Hoechst accumulation between MDCKII-ABCG2 cells lines incubated in the presence or absence of 10  $\mu$ M Ko143, Gefitinib or Raloxifene; \*\*\*\* p < 0.001, \*\*\* p < 0.01, \*\* p < 0.05. Representative data from one of at least 3 independent experiments each performed in 3 replicate wells are shown.

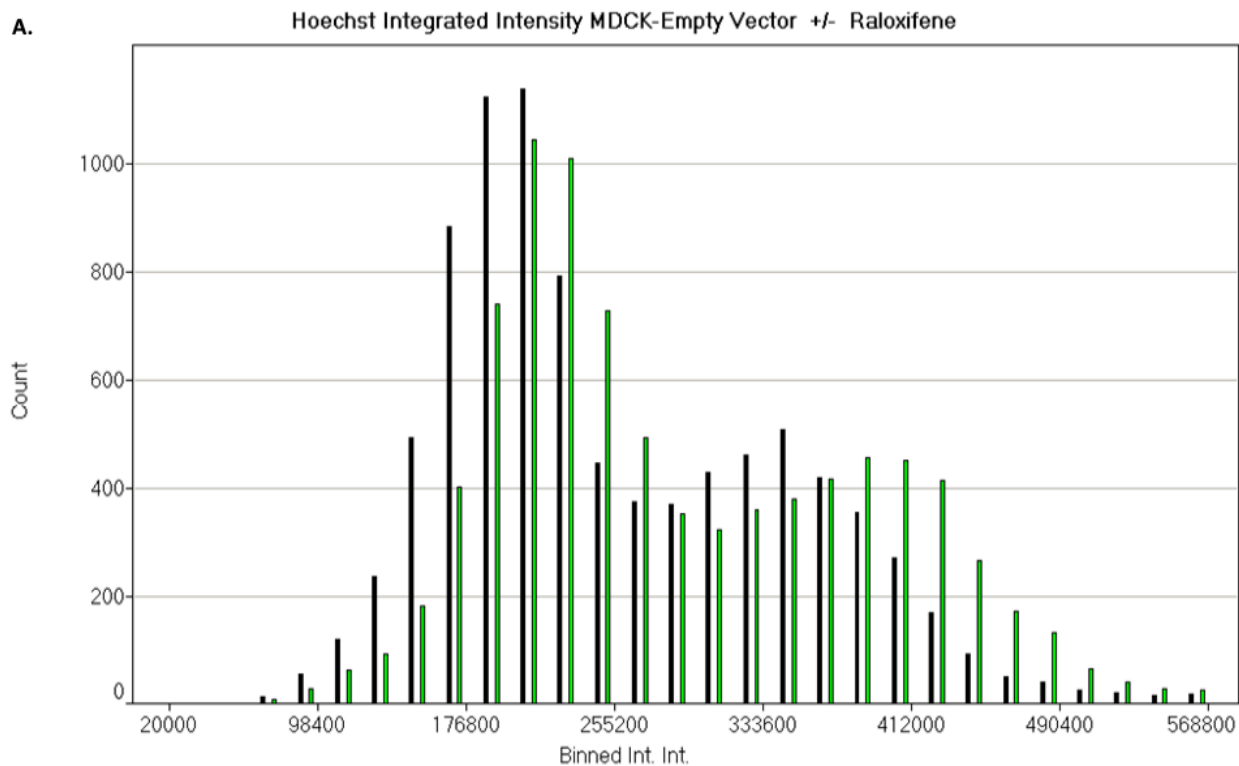
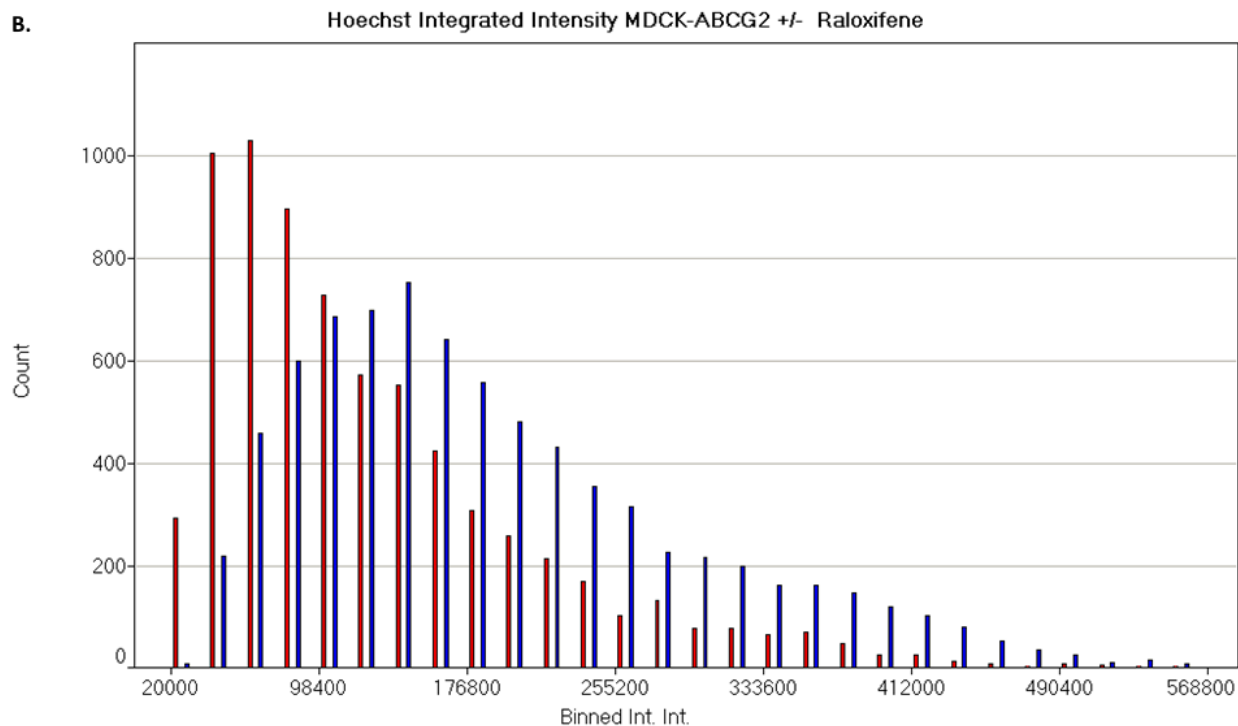


**Figure 12 Effects of Exposure to Raloxifene on Hoechst 33342 Accumulation in MDCKII-EV and MDCKII-ABCG2 Cell Lines**

**A) Results Frequency Distribution of the Mean Integrated Fluorescent Intensities of the Hoechst-stained Nuclei in MDCKII-EV Cell Populations  $\pm$  10  $\mu$ M Raloxifene.**

The binned cellular mean integrated Hoechst fluorescent intensity (MIFI) data output of the multiwavelength cell scoring (MWCS) image analysis module was plotted to quantify and compare the profiles of Hoechst accumulation in MDCKII-EV cell populations in the presence (■) or absence (■) of 10  $\mu$ M Raloxifene for 60 minutes at 37°C in 5 % CO<sub>2</sub> and 95% humidity. The Y-axis represents the number of cells detected in each MIFI bin plotted on the X-axis.



**B) Results Frequency Distribution of the Mean Integrated Fluorescent Intensities of the Hoechst-stained Nuclei in MDCKII-ABCG2 Cell Populations  $\pm$  10  $\mu$ M Raloxifene.** The binned cellular mean integrated Hoechst fluorescent intensity (MIFI) data output of the multiwavelength cell scoring (MWCS) image analysis module was plotted to quantify and compare the profiles of Hoechst accumulation in MDCKII-ABCG2 cell populations in the presence (■) or absence (■) of 10  $\mu$ M Raloxifene for 60 minutes at 37°C in 5 % CO<sub>2</sub> and 95% humidity. The Y-axis represents the number of cells detected in each MIFI bin plotted on the X-axis.

values were also consistently higher in wells treated with raloxifene compared to DMSO, the differences were not considered statistically significant and merits follow up at a higher compound concentration or duration of exposure to investigate the potential for statistically significant inhibition of Hoechst accumulation. Cumulatively these data demonstrated that exposure to 10  $\mu$ M Ko143, gefitinib or raloxifene enhanced Hoechst accumulation in MDCKII-ABCG2 cells but not in MDCKII-EV cells (Figure 11). Either gefitinib and potentially raloxifene are direct inhibitors of the ABCG2 drug efflux transporter, or they are substrates that competitively inhibit ABCG2-mediated Hoechst efflux.

## 2.11 Discussion

The NCI-60 panel of tumor cell lines encompass nine cancer lineages that for >30 years have been used to screen small molecule and natural product extract libraries for compounds that inhibit tumor cell line growth and might then be optimized and developed into cancer drugs.<sup>55, 57, 67-69</sup> Growth inhibition patterns across the 60 cell lines are similar for drugs with closely related MOAs, and the COMPARE algorithm can be used to predict the MOAs of novel molecules that exhibit similar sensitivity and resistance profiles to known anticancer agents.<sup>68, 69</sup> Over the years, the NCI-60 cell lines have been extensively characterized; exome sequencing, DNA methylation, mRNA expression, microRNA expression, protein levels and modifications, ABC drug efflux transporter mRNA expression levels, enzyme activities and metabolomics profiling.<sup>55, 67-69</sup> Recently the NCI established the ALMANAC database which contains data from a DC HTS campaign of

100 FDA approved cancer drugs that were screened in pairwise DCs across the 60 cell lines.<sup>55, 56</sup> Since 75% of the DCs in the ALMANAC database are not listed in the clinical trials database, the data can be mined to identify novel DCs that might be suitable starting points for future clinical development as effective DC regimens.<sup>55, 56</sup> However, primary HTS actives need to be confirmed as qualified hits before they progress into follow up studies designed to determine MOAs and establish value. Using criteria described above, we selected four DCs that were flagged as synergistic interactions in the pilot phase of the DC HTS campaign for confirmation of synergy *in vitro* (Table 1).<sup>56</sup> We prepared 10 x 10 DCMs and analyzed the fraction of cells affected by fixed DC ratios to calculate CI values, plotted the data in isobologram contour graphs, and applied the PDI model to create 3D graphs and calculate the fitted  $\alpha$  parameter (Figure 3, Figures 5-8, and Table 1). All 19 (100%) of the DC and tumor cell line sets were confirmed and classified as synergistic interactions in three distinct pharmacological interaction models (Table 1).

Queries of the ClinicalTrials.Gov database for DC-1 retrieved two clinical trials that are open for enrollment. Gefitinib and mitoxantrone are two of 75 FDA approved drugs in a genomics-based assignment of therapy clinical trial in patients with advanced urothelial carcinoma, NCT02788201. The Co-eXpression ExtrapolatioN (COXEN) model algorithm will be used to determine the best therapy from among the 75 agents (single agent or combination) for urothelial carcinoma patients that have progressed on at least one chemotherapy regimen. Gefitinib and mitoxantrone are also among the agents in a high throughput drug sensitivity assay and genomics-guided treatment clinical trial in patients with relapsed or refractory acute leukemia, NCT02551718. Treatment options will be selected based on high throughput *ex vivo* drug sensitivity assays in combination with

mutation analysis of patients with acute leukemia that has returned after a period of improvement or does not respond to treatment. There is also pre-clinical *in vitro* data which corroborates that the gefitinib and mitoxantrone combination might be more effective against tumor cell lines than single agent treatments. Gefitinib increased the growth inhibitory effect of mitoxantrone in the MCF-7 estrogen receptor alpha-positive human breast cancer cell line, and also in a fulvestrant-resistant cell line (MCF-7/F) derived from MCF-7 cells.<sup>70</sup> The combination of mitoxantrone with gefitinib and cyclopamine produced supra-additive anti-proliferative effects in androgen-sensitive and androgen-independent prostate cancer cell lines.<sup>71</sup> In contrast however, gefitinib did not enhance the cytotoxicity of mitoxantrone, or several other antitumor agents, in a panel of 5 oral squamous cell carcinoma cell lines.<sup>72</sup>

Queries of the ClinicalTrials.Gov database failed to return any clinical trials for DC-2. In pre-clinical *in vitro* studies, a raloxifene analogue partially reversed drug resistance to mitoxantrone in an estrogen receptor beta-positive A2780 ovarian cancer cell line stably transfected with splicing factor SPF45.<sup>73</sup> Queries of the ClinicalTrials.Gov database also didn't return any clinical trials for DC-3. In pre-clinical *in vitro* studies, exposure to raloxifene for 48 hours partially restored the sensitivity of K562/A02 cells to daunorubicin. The K562/A02 cell line is a multidrug resistant variant of the K562 chronic myelogenous leukemia (CML) cell line which is ~100-fold resistant to daunorubicin.<sup>74</sup> Although queries of the ClinicalTrials.Gov database for DC-4 returned 10 clinical trials where these drugs were listed in the treatment regimen, gefitinib and vinorelbine appeared in different comparator treatment arms, never in combination. In pre-clinical *in vitro* studies, gefitinib and vinorelbine DCs have been investigated in Head and Neck Squamous cell Carcinoma

(HNSCC), NSCLC and melanoma tumor cell line models.<sup>56, 75, 76</sup> In HNSCC tumor cell lines, DC-4 had a supra-additive cytotoxic effect in 4/6 cell lines, and additive cytotoxic effects in the other two.<sup>75</sup> It was suggested that since gefitinib and vinorelbine are both metabolized by CYP3A4 P450 isoenzymes, drug-drug interactions may alter their respective exposure levels *in vivo*.<sup>75</sup> In seventeen NSCLC cell lines which included four that overexpressed the ATP binding cassette (ABC) drug efflux transporter ABCB1 (Pgp/MDR1) and three with sensitizing EGF-R mutations, DC-4 exhibited synergism in cell lines lacking EGF-R mutations.<sup>76</sup> Although the synergy between gefitinib and vinorelbine was more robust in ABCB1 overexpressing NSCLC cell lines, it was also apparent in cell lines with efflux transporter expression levels below detection limits.<sup>76</sup> Since gefitinib is an ABCB1 inhibitor and vinorelbine is an ABCB1 substrate, it was considered probable that blocking the efflux transporter active resistance mechanism contributed to the synergy between the two drugs in ABCB1 overexpressing NSCLC cell lines, but that other MOAs of resistance were likely affected in cell lines with no detectable efflux transporter expression.<sup>76</sup> The gefitinib and vinorelbine combination was also confirmed to be synergistic *in vitro* in the SK-MEL-5 melanoma cell line.<sup>56</sup>

Several factors prompted us to investigate drug efflux transporter interactions as a potential MOA for the synergistic inhibition of tumor cell line growth by DCs 1-4 (Tables 1 and 2). ABC transporters actively extrude cancer drugs with diverse chemical structures from tumor cells thereby conferring resistance to these agents, and increased expression of ABC efflux transporter superfamily members contributes to multidrug resistance (MDR) and therapeutic failure.<sup>69, 77, 78</sup>

**Table 2 Selected Drug Combinations, NCI-60 Cell Lines, Drug Efflux Transporter mRNA Expression Levels and Compound Functional Activities**

Drug Combination			NCI-60	Drug Efflux Transporter mRNA Expression Levels			Drug Efflux Transporter Functional Activity	
DC	Drug-A	Drug-B	Cell Line	ABCG2	ABCB1	ABCC1	Drug-A	Drug-B
1	Gefitinib	Mitoxantrone	KM12	High	Low	High	ABCG2 & ABCB1 inhibitor	ABCG2, ABCB1 & ABCC1 substrate
1	Gefitinib	Mitoxantrone	MDA-MB-468	NA	NA	NA	ABCG2 & ABCB1 inhibitor	ABCG2, ABCB1 & ABCC1 substrate
1	Gefitinib	Mitoxantrone	OVCAR-5	Low	Low	Moderate	ABCG2 & ABCB1 inhibitor	ABCG2, ABCB1 & ABCC1 substrate
1	Gefitinib	Mitoxantrone	PC-3	Low	Low	Moderate	ABCG2 & ABCB1 inhibitor	ABCG2, ABCB1 & ABCC1 substrate
2	Raloxifene	Mitoxantrone	HCT-116	Moderate	Low	High	ABCG2 & ABCB1 inhibitor	ABCG2, ABCB1 & ABCC1 substrate
2	Raloxifene	Mitoxantrone	HCT-15	Low	High	Moderate	ABCG2 & ABCB1 inhibitor	ABCG2, ABCB1 & ABCC1 substrate
2	Raloxifene	Mitoxantrone	KM12	High	Low	High	ABCG2 & ABCB1 inhibitor	ABCG2, ABCB1 & ABCC1 substrate
2	Raloxifene	Mitoxantrone	SW-620	Low	High	Moderate	ABCG2 & ABCB1 inhibitor	ABCG2, ABCB1 & ABCC1 substrate
3	Raloxifene	Daunorubicin	DU-145	Moderate	Low	High	ABCG2 & ABCB1 inhibitor	ABCG2, ABCB1 & ABCC1 substrate
3	Raloxifene	Daunorubicin	NCI-H23	High	Low	Moderate	ABCG2 & ABCB1 inhibitor	ABCG2, ABCB1 & ABCC1 substrate
3	Raloxifene	Daunorubicin	NCI-H522	Moderate	Low	High	ABCG2 & ABCB1 inhibitor	ABCG2, ABCB1 & ABCC1 substrate
4	Gefitinib	Vinorelbine	SK-MEL-5	Moderate	High	Low	ABCG2 & ABCB1 inhibitor	ABCB1 & ABCC1 substrate
4	Gefitinib	Vinorelbine	MDA-MB-435	High	Low	Low	ABCG2 & ABCB1 inhibitor	ABCB1 & ABCC1 substrate
4	Gefitinib	Vinorelbine	HL-60	Low	High	Low	ABCG2 & ABCB1 inhibitor	ABCB1 & ABCC1 substrate
4	Gefitinib	Vinorelbine	MOLT-4	Low	Low	Moderate	ABCG2 & ABCB1 inhibitor	ABCB1 & ABCC1 substrate
4	Gefitinib	Vinorelbine	RPMI-8226	High	Low	Moderate	ABCG2 & ABCB1 inhibitor	ABCB1 & ABCC1 substrate

DC = drug combination number

NCI-60 = National Cancer Institute 60 tumor cell line panel.

ABCG2 = ATP-binding cassette super-family G member 2, also known as breast cancer resistance protein (BCRP) or multi-xenobiotic resistance transporter (MXR).

ABCB1 = ATP-binding cassette sub-family B member 1, also known as permeability glycoprotein 1 (P-gp) and multidrug resistance protein 1 (MDR1)

ABCC1 = ATP-binding cassette sub-family C member 1, also known as multidrug resistance protein 1 (MRP1).

Relative drug efflux transporter mRNA expression levels are based on Szakacs et al, Cancer Cell, 2004, 6: 129-137. The mRNA expression levels of 47 ABC transporters were measured across the NCI-60 tumor cell lines using real-time quantitative RT-PCR with specific oligonucleotide primers for each transporter. Individual ABC transporter mRNA expression data were normalized relative to their mean expression across the 60 cell lines. The data was mean centered and multiplied by -1 to generate values relative to the average expression of each transporter in the 60 cell lines: cell lines with scores <-2 exhibited lower than average ABC transporter expression; cell lines with scores >-2 but <2 had moderate expression levels; and cell lines with scores >2 displayed high expression levels.

There is considerable evidence in the literature that gefitinib inhibits both the ABCG2 (BCRP) and ABCB1 (Pgp/MDR1) transporters and can reverse the resistance of cancer cells expressing these proteins to chemotherapeutic agents that are efflux substrates.<sup>79-82</sup> There is also evidence in the literature that raloxifene inhibits ABCB1 (Pgp/MDR1) mediated substrate efflux, and to a lesser extent that of ABCG2 (BCRP).<sup>83-85</sup> However, raloxifene has also been reported to be a substrate of ABCB1.<sup>85</sup>

ABCB1, ABCC1 and ABCG2 transporters efflux a broad and partially redundant set of cancer drug substrates.<sup>78</sup> For example, mitoxantrone and daunorubicin, the two B drugs in DCs 1-3, are substrates of ABCG2, ABCB1 and ABCC1, and vinorelbine the B drug in DC-4, is a substrate of ABCB1 and ABCC1. The most extensively characterized MDR transporters include: ATP-binding cassette sub-family B member 1 (ABCB1) also known as permeability glycoprotein 1 (P-gp) or multidrug resistance protein 1 (MDR1); ATP-binding cassette sub-family C member 1 (ABCC1) also known as multidrug resistance protein 1 (MRP1); and ATP-binding cassette super-family G member 2 (ABCG2) also known as breast cancer resistance protein (BCRP) or multi-xenobiotic resistance transporter (MXR).<sup>78</sup> Correlations between the growth inhibition profiles of drugs and the mRNA expression levels of ABC efflux transporter members in the NCI-60 tumor cell lines have been used to infer which transporters mediated resistance to selected agents.<sup>77</sup> The *in vitro* sensitivity of NCI-60 tumor cell lines to cancer drugs that are substrates of ABC transporters is inversely correlated with transporter expression levels, and efflux transporter inhibitors can reverse drug resistance *in vitro*.<sup>69, 77, 78</sup> We therefore developed an HCS assay to measure and compare the accumulation of the ABCG2 efflux transporter substrate Hoechst 33342 in MDCKII-EV and MDCKII-ABCG2

cell lines and demonstrated that the ABCG2 inhibitor Ko143 enhanced Hoechst accumulation in MDCKII-ABCG2 but not MDCKII-EV cells (Figures 9 & 10). Similarly, we demonstrated that exposure to gefitinib or raloxifene also enhanced Hoechst accumulation in MDCKII-ABCG2 cells but not in MDCKII-EV cells (Figure 11). Our data suggest that gefitinib and potentially raloxifene if a higher concentration is tested and proven statistically significant, are either inhibitors of the ABCG2 drug efflux transporter, or they are substrates that competitively inhibit ABCG2-mediated Hoechst efflux. There is considerable evidence that gefitinib inhibits both the ABCG2 (BCRP) and ABCB1 (Pgp/MDR1) transporters and can reverse the resistance of cancer cells expressing these proteins to chemotherapeutic agents that are efflux substrates.<sup>65, 66, 79-82, 86</sup> Although gefitinib inhibits ABCG2 ~10-fold more potently than ABCB1, both efflux transporters were inhibited at clinically relevant drug concentrations *in vivo*.<sup>65</sup> There is also evidence that raloxifene inhibits ABCB1 (Pgp/MDR1) mediated substrate efflux, and to a lesser extent that of ABCG2 (BCRP).<sup>83-85</sup> However, raloxifene has also been reported to be a substrate of ABCB1.<sup>85</sup> Thus, the two A drugs in DCs 1-4, gefitinib and raloxifene, are inhibitors of ABCG2 (BCRP) and ABCB1 (Pgp/MDR1) drug efflux (Table 2).<sup>77</sup> ABCB1, ABCC1 and ABCG2 transporters efflux a broad and partially redundant set of cancer drug substrates.<sup>78</sup> For example, mitoxantrone and daunorubicin, the two B drugs in DCs 1-3, are substrates of ABCG2, ABCB1 and ABCC1, and vinorelbine the B drug in DC-4, is a substrate of ABCB1 and ABCC1.<sup>78</sup> Furthermore, the NCI-60 cell lines in which DCs 1-4 synergistically inhibited growth (Table 1), express moderate to high levels of one or more of the ABCG2, ABCB1 and ABCC1 efflux transporters (Table 2). It seems plausible therefore that the combination of an ABC efflux inhibitor that has anti-cancer activity with

a chemotherapeutic agent which is a transporter substrate contributes to the synergistic inhibition of tumor cell line growth observed with DCs 1-4. However, we cannot exclude the possibility that other MOAs also contributed to the synergistic effects of DCs 1-4.

The pharmacological inhibition of ABC drug efflux transporters has been actively pursued as a strategy to reverse cancer drug resistance and enhance clinical efficacy.<sup>69</sup> However clinical trials that have used ABC transporter inhibitors to enhance cancer drug efficacy have largely been disappointing, in part because the inhibitors altered the pharmacokinetics of the anticancer agents decreasing their systemic clearance and increasing the severity and/or incidence of adverse events.<sup>69</sup> In addition to exogenous xenobiotics, ABC transporters also mediate the efflux of endogenous molecules and metabolites from cells, and inhibition of these processes may be detrimental to normal cells.<sup>69</sup> Systematic unbiased HTS of DCs in panels of well characterized tumor cell lines provides a means to identify DCs that exhibit greater than additive activity against selected tumor cell lines. The studies presented herein demonstrate that novel synergistic DCs identified in a DC HTS campaign can be selected and confirmed *in vitro*, and plausible MOAs can be explored. Since the drugs in the DC HTS campaign used to create the ALMANAC database are FDA approved anti-cancer agents, effective DCs that are confirmed *in vitro* would have the potential to be advanced rapidly into clinical translation. DC confirmation and MOA data would be used to prioritize specific DCs for testing in mouse xenograft human cancer models, and for any DCs that exhibited superior efficacy *in vivo*, the cumulative data would support their clinical evaluation in patients. Overall, we were able to demonstrate the utility of our confirmation strategy, and the ability to generate testable hypotheses in a data-driven manner. Furthermore, we were able to follow-up and

design an assay to test one such hypothesis for the synergistic mechanism of action between our top drug combination matrices.

### **3.0 Multicellular Tumor Spheroids: Physiological Relevance and Application in Cancer Drug Discovery**

#### **3.1 MCTSs An Improvement to 2D Cell Culture**

The American Cancer Society estimates that in 2019, approximately 1,762,450 new cases of cancer will arise, with 606,880 cancer-related deaths occurring in the United States.<sup>87</sup> Cancer ranks as the second leading cause of death, and unfortunately, the probability of success for cancer drug candidates to progress from clinical trials into patient treatment is a mere 3.4% (averaged from 2000-2015).<sup>88</sup> The low probability for drug candidates to be successful echoes several major challenges: at the *in vivo* and *in vitro* levels of preclinical drug discovery, current animal and cellular models are incapable of accurately predicting treatment outcomes in humans, primarily due to physiological limitations in animal models, and the limited ability of 2D cell culture models to adequately recapitulate tumor physiology, microenvironmental characteristics, and heterogeneity; at the patient level, the design and facilitation of oncological clinical trials is both complex and increasingly rigorous, requiring overall survival as a primary endpoint and the inclusion of patient treatment crossover arms, which makes maintaining an appropriately controlled phase 3 trial difficult.<sup>89-91</sup>

Human tumors are complex cellular structures, composed of both cell-cell and cell-extracellular matrix interactions, which maintain the 3D structure and allow for the development of physiological barriers capable of limiting the diffusion of nutrients, waste, gases, growth factors, and the penetration of drugs into the deeper regions of the tumor.<sup>92</sup>

<sup>93</sup> Solid tumors are capable of interacting with a stroma, essentially a cellular milieu of different cell types associated with the tumor, such as fibroblasts, immune cells, and endothelial cells which contribute to the generation of microenvironments.<sup>92, 94</sup> The microenvironments of solid tumors contribute to innate resistance mechanisms or respond to the selective pressures of chemotherapy to resist and/or survive the influence of a drug by a variety of means. In particular, tumor cells further from blood vessels tend to be less proliferative, decreasing the effectiveness of drugs that target actively dividing cells.<sup>93, 95</sup> In addition, size-limiting diffusion of nutrients and oxygen create a hypoxic and eventually necrotic region of cells, with limited diffusion of drug into the tumor causing an uneven distribution of chemotherapeutics and reducing the overall exposure to distant cells within the tumor.<sup>93, 95</sup> Furthermore, a gradient of high to low extracellular pH from outside of the tumor to its core limits weakly basic drugs from being taken up, such as 5'FU which when ionized at the hydroxyl group on carbon 4, which will have markedly reduced cellular uptake.<sup>93, 95</sup> All of these factors have contributed to the complexity of tumors, and the difficulty in recapitulating such characteristics *in vitro*. In an article published by Hirschhaeuser and colleagues, the authors outline that 3D cell culture is capable of recapitulating the tumor microenvironment, indicating that physiological gradients of nutrients, oxygen, pH, and drug penetration were created by cells in 3D.<sup>96</sup> They also demonstrated that cells as 3D MCTSs displayed differential zones of proliferation, with a quiescent middle sector, and necrotic core, which are all physiologically relevant characteristics resembling a solid tumor.<sup>96</sup> Furthermore, we and several other laboratories have demonstrated that multicellular tumor spheroids (MCTSs), with their high degree of cell-cell interactions and production of

microenvironments, exhibit differential drug penetration and distribution gradients when compared to their 2D counterparts for anthracycline drugs such as doxorubicin.<sup>64, 97</sup>

Antineoplastic drug screening has historically been performed in microtiter plates that supported the growth of cells in 2D monolayers, given their relative simplicity, ease of use, scalability and cost effectiveness. As described in chapter 1, the NCI pioneered the use of miniaturized growth inhibition assays for drug screening that allowed tens to hundreds of thousands of compounds to be screened across a wide spectrum of cell lines and cancer types that were cultured in 2D.<sup>20, 25</sup> This innovation was introduced at time when new methods in drug screening were desperately needed, especially given that other methods lacked the necessary throughput to screen large libraries of drugs efficiently and economically. Despite this milestone, 2D cell culture is still an incomplete representation of a solid tumor. Currently, 3D multicellular tumor spheroids (MCTSs) produced through ultra-low attachment (ULA) conditions or hanging drop methods have been proven to be an innovative cell culture tool with technical flexibility, capable of increasing the success of high throughput screening approaches by more accurately mimicking the complexities of a solid tumor and better capable of translating results from *in vitro* to *in vivo*.

## 3.2 Comparison of Methods for Generating 3D Cell Culture Conditions

### 3.2.1 Anchorage-dependent Models

In order to adequately analyze various physiological solid tumor conditions *in vitro*, a multitude of 3D cell culture models have been developed, namely: anchorage-dependent models, and anchorage-independent models.<sup>94, 98, 99</sup> Anchorage-dependent models typically require the production and design of a synthetic or biological scaffold capable of encouraging ECM formation and support to the 3D cellular structure.<sup>98, 99</sup> Commonly, scaffold addition via hydrogel encapsulation of cells is used to stimulate ECM formation, and assay cell adhesion, proliferation, and migration as a means of observing tumorigenicity and malignancy *in vitro*.<sup>100, 101</sup> Anchorage-dependent methods provide a more meaningful observation of ECM components related to the tumor microenvironment, and allow for cellular migration and related metastatic characteristics to be assayed outside of a human tumor or xenograft model. Despite these advantages, methods using hydrogel scaffolds can have batch-to-batch variability, making reproduction of appropriate conditions challenging; compound or detection reagent penetration into the substrate can be unequal, thereby causing a gradient and leading to inconclusive results; and the production and maintenance of cells in hydrogel scaffolds is both labor intensive and time consuming, which may limit the utility and convenience.<sup>98</sup>

### **3.2.2 Anchorage-Independent Methods for 3D**

Anchorage-independent methods rely on the ability of cells to self-assemble without specific attachment cues to a substrate and include two main classes of methods, soft agar colony formation, and spheroid generation through spontaneous aggregation, one example is the use of ultra-low attachment (ULA) microtiter plates to generate spheroids.<sup>98, 99</sup> One of the most mainstream methods often heralded as a gold standard for determining cellular transformation and clonogenicity, is the soft agar colony formation assay; comprised of cells grown in soft agar with culture medium, where any transformed cells will form colonies independent of specific attachment cues from the ECM, but normal cells will not form any colonies unless such cues exist.<sup>102</sup> This assay has been adapted to include several different approaches capable of highlighting key tumor suppressor or oncogenic contributors to malignancy in transfected cell lines.<sup>102</sup> Some of the major limitations of the soft agar colony formation assay are the time intensive nature (2-3 weeks / assay) of performing and maintaining the assay conditions, and the potential for diminished cell viability after seeding in heated agar.<sup>98</sup>

### **3.2.3 Introduction to Spheroid Generating Methods for 3D**

Spheroid generating methods represent the more commonly used 3D cell culture approaches in cancer drug discovery, as many of them were designed and adapted for high throughput and high content screening projects / campaigns. These approaches include rotary or rotative cell culture, hanging drop, liquid overlay, and ULA microtiter plates.<sup>94, 98, 99</sup> Similar to the soft agar colony formation assay, no attachment cues are

provided in ULA culture environments, and rather, cell-cell interactions are encouraged to occur spontaneously and predominate vs cell-substrate interactions. What's more, 3D MCTSs have been extensively documented as having the ability to adequately recapitulate the characteristics of an avascular tumor nodule, micro-metastases, and or the intervascular regions of a solid tumor.<sup>103-105</sup> These tumor relevant characteristics include: appropriate cell-ECM assembly, cell-ECM and cell-cell binding interactions, gradients of oxygen and nutrients distribution, accumulation of catabolites, and differential zones of cellular proliferation. Among the anticipated benefits of implementing more physiologically relevant MCTS models for cancer drug screening is to better predict the *in vivo* success of drug candidates in the preclinical stage of drug discovery. Two examples where 3D has provided an application of demonstrating a clinical relevance beyond 2D are in Pickl & colleagues (2009) and Wenzel & colleagues (2014), where the former used 3D to illustrate a clinically relevant response of the monoclonal antibody trastuzumab whereby only 3D was able to demonstrate the appropriate HER dimerization to allow successful inhibition; Wenzel *et. al* was able to perform a drug screen in 3D MCTSs that utilized the ability of 3D to maintain dormant cells within the inner region of the MCTSs, something cell culture in 2D is unable to accomplish.<sup>106, 107</sup>

### **3.3 Overview of Spontaneous Aggregation Methods of 3D**

#### **3.3.1 Rotative / Rotary Cell Culture**

Rotative / rotary cell culture represents a method to produce 3D MCTSs using rotational stirring via bioreactor / gyratory rotation and is meant to accommodate a larger suspension of cells in a biological-relevant and controlled environment for pH, media exchange, oxygen, and removal of waste.<sup>108</sup> This method is very capable of recapitulating conditions within a solid tumor, save for microvasculature, but manages to perform similar functions as vasculature with regard to supplying fresh nutrients, oxygen, and removal of waste to the spheroids.<sup>109</sup> Despite the sophistication of this method, its biggest limitations would be scalability for higher throughput, the tendency for irregular 3D aggregates to form, and negative impacts of the rotational shear force on spheroid morphology.<sup>98, 110</sup>

#### **3.3.2 Hanging Drop Method**

The hanging drop technique relies on immersing a cell suspension in a droplet of culture media to prevent substrate-cell interactions. Without any adhesion substrates to interact with, the cells begin to self-aggregate and over time are capable of forming multi-layered spheroids with the outermost layer being reminiscent of a tumor in a region near vasculature. It is a cost-effective method that does not require specialized equipment in order to generate size and shape-controlled spheroids, however, both the throughput and duration of time in culture are limiting; as well, the technique is very labor intensive and does not scale well up for larger drug screening campaigns.<sup>98, 110</sup>

### **3.3.3 Liquid Overlay Technique**

The liquid overlay technique represents another method that prevents cell-substrate interactions, but instead of using agitation or suspension in media to prevent such interactions, the liquid overlay method relies on using non-adherent biomaterials such as agar, agarose, and poly-HEMA to coat plates before seeding cancer cells in an attempt to form aggregates.<sup>98, 110</sup> By coating the well bottom with a non-adherent surface, cell-cell interactions become more prominent and as such within 1-3 days spheroids will form. Of note, Costa *et. al* indicated that development of a spherical cellular aggregate required adaptation of the overlaid well shape, where a flat bottom led to variety of cellular structures not necessarily favoring spheroid architecture, while a concave bottom promoted spheroid formation.<sup>110</sup> This method has been reported to be cost-effective, and easy to handle without the need of specialized equipment for spheroid formation, however, it is limited by its prep time for biomaterials, potential variability in spheroid size or shape depending on the plate / well surface shape, and it is also labor intensive.<sup>98, 110</sup>

### **3.3.4 Magnetic Levitation**

Magnetic levitation and/or bioprinting represents a scaffold-free technology that also utilizes low or ultra-low attachment conditions. Instead of seeding in a microtiter plate with a defined well shape, this technique relies on the uptake of innocuous magnetic nanoparticles by incubated cells prior to harvesting and seeding. After cellular uptake of magnetic nanoparticles, an external magnetic field is applied after cells are seeded into 96-well or 384-well microtiter plates, and the cells form aggregates which encourages

cell-cell interactions and spheroid formation, documented to occur within 12-24hrs, and cultures have been indicated to last for at least 12 weeks.<sup>111, 112</sup> This technique is capable of providing consistent spheroids but with two minor limitations: cultures require approximately 8 days for cell-cell attachments to be independent of the magnetic nanoparticles, and FeO may color the media brown which could limit any brown colorimetric reagents from being appropriately read.<sup>112</sup>

### **3.4 Overview of ULA for Production of 3D Cell Culture**

ULA microtiter plate methods in 3D cell culture represent a simple method compatible with high throughput conditions, automation and a variety of high content applications. Cells are seeded into 96-well or 384-well microtiter plate wells treated with a hydrophilic neutrally charged coating which prevents cells from attaching to the well bottom thereby allowing cell-cell interactions to predominate while suspended in media. Several laboratories including our own have published on the use and characterization of cancer cell lines as MCTSs using ULA conditions.<sup>64, 98, 104, 113, 114</sup> In Vinci *et. al* 2012, the authors establish the use of ULA plates to create MCTSs and established a set of morphological classifications for 3D structure and compactness as modeled after the Ivascu classifications in breast cancer spheroids.<sup>104, 115</sup> Furthermore, Vinci was able to demonstrate that the creation of spheroids was rapid, consistent, and reproducible, especially with regard to generating a consistent size of spheroid.<sup>104</sup> Selby *et. al* 2017 have illustrated the utility of ULA technology with the NCI60 cell line panel, whereby, they characterized both the morphology of the 60 cell lines and 9 tumor types as 3D MCTSs.<sup>113</sup>

In addition, the authors were able to demonstrate many different drug responses between 2D vs 3D: 2D showed more sensitivity than 3D, a similar sensitivity was experienced between both 2D and 3D, and limited or no drug sensitivity was observed in both models.<sup>113</sup>

Our laboratory has also demonstrated the utility of U-bottom well ULA microtiter plates to produce spheroids with consistent and distinct morphologies with regards to size, shape and compaction.<sup>64, 98, 114</sup> These spheroids were capable of being cultured for a up to 12 days with media changes, suitable for a multitude different applications including cancer drug screening.<sup>64, 98, 114</sup> Furthermore, we have illustrated the ability of our head and neck squamous cell carcinoma models to demonstrate differential zones of proliferation, the formation of a necrotic core, and the reduced penetration of cytotoxic drugs into the spheroids.<sup>64, 114</sup> These characteristics are both representative and indicative of the diverse population of cells observed in avascular tumors / distal cells of a vascularized tumor; where cell-cell and cell-ECM interactions limit drug penetration to target the entire tumor population. Of note, we selected HNSCC as our cancer type, as there is an unmet need for therapeutics outlined by many researchers, in addition to little to no change in the 5-year survival over the past 30 years.<sup>116, 117</sup> Some challenges using ULA are that not all cancer types, patient samples, and / or xenografts will form a spheroid, in addition, given the structure of the individual wells within the plate only a single spheroid can be formed per well. For our purposes, we selected ULA given its ease of use and compatibility with the equipment and parameters we used for assay development. Furthermore, the ensuing chapters present both our characterization of head and neck squamous cell carcinoma cell lines as 3D MCTSs and their use in a

miniature drug screen with 19 FDA approved cancer drugs of varying mechanisms of action.

### **3.5 Beyond MCTS Models, a Vision of the Future**

Microfluidic plates represent a bioengineered method of incorporating faux vasculature in the form of fluidic chambers to microtiter plates, which enable the creation of interstitial pressure, removal of waste, and the addition of fresh media to the cultured spheroid / tumoroids.<sup>118, 119</sup> In particular, the presence of fluid shear stress not innate in traditional 3D models, has been linked to changes in endothelial cell transcription, proliferation, barrier function and changes in actin skeleton rearrangement and contributes to the tumor microenvironment and invasion front.<sup>118, 120-124</sup> These conditions aid in the study of tumor aggression and invasion, as interstitial flow and pressure contribute to the formation of a tumor invasion front. A paper published by Aw Yong and colleagues, demonstrated the utility of such a technique for studying tumor invasion in prostate cancer cell lines.<sup>118</sup> In addition, the authors also illustrate the ability to keep a spheroid of sufficient size (500 $\mu$ m) over 3 weeks in culture, using their molded fluidic channel embedded in a collagen hydrogel, which served to provide nutrients and interstitial flow to the “tumoroid” continually, thus allowing measurements to be taken up to 22 days in culture.<sup>118</sup>

Co-culture methods have demonstrated the ability of multicellular-tumor spheroids to form a heterogenous population of cells, with the potential to include different cell types to observe and reproduce the behavior and microenvironmental characteristics of an in

vivo tumor. In particular, Lazzari *et. al* have illustrated that through triple co-culture (pancreatic cancer cells, fibroblasts, endothelial cells), the formation of a distinct heterogenous microenvironment complete with ECM production without the requirement of a synthetic scaffold.<sup>125</sup> The authors also describe the necessity of crosstalk between the tumor and stroma for mimicking tumor aggressiveness and behavior, and through their methods demonstrated that their construct was reminiscent of the complexity, architecture, and behavior of a pancreatic tumor.<sup>125</sup> In addition to the presence of fibroblasts and endothelial cells, other laboratories have included immune cells in order to incorporate both migration and association of immune cells to their 3D models.<sup>126, 127</sup> A paper by Sherman and colleagues demonstrated the ability their novel 3D immune oncology model to produce immune cell homing, 3D tumor cytotoxicity, and tumor immune invasion via a 96-well plate complete with both a ULA component and a permeable transwell support that allowed for immune cell migration to the spheroids.<sup>126</sup> Another paper, by Courau *et. al* 2019, established the ability to coculture human colorectal tumor samples as tumor spheroids with both T and NK immune cells.<sup>127</sup> The authors were able to take their coculture model and illustrate that both allogenic T and NK cells were capable of infiltrating the spheroid, and that with tumor infiltrating lymphocytes in the presence of interleukin 15 stimulation, immune mediated spheroid destruction occurred.<sup>127</sup> Furthermore, the authors were able to demonstrate in this model that the combined application of anti-NKG2A and MICA/B antibodies produced immunomodulatory effects in conjunction to the presence of tumor infiltrating lymphocytes, capable of immune-mediated destruction.<sup>127</sup>

Organoids represent a patient-derived application of 3D culture, whereby tumor “tissue fragments” are obtained and seeded for the purpose of recapitulating and observing a patient’s disease state at a miniaturized level and differ from spheroids as they are not derived from cells grown in monolayers.<sup>128</sup> Because the cells from a patient’s tumor or a xenograft developed from a patient’s tumor are inherently diverse, and already contain their own microenvironment, they are often capable of replicating these characteristics in organoid cultures, allowing for a close facsimile or “avatar” of the disease state. As such, a growing interest in precision medicine through genomic analysis and organoid creation of patient samples has led to an attempt to prioritize and select patient treatments based on the generated genomic and drug screening data. Pauli *et. al* 2017, have demonstrated such a method by pairing whole exome sequencing (WES) with organoid creation of patient tumor samples.<sup>129</sup> The authors were able to determine that using WES alone, while informative, is not sufficient to make informed decisions about therapeutic selection for patients. Rather by pairing patient-derived tumor organoids with the WES information, an informed high-throughput drug screen can be performed that provides unbiased information about potential successful mono and combination therapies, which are then validated *in vivo* PDX models.<sup>129</sup>

In conclusion, the use of side-by-side organoid to xenograft approach paired with genomic sequencing allows for informed selection of putative treatment options using an avatar of the patients very own disease state. However, this approach is still in its nascence and is not without some limitations, such as, the requirement of a sufficient amount of tumor material with viable cancer cells for organoid creation, this may prove difficult with certain cancer types and tumor locations as extraction of cells may not be an

option; culture media requires optimization on a per sample basis, which also requires a sufficient amount of cellular material to perform; the turnover time for such a screening method could be limiting, as evaluation of laboratory treatment candidates may occur after a patient has already succumbed to their cancer; lastly, given the stringency of clinical trials in oncology, it may be insufficient to have an N of 1, to provide actionable information from such a screen.<sup>129</sup> Given what these particular 3D models have to offer, they represent a clinically relevant stepping stone for drug discovery, and the latter has demonstrated the feasibility of a personalized / precision medicine approach albeit with limitations that can be overcome with time and sufficient data.

### **3.6 3D Conclusions and Future**

All of these 3D methods provide the ability to recapitulate key aspects of the physiological and microenvironmental characteristics of an avascular solid tumor. They represent more relevant models for cancer drug discovery and have provided unique insight into tumor biology without the need of an animal. Several laboratories have used 3D culture methodologies to demonstrate the physiological relevance of 3D in a variety of cancers, such as brain, head and neck, pancreatic and other cancer types.<sup>109, 114, 125</sup> As such, 3D tumor cultures have proven to be a more relevant model than 2D cultures, and 3D technologies and techniques have begun to reach a greater level of clinical relevance. While 3D cell culture has previously been limited by the absence of several key conditions, such as the inability of vasculature to be incorporated, the absence of surrounding stroma & associated cell types, and the inability to maintain patient-derived

tissues in 3D culture for prolonged periods of time *in vitro*. With the advent of microfluidic technologies, co-culture techniques, and organoid cultures, respectively, we have been able to overcome these challenges.

## **4.0 High Content Screening Characterization of Head and Neck Squamous Cell Carcinoma Multicellular Tumor Spheroid Cultures Generated in 384-well Ultra-low Attachment Plates to Screen for Better Cancer Drug Leads**

### **4.1 Challenges and Unmet Needs in Head and Neck Drug Discovery**

Head and neck cancers (HNC) are the 8<sup>th</sup> leading cause of cancer worldwide with ~600,000 new cases and ~300,000 deaths occurring per annum.<sup>130-132</sup> In 2018, it's estimated that 51,540 people in the USA will develop oral cavity or pharynx cancer and 10,030 will die of these cancers. Smoking, alcohol, genetics and human papillomavirus (HPV) infection are major risk factors for the development of head and neck squamous cell carcinoma (HNSCC).<sup>130-132</sup> HNC incidence is rising in developed countries despite reductions in cigarette smoking rates, with much of the increase attributable to HPV infection.<sup>130-133</sup> Surgical resection and chemo-radiotherapy are the front-line therapies for localized HNC.<sup>134-138</sup> Although surgical and radiation therapies have improved, cure rates have remained stationary at approximately 50% for >30 years.<sup>130-132, 136, 138, 139</sup> Patients with advanced, recurrent or metastatic HNC have a poor prognosis with median survival rates of 6-12 months.<sup>130, 131, 138</sup> The Federal Drug Administration (FDA) has approved only seven drugs for HNC; methotrexate and 5-fluorouracil in the 1950s, bleomycin and cisplatin in the 1970s, docetaxel and cetuximab in 2006, and pembrolizumab in 2016. However, only 10-25% of HNC patients respond to mono-therapy with the five older chemotherapeutics and/or the EGF-receptor targeted antibody, and these agents have failed to significantly improve either 5-year survival or cure rates.<sup>130, 131</sup> The FDA approved

the monoclonal antibody pembrolizumab (Keytruda®) in patients with recurrent or metastatic HNSCC that continued to progress despite standard-of-care chemotherapy. Pembrolizumab blocks the immune checkpoint anti-programmed death-ligand 1 (PD-1) receptor interactions with its ligands, PD-L1 and PD-L2.<sup>140-142</sup> The FDA accelerated Keytruda® approval based on early clinical trials where it was well tolerated and produced clinically relevant antitumor activity in recurrent or metastatic HNSCC.<sup>140-142</sup> Although tumor responses lasted  $\geq 6$  months in 82% of responders, and some patients experienced lasting (>2 years) and/or complete responses, only 16% of HNSCC patients responded to Keytruda treatment.<sup>140-142</sup> Despite Keytruda®'s success, its low response rate together with the overall lack of efficacy of the other approved drugs for HNSCC underscores the urgent unmet need to discover new and effective HNSCC therapies.

#### **4.1.1 Necessity of Physiologically Relevant Models for Improved Clinical Translation**

Despite significant investments in cancer research, drug discovery and development, <5% of all new small molecule cancer drugs entering phase I clinical trials gain FDA approval.<sup>137, 143-146</sup> New cancer drug leads are usually discovered in growth inhibition (GI) assays conducted in tumor cell line panels maintained and assayed in two dimensional (2D) culture conditions that are compatible with high throughput screening (HTS).<sup>137, 147-149</sup> 2D GI HTS assays typically utilize low cell numbers to reduce the cell culture burden and to maximize drug sensitivity by promoting exponential growth during the compound exposure period.<sup>64, 135, 149, 150</sup> Cells in 2D GI assays experience uniform drug concentrations in a homogenous environment where cell interactions with the extra

cellular matrix (ECM) and cell-cell contacts are either non-existent or substantially reduced.<sup>64, 135, 149, 150</sup> Genomic comparisons of established HNC cell lines to primary tumors revealed that although 51% of genetic alterations were shared at similar mutation frequencies, sub-sets of mutations were unique to patient tumors and cell lines respectively<sup>136</sup>. Mutations unique to cell lines favored immortalization and continuous maintenance in tissue culture<sup>136</sup>. In addition, tumor cell lines adapted to growth in 2D proliferate faster than cells from primary tumors, display altered drug resistance patterns, and respond preferentially to anti-proliferative agents while overlooking the self- and population-renewing tumor stem cells which contribute to recurrence and metastasis<sup>64, 151-155</sup>. 2D tumor GI assays fail to recapitulate the complex 3-dimensional (3D) architecture, cell-cell and cell-ECM interactions, microenvironments, drug diffusion kinetics, and drug responses of solid tumors *in vivo*.<sup>64, 96, 98, 144, 151, 152, 155-161</sup> To identify better leads that have the potential to improve the clinical development success rates of new cancer drugs for solid tumors like HNSCC, more physiologically relevant *in vitro* 3D tumor models that better represent the growth and tumor microenvironments observed in preclinical *in vivo* mouse models and patient tumors are being deployed for lead generation.<sup>64, 98, 152, 154, 155, 157-159, 161-168</sup>

#### **4.1.2 HNSCC MCTS Production using Ultra-low Attachment Technology**

We have shown that the production of HNSCC MCTSs in 384-well ULA-plates is both compatible with automation and scalable for HTS because MCTSs form within 1-3 days, require relatively few cells ( $\leq 2.5K$ ) per well, and both compound exposure and homogeneous assay detection can be performed *in situ*.<sup>98, 157</sup> We have used Cal33 and

FaDu HNSCC MCTSs generated in 384-well ULA-plates to demonstrate that cancer drug accumulation increases as cell numbers and MCTS sizes increase, and that drugs exhibit restricted penetration and distribution gradients, accumulating preferentially in cells in the outer layers of MCTSs relative to those in the inner cores.<sup>64</sup> In addition, 2D Cal33 monolayers are 6-fold, 20-fold, 10-fold and 16-fold more sensitive than Cal33 MCTSs to growth inhibition produced by ellipticine, idarubicin, daunorubicin, and doxorubicin respectively.<sup>64</sup> The present chapter extends these studies to characterize the distinct morphologies, viability, and growth phenotypes of MCTSs formed in 384-well ULA-plates by eleven HNSCC cell lines and an immortalized human “normal” esophageal epithelial cell line. For five HNSCC cell lines with distinct MCTS growth phenotypes, we show the development of microenvironments and uneven drug accumulation in different regions of MCTSs and demonstrate that these more physiologically relevant 3D tumor models can be readily adapted to measure drug-induced cytotoxicity.

## **4.2 Materials and Methods**

### **Reagents**

Thirty-seven percent formaldehyde was purchased from Sigma-Aldrich (St. Louis, MO). Hoechst 33342 was purchased from Life Technologies (Thermo Fisher Scientific, Waltham, MA). Dimethyl sulfoxide (DMSO) 99.9% high-performance liquid chromatography grade was obtained from Alfa Aesar (Ward Hill, MA). Dulbecco’s Mg<sup>2+</sup>- and Ca<sup>2+</sup>-free phosphate-buffered saline (PBS) was purchased from Gibco (Grand Island, NY). Dulbecco’s modified Eagle’s medium (DMEM) and Dulbecco’s modified

Eagle's medium / Ham's F12 50/50 (DMEM/F12) was purchased from Corning (Manassa, VA). Fetal bovine serum (FBS), L-glutamine, penicillin, and streptomycin (P/S) were purchased from Thermo Fisher Scientific. CellTiter-Blue® (CTB) was purchased from Promega Corporation (Madison, WI). Calcein AM (CAM), Ethidium Homodimer (EHD), MitoTracker® Orange (MTO) a thiol-reactive chloromethyl derivative of tetra-methyl-rhodamine, Tetra-methyl-rhodamine methyl ester (TMRM), Click-iT 5-ethynyl-2'-deoxyuridine (EdU), and (5-(and-6)-(((4-chloromethyl)benzoyl)amino)-tetra-methyl-rhodamine CellTracker® Orange (CTO) were all purchased from Life Technologies (Thermo Fisher Scientific, Waltham, MA). Doxorubicin was provided by the National Cancer Institute (NCI).

### **Cells and Tissue Culture**

Eleven human head and neck squamous cell carcinoma (HNSCC) cell lines were provided by Dr. Jennifer Grandis of the Head and Neck Cancer (HNC) Spore at the University of Pittsburgh Medical Center Hillman Cancer Center and were maintained in a humidified incubator at 37°C, 5% CO<sub>2</sub>, and 95% humidity; Cal33, Cal27, FaDu, UM-22B, BICR56, OSC-19, PCI-13, PCI-52, Detroit-562, UM-SCC-1, and SCC-9. The human Het-1A (CRL-2692™) esophageal squamous epithelial cell line transfected with the SV40 large T antigen was purchased from the American Type Culture Collection (ATCC®, Manassas, VA). All cell lines except SCC-9 were cultured in DMEM supplemented with 10% FBS, 1% L-glutamine, and 1% P/S. The culture medium for the FaDu and OSC-19 cell lines was also supplemented with 1% non-essential amino acids, and the medium for the BICR56 and UM-SCC-1 cell lines was supplemented with 0.4µg/mL hydrocortisone. The SCC-9 cell line was cultured in DMEM/F-12 medium supplemented with 10% FBS,

1% L-glutamine, and 1% P/S. HNSCC cell lines were passaged or used to generate multicellular tumor spheroid (MCTSs) after isolated cell suspensions were prepared from tissue culture flasks by dissociating cells with trypsin and centrifugation at 270 x *g* for 5 min at room temperature, and resuspension in growth media. The number of viable trypan blue excluding cells in the cell suspension was counted using a hemocytometer.

### **Generation of HNSCC Multicellular Tumor Spheroids in Ultra-low Attachment Microtiter Plates**

We have previously described the generation of MCTSs after seeding several HNSCC cell lines into 384-well U-bottomed ultra-low attachment (ULA-plates) microtiter plates (Corning, Tewksbury, MA, Cat. No 4516).<sup>64,98,157</sup> Briefly, 384-well ULA-plates were rehydrated by the addition of 50  $\mu$ L of serum free culture medium to each well and incubation in a humidified incubator for 15 minutes. Media was removed from the wells of the ULA-plates and 45 $\mu$ L of a single-cell suspension of the HNSCC cell lines at different seeding densities (625, 1250, 2500, 5000, 10000, or 20000 cells/well) in the appropriate growth medium were transferred into each well using a Matrix automated multichannel pipette (Thermo Fisher Scientific, Waltham, MA), ULA-plates were centrifuged at 17 x *g* for 1 minute, and then placed in an incubator at 37°C, 5% CO<sub>2</sub> and 95% humidity for the indicated time periods. In time course experiments where HNSCC MCTS cultures were maintained in the ULA-plates beyond 3 days, spent media was exchanged for fresh medium every 3 days using a Janus MDT Mini (PerkinElmer, Waltham, MA) automated liquid handler platform equipped with a 384-well transfer head. Each medium exchange cycle consisted of 2 x 20  $\mu$ L aspiration and discard steps followed by 2 x 20  $\mu$ L fresh

media dispense steps. Three media exchange cycles were performed to achieve ~ 85% exchange of fresh medium for spent medium and a uniform volume of 45uL per well.

### **Investigation of HNSCC Multicellular Tumor Spheroid Morphology, Viability and Growth in Ultra-low Attachment Microtiter Plates by High Content Imaging.**

We used an ImageXpress Micro (IXM) automated wide field high content imaging platform integrated with MetaXpress Imaging and Analysis software (Molecular Devices LLC, Sunnyvale, CA) to acquire and analyze images of HNSCC MCTSs. The IXM optical drive uses a 300 W Xenon lamp broad spectrum white light source and a 1.4-megapixel 2/3" chip Cooled CCD Camera and optical train for standard fluorescence imaging and a transmitted light module with phase contrast. The IXM is equipped with Zero Pixel Shift (ZPS) filter sets; DAPI, FITC/ALEXA 488, CY3/TRITC, CY5, and Texas Red. A 4-position objective turret can be loaded with various objectives; a 4X Plan Apo 0.20 NA objective, a 10X Plan Fluor 0.3 NA objective, a 20X Ph1 Plan Fluor ELWD DM objective, a 20X S Plan Fluor ELWD 0.45 NA objective, and a 40X S Plan Fluor ELWD 0.60 NA objective.

Single images of HNSCC MCTSs were sequentially acquired using a 4X Plan Apo 0.20 NA objective in both the transmitted light (TL) and fluorescent image acquisition modes; DAPI, FITC and TRITC.<sup>64, 98, 157, 169</sup> To acquire best focus images of MCTSs we used the IXM automated image-based focus algorithm to acquire both a coarse focus (large  $\mu\text{m}$  steps) set of images of Hoechst stained objects in the DAPI channel for the first MCTS to be imaged, followed by a fine (small  $\mu\text{m}$  steps) set of images to select the best focus image. For all subsequent wells and channels to be imaged only a fine focus set of images were acquired to select the best focus Z-plane.<sup>64, 98, 157, 169</sup> MCTS morphology and growth were assessed daily by the acquisition of 4X TL images on the IXM, and we used

the line-scan tool of the MetaXpress image analysis software to measure the diameters of the HNSCC MCTSs.<sup>169</sup> The change in MCTS diameter over time in culture was used as an indicator of MCTS growth or death.

To label viable and/or dead cells within the HNSCC MCTS cultures, we incubated HNSCC MCTSs with a cocktail of the Hoechst (8 $\mu$ g/mL) DNA stain, the Calcein AM (2.5 $\mu$ M) live reagent, and the Ethidium Homodimer (5 $\mu$ M) dead reagent for 1h, and single images of HNSCC MCTSs were sequentially acquired on the IXM using a 4X objective in both the TL and fluorescent image acquisition modes; DAPI, FITC and Texas Red channels. We used the multiwavelength cell scoring (MWCS) image analysis module to analyze the HNSCC MCTS fluorescent images as described previously.<sup>64, 98, 157</sup> To create a whole MCTS mask we set the approximate minimum width of the Hoechst stained nuclei of the MCTS to be 150  $\mu$ m with an approximate maximum width to be 550  $\mu$ m and applied a threshold intensity above local background of 70. The total MCTS mask from the Hoechst channel was used to count the number of MCTSs per image, typically one. After applying user defined background average intensity thresholds, typically 50-70 in both the FITC and Texas Red channels, the MWCS module image segmentation then created total MCTS masks in all three fluorescent channels. The derived HNSCC total MCTS masks in channels 2 and 3 were then used to quantify the mean integrated fluorescence intensity (MIFI) of the CAM live cell signal in the FITC channel and the EHD dead cell signal in the Texas Red channel. The MIFI values represent the total pixel fluorescent intensities in channels 1, 2 or 3 within the total MCTS masks of positively stained MCTSs above the pre-set background thresholds.

Pseudo-color fluorescence intensity data visualizations were also used to illustrate fluorescent dye/drug uptake, accumulation and distribution in HNSCC MCTS cultures.<sup>64</sup> The relative fluorescent intensities of the pixels in the image were represented as distinct colors with the “hotter” and “brighter” colors (low to high, yellow, red, white) representing higher intensity signals and cooler colors (low to high, purple, cyan, green) representing lower intensity signals. Line-scan fluorescence intensity plots were also used to portray fluorescent dye/drug uptake, accumulation and distribution in HNSCC MCTS cultures.<sup>64</sup> Line-scan fluorescence intensity plots were created using the line scanning tool of the MetaXpress image analysis software to draw a line across the image and plot the fluorescent intensity values versus distance in  $\mu\text{m}$  across the image to provide an intensity profile graph.

### **Determination of HNSCC Multicellular Tumor Spheroid Proliferation**

After 3 days of culture in ULA-plates to allow MCTSs to form, the cell culture medium was exchanged and the HNSCC MCTSs were exposed to 5-ethynyl-2'-deoxyuridine T (EdU) reagent (Life Technologies) according to the manufacturer's instructions for 12, 24 and 48 h prior to fixation in 3.7% formaldehyde and permeabilization with 0.1% Triton-X-100. The modified nucleoside EdU which becomes incorporated into DNA by proliferating cells undergoing DNA synthesis that is detected using an Alexa Fluor 488 picolyl azide fluorescent label which is incorporated via a quick “click chemistry” reaction. Images of HNSCC MCTSs were sequentially acquired on the IXM using a 4X objective in both the transmitted light and FITC channels.

### **Characterization of HNSCC Multicellular Tumor Spheroid Mitochondrial Mass and Membrane Potential**

After 3 days of culture in ULA-plates to allow MCTSs to form, the cell culture medium was exchanged and the HNSCC MCTSs were exposed to 500nM Mitotracker Orange (MTO) or 250 nM Tetramethylrhodamine Methyl Ester (TMRM) (Life Technologies) for 1h at 37°C, 5% CO<sub>2</sub>, and 95% humidity. MTO labeled HNSCC MCTSs were fixed and stained with 3.7% formaldehyde containing 8 µg/mL Hoechst and then washed 3x with PBS before images were acquired on the IXM using a 4X objective in the TL, DAPI and TRITC channels. Images of TMRM labeled live HNSCC MCTSs were acquired on the IXM using a 4X objective in both the TL and TRITC channels. HNSCC MCTSs images were analyzed using the MWCS image analysis module described above to quantify the MIFI of the MTO and TMRM fluorescent dyes, and both pseudo-color visualizations and line scan plots were used to illustrate their distribution throughout the HNSCC MCTSs.

### **Drug Penetration and Distribution in HNSCC Multicellular Tumor Spheroids**

Analysis of drug penetration was performed as previously described for the Cal33 and FaDu HNSCC cell lines.<sup>64</sup> Briefly, HNSCC cell lines were cultured for 3 days to allow MCTSs to form before a media exchange was performed and the MCTSs were then exposed to 10 µM doxorubicin and incubated at 37°C, 5% CO<sub>2</sub>, and 95% humidity for 0.5, 3, 6, 12, and 24h prior to fixation in 3.7% formaldehyde for 30-45 minutes, 3x washes with PBS, and acquisition of 4X images on the IXM in the transmitted light and TRITC channels. The MWCS image analysis module described above was used to quantify the fluorescent intensity of doxorubicin in HNSCC MCTSs TRITC channel images by using the doxorubicin stained nuclei in the TRITC channel to identify and define the whole MCTS mask. The MIFI parameter represents the total pixel fluorescent intensity of

doxorubicin within the MCTS.<sup>64</sup> Pseudo-color visualizations and line scan plots were also used to illustrate doxorubicin accumulation and distribution throughout HNSCC MCTSs.

### **Analysis of HNSCC Multicellular Tumor Spheroid Viability and Growth using the Cell Titer Blue® Reagent.**

The homogeneous CellTiter-Blue® (CTB) cell viability reagent provides a fluorescent method for monitoring cell viability and/or growth inhibition that is based on the ability of living cells to convert the redox dye resazurin into a fluorescent end-product resorufin. HNSCC cell lines were seeded at the indicated cell densities into 384-well ULA-plates in 45µL of growth medium incubated at 37°C, 5% CO<sub>2</sub> and 95% humidity for the indicated time periods. After the prescribed time in culture 10 µL of the CTB cell viability detection reagent was dispensed into the wells of HNSCC MCTS assay plates, and incubated for 4h at 37°C, 5% CO<sub>2</sub> and 95% humidity before capturing the relative fluorescent unit (RFUs) signals (Ex. 560 nm/ EM. 590 nm) on a SpectraMax M5e (Molecular Devices, LLC, Sunnyvale, CA) micro-titer plate reader platform.

### **Data Processing, Analysis and Curve Fitting**

For HNSCC MCTS growth assays in 384-well ULA-plates, the measured diameters of the HNSCC MCTSs and their corresponding CTB RFU signals were fit to a linear regression model. The MIFI data from HNSCC MCTSs exposed to CAM, EHD, MTO, TMRM or doxorubicin are presented as the mean ± SD (n = 3). For HNSCC MCTS growth inhibition (GI<sub>50</sub>) assays, the DMSO control wells (Max controls n=14) and 200µM doxorubicin control wells (Min controls, n=32) were used to represent uninhibited growth and 100% cytotoxicity, respectively. The mean maximum and minimum plate control CTB RFUs were used to normalize the RFU data from the compound treated wells as %

inhibition of growth. The GI<sub>50</sub> data were fit to a non-linear sigmoidal log (inhibitor) vs. normalized response variable slope model using the equation:  $Y=100/(1+10^{((\text{LogIC50}-X) * \text{Hillslope}))})$ , where y was the percent growth inhibition and x was the corresponding log<sub>10</sub> of the compound concentration. The GI<sub>50</sub> is the concentration of compound that gives a 50% response, half way between 0% and 100%. The Hillslope describes the steepness of the curve. All curve fitting, linear regression analysis, and graphs were created using the GraphPad Prism 6 software.

## **4.3 Results**

### **4.3.1 Morphology and viability of HNSCC Multicellular Tumor Spheroids formed in 384-well U-bottomed Ultra Low Attachment Microtiter Plates**

We have previously shown that six HNSCC tumor cell lines form MCTSs within 24h of seeding into 384-well ULA-plates.<sup>64, 98, 157</sup> To extend these studies, we selected five additional HNSCC cell lines that have previously been used for HNC drug discovery.<sup>135, 136, 150</sup> The Het-1A SV40 T-antigen immortalized human esophageal epithelial cell line was included to represent a “normal” control cell line model, since these cells do not grow as xenograft tumors in immuno-deficient mice<sup>170-173</sup> To characterize the morphology and viability of the HNSCC MCTSs formed, 11 HNSCC cell lines and Het-1A cells were seeded into 384-well ULA-plates and cultured for 3 days before they were stained with live cell CAM and dead cell EHD reagents, and 4X images were acquired on the IXM in the TL, FITC and Texas Red channels (Figure 13). Although some HNSCC

cell lines formed MCTSs within 24h of seeding into 384-well ULA-plates, others required 2-3 days to self-assemble. The morphologies (shape and compact-ness) and sizes of the

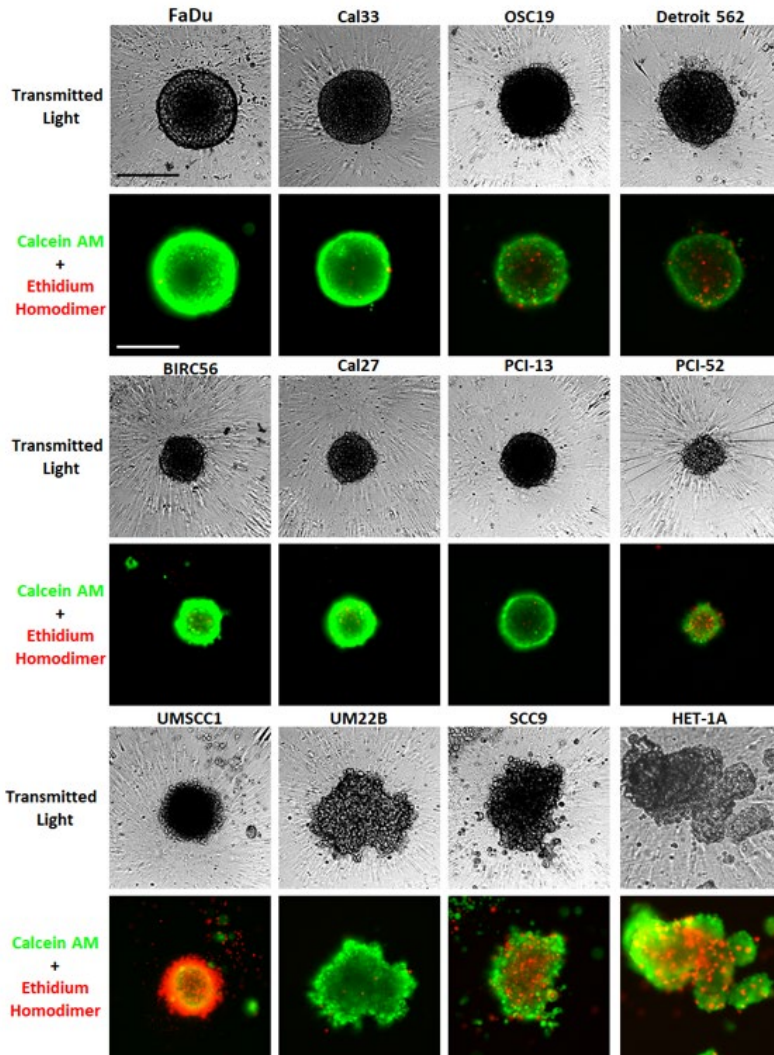


**Figure 13 Characterization of HNSCC multicellular tumor spheroid morphology and viability in Ultra-low Attachment Plates**

11 HNSCC cell lines and Het-1A cells were seeded at 2,500 cells per well in 384-well ULA-plates and cultured for 3 days. MCTSs were then stained with the live cell CAM and dead cell EHD reagents and 4X images were acquired on the IXM in the TL, FITC and Texas Red channels. Greyscale TL images are presented along with color composite fluorescent images of live cell CAM and dead cell EHD staining depicted as green and

red, respectively. Representative images from multiple independent experiments are presented. All scale bars represent 300  $\mu\text{m}$ .

MCTSs varied with each HNSCC cell line (Figure 13). After 72h in culture, FaDu, Cal33, Cal27 and PCI-13 cell lines formed condensed MCTSs with a smooth and even periphery. OSC19, Detroit 562, BICR56, PC1-52 and UMSCC1 cell lines produced rounded MCTSs with uneven perimeters, and the Het-1A, UM22B and SCC9 cell lines formed cell aggregates with irregular outer margins. FaDu, Cal33, OSC19 and Detroit 562 cells formed larger MCTSs  $\sim 350\text{-}400\ \mu\text{m}$  in diameter, while BICR56, Cal27, PC13, PCI-52 and UMSCC1 formed smaller MCTSs with  $\sim 200\text{-}250\ \mu\text{m}$  diameters. FaDu, Cal33, BICR56, and PC1-52 MCTSs and UM22B aggregates exhibited strong CAM staining with little or no EHD staining, indicating that all the cells were viable. OSC19, Detroit 562, and PCI-52 MCTSs also exhibited strong CAM staining, and although there was some EHD staining, most cells were viable. In contrast, UMSCC1 MCTSs exhibited strong EHD staining and much lower CAM staining, indicating that most cells were dead. The SCC9 and Het-1A irregular aggregates exhibited strong CAM staining together with some significant EHD staining.

#### **4.3.2 HNSCC Multicellular Tumor Spheroid Growth Phenotypes in ULA-plates**

To further characterize the morphologies, viability, and growth behavior of HNSCC MCTSs cultured in 384-well ULA-plates over time, we conducted a series of cell seeding density and time course experiments. The eleven HNSCC cell lines were seeded into 384-well ULA-plates at densities ranging between 625 and 20,000 cells per well and were

cultured for 12-14 days, with media exchanges every 3 days. MCTS growth and viability were evaluated by TL imaging, CAM/EHD staining, and CTB RFUs. The 11 HNSCC cell lines exhibited six distinct MCTS growth phenotypes; rapid growth (FaDu), moderate growth (UM22B), slow growth (Cal33), dormant (BICR56, Cal27, Detroit 562, & PCI-13), progressive slow death (OSC19, PCI-52, & SCC9), and rapid death (UMSCC1). Figure 4.14 shows time course data for 5 HNSCC cell lines seeded at 2,500 cells per well in 384-well ULA-plates that represent five of the MCTS growth phenotypes. Consistent with Figure 13, the TL images indicated that MCTS morphologies and sizes were different for each HNSCC cell line, and furthermore that these changed with time in culture (Figure 14A). In general, HNSCC MCTS TL images became progressively darker with longer time in culture, especially in the MCTS core regions, perhaps indicating that the cells were becoming more densely packed. The UM22B line exhibited the most dramatic change in morphology with increasing time in culture, coalescing from a loose aggregate of cells into a compact MCTS with a smooth and even periphery after several days (Figure 14A). To assess the changes in HNSCC MCTS size over time we used the line-scan tool of the image analysis software to measure the diameters of the HNSCC MCTSs in TL images acquired daily (Figure 14B). The diameters of the FaDu, UM22B and Cal33 MCTSs increased linearly with respect to time in culture throughout the 10-14-day culture period. In contrast, BICR56 MCTSs exhibited almost no change in diameter, and OSC19 MCTSs diameters became progressively smaller with extended time in culture. Based on the observed changes in MCTS diameter over time the rank order of HNSCC MCTS growth was FaDu>UM22B>>Cal33. BICR56 MCTS diameters remained constant over time, while OSC19 MCTS diameters declines gradually with time in culture.

The homogeneous Cell Titer Glo® (CTG) ATP detection reagent has frequently been used to measure growth and compound mediated cytotoxicity in MCTS cultures produced and maintained in 96- and 384-well ULA-plates.<sup>64, 98, 152, 157, 162, 167</sup>

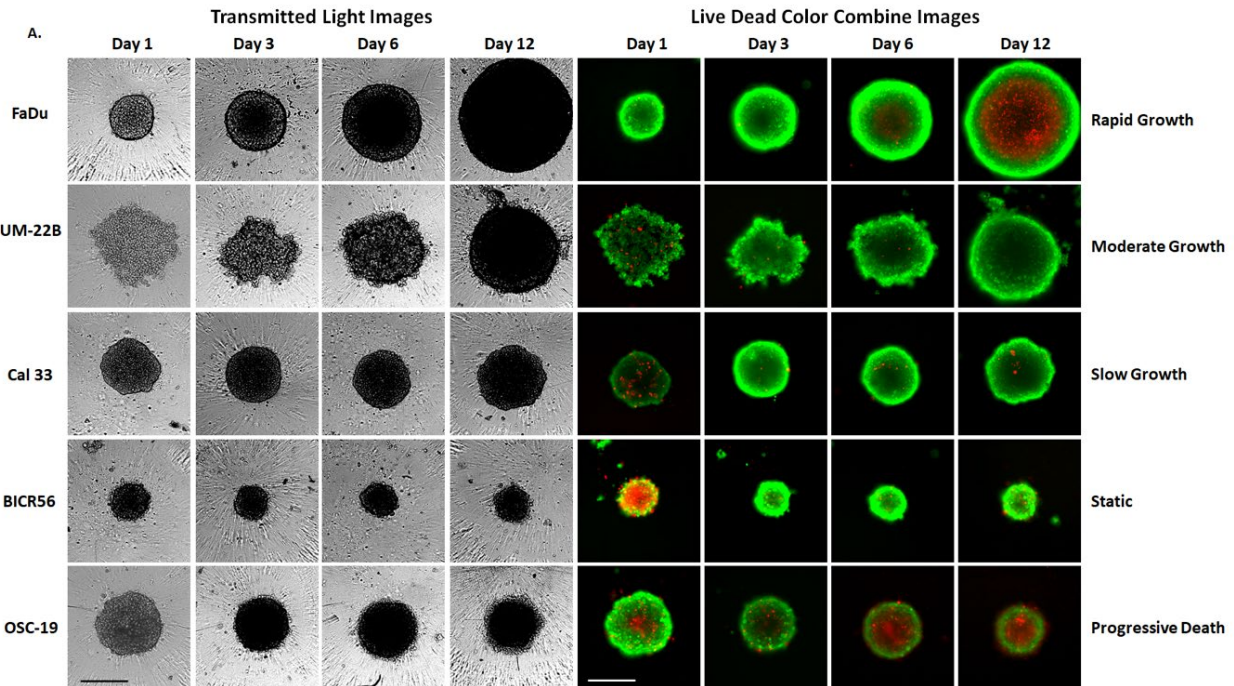
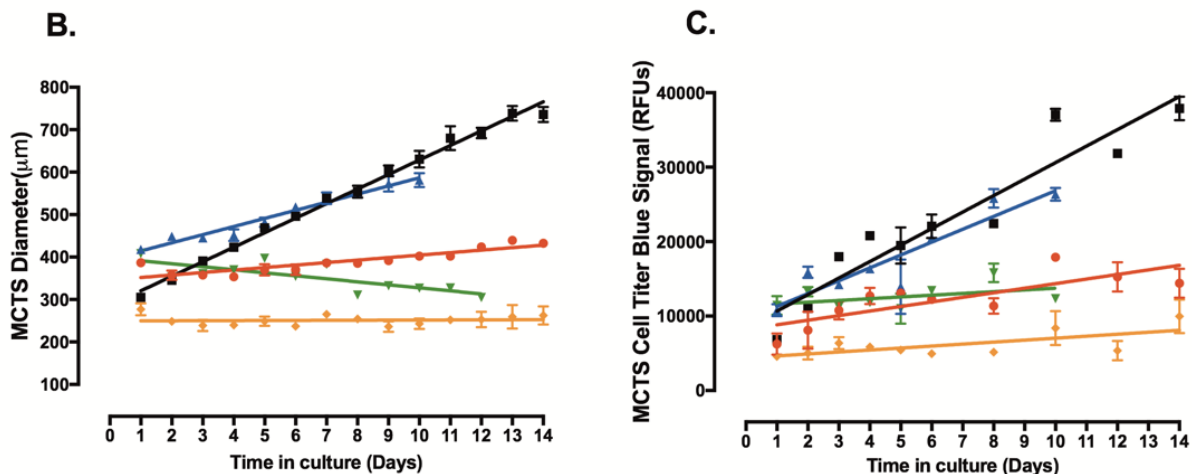


**Figure 14 Growth phenotypes of multicellular tumor spheroids produced by five representative HNSCC cell lines seeded and maintained in Ultra-low Attachment Plates**

**(A)** Five HNSCC cell lines were seeded at 2,500 cells per well in 384-well ULA-plates and were cultured for 12 days with fresh media exchanges performed every 3 days. MCTSs were stained after 1, 3, 6 or 12 days in culture with the live cell CAM and dead cell EHD reagents and 4X images were acquired on the IXM in the TL, FITC and Texas Red channels. Greyscale TL images are presented along with color composite fluorescent images of live cell CAM and dead cell EHD staining depicted as green and red, respectively. Representative images from multiple independent experiments are presented. All scale bars represent 300 μm.



**(B)** The line-scan tool of the MetaXpress image analysis software was used to measure the diameters of the five HNSCC MCTSs in TL images that were acquired daily throughout the 10- to 14-day culture period. **(C)** Cell Titer-Blue™ RFU signals of the five HNSCC MCTS cultures were measured at the indicated time points throughout the 10- to 14-day culture period. MCTS diameters in μm **(B)** and CTB RFUs **(C)** were measured in triplicate wells ( $n=3$ ) and are presented as the mean  $\pm$  SD for the following HNSCC cell lines; UM-22B(▲), OSC-19(▼), FaDu(■), BICR56(◆), and Cal33 (●). A linear regression of the mean MCTS diameter and CTB RFU data for each of the HNSCC cell lines was performed using the GraphPad Prism 6 software. Representative data from three independent experiments are presented.

However we switched to CTB when we found that the RLUs produced by CTG for the same number of cells in 2D and 3D cultures was ~10-fold lower in 3D cultures, whereas we observed little or no difference in the CTB RFUs between 2D and 3D cultures comprised of the same cell numbers (data not shown). To illustrate the correlation between CTB RFUs and the number of viable HNSCC cells in MCTS cultures we seeded between 625 and 20,000 FaDu cells per well into 384-well ULA-plates and cultured them for 24h to allow MCTSs to form. After 24h we acquired 4X TL images of the MCTSs on the IXM (Figure 15A), measured the diameters of the MCTSs using the line-scan tool, and measured the CTB RFUs 4h after reagent addition (Figure 15B). In the 625 to 5,000 cells per well range, MCTS diameters and CTB RFUs increased similarly with respect to the number of viable FaDu cells seeded per well, and although MCTS diameters and CTB RFUs continued to increase as more cells were added to wells, the increase was no longer linear with respect to cell number (Figure 15B). The MCTS diameter and CTB RFU data were almost superimposable indicating that they are closely correlated (Figure 15B). Similar CTB data were observed for all HNSCC MCTS cultures (data not shown). Based on the observed changes in CTB signal over time the rank order of MCTS growth rates was the same as that indicated by the change in MCTS diameter (Figures 14B and 14C).

The corresponding CAM/EHD time course images suggest that at most timepoints a large majority of cells in the FaDu, UM22B, Cal33 and BICR56 MCTSs were viable, although FaDu MCTSs appeared to develop necrotic cores by day 6 through 12 as they became progressively larger, and OSC19 MCTSs appeared to have a necrotic core at all timepoints (Figure 14A). To further explore the development of necrotic cores in HNSCC MCTSs, we seeded the FaDu and OSC19 cell lines into 384-well ULA-plates and cultured

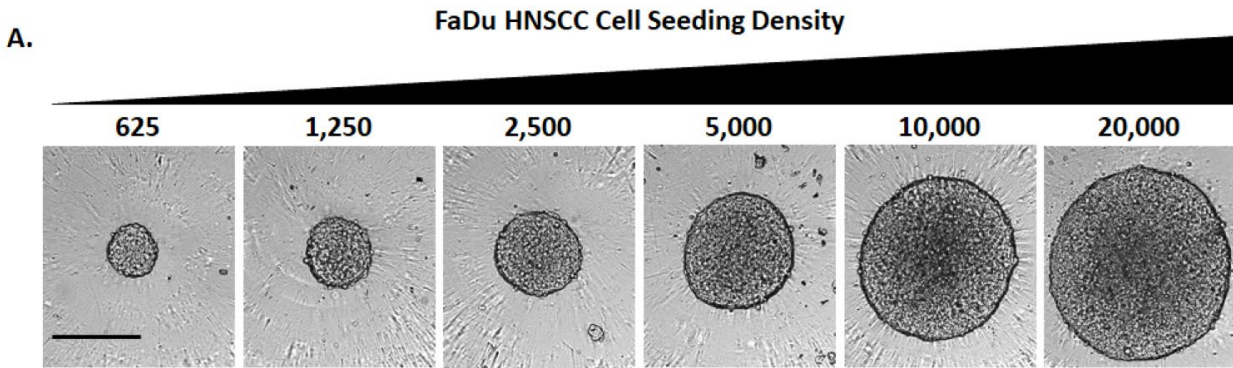
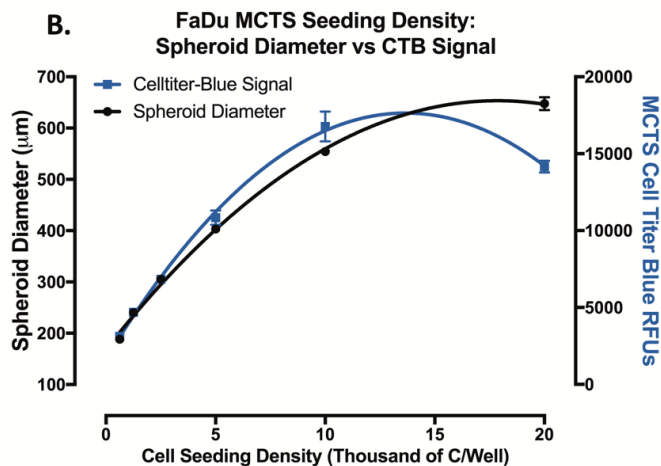


**Figure 15 Correlation between FaDu cell seeding density multicellular tumor spheroid diameter and Cell Titer Blue® RFU Signals**



**(A)** FaDu HNSCC cells were seeded at seeding densities ranging from 625 to 20,000 cells per well into 384-well ULA-plates and after 24h in culture 4X TL images of the MCTSs were acquired on the IXM. All scale bars represent 300 µm. **(B)** We measured the diameters of the FaDu MCTSs in the TL images using the line-scan tool and measured the CTB RFUs 4h after reagent addition. The mean ± SD (n=3) of the FaDu MCTS diameter measurements in µm (●) and CTB RFU signals (■) from three wells for each seeding density are presented. The MCTS diameter measurements in µm are plotted on the Y axis on the left and the CTB RFUs are plotted on the Y axis on the right. Representative experimental data from multiple independent experiments are shown.

them for up to 12 days, with media exchanges every 3 days. MCTS growth and viability were evaluated by TL microscopy and CAM/EHD staining (Figure 16A), and we used the MWCS image analysis module to quantify and compare the CAM and EHD MIFI signals in FaDu (Figure 16B) and OSC-19 (Figure 16C) MCTSs. Consistent with its rapid growth phenotype (Figure 14), FaDu MCTS size increased over time in culture (Figure 16A), and the corresponding CAM MIFI signals also increased (Figure 16B). At most time points the FaDu MCTS CAM MIFIs were greater than the corresponding EHD MIFIs, but after day 4 the development of a necrotic core was indicated by both the CAM/EHD images and by an apparent larger increase in EHD MIFIs (Figure 16A and 16B). The slow progressive death phenotype of OSC19 cell line was illustrated by the decrease in MCTS size observed in the TL and CAM/EHD images (Figure 16A), the lack of any change in CAM MIFIs between day 2 and 12, with a trend towards increased EHD MIFIs over the same period (Figure 16C).

Images of HNSCC MCTSs stained with the live cell CAM reagent exhibited a donut-like staining pattern, where cells in the outer edges of the MCTSs exhibited higher intensities relative to cells in the inner cores, irrespective of MCTS size or HNSCC cell line (Figures 13, 14A, and 16A). To show that the differential distribution of CAM observed in the outer layers of HNSCC MCTSs was not due to an imaging artifact caused by inefficient excitation light penetration and/or fluorescent emission light detection, we pre-labeled HNSCC cell lines with cell tracker orange (CTO) prior to seeding them into

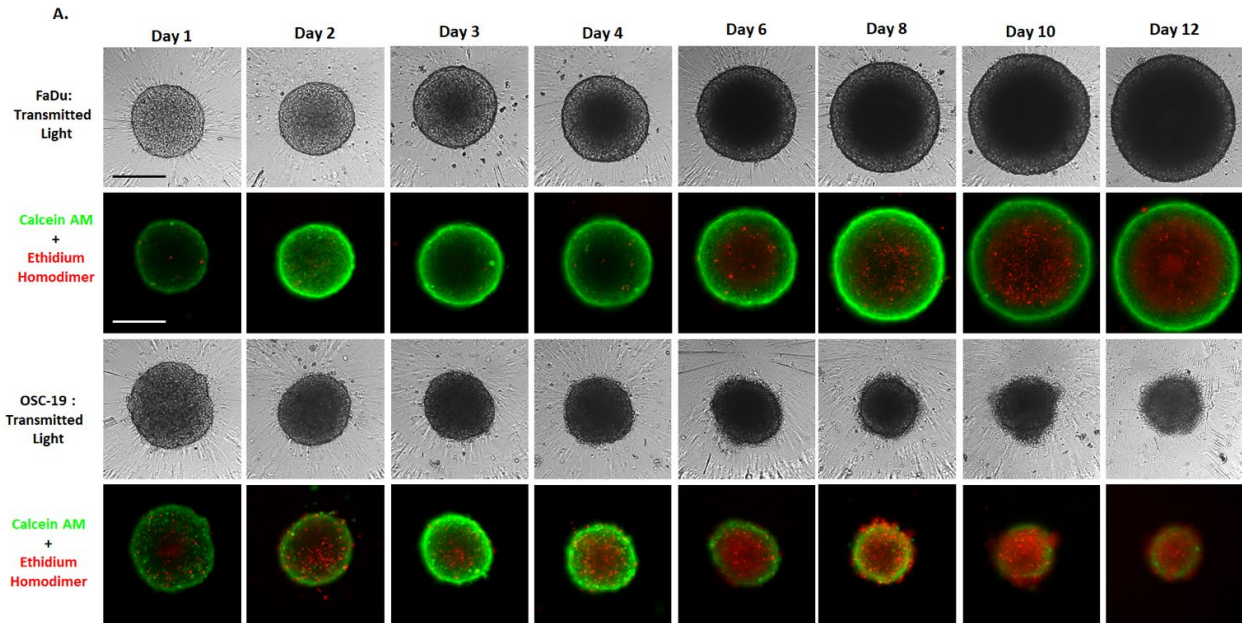
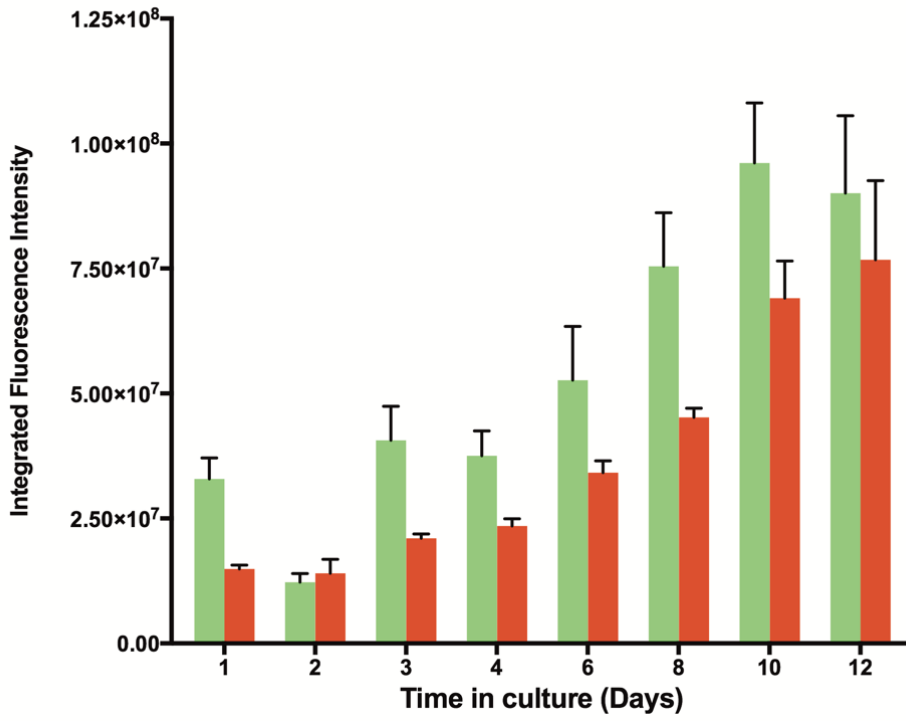


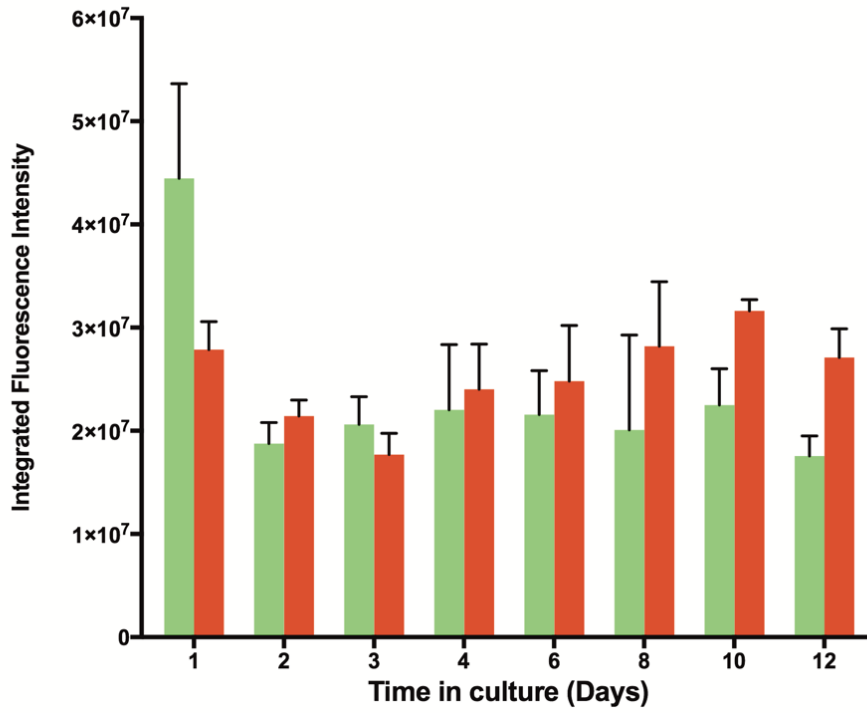
**Figure 16 Development of a necrotic core in multicellular tumor spheroids formed by the FaDu and OSC19 HNSCC cell lines seeded and maintained in Ultra-low Attachment Plates**

(A) The FaDu and OSC19 HNSCC cell lines were seeded at 2,500 cells per well in 384-well ULA-plates and were cultured for 12 days with fresh media exchanges performed every 3 days. MCTSs were stained after the indicated days in culture with the live cell CAM and dead cell EHD reagents and 4X images were acquired on the IXM in the TL, FITC and Texas Red channels. Greyscale TL images are presented along with color composite fluorescent images of live cell CAM and dead cell EHD staining depicted as green and red, respectively. Representative images from multiple independent experiments are presented. All scale bars represent 300  $\mu\text{m}$ .

**B.**



**C.**



The multiwavelength cell scoring (MWCS) image analysis module of the MetaXpress software was used to quantify the live cell CAM and dead cell EHD mean integrated fluorescent intensity (MIFI) signals in **(B) FaDu** and **(C) OSC-19** MCTSs over time in culture. The MWCS image module segmented Hoechst channel images to create a whole MCTS mask and then applied user defined background average intensity thresholds to create whole MCTS masks for the FITC and Texas Red channels. The whole MCTS masks were used to quantify the MIFIs of the CAM live cell signal (■) in the FITC channel and the EHD dead cell signal (■) in the Texas Red channel. MIFIs were measured in triplicate wells ( $n=3$ ) at the indicated time points and are presented as the mean  $\pm$  SD. Representative data from three independent experiments are presented.

384-well ULA-plates to form MCTSs (Figure 17). The TRITC images, pseudo-color visualizations, and line-scan plots showed that CTO fluorescence was distributed uniformly throughout the MCTSs, or if anything, the fluorescent intensities were slightly higher in the inner cores of MCTSs relative to the outer layers. Since the CAM reagent must be metabolized by live cells into the fluorescent end-product, it is possible that the higher CAM fluorescent intensities observed in cells in the outer layers of HNSCC MCTSs reflects their higher metabolic activity relative to cells in the inner cores.

#### **4.3.3 HNSCC Multicellular Tumor Spheroid Cell Proliferation**

To investigate whether cells in HNSCC MCTSs formed and maintained in ULA-plates exhibited different rates of cell proliferation in distinct MCTS regions, we seeded 2,500 HNSCC cell lines into 384-well ULA-plates and allowed MCTSs to form for 3 days before the culture media was exchanged and during the next 3 days MCTSs were exposed to EdU for 12h, 24h or 48h (Figure 18). Six-day FaDu MCTS cultures that were

exposed to EdU for 12h, 24h or 48h exhibited a distinct gradient of EdU staining, with cells in the outer layers of the MCTSs exhibiting higher intensities relative to cells in the inner cores at all EdU exposure periods (Figure 18A). In six-day HNSCC MCTS cultures representing the five growth phenotypes, only the rapidly (FaDu) and moderately (UM22B) growing MCTSs displayed evidence of detectable EdU incorporation after 24h of exposure (Figure 18B). Similar results were observed after 48h of EdU exposure (data not shown). These data indicate that in HNSCC MCTSs that exhibit rapid and moderate growth rates in ULA-plates, the more quiescent cells in the interior are surrounded by outer layers of proliferating cells.

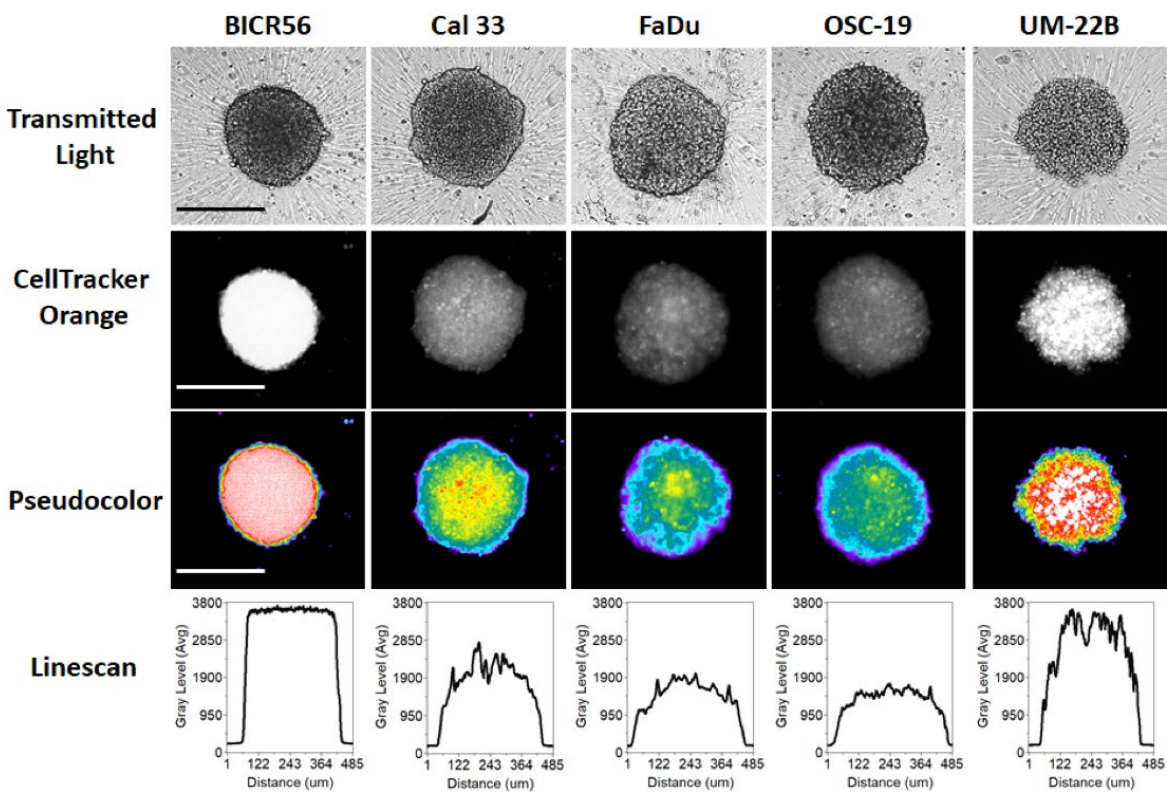
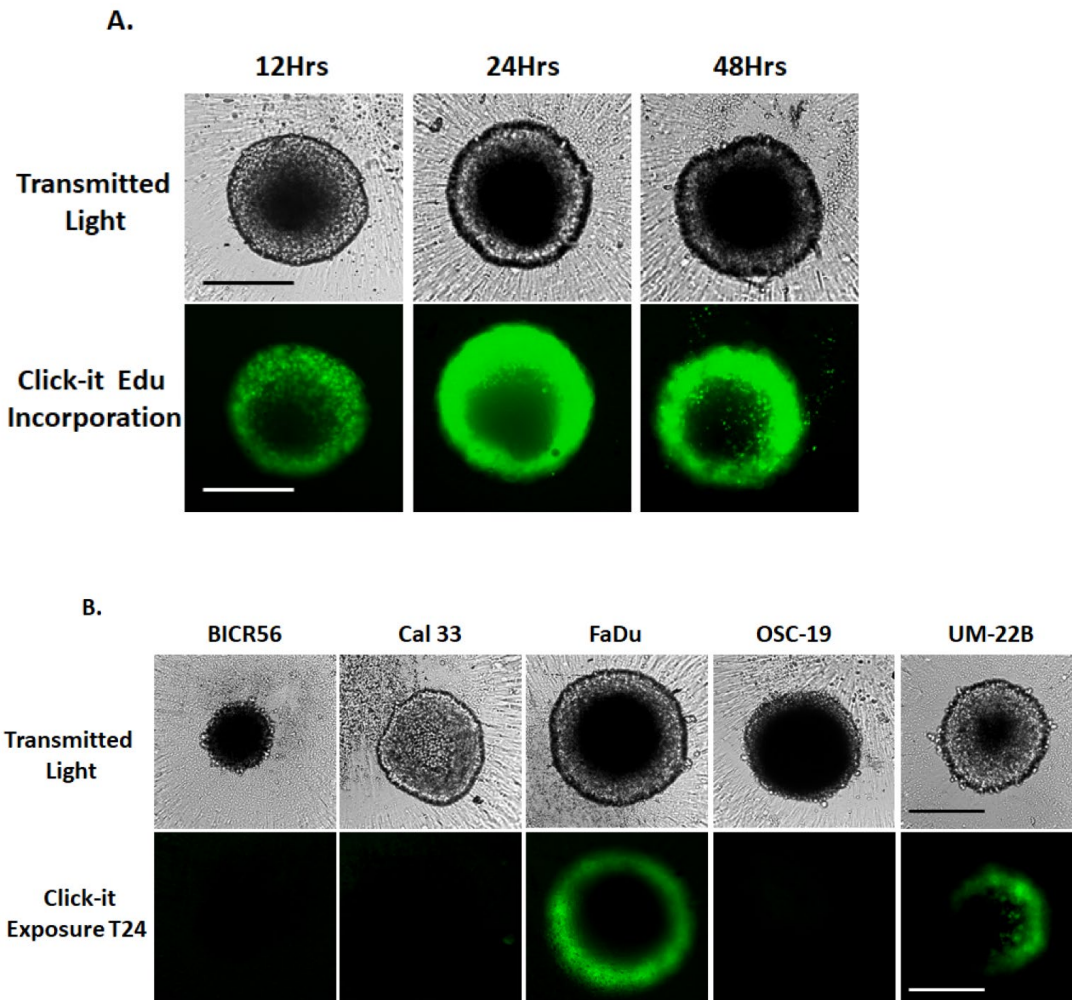


**Figure 17 Distribution of the fluorescence in multicellular tumor spheroids formed from HNSCC cell lines pre-labeled with Celltracker Orange® prior to cell seeding into Ultra-low Attachment plates**

Prior to cell harvesting, counting and seeding into ULA-plates, the five HNSCC cell lines were pre-labeled with the Celltracker Orange (CTO) reagent according to the manufacturer's instructions. The five HNSCC cell lines were seeded at 2,500 cells per well in 384-well ULA-plates and cultured for 3 days, before 4X images were acquired on the IXM in the TL and Texas Red channels. Greyscale TL and CTO fluorescent images are presented along with presented along with the corresponding pseudo-color pixel intensity visualizations, and line-scan fluorescent intensity profiles. Representative images and data from multiple independent experiments are shown. All scale bars represent 300  $\mu\text{m}$ .

**Figure 18 Cell proliferation in HNSCC multicellular tumor spheroids produced and cultured in Ultra-low Attachment Plates**



HNSCC cell lines were seeded at 2,500 cells per well into 384-well ULA-plates and allowed to form MCTSs for 3 days before the culture media was exchanged and over the next 3 days MCTSs were exposed to EdU for the indicated time periods and developed with the Click-iT® reagent according to the manufacturer's recommendations. MCTSs were fixed in 3.7% formaldehyde and 4X images were acquired on the IXM in the TL and FITC channels to capture the Click-iT® EdU (green) fluorescent signal. **(A)** Six-day FaDu MCTS cultures that were exposed to EdU for 12h, 24h or 48h before fixation. **(B)** Six-day MCTS cultures prepared from each of the five representative HNSCC cell lines (UM-22B, OSC-19, FaDu, BICR56 and Cal33) that were exposed to EdU for 24h before fixation. All scale bars represent 300 µm.

#### **4.3.4 HNSCC Multicellular Tumor Spheroid Mitochondrial Mass and Membrane Potential**

We used the mitotracker orange (MTO) and tetramethyl-rhodamine methyl ester (TMRM) dyes to determine the mass and membrane potential of active mitochondria in the cells of HNSCC MCTS cultures (Figure 19).<sup>174, 175</sup> HNSCC cell lines were seeded into 384-well ULA-plates and after 3 days in culture the culture media was exchanged and MCTS were exposed to MTO (Figure 19A and 19B) or TMRM (Figure 19C and 19D) for 1h. The TRITC images, pseudo-color visualizations, and line-scan plots showed that the MTO fluorescence was distributed uniformly throughout formaldehyde fixed HNSCC MCTSs, although the fluorescent intensities were perhaps marginally higher in cells in the inner cores of MCTSs relative to the outer layers (Figure 19A). These data indicate that cells in HNSCC MCTS cultures contain active mitochondria irrespective of their location within the MCTS. Using the MWCS image analysis module to quantify MCTS MTO MIFI showed that mitochondrial mass tracks with MCTS size;

FaDu>OSC19>UM22B>Cal33>BICR56 (Figure 19B). In contrast, TRITC images, pseudo-color visualizations, and line-scan plots of HNSCC MCTSs stained with the live cell TMRM mitochondrial potential dye exhibited a differential staining pattern, where cells in the outer layers of MCTSs exhibited higher intensities relative to cells in the inner cores, irrespective of MCTS size or HNSCC cell line (Figure 19C). These data show that mitochondria in cells in the outer layers of the

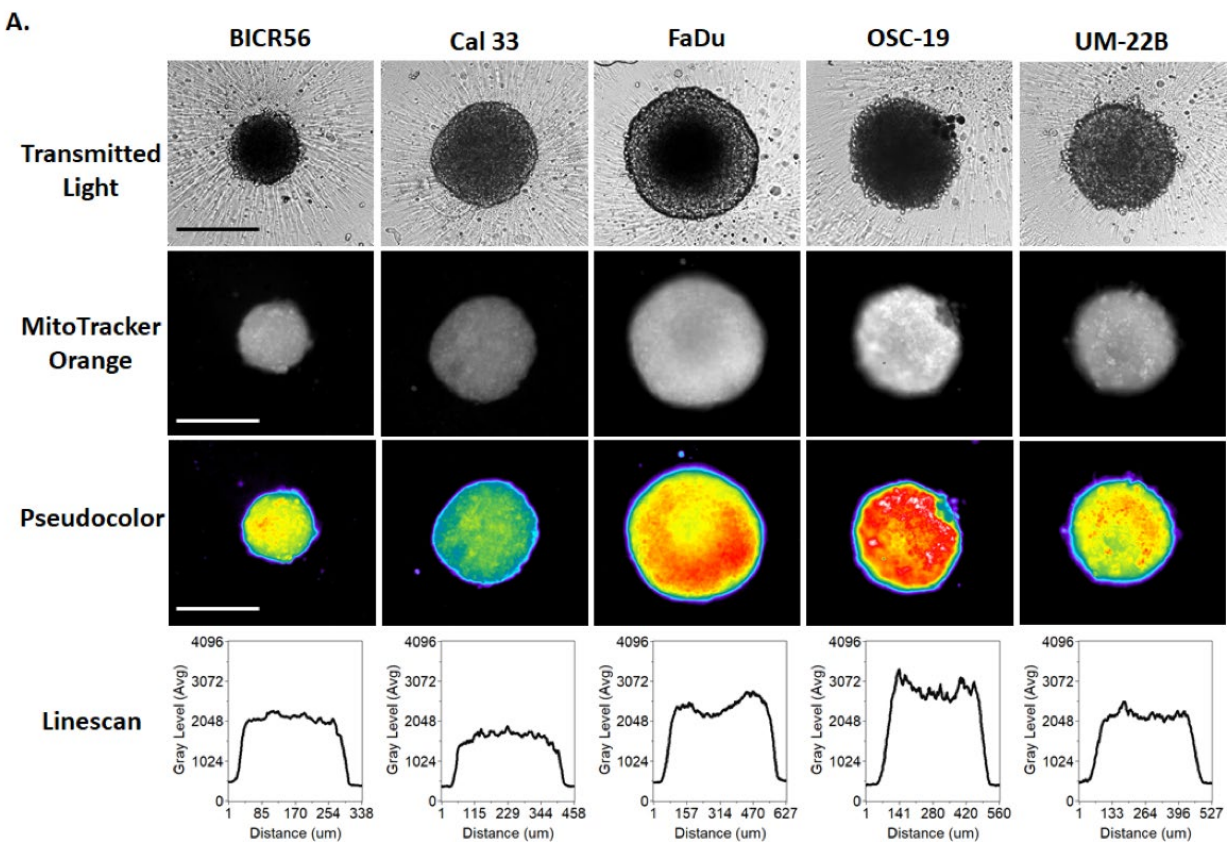
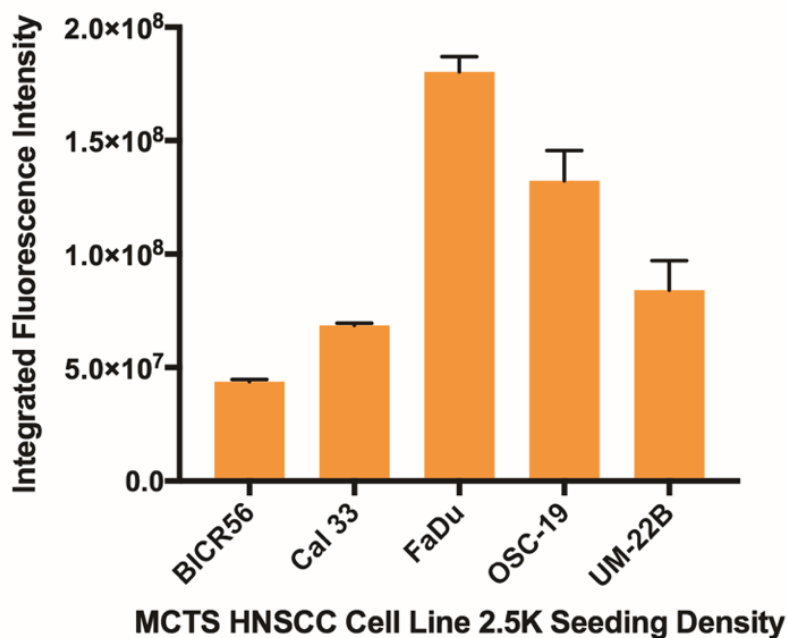


**Figure 19 Mitochondrial mass and Membrane potential in HNSCC multicellular tumor spheroids produced in Ultra-low Attachment Plates**

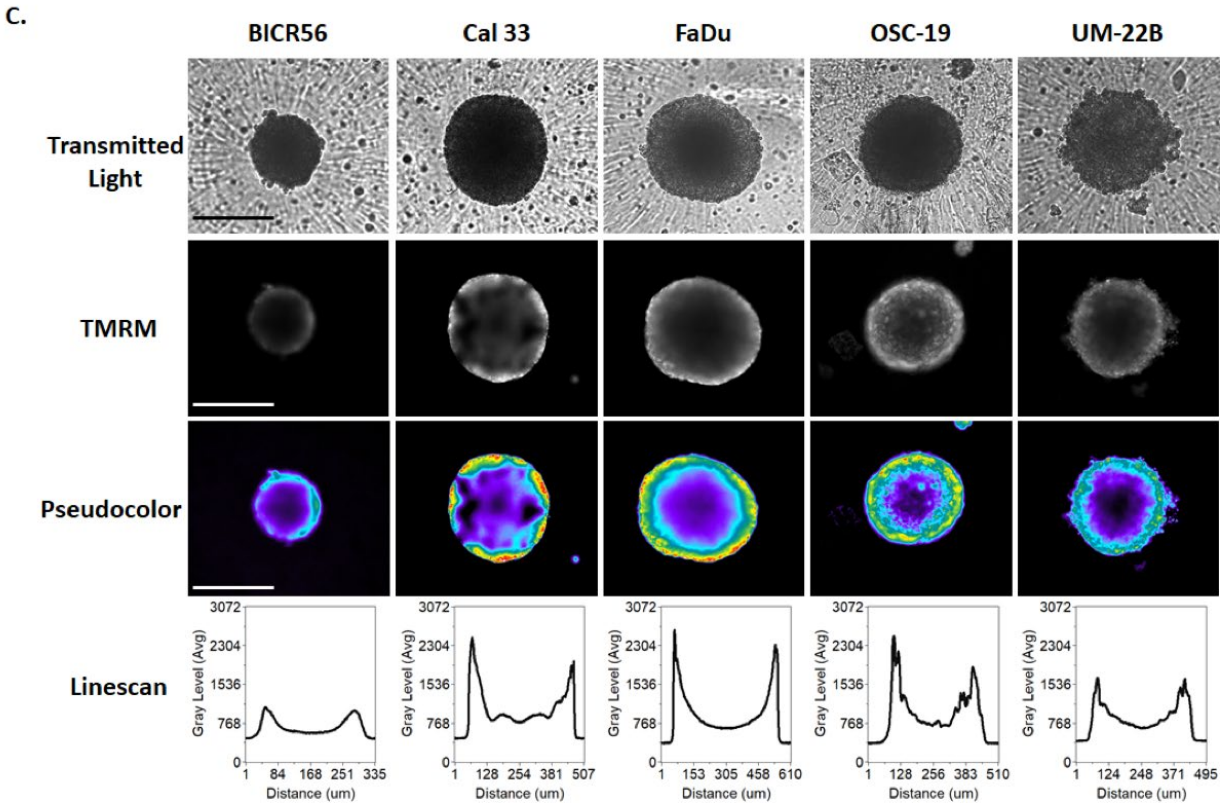
2,500 cells of the five representative HNSCC cell lines were seeded into 384-well ULA-plates and after 3 days in culture the culture media was exchanged and MCTS were exposed to 500 nM mitotracker orange (MTO) or 250 nM tetra-methyl-rhodamine methyl ester (TMRM) for 1h. **(A)** HNSCC MCTSs that were stained with MTO were fixed in 3.7%

formaldehyde and 4X images were acquired on the IXM in the TL and TRITC channels. Representative grey scale TL and MTO (TRITC) images are presented along with the corresponding pseudo-color pixel intensity visualizations and line-scan fluorescent intensity plots. In pseudo-color pixel intensity visualizations, the relative fluorescent intensities of the pixels in the images are indicated as distinct colors. The “hotter” and “brighter” colors (low to high, yellow, red, white) represent higher intensity signals and cooler colors (low to high, purple, cyan, green) represent lower intensity signals. In line-scan fluorescence intensity plots the line scanning tool of the MetaXpress image analysis software to draw a line across the image and plot the fluorescent intensity values versus distance in  $\mu\text{m}$  across the image to provide an intensity profile graph. All scale bars represent 300  $\mu\text{m}$ .

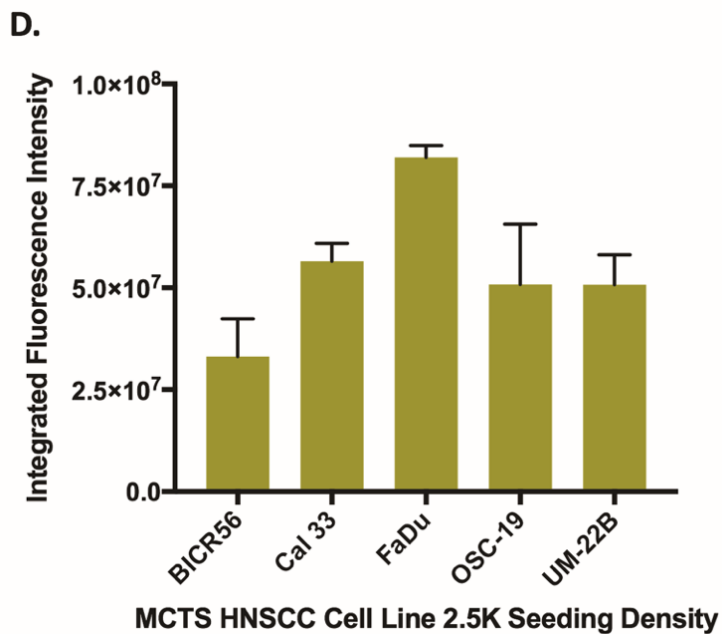
**B.**



**(B)** The multiwavelength cell scoring (MWCS) image analysis module was used to create a whole MCTS mask and quantify MTO mean integrated fluorescent intensity (MIFI) signals in the HNSCC MCTSs. HNSCC MCTS MTO MIFIs were measured in triplicate wells ( $n=3$ ) and are presented as the mean  $\pm$  SD. Representative data from three independent experiments are presented.



C) 4X images HNSCC MCTSs that were stained with TMRM were acquired on the IXM in the TL and TRITC channels. Representative grey scale TL and TMRM (TRITC) images are presented along with the corresponding pseudo-color pixel intensity visualizations and line-scan fluorescent intensity plots. All scale bars represent 300  $\mu\text{m}$ .



**(D)** The MWCS image analysis module was used to create a whole MCTS mask and quantify TMRM MIFI signals in the HNSCC MCTSs. HNSCC MCTS TMRM MIFIs were measured in triplicate wells ( $n=3$ ) and are presented as the mean  $\pm$  SD. Representative data from three independent experiments are presented.

HNSCC MCTSs had higher membrane potentials than mitochondria in cells in the inner regions, indicating that mitochondria in cells in the outer layers were more functionally active. MCTS TMRM MIFI values among the 5 HNSCC cell lines did not however track with MCTS size; FaDu>OSC19=UM22B=Cal33>BICR56 (Figure 19D).

#### **4.3.5 Doxorubicin Penetration and Cytotoxicity in HNSCC Multicellular Tumor Spheroid Cultures**

To investigate cancer drug uptake, penetration and distribution in HNSCC MCTS we seeded 2,500 cells of the HNSCC cell lines into 384-well ULA-plates and after 3 days the culture media was exchanged and MCTSs were exposed to 10  $\mu$ M doxorubicin for 0.5h (Figure 20A) and 24h (Figure 20B). As expected, the TRITC images, pseudo-color visualizations, and line-scan plots of all five HNSCC MCTSs exposed to doxorubicin for 0.5h exhibited an apparent donut-like staining pattern, where cells in the outer edges of the MCTSs had higher doxorubicin staining intensities relative to cells in the inner cores (Figure 20A). After 24h of doxorubicin exposure however, the TRITC images, pseudo-color visualizations, and line-scan plots showed that doxorubicin fluorescence was distributed throughout the HNSCC MCTSs and was perhaps slightly higher in cells in the inner cores of MCTSs relative to cells in the outer layers (Figure 20A). A comparison of the TL images of HNSCC MCTS exposed to 10  $\mu$ M doxorubicin for 0.5h (Figure 20A) and

24h (Figure 20B), revealed that the longer drug exposure had a significant morphological impact producing less rounded MCTSs with uneven perimeters surrounded by a halo of single cells and generally darker inner cores. Furthermore, in time course TL images for

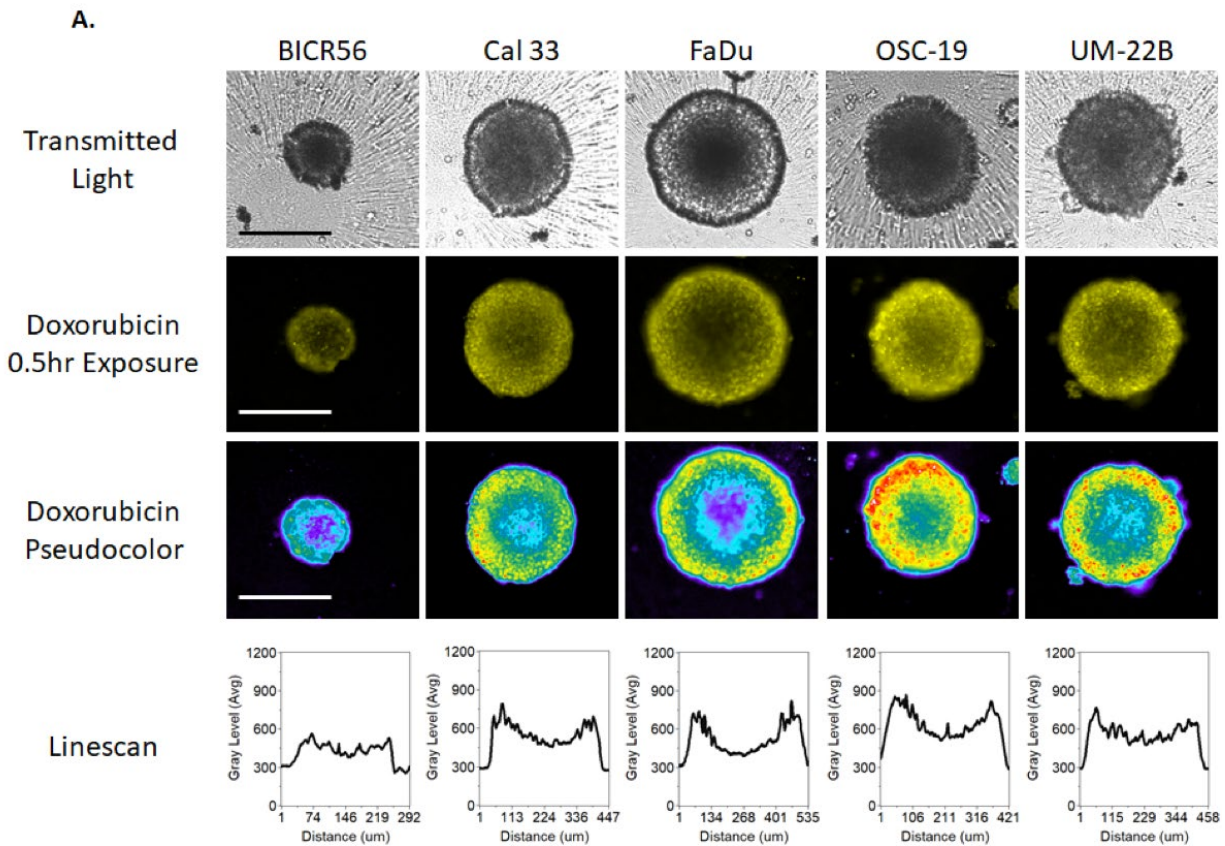
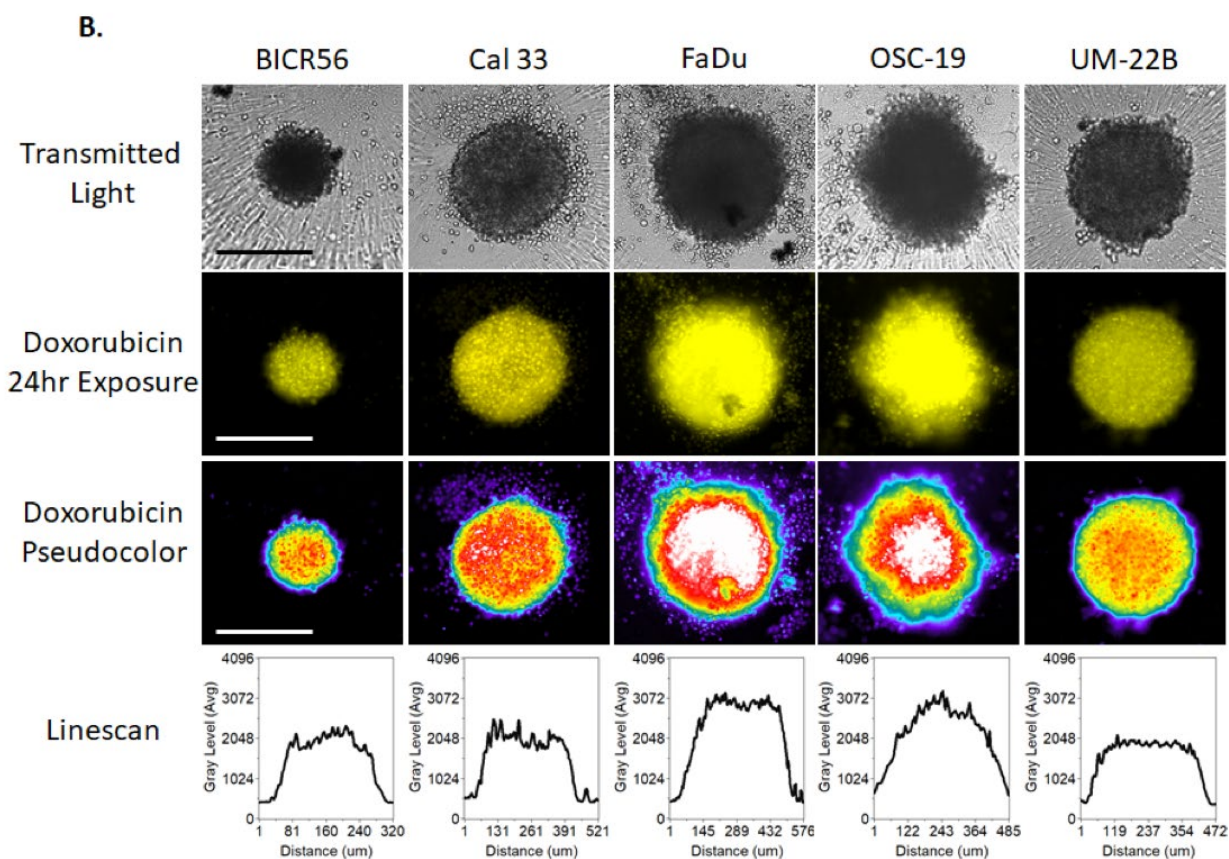


**Figure 20 Doxorubicin Drug Distribution in multicellular tumor spheroids formed in Ultra-low Attachment Plates**

HNSCC cell lines were seeded at 2,500 cells per well into 384-well ULA-plates and after 3 days in culture the culture media was exchanged and MCTS were then exposed to 10  $\mu$ M doxorubicin for either 0.5h (**A**) or 24h (**B**). HNSCC MCTSs that were exposed to 10  $\mu$ M doxorubicin were then fixed in 3.7% formaldehyde and 4X images were acquired on the IXM in the TL and TRITC channels. Representative grey scale TL and doxorubicin (TRITC) images are presented along with the corresponding pseudo-color pixel intensity visualizations and line-scan fluorescent intensity plots. Representative data from three independent experiments are presented. All scale bars represent 300  $\mu$ m.



each of the five cell lines exposed to doxorubicin, we observed that the most distinctive morphological changes occurred between 12h and 24h post treatment, as indicated by changes in MCTS size, loss of roundedness, and a reduction of inner core density (Figure 21). Interestingly, UM-22B MCTSs only displayed modest morphological changes over time in comparison to the other cell lines (Figure 21).

To investigate doxorubicin-induced cytotoxicity in HNSCC MCTS we seeded 2,500 cells of the HNSCC cell lines into 384-well ULA-plates and after 3 days in culture the culture media was exchanged. The MCTSs were then exposed to 0.01 to 200  $\mu$ M doxorubicin for 72h prior to the addition of the CTB detection reagent and subsequent measurement of the RFU signals. To define the dynamic range of the 72h compound

exposure in HNSCC MCTS assays, we used 0.2% DMSO control wells to represent uninhibited growth (Max controls, n=32), and 200 $\mu$ M Doxorubicin + 0.2% DMSO control wells to represent 100% growth inhibition (Min controls, n=32) respectively. Doxorubicin inhibited the growth of all five HNSCC MCTS cultures in a concentration dependent manner with GI<sub>50</sub>s in the low to sub-micromolar range; 0.31, 0.42, 1.59, 1.97 and 2.07  $\mu$ M for the UM22B, Cal33, FaDu, BICR56 and OSC19 cell lines respectively (Figure 22A). To determine the effects of 72h doxorubicin exposure on HNSCC MCTS morphology and viability, we acquired TL and CAM/EHD fluorescent images of doxorubicin treated HNSCC MCTSs (Figure 22B). All five HNSCC MCTSs were totally disrupted after 72h exposure to the top three concentrations of doxorubicin tested (200, 66.7 and 22.2  $\mu$ M) and the images provided no additional information (not shown). After 72h exposure to 7.4  $\mu$ M doxorubicin however, the TL and CAM/EHD images reveal profound differences when compared to images acquired from DMSO control wells. In TL images of DMSO control wells, FaDu, Cal33, and UM22B cell lines formed condensed MCTSs with a smooth and even periphery, while OSC19 and BICR56 formed rounded MCTSs with uneven perimeters. Exposure to 7.4  $\mu$ M doxorubicin for 72h dramatically altered HNSCC MCTS morphologies: OSC19 MCTSs became irregular loose cell aggregates; BICR56 MCTSs became dark irregular cell aggregates with uneven outlines surrounded by single cells; Cal33 and UM22B MCTS became smaller and less rounded with dark inner cores and uneven perimeters surrounded by a halo of single cells; and FaDu MCTSs became bigger and darker with a rounded uneven perimeter. However, the CAM/EHD images revealed the most dramatic differences between doxorubicin treated and DMSO control wells.

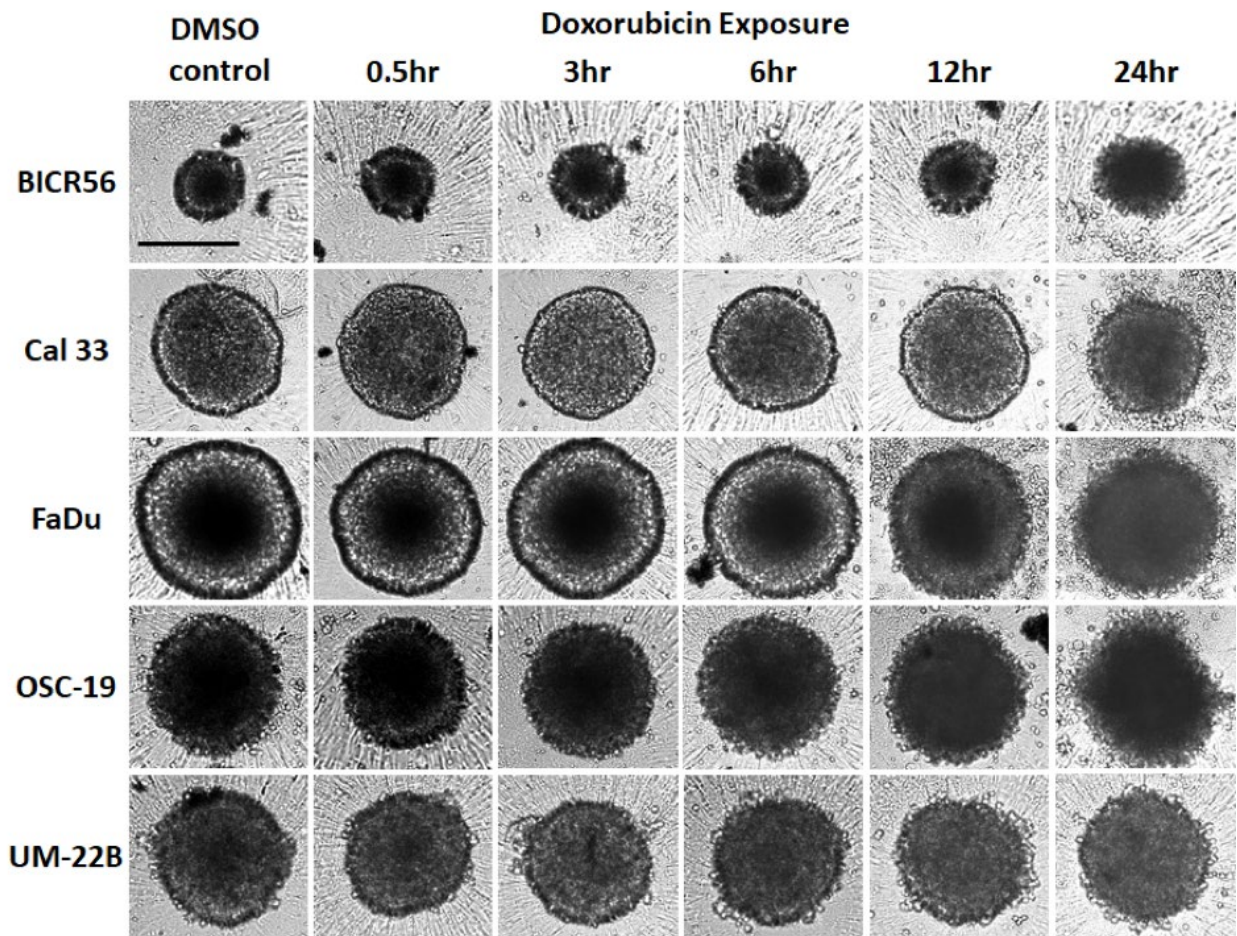


**Figure 21 MCTS Morphological Effects by Doxorubicin Treatment Over Time**

Five HNSCC cell lines were seeded at 2,500 cells per well into ULA-plates and allowed to form spheroids. After 72h media was exchanged, and cells were then exposed to 10  $\mu$ M doxorubicin for 0.5h, 3h, 6h, 12h, and 24h, followed by acquisition of 4X TL images on the IXM platform to determine changes in spheroid morphology. Representative images from multiple experiments are shown. All scale bars represent 300  $\mu$ m.

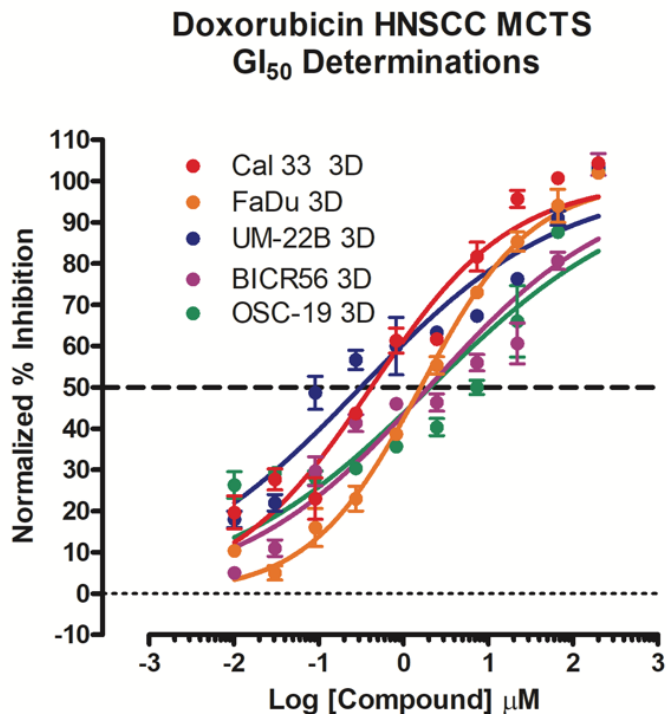
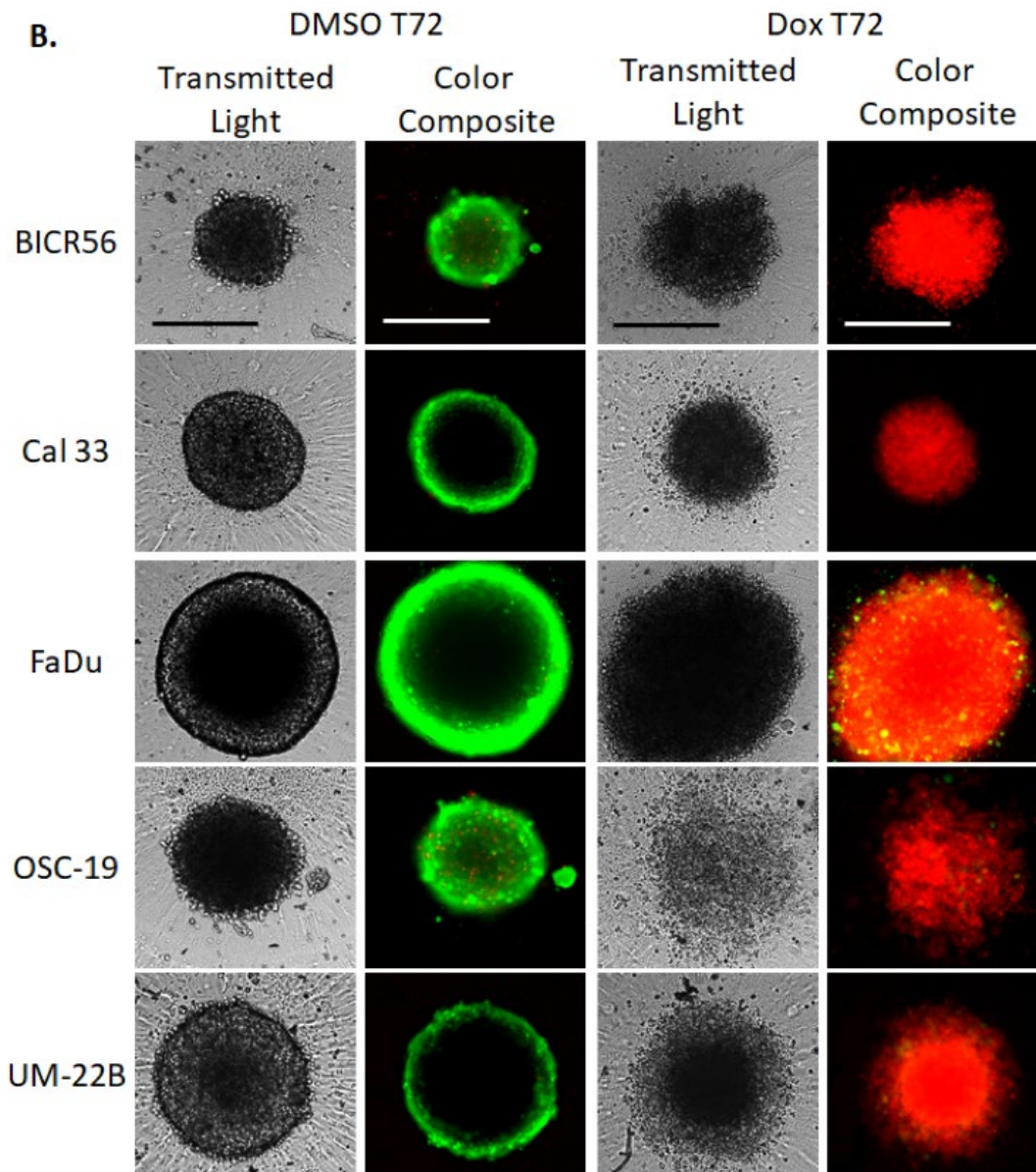


**Figure 22 Doxorubicin-induced cytotoxicity in multicellular tumor spheroids formed in Ultra-low Attachment Plates**

HNSCC cell lines were seeded at 2,500 cells per well in 384-well ULA-plates and after 3 days in culture the culture media was exchanged, and then MCTSs were exposed to the indicated concentrations of doxorubicin for 72h prior to the addition of the CTB detection reagent and subsequent measurement of the RFU signals. **(A)** The mean maximum (0.5% DMSO) and minimum (200  $\mu\text{M}$  doxorubicin + 0.5% DMSO) plate control CTB RFUs were used to normalize the RFU data from the compound treated wells as % inhibition of growth and the GI<sub>50</sub> data were fit to a non-linear sigmoidal log inhibitor concentration versus the normalized response variable slope model using the GraphPad Prism 6 software. The normalized mean  $\pm$  SD (n=3) growth inhibition data from triplicate wells for each compound concentration are presented. Representative experimental data from one of four independent experiments are shown.



**(B)** To examine the effects of 72h doxorubicin exposure on HNSCC MCTS morphology and viability we acquired 4X TL and CAM/EHD fluorescent images of HNSCC MCTSs exposed to 7.4  $\mu\text{M}$  doxorubicin for 72h. Greyscale TL images are presented along with color composite fluorescent images of live cell CAM and dead cell EHD staining depicted as green and red, respectively. Representative images from four independent experiments are presented. All scale bars represent 300  $\mu\text{m}$ .

The strong CAM and almost non-existent EHD fluorescence in the CAM/EHD composite images of the five HNSCC MCTSs from DMSO control wells indicated that most of the cells in the MCTSs were viable. In sharp contrast, the very weak CAM and strong EHD fluorescence in the CAM/EHD composite images of the five HNSCC MCTSs from wells exposed to 7.4 $\mu$ M doxorubicin indicated that most of the cells in the MCTSs were dead. These data demonstrate that although different HNSCC cell lines seeded into ULA-plates produced MCTSs with distinct morphologies and growth phenotypes, these more physiologically relevant 3D tumor models can be readily adapted to measure compound mediated cytotoxicity.

#### **4.4 Discussion**

MCTS cultures represent more physiologically relevant *in vitro* cell tumor models that recapitulate the microenvironments and cell-cell or cell-ECM interactions which occur in solid tumors.<sup>98, 159, 166, 167, 176</sup> We set out to characterize the morphologies, viability, and growth behaviors of MCTSs produced by 11 different HNSCC cell lines seeded into and cultured in ULA-plates over extended periods of time (Figures 13 & 14). The eleven HNSCC cell lines form xenografts in immuno-deficient mice, have similar genetic profiles to patient tumors, and have previously been used for HNSCC drug discovery.<sup>135, 136, 150</sup> The Het-1A SV40 T-antigen immortalized human esophageal epithelial cell line does not grow as xenograft tumor in immuno-deficient mice.<sup>170-173</sup> We characterized the development of distinct microenvironments and the penetration and distribution of drugs in different regions of the MCTSs (Figures 16 and 18-20) and investigated drug-induced

cytotoxicity (Chapter 4. Figures 21 and 22). Our goal was to obtain a better understanding of how HNSCC MCTS cultures behaved so that we could apply these models in HTS campaigns designed to identify cancer drug leads that will be more translatable into efficacy in *in vivo* animal models and patients.

Nine of the eleven HNSCC cell lines seeded into 384-well ULA plates formed condensed MCTSs with either a smooth or uneven periphery after 3 days. The UM22B and SCC9 HNSCC cell lines and Het-1A esophageal epithelial cell line formed cell aggregates with irregular outer margins. After several days in culture however, the UM22B cell line coalesced into a compact MCTS with an even periphery. The HNSCC MCTS morphologies are consistent with our previous observations,<sup>64, 98, 157</sup> and similar HNSCC MCTS morphologies were described in studies conducted in 96-well ULA-plates.<sup>167, 177</sup> In a study of six HNSCC cell lines, that included the Cal27 and Detroit 562 cell lines of the present study, four formed tight spheroids and two formed compact cell aggregates.<sup>167</sup> In a study of ten HNSCC cell lines, that included the Cal27 and FaDu cell lines of the present study, six formed tight compact spheroids, three formed intermediate spheroids, and one produced loose irregular cell aggregates.<sup>177</sup> It's been reported that H-RAS-transformed fibroblast cell lines form MCTSs that grow when seeded into 96-well ULA-plates, whereas non-transformed fibroblasts do not.<sup>178</sup> It was suggested that the ability to form MCTS in ULA-plates was similar to soft agar colony formation clonogenicity assays, where only transformed cells can form colonies. In our study however, both the SCC9 HNSCC cell line and the Het-1A SV40 T-antigen immortalized human esophageal epithelial cell line formed irregularly shaped cell aggregates in ULA-plates that did not self-assemble into MCTSs. Some HNSCC MCTSs, most noticeably those formed by the

FaDu, Cal33, Cal27 and PCI-13 cell lines, exhibited two distinct spheroid regions, a darker or denser inner core surrounded by lighter outer layers that were two to several layers of cells thick depending upon the cell line. The two distinct spheroid regions have been observed previously in MCTSs formed by the FaDu and Cal33 cell lines.<sup>64, 177</sup> In addition to morphology differences, we observed that HNSCC cell lines produced MCTSs of two different size ranges when they were seeded into ULA-plates at the same cell number; either smaller more compact MCTSs ~200-250  $\mu\text{m}$  in diameter, or larger MCTSs ~350-400  $\mu\text{m}$  in diameter. HNSCC develops at multiple anatomic sites in different cell types within the head and neck region; paranasal sinuses, nasal cavity, oral cavity, pharynx, larynx, salivary gland and thyroid.<sup>132, 179-181</sup> Histology, molecular characteristics and clinical outcomes vary widely across different sites.<sup>132, 179-181</sup> In the present study, UMSCC1, SCC9, PCI-13, Cal33, Cal27 and BICR56 HNSCC cell lines were established from oral cavity tumors, the OSC-19 tumor originated in the tongue but the cell line was established from a metastatic site in the cervical lymph node, the FaDu and UM22B cell lines were established from hypopharynx tumors, the PCI-52 cell line was established from a larynx tumor, and the Detroit 562 tumor originated in the larynx but the cell line was established from a pleural effusion metastasis.<sup>136</sup> HNSCC patient tumors have on average 130 coding mutations and 141 gene copy number alterations (gains/deletions) per tumor,<sup>132, 180, 181</sup> and exhibit four gene expression signature subtypes; basal, mesenchymal, atypical, and classical.<sup>182</sup> It is likely that the complexity and heterogeneity of HNSCC contributes to the variety in MCTS sizes and morphologies that we observed.

We measured the changes in MCTS diameters and CTB RFUs over time in culture to assess the growth of HNSCC MCTS cultures in ULA-plates (Figure 14B & 14C). MCTS

diameters and CTB RFUs both increased linearly over time in culture throughout the 10-14-day culture period for FaDu, UM22B and Cal33 MCTSs. In contrast, BICR56 MCTSs were static and OSC19 MCTSs exhibited gradual declines for both indicators over time. Time course CAM/EHD images demonstrated that most of the cells in UM22B, Cal33 and BICR56 MCTSs were viable at all timepoints (Figures 14A & 16A). FaDu MCTSs appeared to develop necrotic cores as they became progressively larger, and OSC19 MCTSs appeared to have a necrotic core at all timepoints. The presence of necrotic cores in OSC19 and FaDu MCTSs were confirmed by both the CAM/EHD images and the quantitative MIFI data presented in Figure 16A. The necrotic core in FaDu MCTSs developed between day 4 and 6 in culture after the MCTSs reached ~ 500  $\mu\text{m}$  in diameter (Figure 14B), and we speculate that diffusion was no longer able to support efficient nutrient and/or oxygen uptake and distribution to interior cells, and/or to remove waste products. Several methods have been used to label actively proliferating cells in MCTS cultures including Ki67 staining and the incorporation of either  $\text{H}^3$ -thymidine or  $\text{H}^3$ -bromodeoxyuridine incorporation into DNA.<sup>98, 104, 165, 166, 183</sup> Previous MCTS proliferation studies have shown that MCTS cultures exhibit differential zones of proliferation characterized by outer layers of proliferating cells surrounding inner layers of quiescent cells, and inner cores that may become necrotic.<sup>98, 104, 165, 166, 183</sup> Consistent with these observations, cells in the outer layers of the FaDu and UM22B MCTSs exhibited EdU incorporation (Figure 18). However, none of the cells in Cal33, BICR56 and OSC19 MCTSs exhibited detectable levels of EdU incorporation, even with 48h EdU exposure. Only HNSCC MCTSs that showed substantial increases in MCTS diameters and CTB RFUs with time in culture contained actively proliferating cells detectable by EdU incorporation. Despite

the apparent viability of the cells in Cal33 and BICR56 MCTSs demonstrated by the CAM/EHD (live/dead) stains, their rates of proliferation were below the detection limits of EdU incorporation. OSC19 MCTSs exhibit a slow progressive death phenotype, and none of the cells in OSC19 MCTSs were positive for EdU incorporation. Based on Ki67 staining, the rates of proliferation of eight of nine HNSCC cell lines that formed MCTS cultures in 96-well ULA-plates decreased substantially compared to the corresponding 2D cultures, especially for those that formed tight spheroids.<sup>177</sup> Only the FaDu cell line exhibited comparable Ki67 staining in 2D and 3D cultures.<sup>177</sup>

The rates of proliferation and growth of HNSCC cell lines in ULA-plate MCTS cultures is dramatically different from that in 2D cultures.<sup>135, 150</sup> When HNSCC cell lines are seeded at 1,000 cells per well into standard tissue culture treated 384-well microtiter plates, they proliferate exponentially throughout a 96h culture period, and typically undergo >2 but <3 doublings.<sup>135, 150</sup> Tumor cell lines adapted to growth in 2D proliferate faster than cells from primary tumors, exhibit altered drug response profiles, and are very sensitivity to anti-proliferative agents while under-representing the self- and population-renewing tumor stem cells that contribute to recurrence and metastasis.<sup>64, 151-155</sup> Dormant or quiescent tumor cells which have stopped replicating, or that proliferate slowly due to reduced nutrient and/or oxygen microenvironments, are resistant to molecules targeting cell proliferation mechanisms.<sup>184-186</sup> The reduced proliferation and growth of HNSCC cell lines that we observed in MCTS culture conditions may more accurately align with tumor growth *in vivo*, which may be critical to screening for new solid tumor cancer drug leads that will translate better in *in vivo* animal models and in patients.

Images of CAM stained HNSCC MCTS cultures indicated that cells in the outer layers of MCTSs exhibited higher intensities relative to cells in the interior, irrespective of MCTS size or HNSCC cell line (Figures 13, 14A, and 16A). The uniform distribution of fluorescence observed in HNSCC MCTSs prelabeled with CTO prior to MCTS formation (Figure 17) suggests that the gradient of CAM fluorescence was not due to an imaging artifact caused by inefficient excitation light penetration into MCTS cores and/or fluorescent emission light detection from these regions. Since the CAM reagent is metabolized by live cells into a fluorescent end-product, the higher CAM signals in cells in the outer layers of HNSCC MCTSs may be due to their higher metabolic activity relative to cells in the inner cores. We cannot however exclude the possibility that poor CAM reagent permeability might have produced uneven reagent penetration and distribution within the MCTSs, and that the apparent gradient of CAM staining was due to its preferential uptake, accumulation and metabolism by cells in the outer layers of HNSCC MCTSs. Mitochondria are critical to cellular energy production, and we used the MTO and TMRM dyes to evaluate the mass and membrane potential of active mitochondria in the cells of HNSCC MCTS cultures (Figure 19).<sup>174, 175</sup> The MTO data indicated that all of the cells in HNSCC MCTS cultures contain active mitochondria irrespective of their location within the MCTS (Figure 19A), and that MCTS mitochondrial mass appears to track with MCTS size (Figure 19B). The TMRM data indicated that the mitochondria in cells in the outer layers of HNSCC MCTSs had higher membrane potentials than mitochondria in cells in the inner regions, indicating that cells in the outer layers of MCTS have more functionally active mitochondria. Both the CAM and TMRM data indicated that cells in the

outer layers of HNSCC MCTSs were more metabolically active than cells in the interior regions.

When MCTSs are initially exposed to doxorubicin, cells in the outer layers of HNSCC MCTSs exhibit higher doxorubicin fluorescent intensities than cells in the inner cores (Figure 20A). After 24h however, doxorubicin alters the integrity and morphologies of MCTSs, and becomes uniformly distributed throughout MCTSs (Figure 20B). These data are consistent with our previous observations that Cal33 and FaDu MCTSs exhibited permeability barriers that resulted in uneven drug distribution and exposure gradients which coincided with enhanced resistance relative to monolayer cultures.<sup>64</sup> Adhesion junctions between adjacent cells, cell-ECM contacts, and high tumor cell packing densities constitute drug permeability barriers that limit cancer drug penetration, distribution, and efficacy.<sup>184-189</sup> Drug physiochemical properties also affects their distribution in tissues, and cells in solid tumors which are distal to blood vessels experience lower drug concentrations due to reduced drug access <sup>186-188</sup> Exposure to doxorubicin for 72h inhibited the growth and viability of all five HNSCC MCTS cultures in a concentration dependent manner with GI<sub>50</sub>s in the low to sub-micromolar range; 0.31, 0.42, 1.59, 1.97 and 2.07  $\mu\text{M}$  for the UM22B, Cal33, FaDu, BICR56 and OSC19 MCTSs respectively (Figure 21A). The top three concentrations of doxorubicin totally disrupted the integrity and viability of all five HNSCC MCTSs. At 7.4  $\mu\text{M}$  doxorubicin, HNSCC MCTS integrity and morphologies were profoundly altered and the CAM/EHD images indicated that most of the cells were dead (Figure 22B).

HNSCC MCTS cultures develop microenvironments which result in differences in proliferation rates, metabolic activity, and mitochondrial functional activity between cells

located in the outer layers of the MCTS and cells in the interior. Some HNSCC MCTS cultures have necrotic cores that gradually increase as MCTS size and viability decline, while others develop necrotic cores surrounded by viable layers of cells as MCTSs achieve a critical size threshold. HNSCC MCTS cultures also exhibit drug penetration and distribution gradients that coincide with enhanced resistance. Perhaps the most profound effect of culturing HNSCC cell lines in MCTS cultures was their dramatically altered and varied growth phenotypes. Instead of the exponential growth that are characteristic of 2D HNSCC growth inhibition assays, some MCTS cultures displayed linear growth rates, categorized as either rapid, moderate or slow, dormant MCTSs remained viable but did not grow, and some MCTSs exhibited death phenotypes that were either progressive and slow or rapid. The ability of MCTS cultures to develop microenvironments and to display a variety of different growth phenotypes provide *in vitro* models that are more closely aligned with solid tumors *in vivo*. We anticipate that the implementation MCTS models to screen for new cancer drugs for solid tumors like HNSCC will produce leads that will translate better in *in vivo* animal models and patients. Overall, we demonstrated our ability to characterize several aspects of a multicellular tumor spheroids both specific to 3D cell culture and relevant to an avascular solid tumor, therefore providing a more physiologically relevant *in vitro* model for drug discovery.

## **5.0 Determination of Drug Sensitivity in Head and Neck Squamous Cell Carcinoma using Multicellular Tumor Spheroids and 2D Cell Culture Models**

### **5.1 Overview of Head and Neck Squamous Cell Carcinoma**

As described in more detail in chapter 4, head and neck squamous cell carcinoma (HNSCC) represents the sixth most common cancer worldwide, presenting over 600,000 new cases annually, and 65,410 cases projected to occur in the United States alone with 14,620 deaths anticipated (Cancer.net).<sup>190</sup> Risk factors for cancers of the head and neck include the consumption of alcohol, use of tobacco products, exposure to human papilloma virus, and innate genetic factors. Because of the location and complex nature of the anatomical sites (lip, tongue, nasopharynx, oropharynx, larynx, hypopharynx) where HNSCC can develop, facilitating appropriate surgical and/or radiological treatment can be challenging and potentially deforming in patients. Given both the etiologies and the various anatomical sites that HNSCC can arise from, researchers have documented vast heterogeneity with major influence from genetic alterations in TP53, Rb, CDKN2A, CASP8, PIK3CA, EGFR, NOTCH1, HRas and many others; with alterations in tumor suppressor pathways appearing to be the most prevalent.<sup>117, 190-192</sup> Pharmacological treatment of HNSCC has remained a challenge and has stagnated for the past 3 decades, even with advent of molecularly targeting agents (MTA), patient responses are variable and often very modest. For example, only 13% of patients receiving therapy with the epidermal growth factor receptor (EGFR) MTA cetuximab exhibit a response.<sup>193, 194</sup>

### 5.1.1 MCTS as Physiological Relevant In Vitro Models for Screening Drug

#### Candidates

Cancer drug approval rates have been and continue to be abysmal, with a recent report summarizing that from 2000 to 2015 the probability of new chemical agent success in oncology was on average only 3.4%.<sup>88</sup> One of the major factors limiting the success of drug candidates in the clinic is the physiological relevance of preclinical models, which currently, fail to adequately recapitulate the characteristics of a solid tumor.<sup>96, 104</sup> In cancer drug discovery the more accurately we can mimic the characteristics of a solid tumor, the more accurately we can predict the success of a drug candidate at effectively targeting a malignancy. There is a large body of evidence in support of using 3-dimensional (3D) cell culture models for the purpose of drug discovery given their ability to better recapitulate *in vivo* characteristics, gene expression, and tumor physiology than traditional 2D models.<sup>107, 109, 195</sup> In particular, the cell-cell / cell-extracellular matrix interactions created in 3D conditions are capable of producing physiological gradients of nutrients, oxygen, waste, and drugs; conditions which lend themselves to produce differential zones of proliferation within the multicellular tumor spheroids (MCTSs) and better recapitulate the tumor microenvironment.<sup>96, 196</sup> Furthermore, use of drug screening and compound treatment in 3D models has identified unique applications, undetected in 2D culture systems, such as clinically relevant responses to the HER2 inhibitor trastuzumab observed in 3D but not 2D cultures, and effectively targeting dormant cells within MCTSs.<sup>106, 107</sup>

### 5.1.2 Overview and Review of MCTS Characterization

Chapter 4 described the characterization of 11 different HNSCC cell lines in 3D MCTSs for the purposes of conducting more physiologically relevant cancer drug screening.<sup>114</sup> We optimized both MCTS cell seeding density and time in culture based on CellTiter-Blue viability reagent RFU's, morphology and diameter measurements, live/dead imaging, and staining for mitochondrial mass and functional activity. HNSCC MCTS cultures develop microenvironments which result in differences in proliferation rates, metabolic activity, and mitochondrial functional activity between cells located in the outer layers of the MCTS and cells in the interior. Some HNSCC MCTS cultures have necrotic cores that gradually increase as MCTS size and viability decline, while others develop necrotic cores surrounded by viable layers of cells as MCTSs achieve a critical size threshold. HNSCC MCTS cultures also exhibit drug penetration and distribution gradients that coincided with enhanced resistance to doxorubicin. Perhaps the most profound effect of culturing HNSCC cell lines in MCTS cultures was their dramatically altered and varied growth phenotypes. Some MCTS cultures displayed linear growth rates, categorized as either rapid, moderate or slow, dormant MCTSs remained viable but did not grow, and some MCTSs exhibited death phenotypes that were either progressive and slow or rapid. Only cells in the outer layers of MCTSs with rapid or moderate growth phenotypes incorporated click-it Edu reagent, indicating that the more quiescent cells in the MCTS interior were surrounded by outer layers of proliferating cells that were actively replicating DNA.<sup>114</sup> The ability of HNSCC MCTS cultures to develop microenvironments and to display a variety of different growth phenotypes provide *in vitro* models that are more closely aligned with solid tumors *in vivo*. We anticipate that the

implementation MCTS models to screen for new cancer drugs for solid tumors like HNSCC will produce leads that will translate better in *in vivo* animal models and patients. This chapter describes the use of 2D and MCTS HNSCC cultures to perform a drug screen with 19 FDA approved cancer compounds and the use of a high content imaging approaches to investigate the differential drug sensitivities observed between the two models.

## 5.2 Materials and Methods

### Reagents

Thirty-seven percent formaldehyde was purchased from Sigma-Aldrich (St. Louis, MO). Hoechst 33342 was purchased from Life Technologies (Thermo Fisher Scientific, Waltham, MA). Dimethyl sulfoxide (DMSO) 99.9% high-performance liquid chromatography grade was obtained from Alfa Aesar (Ward Hill, MA). Dulbecco's Mg<sup>2+</sup>- and Ca<sup>2+</sup>-free phosphate-buffered saline (PBS) was purchased from Gibco (Grand Island, NY). Dulbecco's modified Eagle's medium (DMEM) was purchased from Corning (Manassa, VA). Fetal bovine serum (FBS), L-glutamine, penicillin, and streptomycin (P/S) were purchased from Thermo Fisher Scientific. CellTiter-Blue<sup>®</sup> (CTB) was purchased from Promega Corporation (Madison, WI). Calcein AM (CAM), Ethidium Homodimer (EHD), were all purchased from Life Technologies (Thermo Fisher Scientific, Waltham, MA). All nineteen compounds (Chapter 5. Table 5.3) where Doxorubicin was provided by the National Cancer Institute (NCI).

## **Cells and Tissue Culture**

Five human head and neck squamous cell carcinoma (HNSCC) cell lines were provided by Dr. Jennifer Grandis of the Head and Neck Cancer (HNC) Spore at the University of Pittsburgh Medical Center Hillman Cancer Center and were maintained in a humidified incubator at 37°C, 5% CO<sub>2</sub>, and 95% humidity; Cal 33, FaDu, UM-22B, BICR56, and OSC-19. All cell lines were cultured in DMEM supplemented with 10% FBS, 1% L-glutamine, and 1% P/S. The culture medium for the FaDu and OSC-19 cell lines was also supplemented with 1% non-essential amino acids, and the medium for the BICR56 cell line was supplemented with 0.4µg/mL hydrocortisone. HNSCC cell lines were passaged or used to generate multicellular tumor spheroids (MCTSs) after isolated cell suspensions were prepared from tissue culture flasks by dissociating cells with trypsin and centrifugation at 1,200 rpm for 5 min at room temperature, and resuspension in growth media. The number of viable trypan blue excluding cells in the cell suspension was counted using a hemocytometer.

## **Generation of HNSCC Multicellular Tumor Spheroids in Ultra-low Attachment Microtiter Plates**

We have previously described the generation of MCTSs after seeding several HNSCC cell lines into 384-well U-bottomed ultra-low attachment (ULA-plates) microtiter plates (Corning, Tewksbury, MA, Cat. No 4516).<sup>64, 98, 114, 157</sup> Briefly, 384-well ULA-plates were rehydrated by the addition of 50 µL of serum free culture medium to each well and incubation in a humidified incubator for 15 minutes. Media was removed from the wells of the ULA-plates and 45µL of a single-cell suspension of the HNSCC cell lines at different seeding densities (2500 cells/well) in the appropriate growth medium were transferred into

each well using a Matrix automated multichannel pipette (Thermo Fisher Scientific, Waltham, MA), ULA-plates were centrifuged at 100 rpm for 1 minute, and then placed in an incubator at 37°C, 5% CO<sub>2</sub> and 95% humidity for the indicated time periods. In time course experiments where HNSCC MCTS cultures were maintained in the ULA-plates beyond 3 days, spent media was exchanged for fresh medium before compound addition using a Janus MDT Mini (PerkinElmer, Waltham, MA) automated liquid handler platform equipped with a 384-well transfer head. Each medium exchange cycle consisted of 2 x 20 µL aspiration and discard steps followed by 2 x 20 µL fresh media dispense steps. Three media exchange cycles were performed to achieve ~ 85% exchange of fresh medium for spent medium and a uniform volume of 45µL per well.

### **Growth Inhibition Studies in HNSCC Multicellular Tumor Spheroids Produced via Ultra-low Attachment Microtiter Plates with High Content Imaging.**

Individual drug GI / IC<sub>50</sub> values were determined in 10pt 3-fold serial dilutions, with only cisplatin as a 2-fold serial dilution all conducted in triplicate per concentration. The maximum starting concentration for each compound is displayed in Table 1. Compound addition was performed to assay plates via two daughter plates with 10 compounds per plate and 32 wells each of maximum (0.2% DMSO) and minimum (200µM Doxorubicin) signal controls. Five microliters were delivered to each well of the assay plate with the appropriate compound / control using the Janus automated Janus MDT Mini (PerkinElmer, Waltham, MA) automated liquid handler platform with specific liquid handling protocols we developed for this set of assays.

For imaging cell viability, we used an ImageXpress Micro (IXM) automated wide field high content imaging platform integrated with MetaXpress Imaging and Analysis

software (Molecular Devices LLC, Sunnyvale, CA) to acquire and analyze images of HNSCC MCTSs. The IXM optical drive uses a 300 W Xenon lamp broad spectrum white light source and a 1.4-megapixel 2/3" chip Cooled CCD Camera and optical train for standard fluorescence imaging and a transmitted light module with phase contrast. The IXM is equipped with Zero Pixel Shift (ZPS) filter sets; DAPI, FITC/ALEXA 488, CY3/TRITC, CY5, and Texas Red. A 4-position objective turret can be loaded with various objectives; a 4X Plan Apo 0.20 NA objective, a 10X Plan Fluor 0.3 NA objective, a 20X Ph1 Plan Fluor extra-long working distance (ELWD) dark medium objective, a 20X S Plan Fluor ELWD 0.45 NA objective, and a 40X S Plan Fluor ELWD 0.60 NA objective.

Single images of HNSCC MCTSs were sequentially acquired using a 4X Plan Apo 0.20 NA objective in both the transmitted light (TL) and fluorescent image acquisition modes; DAPI, FITC and TRITC.<sup>64, 98, 157, 169</sup> To acquire best focus images of MCTSs we used the IXM automated image-based focus algorithm to acquire both a coarse focus (large  $\mu\text{m}$  steps) set of images of Hoechst stained objects in the DAPI channel for the first MCTS to be imaged, followed by a fine (small  $\mu\text{m}$  steps) set of images to select the best focus image. For all subsequent wells and channels to be imaged only a fine focus set of images were acquired to select the best focus Z-plane.<sup>64, 98, 114, 157, 169</sup>

To label viable and/or dead cells within the HNSCC MCTS cultures, we incubated HNSCC MCTSs with a cocktail of the Hoechst (8 $\mu\text{g}/\text{mL}$ ) DNA stain, the Calcein AM (2.5 $\mu\text{M}$ ) live reagent, and the Ethidium Homodimer (5 $\mu\text{M}$ ) dead reagent for 1h, and single images of HNSCC MCTSs were sequentially acquired on the IXM using a 4X objective in both the TL and fluorescent image acquisition modes; DAPI, FITC and Texas Red

channels. We used the multiwavelength cell scoring (MWCS) image analysis module to analyze the HNSCC MCTS fluorescent images as described previously.<sup>64, 98, 114, 157</sup>

### **Analysis of HNSCC Multicellular Tumor Spheroid Viability and Growth using the Cell Titer Blue® Reagent.**

The homogeneous CellTiter-Blue® (CTB) cell viability reagent provides a fluorescent method for monitoring cell viability and/or growth inhibition that is based on the ability of living cells to convert the redox dye resazurin into a fluorescent end-product resorufin. HNSCC cell lines were seeded at the indicated cell densities into 384-well ULA-plates in 45µL of growth medium incubated at 37°C, 5% CO<sub>2</sub> and 95% humidity for the indicated time periods. After the prescribed time in culture 10 µL of the CTB cell viability detection reagent was dispensed into the wells of HNSCC MCTS assay plates, and incubated for 4h at 37°C, 5% CO<sub>2</sub> and 95% humidity before capturing the relative fluorescent unit (RFUs) signals (Ex. 560 nm/ EM. 590 nm) on a SpectraMax M5e (Molecular Devices, LLC, Sunnyvale, CA) micro-titer plate reader platform.

### **Data Analysis and Curve Fitting**

For HNSCC MCTS growth inhibition assays in 384-well ULA-plates, % inhibition was calculated as follows: % activity – 100, where % activity is = (experimental well – minimum control) / (Maximum control – minimum control) \*100. The GI<sub>50</sub> data were fit to a non-linear sigmoidal log (inhibitor) vs. normalized response variable slope model using the equation:  $Y=100/(1+10^{((\text{Log}I_{50}-X) *Hillslope))})$ , where y was the percent growth inhibition and x was the corresponding log<sub>10</sub> of the compound concentration. The GI<sub>50</sub> is the concentration of compound that gives a 50% response, half way between 0% and

100%. The Hillslope describes the steepness of the curve. All curve fitting, linear regression analysis, and graphs were created using the GraphPad Prism 6 software.

### MCTS Drug Impact Scoring

MCTS Drug impact was assessed by scoring several qualifiers as either 0 or 1 where 0 indicated no change compared to our DMSO control and 1 indicates a change that was greater than our set thresholds which include the ability of a drug to; induce growth inhibitory effects sufficient to generate a calculable GI<sub>50</sub> value from the CTB RLU data; the presence of a decrease in live stain, the presence of an increase in dead stain, changes in morphology, and changes in diameter. Changes in live and dead stain were only qualified as impactful if they were 2 standard deviations from our DMSO control mean live and dead stain mean fluorescent integrated intensity values.

**Table 3 CellTiter Blue Drug GI<sub>50</sub> Comparison HNSCC 2D Monolayers Vs MCTS Cultures**

Compound	MOA	Max Conc(μM)	2D Monolayer cultures								3D MCTS cultures											
			FaDu		UM-22B		Cal 33		BICR56		OSC-19		FaDu		UM-22B		Cal 33		BICR56		OSC-19	
			Mean	sd	Mean	sd	Mean	sd	Mean	sd	Mean	sd	Mean	sd	Mean	sd	Mean	sd	Mean	sd	Mean	sd
5-FU*	DNA-Syn	500	24.64	7.03	10	3.9	2.8	1.07	2.37	1.07	14.8	4.0	>500		135.4	54.1	>500		>500	0.0	>500	
Methotrexate*	DNA-Syn	20	10.6	6.3	6.2	4.4	4.7	1.0	3.3	2.1	>20		>20		>20		>20		>20		>20	
Bleomycin*	DNA-Syn	20	16.5	2.3	5.2	1.0	12.4	1.5	6.6	1.5	18.3	1.9	>20		18.1	1.2	>20		>20		>20	
Docetaxel*	MT-Stb	100	1.2	NA	1.4	NA	0.7	NA	0.8	NA	2.3	NA	20.6	NA	6.1	NA	>100	NA	3.73	NA	17.7	NA
Cisplatin*	DNA-Rep	500	11.1	3.9	8.7	2.8	6.0	0.6	6.7	1.1	17.0	3.7	99.8	40.3	52.2	29.1	88.4	8.6	80.5	20.9	114	32.2
Gefitinib	EGF-TKI	100	6.9	1.6	55.6	31.5	8.5	2.4	7.3	3.8	67.5	24.8	>100		>100		>100		>100		>100	
Erlotinib	EGF-TKI	500	>500		433	21.6	>500		>500		>500		>500		>500		>500		>500		>500	
Dasatinib	SRC-TKI	20	13.1	3.1	17.0	2.8	4.5	1.0	4.1	2.5	>20		>20		>20		>20		>20		>20	
Sunitinib	RTKI	100	5.4	1.7	5.2	1.0	11.5	2.4	5.9	2.3	8.6	2.0	21.7	3.4	14.2	0.8	12.5	2.4	15.3	8.9	19.8	5.5
Ruxolitinib	JAK-TKI	200	30.9	2.1	38.1	7.9	35.5	4.4	43.5	7.2	75.5	6.4	>200		>200		>200		111	15.1	>200	
Doxorubicin	TOPO-II	200	0.017	0.004	0.013	0.01	0.025	0.007	0.03	0.01	0.01	0.00	3.45	1.17	0.89	0.63	1.13	0.65	5.40	2.97	5.15	2.98
Etoposide	TOPO-I	100	32.6	6.0	36.2	9.1	50.2	10.7	31.5	11.6	>100		>100		>100		>100		>100		>100	
Topotecan	TOPO-I	1	>1		>1		>1		>1		>1		>1		>1		>1		>1		>1	
Dactolisib	PI3K	50	7.6	4.1	>50		1.4	0.4	>50		>50		>50		>50		>50		>50		>50	
Buparlisib	PI3K	20	>20		>20		>20		>20		>20		>20		>20		>20		>20		>20	
Romidepsin	HDAC	0.5	>0.5		>0.5		>0.5		>0.5		>0.5		>0.5		>0.5		>0.5		>0.5		>0.5	
Bortezomib	26S	0.5	0.3	0.0	0.1	0.0	0.1	0.02	0.2	0.1	0.3	0.14	>0.5		>0.5		>0.5		>0.5		>0.5	
Everolimus	mTOR	100	29.8	6.2	28.8	4.7	34.0	6.2	28.5	8.7	40.1	3.1	88.7	6.8	32.5	9.1	48.0	8.4	66.9	19.4	90.2	5.19
Ganetespib	HSP90	1	>1		>1		>1		>1		>1		>1		>1		>1		>1		>1	

Compounds are ordered by FDA approved for HNSCC as indicated with an asterisk \*, tyrosine kinase inhibitor, topoisomerase and PI3K inhibitors, and miscellaneous targeted agents. Top concentrations are represented in μM, and compound effect is presented with conditional formatting where green to yellow to red indicates low values to moderate

to high GI<sub>50</sub>. Both mean and standard deviation values are representative of at least 3 independent experiments, with docetaxel only having one available data set, as its top concentration was adjusted in the final run due to little or no observed activity in previous runs at a much lower concentration. MOA = Mechanism of action, DNA-Syn = disruptor of DNA synthesis, MT-Stb = microtubule stabilizer, DNA-Rep = inhibition or disruption of DNA repair, EGF-TKI = Epidermal growth factor tyrosine kinase inhibitor, SRC-TKI = Src tyrosine kinase inhibitor, RTKI = receptor tyrosine kinase inhibitor, JAK-TKI = Janus kinase inhibitor, TOPO-II = Topoisomerase 2 inhibitor, TOPO-I = Topoisomerase 1 inhibitor, PI3K = phosphoinositide 3-kinase inhibitor, HDAC = Histone deacetylase inhibitor, 26S = 26S proteasome inhibitor, mTOR = mammalian target of rapamycin inhibitor, HSP90 = heat-shock protein 90 inhibitor.

## **5.3 Results and Discussion**

### **5.3.1 3D and 2D Drug Screen Assay Development and Performance**

Previously, our laboratory has published on the characterization and optimization of cell culture techniques for the use of HNSCC cell lines as MCTSs for screening compounds.<sup>64, 114, 157</sup> 5 HNSCC cell lines were selected to represent 5 of the 6 distinct MCTS morphologies and growth phenotypes observed across the 11 cell lines.<sup>114</sup> These phenotypes included: rapid growth (FaDu), moderate growth (UM-22B), slow growth (Cal 33), dormant (BICR56), and slow-progressive death (OSC-19) as previously described by Kochanek *et. al* 2019.<sup>114</sup> We implemented a comparative study to determine the effectiveness of 19 FDA approved compounds, 5 of which have been approved by the FDA for the treatment of HNSCC, and compare the sensitivity of MCTS cultures to the 2D cultures more typically employed for cancer drug growth inhibition studies. Through

our assay development and optimization experiments we determined that the best seeding density was 2,500 cells/well and 500 cells/well for the 384-well 3D and 2D growth inhibition assays respectively (data not shown). After seeding HNSCC cells into 384-well ULA microtiter plates we cultured them for three days to allow MCTSs to form before performing a media exchange and adding test compounds. For 2D growth inhibition assays, cell seeding occurred 24h before compound transfer. For both 3D and 2D growth inhibition assays, plates were incubated for an additional 72h after compounds were transferred from the daughter plate (Figure 23A).

We observed the same distinct MCTS growth phenotypes and morphologies during time in culture as previously reported, and our general 3D assay workflow is depicted in Figure 23A.<sup>114</sup> In particular, after 3 days in culture, MCTS formation is visible across all cell lines, save for the UM-22B cell line, which displayed an unorganized periphery that became sharper and more nuanced after 6 days in culture. This observation was especially true in the rapid and moderate growth phenotypes as changes in size, shape, and compactness were most prominent over time (Figure 23A).<sup>114</sup> The FaDu cell line developed tight and compact spheroids with an organized outer periphery that became larger over time in culture, whereby the size-dependent development of a necrotic core was visible after 6 days in culture via dead staining (Figure 23A). As for the other cell lines, only minor differences were observed with Cal 33 forming a tight and compact spheroid with a clear, organized periphery, and BICR56 showing a slight change in spheroid shape after 6 days in culture (Figure 23A). OSC-19 became a more diffuse spheroid after time in culture which was also demonstrated in our previous studies.<sup>114</sup>

As previously reported in Kochanek *et. al* 2019, MCTS morphology, diameter, viability, and live & dead staining intensity were analyzed to examine HNSCC MCTS phenotypes (Figure 23B-D).<sup>114</sup> We observed that the FaDu cell line had the largest increase in diameter, and after the UM-22B cell line forms an organized spheroid it also increases in size over time, the Cal 33 and BICR56 cell lines demonstrated only a minor increase in size over time, and the OSC-19 cell line remained unchanged

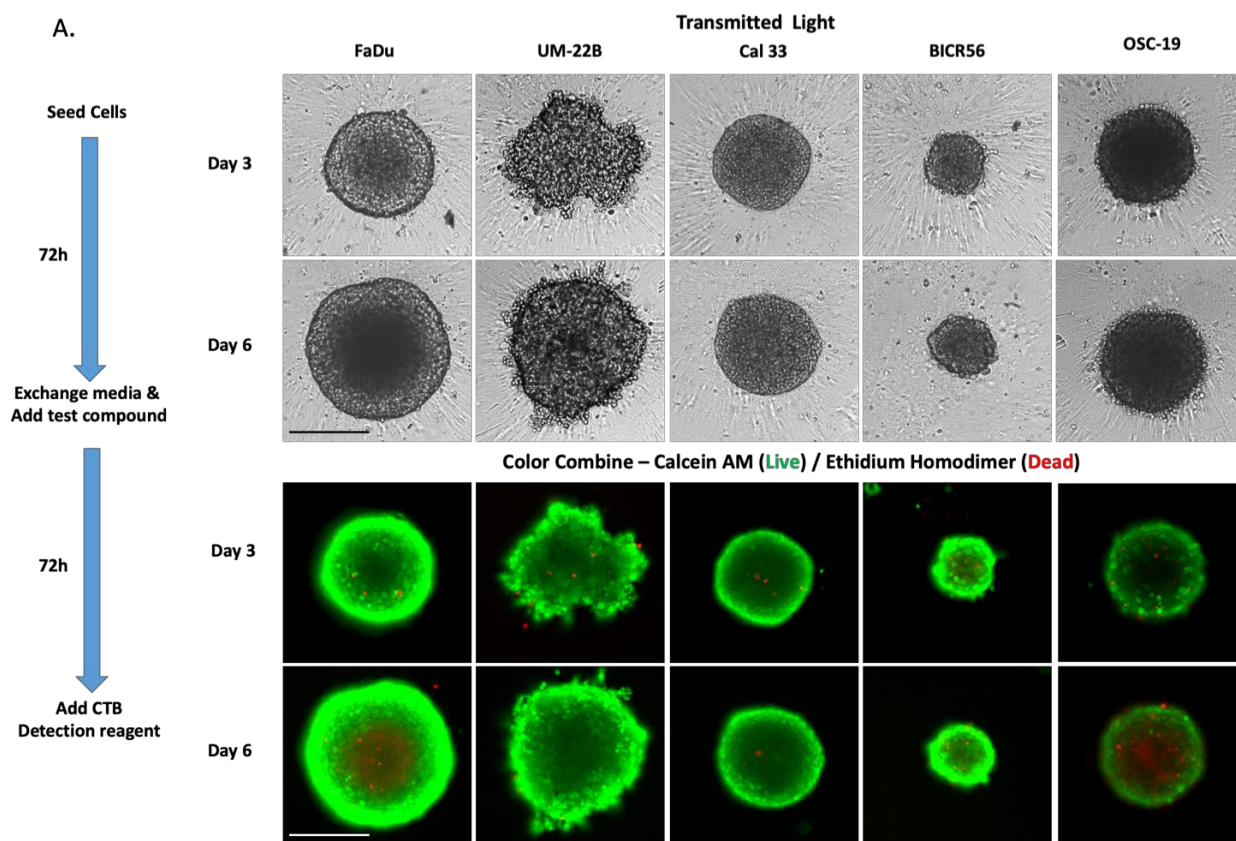
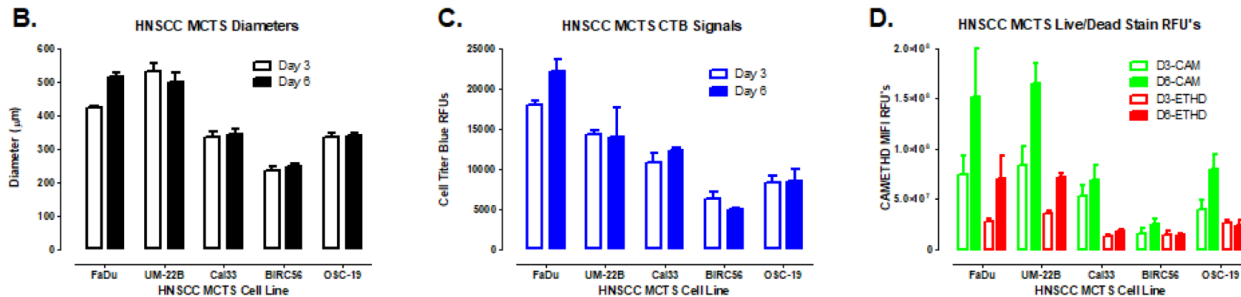


**Figure 23 Assay work flow and representative images and quantitative data of HNSCC multicellular tumor spheroids**

**(A)** Work flow schematic of growth inhibition assays within the 19-compound drug screen with representative TL and LD images on days 3 and 6, which were acquired on the IXM at 4X in the TL, FITC, and Texas Red channels. Images were represented as Greyscale TL, or color composite including both live CAM stain in green and dead ETHD stain in red

indicating the presence of either live or dead cells within the field of view.



(B), cellular viability via CTB signal (C), and changes in live and dead staining intensity (D) were graphed as a grouped plot, representative of day 3 with the unfilled bars and day 6 with the filled bars. Representative images from multiple independent experiments are presented. All scale bars represent 300 μm. All bar graphs are representative of triplicate (n=3) samples and error bars are indicative of mean ± SD.

(Figure 23B). Using CellTiter-Blue (CTB) homogenous viability reagent, we were able to observe a correlation between increase in spheroid diameter and # of viable cells as seen with the FaDu cell line and Cal 33, with the UM-22B & OSC-19 cell lines remaining unchanged and BICR56 displaying a modest decrease from day 3 to 6 (Figure 23C). Through image analysis of our MCTS's live and dead staining intensity, we were able to observe changes over time in culture in all five HNSCC MCTS cultures (Figure 23D). In DMSO control wells the relative Calcein AM live staining intensity increased in all five HNSCC MCTS cultures on day 6 compared to day 3, demonstrating that cell viability increased over the 72h compound exposure period. Under the same conditions we observed an increase in dead staining in both the FaDu and UM-22B MCTS DMSO controls, consistent with the development of a necrotic core (Figure 23D).

### 5.3.2 Drug Sensitivity in 2D and 3D HNSCC Cell Culture

We have previously shown that 2D HNSCC monolayer cultures are significantly more sensitive than the corresponding MCTS cultures to growth inhibition by ellipticine and anthracycline antibiotics including doxorubicin.<sup>64, 114</sup> We selected 19 FDA approved cancer drugs for our test set with several rationales in mind (Table 3). The first 5 compounds listed in Table 3 are specifically approved for HNSCC as indicated by an asterisk, and include several classical chemotherapeutics; gefitinib and erlotinib were selected to replicate the EGFR inhibitory effects of the monoclonal antibody cetuximab, which is also approved for HNSCC as well; dasatinib, a src family kinase inhibitor (SRC-TKI) was selected because of its ability to mediate EGFR ligand cleavage and other molecular characteristics related to HNSCC as published by Zhang *et. al* 2004; sunitinib, a multi-receptor tyrosine kinase inhibitor with an ability to target vascular endothelial growth factor receptors (VEGFRs) was also selected on the basis of published information about reported expression levels of VEGFRs in HNSCC; ruxolitinib, a Janus kinase inhibitor was selected as it is capable of modulating the JAK/STAT pathway, specifically affecting STAT 3, a signal transducer and activator of transcription (STAT) commonly associated with cell proliferation and survival; doxorubicin, was selected as part of the classical chemotherapeutics regimen consistently shown to be effective at growth inhibition in several cancers; etoposide and topotecan were both included as topoisomerase inhibitors / modulators commonly used for cancer treatment; Phosphoinositide 3-Kinase (PI3K) pathway inhibitors dactolisib and buparlisib were included in the screen given that the PI3K is frequently mutated in HNSCC; bortezomib, a 26S proteasome inhibitor was selected for its ability to induce pro-apoptotic pathways

in HNSCC; Everolimus, an mTOR inhibitor, was included given that one of the most commonly altered pathways in HNSCC is PI3K / mTOR; and lastly ganetespib, a heat-shock protein 90 inhibitor, was included as HSP90 inhibition has been shown to sensitize HNSCC to radiotherapy and chemotherapy.<sup>197-203</sup>

To measure drug-induced cytotoxicity in our 2D and 3D Cell Titer Blue (CTB) growth inhibition assays, we used 0.2% DMSO as our maximum plate controls (n=32) and 200 $\mu$ M doxorubicin as our minimum plate controls (n=32) to normalize the CTB signals from treated wells to % inhibition (Figure 24 and Table 4). Each compound was tested in 10-point, 3-fold serial dilution (2-fold for cisplatin) concentration response assays, in three to four independent experiments. We used a Janus MDT mini automated

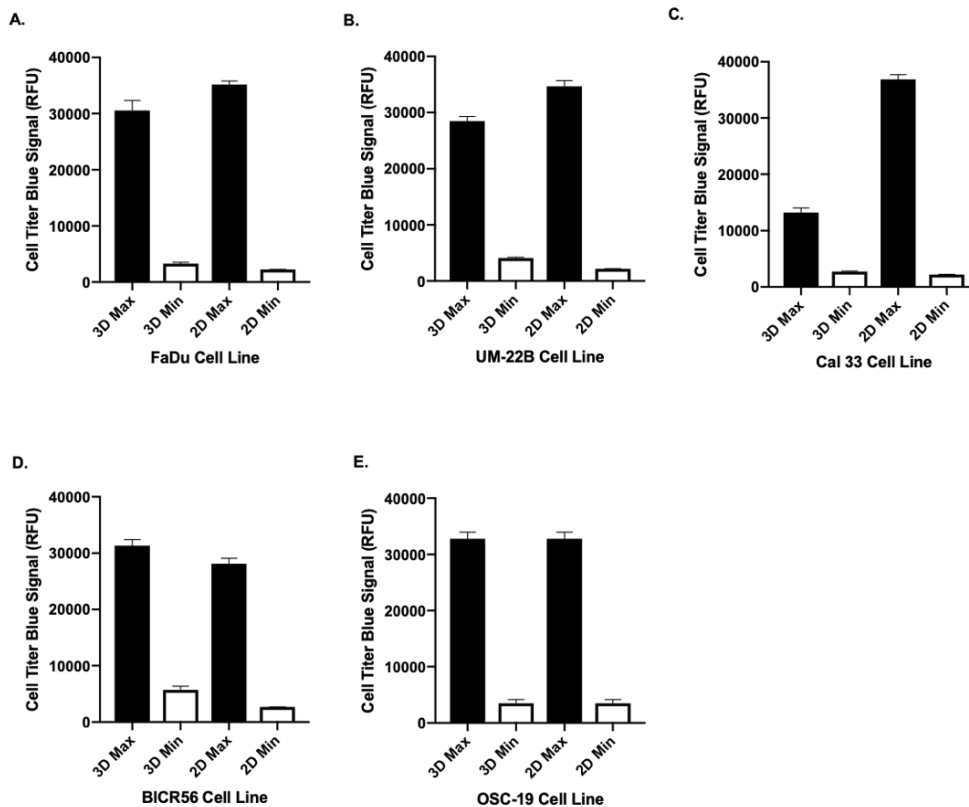


**Figure 24 QC values of maximum and minimum controls in both 3D and 2D culture conditions**

Representative graphs of the quantitative CTB viability data present between FaDu **(A)**, UM-22B **(B)**, Cal 33 **(C)**, BICR56 **(D)**, and OSC-19 **(E)** cell lines where filled bars represent the maximum control of 0.2% DMSO in both 3D and 2D cell culture, and unfilled bars represent the minimum control of 200 $\mu$  doxorubicin in both 3D and 2D cell culture as well. All bar graphs are representative of triplicate (n=3) samples and error bars are indicative of mean  $\pm$  SD.

liquid handler to generate several daughter plates from compound master plates, with 2 $\mu$ L aliquots that were diluted in 98 $\mu$ L of SFM before transfer of 5  $\mu$ L into assay plates. To determine if our 2D and MCTS growth inhibition assays were performing robustly and were compatible with HTS, we calculated both signal-to-background (S:B) ratios and Z'-factor coefficients (Table 4). The S:B ratios for the majority of cell lines was noticeably higher (~2-fold) in 2D cultures compared to the corresponding MCTS cultures, with OSC-19 having the closest 2D vs 3D S:B ratio comparison (Table 4). In addition, with Z'-factor coefficients  $\geq$  0.5 for both the 2D and MCTS CTB growth inhibition assays, the assay signal window separations were robust and reproducible enough to be classified excellent for HTS. HNSCC cell lines cultured in 2D monolayers under these conditions exhibited exponential growth rates and based on their doubling times their growth rates were ranked as, Cal33=UM22B=FaDu<BIRC56<<OSC19 (Data not shown). In marked contrast, MCTS growth rates were only linear and were ranked as FaDu<UM22B<<Cal33, with BIRC56 remaining static but viable and OSC19 declining over time in culture (Chapter 4). Compounds either effectively inhibited the growth of both 2D and MCTS cultures, were only effective against 2D monolayers, or were ineffective in both culture formats (Table 3). Of the 19 drugs tested, 14 produced calculable GI<sub>50</sub> values in 2D cultures of FaDu and Cal 33 cell lines, UM22B and BIRC56 were sensitive to 13 of

the agents, and OSC-19 only responded to 10 (Table 4). In the same cell lines grown as MCTS cultures, we observed significantly diminished growth inhibitory effects across the five cell lines with 7 out of 19 producing calculable  $GI_{50}$  values in UM-22B MCTSs, 6 in BIR56 MCTSs, 5 in FaDu and OSC-19 MCTSs, and only 4 in Cal 33 MCTSs (Table 4). Overall, only 4 compounds consistently inhibited the growth all cell lines in both 2D monolayers and 3D MCTSs; cisplatin, sunitinib, doxorubicin, and everolimus (Table 3).

**Table 4 Screening Statistics for QC Evaluation of Assay Performance**

Cell Line	Plate #	2D		3D	
		S:B	Z-Factor	S:B	Z-Factor
Cal 33	1	16.3	0.88	6.19	0.81
Cal 33	2	13.6	0.90	5.19	0.83
FaDu	1	13.8	0.93	9.97	0.71
FaDu	2	11.2	0.84	8.40	0.63
UM-22B	1	18.3	0.95	8.09	0.86
UM-22B	2	15.9	0.92	7.90	0.78
BICR56	1	17.5	0.91	7.65	0.81
BICR56	2	14.6	0.89	7.04	0.80
OSC-19	1	12.8	0.89	10.7	0.86
OSC-19	2	12.2	0.86	10.5	0.79

Representative signal-to-background (S:B) and Z-factor coefficient screening statistics which are barometers of assay performance and quality, whereby, the signal-to-background ratio represents the separation between an obtained signal from a particular assay condition or treatment vs an established baseline; and the Z-factor coefficient represents a statistical parameter that takes into account the assay signal dynamic range with any calculated values failing in this range  $1 > Z \geq 0.5$  considered an excellent assay.

In addition, we also analyzed how the drugs impacted the morphology (shape, compactness and diameter) and live/dead staining intensity as HNSCC MCTSs (Tables

5 & 6, respectively). Interestingly, while only 4-7 drugs produced calculable GI<sub>50</sub>s in the CTB MCTS growth inhibition assays (Table 3), 10-19 drugs produced changes in spheroid morphology across the HNSCC cell lines (Table 5).

### **5.3.3 Determination of Overall Drug Impact Across All Five Cell Lines**

In order to assess the global effect of each of the drugs in our 19 compound screen, we determined several qualifiers for drug impact: the ability of the drug to produce a GI<sub>50</sub> in CTB growth inhibition assays, decrease in live stain integrated intensity greater than 2 standard deviations below the DMSO control mean, increase in dead stain integrated intensity greater than 2 standard deviations above the DMSO control mean, change in morphology versus DMSO control treated MCTS, and any change in diameter versus MCTS control treated MCTS (Table 5, Table 6, Table 7 and 8, respectively). A score of either 1 or 0 was applied depending on if the drug impact requirements were met, where a score of 1 indicates that the drug had an effect / impact and a score of 0 indicates no change or an inability to produce a measurable impact. Each individual score provided insight into the ability of the drug to produce an effect in metabolic viability via CTB, physiological response by live / dead staining, and impact on cell-cell interactions and cellular organization indicated by changes in morphology and diameter, respectively. A maximum score of 5 indicates that the drug elicited a measurable effect in all categories, and score of 0 indicates that the drug had no effect on any of the categories.

**Table 5 Drug Mediated Effects on HNSCC MCTS Morphology**

		Max	FaDu MCTS: Rounded/Tight				UM-22B 3D: Irregular/Loose				Cal 33 3D: Rounded/Tight			
Compound	MOA	Conc(μM)	Shape	Compactness	Δ Diam	Δ Morph	Shape	Compactness	Δ Diam	Δ Morph	Shape	Compactness	Δ Diam	Δ Morph
5-FU*	DNA-Syn	500	Rounded	Loose	Dec	Yes	Irregular	Dispersed	Inc	Yes	Rounded	Tight	Unc	No
Methotrexate*	DNA-Syn	20	Rounded	Loose	Dec	Yes	Rounded	Tight	Dec	Yes	Rounded	Tight	Unc	No
Bleomycin*	DNA-Syn	20	Rounded	Tight	Unc	No	Irregular	Tight	Dec	Yes	Rounded	Tight	Dec	No
Docetaxel*	MT-Stb	100	Irregular	Dispersed	Inc	Yes	Irregular	Dispersed	Inc	Yes	Irregular	Dispersed	Dec	Yes
Gasplatin*	DNA-Rep	500	Rounded	Loose	Inc	Yes	Irregular	Dispersed	Inc	Yes	Irregular	Tight	Inc	Yes
Gefitinib	EGF-TKI	100	Rounded	Loose	Dec	Yes	Irregular	Dispersed	Inc	Yes	Irregular	Loose	Inc	Yes
Erlotinib	EGF-TKI	500	Rounded	Tight	Dec	No	Rounded	Loose	Dec	Yes	Rounded	Tight	Dec	No
Dasatinib	SRC-TKI	20	Irregular	Loose	Dec	Yes	Rounded	Tight	Dec	Yes	Rounded	Tight	Inc	No
Sunitinib	RTKI	100	Rounded	Loose	Dec	Yes	Irregular	Dispersed	Dec	Yes	Rounded	Tight	Unc	No
Ruxolitinib	JAK-TKI	200	Rounded	Loose	Dec	Yes	Irregular	Loose	Dec	No	Rounded	Tight	Dec	No
Doxorubicin	TOPO-I	200	Rounded	Loose	Inc	Yes	Irregular	Dispersed	Inc	Yes	Rounded	Loose	Inc	Yes
Etoposide	TOPO-I	100	Rounded	Loose	Dec	Yes	Rounded	Loose	Dec	Yes	Rounded	Tight	Dec	No
Topotecan	TOPO-I	1	Rounded	Loose	Dec	Yes	Rounded	Tight	Dec	Yes	Rounded	Tight	Inc	No
Dactolisib	PEBK	50	Rounded	Tight	Dec	No	Rounded	Tight	Dec	Yes	Rounded	Tight	Dec	No
Buparlisib	PEBK	20	Irregular	Loose	Dec	Yes	Irregular	Tight	Dec	Yes	Rounded	Tight	Dec	No
Romidepsin	HDAC	0.5	Irregular	Loose	Dec	Yes	Irregular	Loose	Dec	No	Rounded	Loose	Dec	Yes
Bortezomib	26S	0.5	Irregular	Loose	Inc	Yes	Irregular	Dispersed	Inc	Yes	Rounded	Tight	Inc	No
Everolimus	mTOR	100	Irregular	Loose	Inc	Yes	Irregular	Dispersed	Inc	Yes	Irregular	Loose	Inc	Yes
Ganetespib	HSP90	1	Rounded	Loose	Dec	Yes	Irregular	Tight	Dec	Yes	Rounded	Loose	Dec	Yes
		Max	BICR56 3D: Rounded/Tight				OSC-19 3D: Rounded/Loose							
Compound	MOA	Conc(μM)	Shape	Compactness	Δ Diam	Δ Morph	Shape	Compactness	Δ Diam	Δ Morph				
5-FU*	DNA-Syn	500	Rounded	Tight	Unc	No	Irregular	Dispersed	Dec	Yes				
Methotrexate*	DNA-Syn	20	Rounded	Tight	Dec	No	Rounded	Loose	Unc	No				
Bleomycin*	DNA-Syn	20	Rounded	Tight	Unc	No	Rounded	Loose	Dec	Yes				
Docetaxel*	MT-Stb	100	Irregular	Loose	Inc	Yes	Irregular	Dispersed	Inc	Yes				
Gasplatin*	DNA-Rep	500	Rounded	Tight	Dec	No	Irregular	Loose	Inc	Yes				
Gefitinib	EGF-TKI	100	Rounded	Tight	Unc	No	Irregular	Loose	Dec	Yes				
Erlotinib	EGF-TKI	500	Rounded	Tight	Unc	No	Irregular	Loose	Dec	Yes				
Dasatinib	SRC-TKI	20	Rounded	Loose	Unc	Yes	Irregular	Loose	Inc	Yes				
Sunitinib	RTKI	100	Rounded	Tight	Dec	No	Irregular	Loose	Inc	Yes				
Ruxolitinib	JAK-TKI	200	Irregular	Loose	Inc	Yes	Irregular	Loose	Inc	Yes				
Doxorubicin	TOPO-I	200	Irregular	Loose	Unc	Yes	Irregular	Loose*	Inc	Yes				
Etoposide	TOPO-I	100	Rounded	Tight	Unc	No	Rounded	Loose	Dec	No				
Topotecan	TOPO-I	1	Rounded	Tight	Unc	No	Rounded	Loose	Unc	No				
Dactolisib	PEBK	50	Rounded	Loose	Dec	Yes	Rounded	Loose	Dec	No				
Buparlisib	PEBK	20	Irregular	Loose	Dec	Yes	Irregular	Loose	Inc	Yes				
Romidepsin	HDAC	0.5	Irregular	Loose	Inc	Yes	Irregular	Loose	Inc	Yes				
Bortezomib	26S	0.5	Rounded	Tight	Dec	No	Irregular	Dispersed	Inc	Yes				
Everolimus	mTOR	100	Irregular*	Tight*	Unc	Yes	Irregular	Dispersed	Inc	Yes				
Ganetespib	HSP90	1	Irregular	Dispersed	Inc	Yes	Irregular	Loose	Inc	No				

Described effects of drug impact of all 19 compounds included in our screen against the morphology and size of the 5 HNSCC cell lines as MCTSs. The DMSO control treated shape and compactness of MCTSs are included in bold below the Shape and Compactness columns, with the preceding drug effects listed in the same row as the signified compound at the Max concentration. Any changes in morphology were conditionally formatted in green for “yes a change was present”, orange for “no a change was not present”, and if both morphology and size were unchanged the two fields were highlighted in red. We described two distinct spheroid morphologies present, either

rounded, if we observed an organized circular structure in contrast to irregular, whereby the outer periphery was considered unorganized and without a clear shape; compaction was categorized as tight, loose, or dispersed, whereby tight represents a very compact spheroid, loose represents a mildly compact spheroid, and dispersed represents little or no compaction present. Drugs with an asterisk beside them represent FDA approved compounds for HNSCC.  $\Delta$  Diam and  $\Delta$  Morph columns represent change in either diameter or morphology.

**Table 6 Drug Mediated Effects on HNSCC MCTS Live/Dead Staining**

Compound	MOA	Max Conc( $\mu$ M)	Live Calcein AM Fold Change vs DMSO Control					Dead ETHD Fold Change vs DMSO Control				
			FaDu	UM2-22B	Cal33	BIRC56	OSC-19	FaDu	UM2-22B	Cal33	BIRC56	OSC-19
5-FU*	DNA-Syn	500	-4.7	-1.3	-1.2	-1.3	-1.0	-2.1	1.5	4.0	1.1	3.6
Methotrexate*	DNA-Syn	20	-3.8	-2.3	-1.0	-1.7	-1.3	1.2	-1.0	1.4	-1.6	1.0
Bleomycin*	DNA-Syn	20	-2.9	-2.9	-1.1	-1.1	-2.0	-1.8	1.3	-1.0	-1.1	1.2
Docetaxel*	MT-Stb	100	-2.1	-1.6	-1.0	-1.4	-1.3	3.2	5.7	3.6	3.0	3.3
Cisplatin*	DNA-Rep	500	-2.0	-1.3	-1.1	-1.8	-1.1	4.1	6.4	4.7	2.7	4.9
Gefitinib	EGF-TKI	100	-3.7	-2.5	-1.5	-2.1	-2.3	2.0	4.1	1.8	2.5	2.3
Erlotinib	EGF-TKI	500	-2.1	-1.7	-1.2	1.3	-1.1	-1.3	3.7	2.5	-1.1	1.1
Dasatinib	SRC-TKI	20	-1.7	-2.6	-1.0	-1.3	-1.2	2.2	-1.3	1.7	1.5	2.0
Sunitinib	RTKI	100	-8.7	-4.6	-3.4	-3.0	-1.6	2.0	2.8	1.3	1.6	1.7
Ruxolitinib	JAK-TKI	200	-2.1	-1.9	1.1	-1.5	-1.2	2.7	3.7	5.6	1.8	1.6
Doxorubicin	TOPO-I	200	NACI	NACI	NACI	NACI	NACI	NACI	NACI	NACI	NACI	NACI
Etoposide	TOPO-I	100	-5.0	-3.7	1.2	-1.4	-1.3	1.2	1.3	3.1	-1.2	1.6
Topotecan	TOPO-I	1	-4.2	-1.5	1.3	1.1	-1.3	1.4	2.3	2.2	-1.1	1.1
Dactolisib	PI3K	50	-1.9	-2.1	-1.2	-1.2	-1.2	-1.4	-2.1	1.5	1.6	1.0
Buparlisib	PI3K	20	-1.5	-1.6	1.1	1.0	-1.0	2.5	1.8	4.0	2.0	1.6
Romidepsin	HDAC	0.5	-1.7	-1.2	1.0	-1.3	1.1	2.7	3.2	3.1	2.2	2.5
Bortezomib	26S	0.5	1.0	-1.2	1.5	-1.2	1.0	4.6	4.9	6.9	1.3	2.3
Everolimus	mTOR	100	-2.9	1.3	1.9	-2.0	-2.5	3.5	10.4	6.7	4.0	2.7
Ganetespib	HSP90	1	-1.7	-1.5	1.5	-1.1	1.1	1.9	-1.0	5.9	1.4	2.7

Calculated fold changes in live / dead staining intensity vs DMSO control treated HNSCC spheroids across all five cell lines. Both fold change in live and dead stain were conditionally formatted so that values with a decrease in fold-change were cooler greens and values that displayed an increase in fold-change were warmer reds, respectively. MOA stands for mechanism of action. NACI indicates that these set of values was not able to be calculated by our conventional image analysis algorithm and had to be manually analyzed. Drugs with an asterisk beside them represent FDA approved compounds for HNSCC.

**Table 7 Ranked Scores of Drug Impact on HNSCC MCTS By Compound**

Drugs	Total Score	Cell Line Individual Impact Score				
		FaDu	UM-22B	Cal33	BICR56	OSC-19
Doxorubicin	25	5	5	5	5	5
Everolimus	22	5	4	4	4	5
Docetaxel*	20	4	5	3	4	4
Sunitinib	19	4	5	3	4	3
Cisplatin*	18	4	4	4	3	4
Gefitinib	17	4	4	3	2	4
Buparlisib	14	3	4	2	2	3
Romidepsin	14	3	2	3	3	3
Ganetespib	14	3	3	3	3	2
Dasatinib	13	3	3	2	2	3
Ruxolitinib	13	3	3	2	2	3
Bortezomib	12	3	3	2	1	3
Topotecan	11	3	4	2	1	1
5-FU*	10	3	3	1	0	3
Etoposide	10	3	4	2	0	1
Dactolisib	10	1	3	2	3	1
Bleomycin*	10	1	5	1	0	3
Erlotinib	9	1	4	2	0	2
Methotrexate*	8	3	3	1	1	0

Ranked scores of drug impact using our qualifiers: the ability of the drug to produce a GI<sub>50</sub> value through CTB fluorescence detection, decrease in live stain integrated intensity greater than 2 standard deviations of the DMSO control mean, increase in dead stain integrated intensity greater than 2 standard deviations of the DMSO control mean, change in morphology versus DMSO control treated MCTS, and any change in diameter versus MCTS control treated MCTS. Drugs were scored on an individual cell line basis and the cumulative score is displayed and ranked out of 25 across all 19 compounds. Drugs with an asterisk beside them represent FDA approved compounds for HNSCC.

**Table 8 Representative Example of Drug Impact Scoring in UM-22B Cell Line**

Cell Line	Drug	GI50 Produced	Dec Live Stain	Inc Dead Stain	Morphology	Diameter	Drug Impact Score
UM-22B	Bleomycin*	1	1	1	1	1	5
UM-22B	Docetaxel*	1	1	1	1	1	5
UM-22B	Sunitinib	1	1	1	1	1	5
UM-22B	<b>Doxorubicin</b>	1	1	1	1	1	5
UM-22B	Cisplatin*	1	0	1	1	1	4
UM-22B	Gefitinib	0	1	1	1	1	4
UM-22B	Erlotinib	0	1	1	1	1	4
UM-22B	Etoposide	0	1	1	1	1	4
UM-22B	Topotecan	0	1	1	1	1	4
UM-22B	Buparlisib	0	1	1	1	1	4
UM-22B	Everolimus	1	0	1	1	1	4
UM-22B	5-FU*	1	0	1	0	1	3
UM-22B	Methotrexate*	0	1	0	1	1	3
UM-22B	Dasatinib	0	1	0	1	1	3
UM-22B	Ruxolitinib	0	1	1	0	1	3
UM-22B	Dactolisib	0	1	0	1	1	3
UM-22B	Bortezomib	0	0	1	1	1	3
UM-22B	Ganetespib	0	1	0	1	1	3
UM-22B	Romidepsin	0	0	1	0	1	2

Representative drug impact scoring in the UM-22B cell line, ranked by highest drug impact score to lowest drug impact score. Scores were based on the ability of the drug to produce a GI<sub>50</sub> value through CTB fluorescence detection, decrease in live stain integrated intensity greater than 2 standard deviations of the DMSO control mean, increase in dead stain integrated intensity greater than 2 standard deviations of the DMSO control mean, change in morphology versus DMSO control treated MCTS, and any change in diameter versus MCTS control treated MCTS. Drugs with an asterisk beside them represent FDA approved compounds for HNSCC.

### 5.3.4 FDA Approved Drugs for Head and Neck Cancer

All 5 of the drugs approved by the FDA for HNSCC therapy produced GI<sub>50</sub>s in 2D monolayer growth inhibition assays in all five cell lines, with only cisplatin and docetaxel also producing GI<sub>50</sub>s in MCTSs across all cell lines (Table 3, Figures 25B-H and 26B-H). Of note, MCTSs generated with the UM-22B cell line were sensitive to growth inhibition

by 4 of the 5 FDA approved drugs, with only methotrexate failing to achieve > 50% growth inhibition (Table 3).

### 5.3.5 HNSCC Sensitivity to Cisplatin

Cisplatin is approved by the FDA for HNSCC therapy and represents a classical chemotherapeutic agent that binds to purine bases within the DNA strand and creates adducts which eventually leads to DNA strand breaks and cell death.<sup>95</sup> Figure 25A compares the effects of 72h exposure to 500  $\mu$ M cisplatin to DMSO vehicle on HNSCC MCTS morphology and cell viability in transmitted light (TL) images and fluorescence images of Hoechst stained nuclei (DAPI channel) and cells stained with the live (CAM, FITC channel) and dead (ETHD, Texas Red channel) reagents. Figure 25B to 25F compares the concentration dependent inhibition of 2D monolayer and MCTS HNSCC growth determined in CTB growth inhibition assays. Figure 24G and 24H compare the effects of 72h exposure to 500  $\mu$ M cisplatin to DMSO vehicle on HNSCC MCTS diameters and the mean integrated intensities of the live/dead staining respectively.

The TL images indicated that the morphologies of 4 out of the 5 HNSCC MCTSs were dramatically altered after 72h exposure to 500  $\mu$ M cisplatin (Figure 25A, Table 3). In particular the FaDu, UM-22B, and OSC-19 cell lines, which formed tight compact spheroids with defined edges in DMSO control wells, exposure to cisplatin resulted in diffuse, cloudy structures lacking the cell-cell interactions that maintain MCTS structural integrity and architecture. (Figure 25A and Table 5). The UM-22B cell line was particularly affected morphologically with a spheroid structure that was blown out forming a cloudy and dispersed aggregate (Figure 25A). Except for the BICR56 cell line, images of the

MCTS Hoechst staining indicated that exposure to cisplatin substantially reduced the staining intensity or altered the staining pattern (FaDu). This was also true for the HNSCC MCTS live cell staining, where cisplatin exposure obliterated CAM staining except in BICR56 MCTSs. In contrast, cisplatin treatment increased the levels of ETHD dead staining in all five of the HNSCC MCTS cultures.

Cisplatin exposure effectively inhibited the growth of 2D monolayer and MCTS cultures of the five HNSCC cell lines in a concentration dependent manner (Figure 25B-25F). In the 2D CTB growth inhibition assays, cisplatin exhibited average  $GI_{50}$ s of 11.1, 7.1, 6.0, 6.7, and 17.0  $\mu$ M in the FaDu, UM22B, Cal33, BICR56 and OSC19 HNSCC cell lines respectively. In the MCTS CTB growth inhibition assays, cisplatin exhibited average  $GI_{50}$ s of 99.8, 52.2, 88.4, 80.5, and 114  $\mu$ M in the FaDu, UM-22B, Cal33, BICR56 and OSC-19 HNSCC cell lines respectively. The apparent reduction in sensitivity

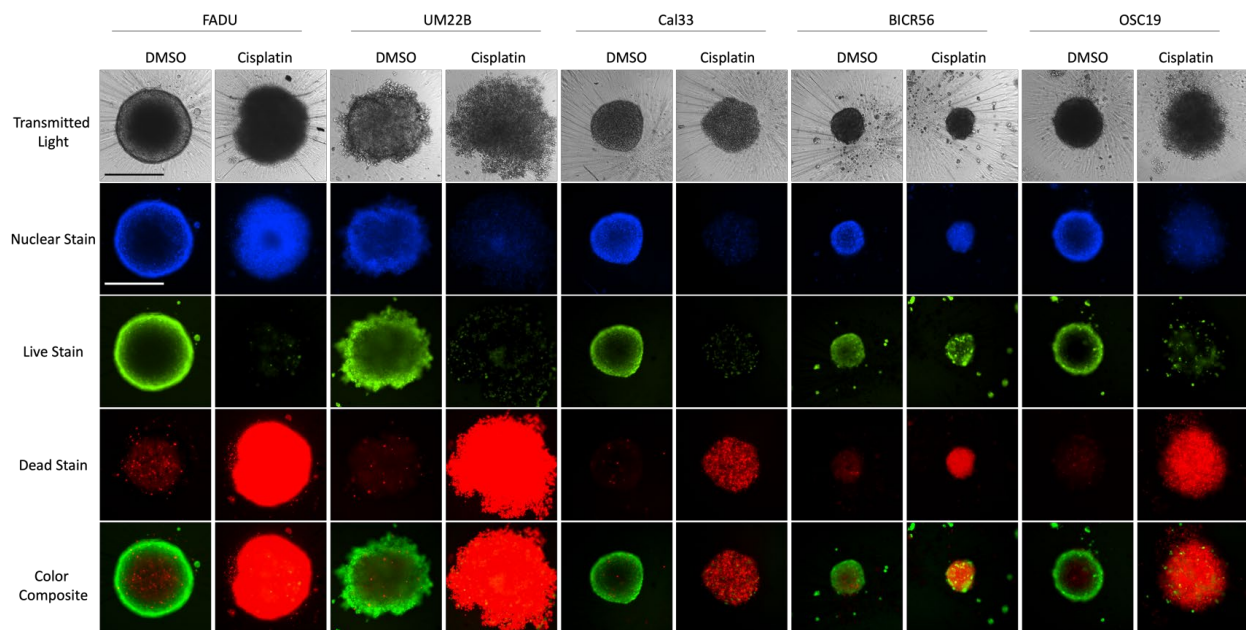
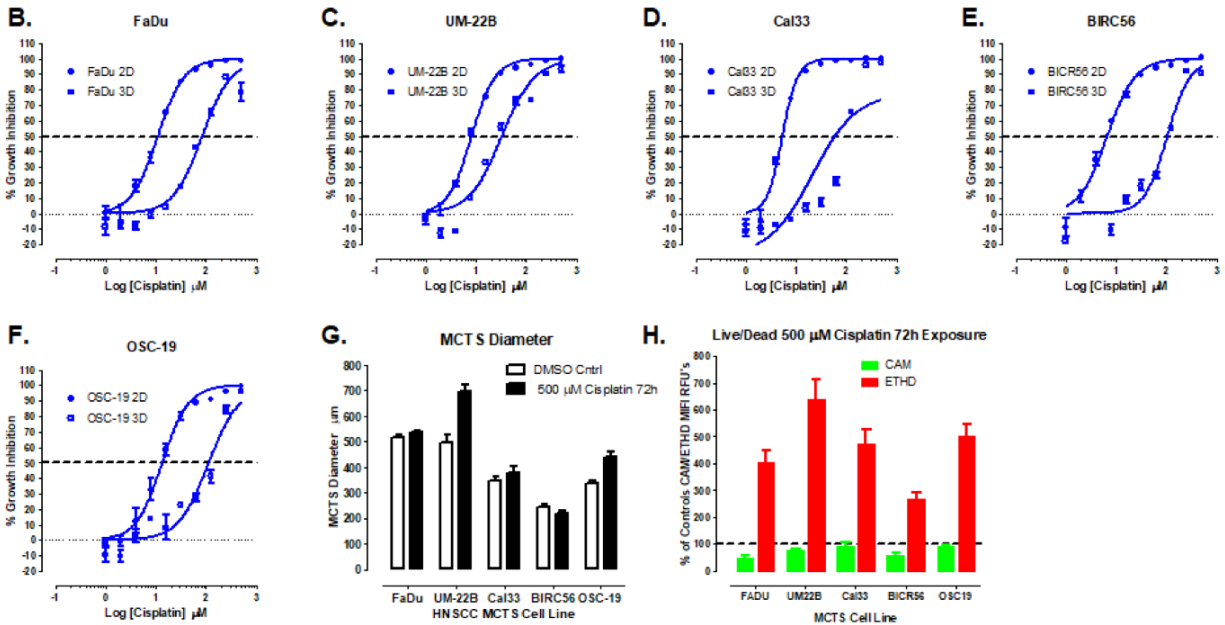


**Figure 25 Cisplatin sensitivity in HNSCC 3D multicellular tumor spheroids and 2D cell culture conditions**

**(A)** Representative images of 5 HNSCC cell lines seeded at 2,500 cells / well after 3 days of cisplatin treatment and 6 total days in culture, acquired at 4X on the IXM with the TL, DAPI, FITC, and Texas Red channels. Greyscale TL images are presented along with, Hoechst nuclear stain in blue, and color composite fluorescent images of live cell CAM and dead cell EHD staining depicted as green and red, respectively. All scale bars represent 300  $\mu\text{m}$ .



Corresponding CTB viability measurements displayed as % growth inhibition were graphed as XY plots with symbols (●) and (■) representative of 2D and 3D culture conditions, respectively, across FaDu (**B**), UM-22B (**C**), Cal 33 (**D**), BICR56 (**E**), and OSC-19 (**F**) cell lines. (**G**) The line-scan tool of the MetaXpress image analysis software was used to measure the diameters and values were plotted in a bar graph where unfilled bars represent the DMSO control, and filled bars represent cisplatin treatment at its top concentration after 72hrs. (**H**) Live and dead staining intensity across all five HNSCC MCTSs after 5'FU treatment were obtained using the MetaXpress image analysis software, plotted as % of control live and dead staining intensity, with live stain represented as green filled bars and dead stain represented as red filled bars. Representative images from multiple independent experiments are presented. Data is representative of multiple independent experiments, and at least triplicate (n=3) well

measurements. All bar graphs are representative of triplicate (n=3) samples and error bars are indicative of mean  $\pm$  SD.

(rightward shift in  $GI_{50}$ s) between MCTS cultures and 2D monolayers was 9-fold in FaDu, 6-fold in UM-22B, 14.7-fold in Cal 33, 12-fold in BICR56, and 6.7-fold in OSC-19 (Figure 25B-F). Consistent with the morphological effects of cisplatin exposure observed in the TL images, MCTSs formed by 4 of the five HNSCC cell lines displayed an increase in diameter, with only BICR56 MCTSs exhibiting a minor decrease in diameter (Figure 25G). Similarly, quantifying the mean integrated intensities of the live and dead stains in MCTSs was also consistent with their respective images, with all five cell lines exhibiting cisplatin-induced decreased CAM staining relative to DMSO controls and corresponding increases in ETHD staining (Figure 25H and Table 6). In terms of a drug impact score against HNSCC MCTS's, cisplatin scored 4/5 against four of the cell lines, but only 3/4 in BIRC56 MCTSs, for an overall impact score of 18/25 making it the fifth most effective drug against HNSCC MCTSs in our test set (Table 7).

### **5.3.6 HNSCC Sensitivity to Docetaxel**

Docetaxel is approved by the FDA for HNSCC therapy and represents one of the most commonly used chemotherapeutics for the treatment of cancer, it is capable of disrupting mitosis in the cell cycle via inhibition of microtubular depolymerization which ultimately leads to apoptosis as the primary mechanisms of cell death.<sup>95</sup> Figure 26 summarizes the results from a similar multi-parameter comparison and analysis of the effects of docetaxel treatment of 2D monolayer and MCTS HNSCC cultures as described

for Figure 25. We observed effects on MCTSs' morphology with docetaxel similarly to cisplatin, whereby, spheroids that traditionally resembled compact and tight spheroids became diffuse and cloudy cellular aggregates after 72hr exposure to 100 $\mu$ M docetaxel. (Figure 26A and Table 5). Furthermore, docetaxel was capable of more severely distorting the spheroid morphology as 4 of the 5 cell lines became cellular aggregates after compound exposure, but all 5 were classified as having a change in morphology vs DMSO control, with only the BICR56 cell line displaying an irregular spheroid morphology rather than complete disruption (Figure 26A and Table 5).

CAM live stain was severely diminished after docetaxel exposure across all cell lines vs DMSO control, with FaDU, UM-22B, and OSC-19 cell lines being impacted the greatest with little or no remaining stained cells (Figure 26A). In contrast, small viable aggregates of cells were visible in Cal33 and BICR56 that still maintained CAM stain, and Hoechst nuclei staining outlined these structures (Figure 26A). ETHD staining was visibly increased across all 5 cell lines, with UM-22B demonstrating the largest change vs DMSO control, followed by Cal 33, and similar changes in FaDu, BICR56, and OSC-19 respectively, which was also corroborated by image analysis and quantification of the mean integrated intensity (Figure 26A and H). Given that the FaDu cell line has been characterized to develop a necrotic core as indicated in Chapter 4, we observed this in its DMSO control vs docetaxel treatment, which is why the change is not as dramatic as observed in the LD images (Figure 26A and H).

In both 2D monolayers and MCTSs we observed that docetaxel was capable of producing a measurable growth inhibitory effect across all cell lines in 2D but only 4 out of the 5 cell lines in 3D, with GI<sub>50</sub> values in 2D of 1.2, 1.4, 0.7, 0.8, and 2.3 $\mu$ M

corresponding with the FaDu, UM-22B, Cal 33, BICR56, and OSC-19 cell lines, respectfully (Figure 26B-F). In comparison to 2D monolayer culture  $GI_{50}$  values in 3D were shifted right, indicating less sensitivity with values of 20.1, 6.1, N/A, 3.73, and 17.7 $\mu$ M in the FaDu, UM-22B, Cal 33, BICR56, and OSC-19 cell lines, respectfully, as 3D which were 17.2-fold less sensitive in FaDu, 4.36-fold less sensitive in UM-22B, no effect in Cal 33 3D, 4.66-fold less sensitive in BICR56, and 7.70-fold less sensitive in OSC-19 (Figure 26B-F and Table 3). These results indicate that of the MCTSs capable of a measurable  $GI_{50}$ , FaDu are the least sensitive to docetaxel. Cal 33 consistently produced no measurable growth inhibitory affects with CTB, despite clear morphological changes and a prominent increase in cell death staining (Figure 26A-F). This incidence highlighted one of the limitations we experienced with CTB, whereby, despite measurable response with our imaging and image analysis, no detectable change in viability via CTB could be determined.

We observed an increase in diameter vs DMSO control treated spheroids in 4 of the 5 spheroids, similarly to cisplatin treatment, and as mentioned before, this increase is associated with the destruction of the spheroid structure and breakdown of cell-cell interactions (Figure 26A and G). The increase in diameter was most distinct in the OSC-19, UM-22B, and FaDu as seen in by the TL imaging and diameter measurements, but not as clear in the BICR56 which only displayed modest morphological changes (Figure 26A and G). Through analysis of the mean integrated intensity of both CAM we observed that all cell lines registered a decrease in live stain and FaDu, UM-22B, and OSC-19 cell lines were the most prominent (Figure 26H). Analysis of ETHD integrated intensity

illustrated that all 5 cell lines were severely impacted by docetaxel producing greatly increased dead stain beyond what was present in any of the DMSO control treated wells

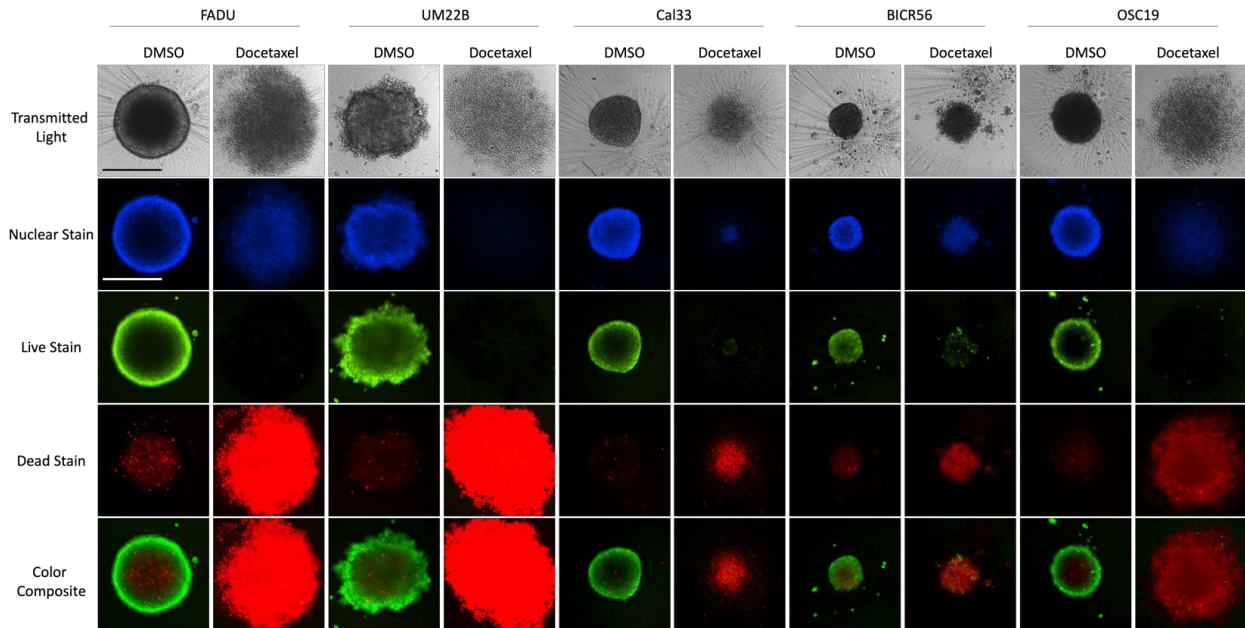
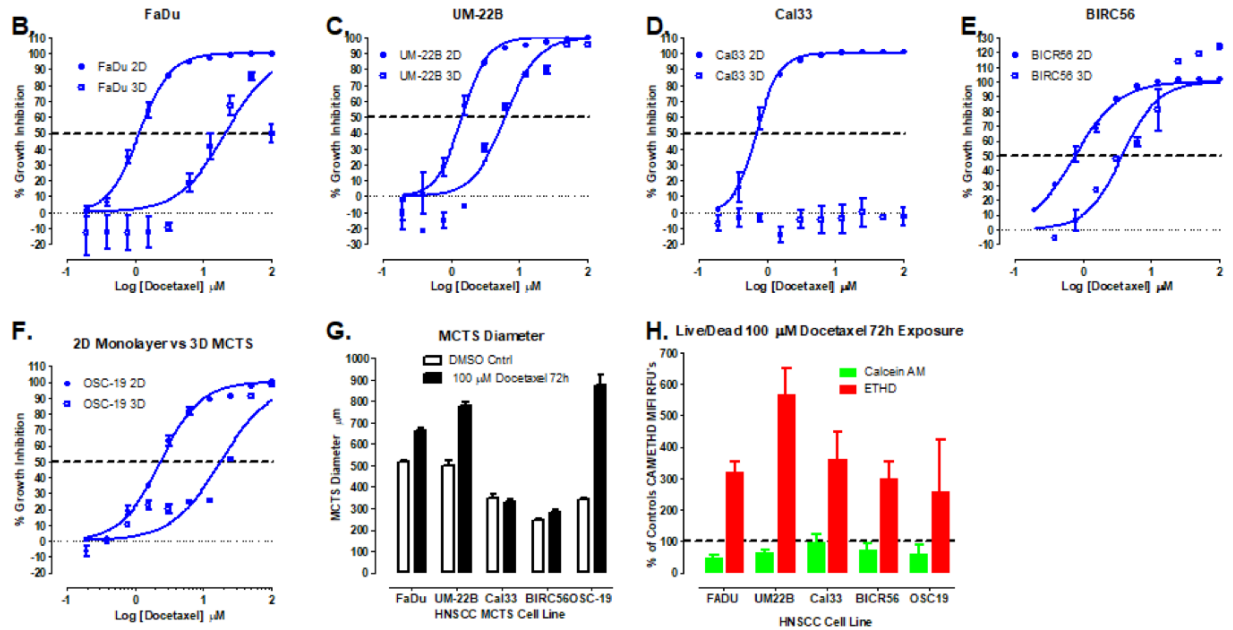


**Figure 26 Docetaxel sensitivity in HNSCC 3D multicellular tumor spheroids and 2D cell culture conditions**

**(A)** Representative images of 5 HNSCC cell lines seeded at 2,500 cells / well after 3 days of docetaxel treatment and 6 total days in culture, acquired at 4X on the IXM with the TL, DAPI, FITC, and Texas Red channels. Greyscale TL images are presented along with, Hoechst nuclear stain in blue, and color composite fluorescent images of live cell CAM and dead cell EHD staining depicted as green and red, respectively.



Corresponding CTB viability measurements displayed as % growth inhibition were graphed as XY plots with symbols (●) and (■) representative of 2D and 3D culture conditions, respectively, across FaDu (B), UM-22B (C), Cal 33 (D), BICR56 (E), and OSC-19 (F) cell lines. (G) The line-scan tool of the MetaXpress image analysis software was used to measure the diameters and values were plotted in a bar graph where unfilled bars represent the DMSO control, and filled bars represent docetaxel treatment at its top concentration after 72hrs. (H) Live and dead staining intensity across all five HNSCC MCTSs after docetaxel treatment were obtained using the MetaXpress image analysis software, plotted as % of control live and dead staining intensity, with live stain represented as green filled bars and dead stain represented as red filled bars. Representative images from multiple independent experiments are presented. All scale bars represent 300  $\mu\text{m}$ . Data is representative of multiple independent experiments, and at least triplicate (n=3) well measurements. All bar graphs are representative of triplicate (n=3) samples and error bars are indicative of mean  $\pm$  SD.

(Figure 26H). In terms of MCTS drug impact, docetaxel was scored as 5/5 in UM-22B 4/5 in FaDu, BICR56, OSC-19, and 3/5 in Cal 33 (Table 7). These results indicate that despite

not producing a GI<sub>50</sub> in Cal 33 MCTSs, docetaxel still ranks as the third most effective compound against HNSCC MCTSs with a drug impact score of 20/25.

### **5.3.7 HNSCC Sensitivity to Methotrexate**

Methotrexate represents an approved drug for HNSCC, and a classic antifolate compound that functions by competitively inhibiting dihydrofolate reductase, an essential enzyme in the folate metabolism pathway, and by extension limiting DNA and RNA synthesis.<sup>95</sup> Through TL imaging we observed that methotrexate exposure for 72hr at 20 $\mu$ M was incapable of disrupting spheroid morphology in the same way that either cisplatin or docetaxel did (Figure 27A). Instead, we observed that the size and morphology of the FaDu and UM-22B cell lines became truncated in comparison to their DMSO treated control spheroids (Figure 27A and Table 5). For FaDu, spheroid morphology and diameter were altered from tight and round, to a loose, rounded spheroid with less well-defined edges (Figure 27A). For UM-22B, exposure to methotrexate actually caused the spheroid to become more compact and organized than its traditionally unorganized cellular periphery (Figure 27A). No observable changes were present in the Cal 33 or BICR56 cell lines, with the OSC-19 demonstrating only a change in its periphery, from organized and defined edges of the spheroid periphery to disorganized with diffuse aggregates of cells surrounding the periphery (Figure 27A). CAM staining in all of the cell lines showed a noticeable decrease in intensity, which was most prominent in both the FaDu and UM-22B cell lines (Figure 27A). ETHD staining showed an increase in cell death across 4 out of the 5 cell lines, with FaDu, and OSC-19 displaying the highest

increases in staining, and no visible change was observed in the BICR56 cell line (Figure 27A).

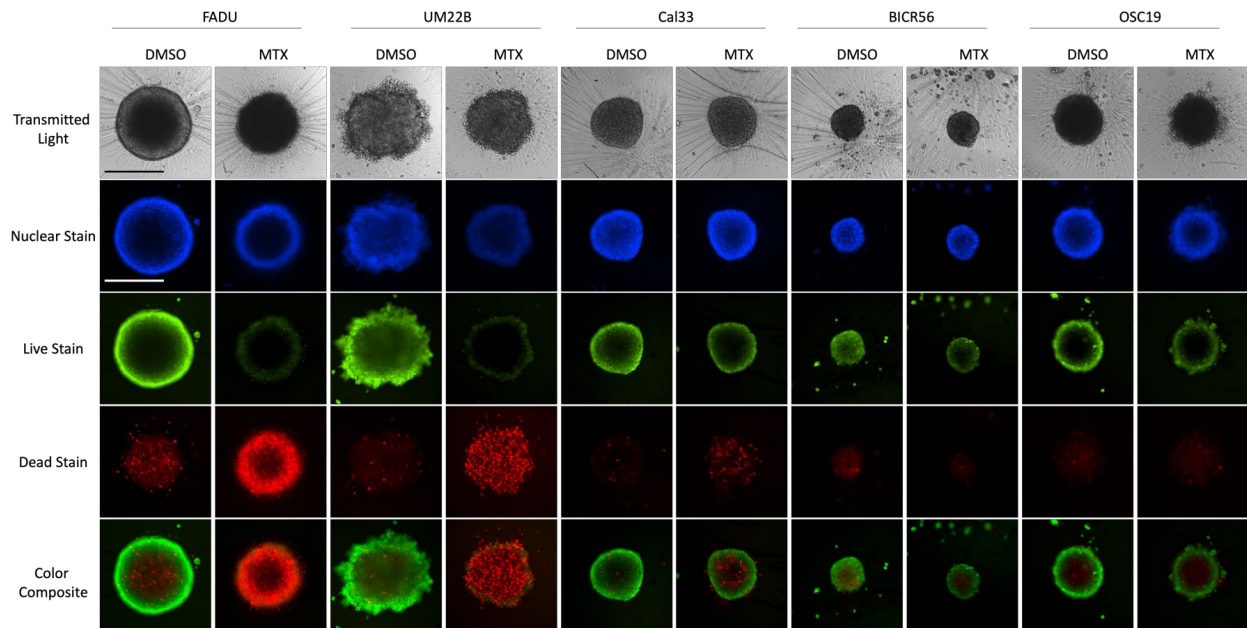
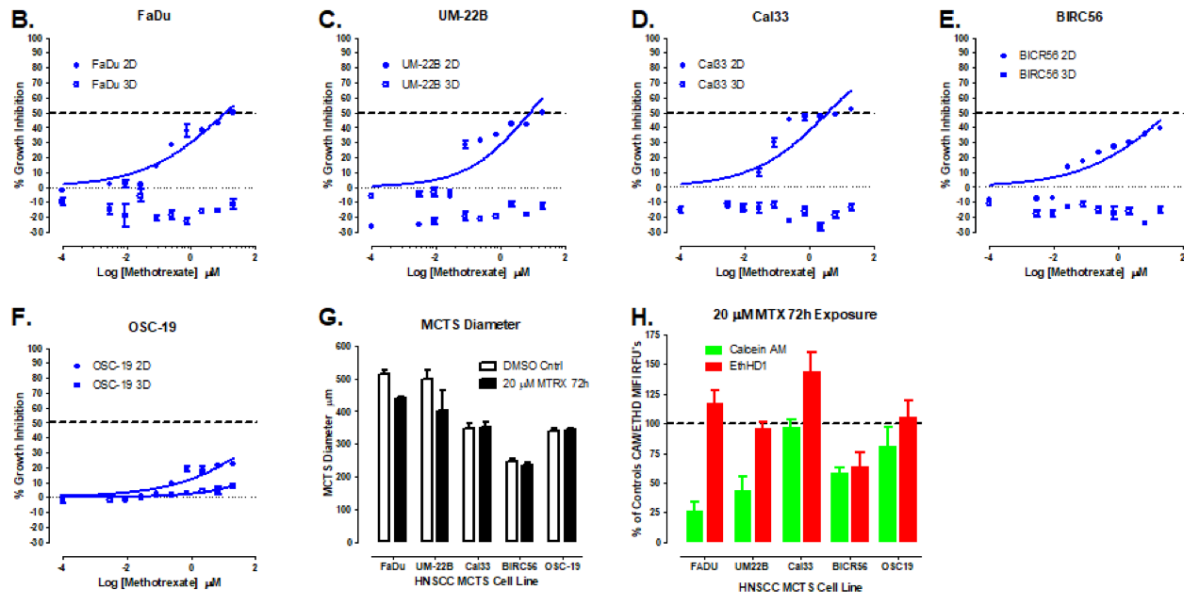


**Figure 27 Methotrexate sensitivity in HNSCC 3D multicellular tumor spheroids and 2D cell culture conditions**

**A)** Representative images of 5 HNSCC cell lines seeded at 2,500 cells / well after 3 days of methotrexate treatment and 6 total days in culture, acquired at 4X on the IXM with the TL, DAPI, FITC, and Texas Red channels. Greyscale TL images are presented along with, Hoechst nuclear stain in blue, and color composite fluorescent images of live cell CAM and dead cell EHD staining depicted as green and red, respectively.



Corresponding CTB viability measurements displayed as % growth inhibition were graphed as XY plots with symbols (●) and (■) representative of 2D and 3D culture conditions, respectively, across FaDU (B), UM-22B (C), Cal 33 (D), BICR56 (E), and OSC-19 (F) cell lines. (G) The line-scan tool of the MetaXpress image analysis software was used to measure the diameters and values were plotted in a bar graph where unfilled bars represent the DMSO control, and filled bars represent methotrexate treatment at its top concentration after 72hrs. (H) Live and dead staining intensity across all five HNSCC MCTSs after methotrexate treatment were obtained using the MetaXpress image analysis software, plotted as % of control live and dead staining intensity, with live stain represented as green filled bars and dead stain represented as red filled bars. Representative images from multiple independent experiments are presented. All scale bars represent 300  $\mu\text{m}$ . Data is representative of multiple independent experiments, and at least triplicate (n=3) well measurements. All bar graphs are representative of triplicate (n=3) samples and error bars are indicative of mean  $\pm$  SD.

In 2D monolayers methotrexate was capable of growth inhibitory effects in all 5 cell lines, but not capable of producing growth inhibition beyond ~55% in any of the cell lines (Figure 27B-F). In contrast, methotrexate was incapable of producing an impactful

growth inhibitory response in 3D, as no calculable  $GI_{50}$  values were present (Figure 27B-F). Despite the lack of inhibition of CTB signal, we did observe that methotrexate was able to measurably decrease the diameter of both the FaDu and UM-22B cell lines, but not in any of the other 3 (Figure 5.27G). As corroborated by our LD images, image analysis of the mean integrated intensity of our live stain indicated a decrease in all of the 5 cell lines, with both FaDu, UM-22B, and BICR56 being most impacted, and only a minor decrease in both Cal 33 and OSC-19. In contrast, increase in ETHD staining was highest in the Cal 33 cell line, followed by FaDu, OSC-19, and UM-22B respectfully (Figure 27H). Of note, there was a decrease in dead stain in the BICR56 cell line and the LD images indicate this as well, as the DMSO treated control displays a greater presence of dead stain than the methotrexate treated (Figure 27A and H). Despite being an FDA approved drug for HNSCC, methotrexate was only capable of modest cytostatic effects, with MCTS impact scores of 3/5 in both FaDu and UM-22B cell lines, 1/5 in Cal 33 and BICR56 cell lines, and 0 in the OSC-19 cell line for an overall impact score of 8 (Table 7). The overall MCTS impact score of 8/25 indicate that methotrexate is the least impactful of the 19 drugs against HNSCC MCTSs.

### **5.3.8 HNSCC Sensitivity to Bleomycin**

Bleomycin represents an antitumor antibiotic that was discovered from *Streptomyces verticillus* and is capable of producing DNA damage through oxidative cleavage.<sup>204</sup> Despite being approved for HNSCC, bleomycin was not able to demonstrate consistent effectiveness in the majority of cell lines as MCTS at 20 $\mu$ M over 72hrs (Figure 28A and C). Through TL imaging, we observed that morphology was only

impacted in the UM-22B and OSC-19 cell lines, and spheroid size was reduced in UM-22B, Cal 33, and OSC-19 cell lines as MCTSs (Figure 28A). UM-22B and OSC-19 MCTSs displayed changes in morphology from their DMSO control treated spheroids becoming small dispersed cellular aggregates, lacking in both the defined peripheries and rounded features of spheroids (Figure 28A). A decrease in CAM staining was observed in all 5 cell lines vs their DMSO treated controls, with FaDu, UM-22B, and OSC-19 cell lines being most noticeably impacted (Figure 28A). Only UM-22B and OSC-19 cell lines demonstrated an increase in ETHD dead stain vs control as indicated by the increased presence of red stain in both the dead stain and color composite images (Figure 28A).

HNSCC cells lines cultured as 2D monolayers all produced a GI<sub>50</sub> value for methotrexate treatment, but only capable of 100% growth inhibition in the UM-22B cell line (Figure 28B-F). In contrast, only 3 of the 5 cell lines as MCTSs displayed sensitivity, with only the UM-22B MCTSs producing a consistent GI<sub>50</sub> value (Figure 28B-F).

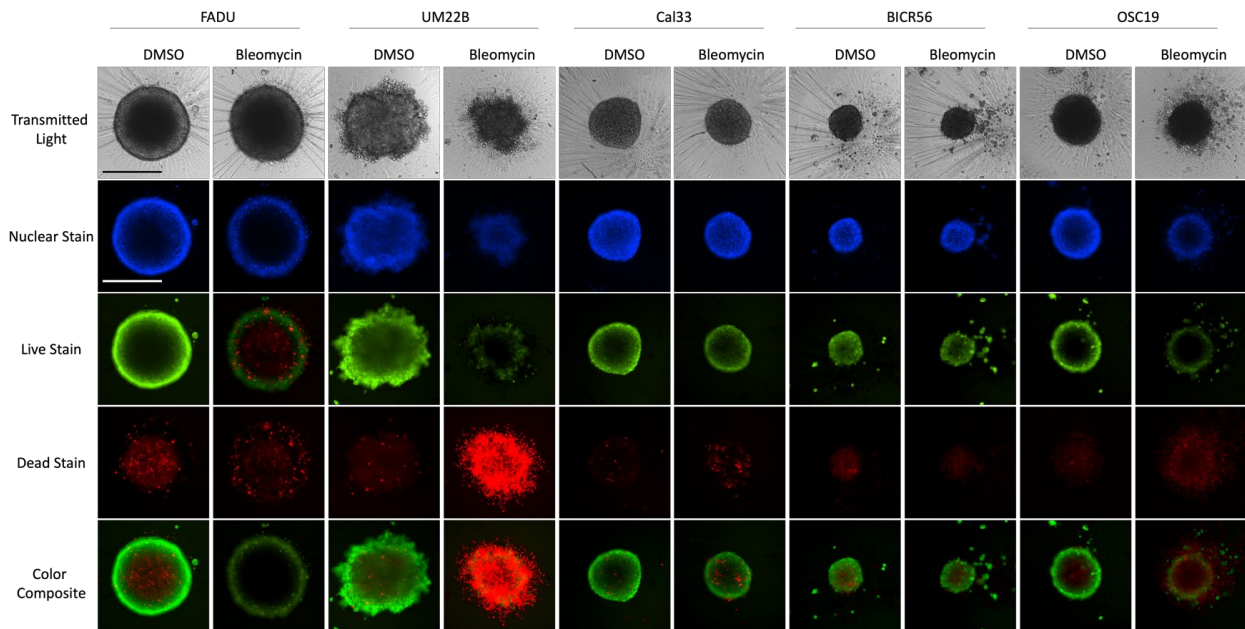
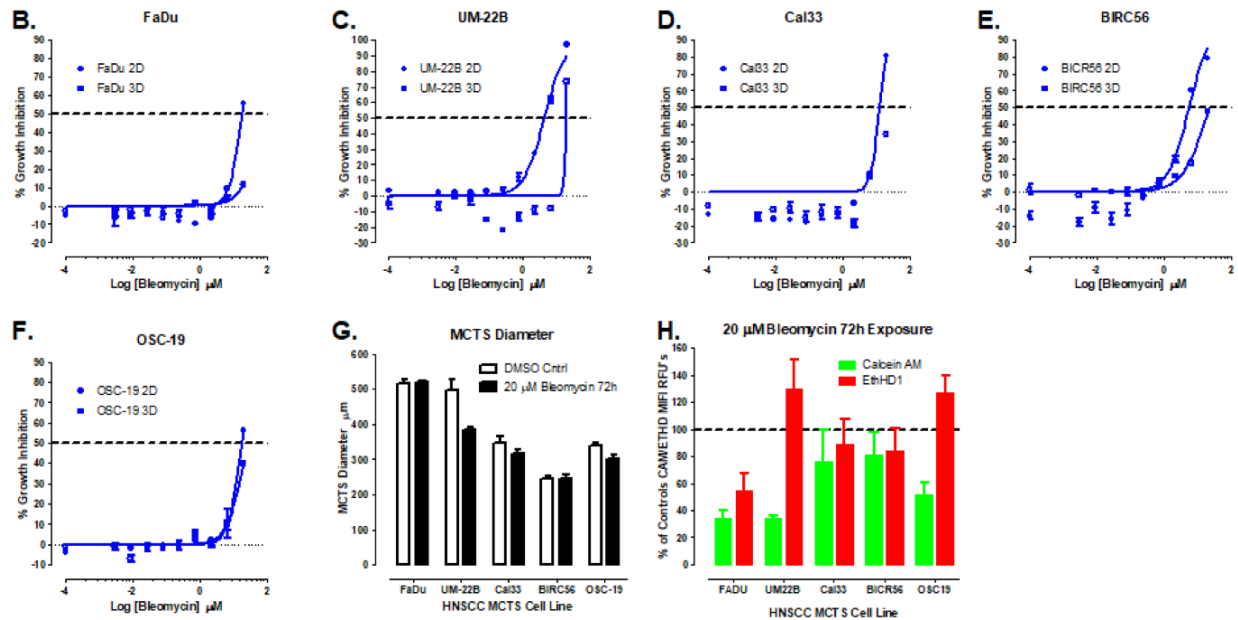


**Figure 28 Bleomycin sensitivity in HNSCC 3D multicellular tumor spheroids and 2D cell culture conditions**

**(A)** Representative images of 5 HNSCC cell lines seeded at 2,500 cells / well after 3 days of bleomycin treatment and 6 total days in culture, acquired at 4X on the IXM with the TL, DAPI, FITC, and Texas Red channels. Greyscale TL images are presented along with, Hoechst nuclear stain in blue, and color composite fluorescent images of live cell CAM and dead cell EHD staining depicted as green and red, respectively.



Corresponding CTB viability measurements displayed as % growth inhibition were graphed as XY plots with symbols (●) and (■) representative of 2D and 3D culture conditions, respectively, across FaDu (**B**), UM-22B (**C**), Cal 33 (**D**), BIRC56 (**E**), and OSC-19 (**F**) cell lines. (**G**) The line-scan tool of the MetaXpress image analysis software was used to measure the diameters and values were plotted in a bar graph where unfilled bars represent the DMSO control, and filled bars represent bleomycin treatment at its top concentration after 72hrs. (**H**) Live and dead staining intensity across all five HNSCC MCTSs after bleomycin treatment were obtained using the MetaXpress image analysis software, plotted as % of control live and dead staining intensity, with live stain represented as green filled bars and dead stain represented as red filled bars. Representative images from multiple independent experiments are presented. All scale bars represent 300  $\mu\text{m}$ . Data is representative of multiple independent experiments, and at least triplicate (n=3) well measurements. All bar graphs are representative of triplicate (n=3) samples and error bars are indicative of mean  $\pm$  SD.

The BICR56 and OSC-19 cell lines both demonstrated growth inhibitory effects with bleomycin that approached ~47% and 42%, respectively, in several independent experiments (Figure 28E and F). Furthermore, only the UM-22B, Cal 33, and OSC-19 cell lines displayed a measurable decrease in diameter, with UM-22B displaying the largest decrease of ~100 $\mu$  (Figure 28G). In analyzing the integrated intensity of our live stain, we were able to corroborate that bleomycin decreased the CAM signal substantially in FaDu, UM-22B, and OSC-19 with only a modest decrease present in the Cal 33 and BICR56 cell lines (Figure 28H). In contrast, ETHD staining intensity showed an increase in only the UM-22B and OSC-19 cell lines as corroborated by our LD images (Figure 28A and H). In terms of MCTS drug impact, bleomycin scored 4/5 in UM-22B, 2/5 in Cal 33 and OSC-19, 1/5 in FaDu, and 0/5 in BICR56, for an overall drug impact score of 9 (Table 7). These results indicate that bleomycin was one of the least impactful compounds in our screen across all 5 cell lines as MCTSs, despite being FDA approved for HNSCC.

### **5.3.9 HNSCC Sensitivity to 5'FU**

5' Fluorouracil represents a classical chemotherapeutic, that is an FDA approved antineoplastic agent for HNSCC which acts as a pyrimidine analogue capable of both disrupting DNA synthesis through enzymatic inhibition as well as having its metabolite incorporated into RNA rather than uracil, leading to inhibition of cellular proliferation as the end result.<sup>95</sup> Through TL imaging of our 5 HNSCC cell lines as MCTSs, exposed to 500 $\mu$ M 5'FU for 72hrs, we observed that 5'FU was capable of producing an effect that altered spheroid morphology in 3 of the 5 cell lines showing a visible differences vs DMSO controls (Figure 29A). The FaDu cell line displayed a substantial decrease in spheroid

size and compaction, UM-22B developed a more disorganized outer periphery and no longer maintaining its compaction, and the OSC-19 cell line seemed to become more irregular in shape and greatly dispersed compared to its tight and more well-defined DMSO treated control spheroid (Figure 29A and Table 5). We observed that CAM live staining intensity was visibly decreased in five cell lines, with the FaDu cell line demonstrating the most marked reduction in staining intensity and only a modestly reduction in the other 4. (Figure 29A). ETHD dead staining was increased in 3 of the 5 cell lines, with the Cal 33 cell line demonstrating the largest increase vs DMSO control treated wells, with apparent dead staining present all throughout the spheroid rather than focused on any specific region (Figure 29A) This trend was also observed in both the UM-22B and OSC-19, though, staining in the UM-22B cell line was much more dispersed rather than tightly focused across a large region, as seen in the OSC-19 cell line (Figure 29A).

Despite the increase in cell death via ETHD stain, CTB viability detection did not consistently correlate with these observations. While all cell lines in 2D demonstrated sensitivity to the effects of 5'FU as seen in the increase of % growth inhibition in Figure 7B-F, there were mixed responses for the cell lines as MCTS (Figure 29B-F). In particular, the FaDu, UM-22B, BICR56, and OSC-19 cell lines all demonstrated measurable CTB signals of ~40, 60, 20, and 18% growth inhibition respectively (Figure 29B-F). In comparison, the Cal 33 cell line as an MCTS did not display growth inhibition via CTB signal (Figure 29A and D). Though measurements of the spheroid diameter, we observed that only FaDu and OSC-19 cell lines were reduced in size after exposure to 5'FU for 72hrs by ~50 $\mu$ m and ~20 $\mu$ m respectively (Figure 29G).

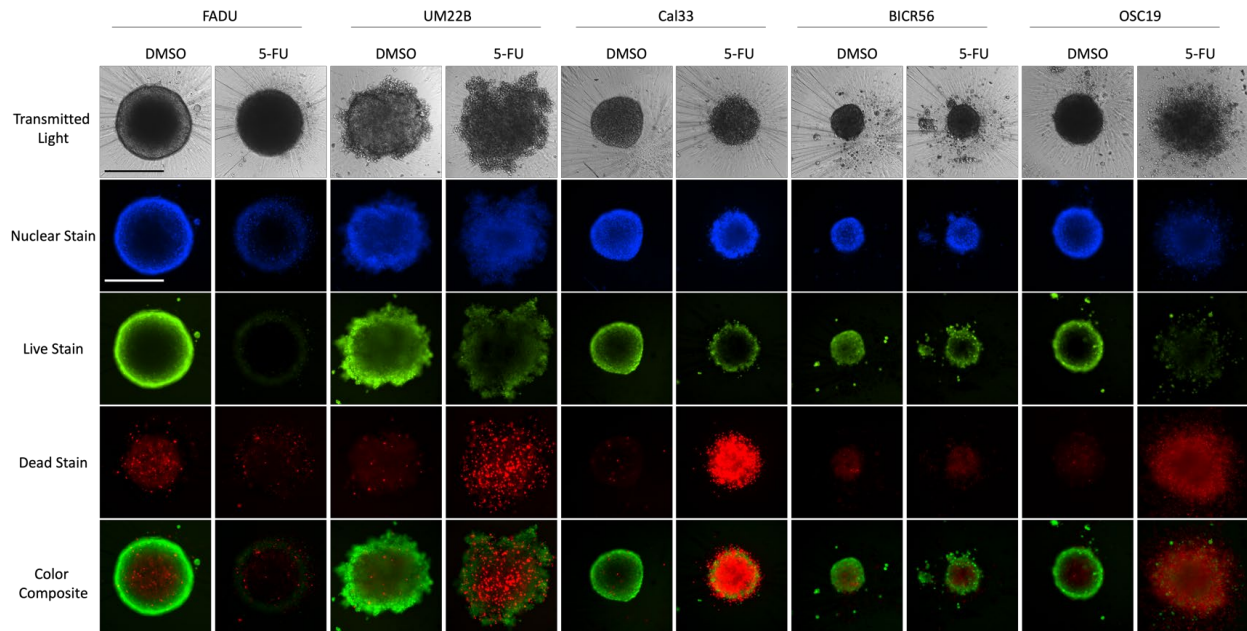
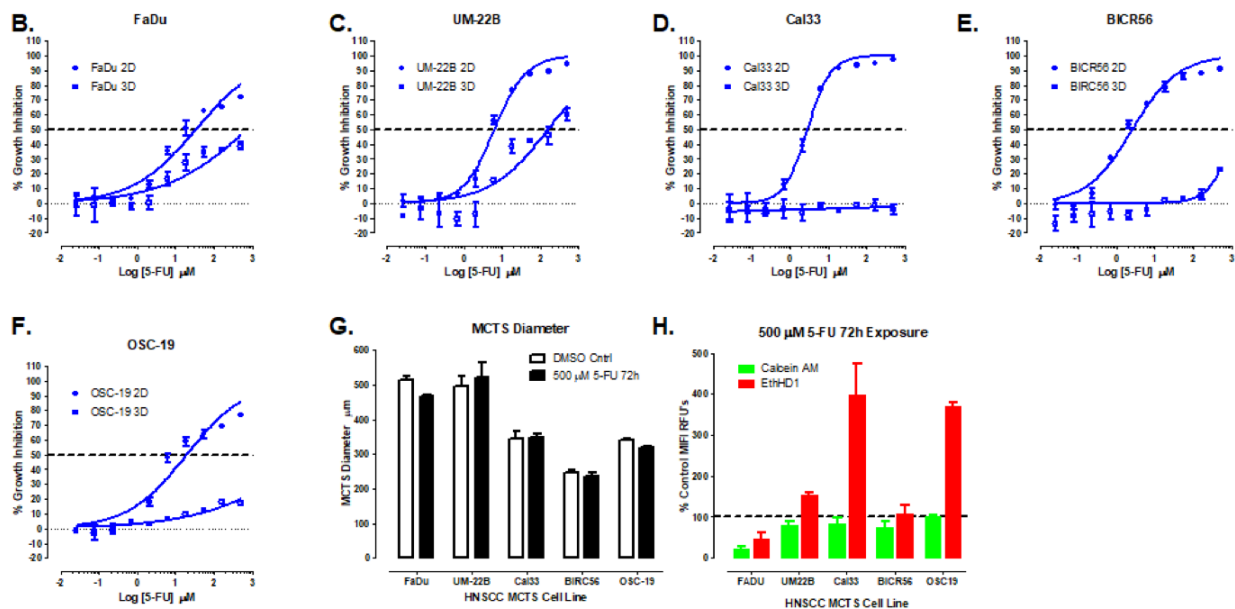


**Figure 29 5’FU sensitivity in HNSCC 3D multicellular tumor spheroids and 2D cell culture conditions**

**(A)** Representative images of 5 HNSCC cell lines seeded at 2,500 cells / well after 3 days of 5’FU treatment and 6 total days in MCTS culture, acquired at 4X on the IXM with the TL, DAPI, FITC, and Texas Red channels. Greyscale TL images are presented along with, Hoechst nuclear stain in blue, and color composite fluorescent images of live cell CAM and dead cell EHD staining depicted as green and red, respectively.



Corresponding CTB viability measurements displayed as % growth inhibition were graphed as XY plots with symbols (●) and (■) representative of 2D and 3D culture conditions, respectively, across FaDU (B), UM-22B (C), Cal 33 (D), BICR56 (E), and OSC-19 (F) cell lines. (G) The line-scan tool of the MetaXpress image analysis software was used to measure the diameters and values were plotted in a bar graph where unfilled bars represent the DMSO control, and filled bars represent 5'FU treatment at its top concentration after 72hrs. (H) Live and dead staining intensity across all five HNSCC MCTSs after 5'FU treatment were obtained using the MetaXpress image analysis software, plotted as % of control live and dead staining intensity, with live stain represented as green filled bars and dead stain represented as red filled bars. Representative images from multiple independent experiments are presented. All scale bars represent 300 μm. Data is representative of multiple independent experiments, and at least triplicate (n=3) well measurements. All bar graphs are representative of triplicate (n=3) samples and error bars are indicative of mean ± SD.

measurable decrease in size after exposure to 5'FU for 72hrs, with FaDu reduced by ~50μm and OSC-19 by ~20μm (Figure 29G). Image analysis of our LD images corroborated our observations that there was a decrease in live stain across all of the cell lines especially in the FaDu (Figure 29H). While the OSC-19 cell line indicated a visual change in the presence of CAM staining from LD images, this was determined to be only a small change in staining intensity after image analysis of replicate wells (Figure 29H). Similarly, the ETHD staining intensity also confirmed our observations that Cal 33 had the largest increase in dead staining intensity with OSC-19 also demonstrating a large presence of cell death almost equivalent to what was observed in the Cal 33 (Figure 29H). In terms of drug impact in our screen, 5'FU was only able to achieve a total score of 10, with 3/5 for FaDu, UM-22B, and OSC-19 but only a 1 and 0/5 in Cal 33 and BICR56, respectfully (Table 7). Despite being an approved drug for HNSCC, it did not consistently

provide sufficient growth inhibitory effects and ranks in the bottom 6 of the 19 compounds (Table 7).

### **5.3.10 HNSCC Sensitivity to Gefitinib as a Proxy of Cetuximab**

Gefitinib represents a small-molecule competitive inhibitor of ATP binding in the EGFR that was used to mimic the effects of FDA approved monoclonal antibody cetuximab in our compound screen.<sup>95</sup> Through TL imaging we were able to determine that 4 of the 5 HNSCC cell lines were morphologically impacted by gefitinib treatment at 100 $\mu$ M over 72hrs (Figure 30A and Table 5). In particular, the FaDu, Cal 33, and OSC-19 cell lines all demonstrated changes from their DMSO control morphologies, to greatly diffuse but still rounded spheroids, and the UM-22B cell line became a dispersed aggregate of cells that no longer resembled its original morphology (Figure 30A and Table 5). CAM staining revealed that all 5 cell lines had a substantial decrease in the presence of live cells, with little indication that live staining remained, which correlated with our observation of the morphological impact of gefitinib exposure (Figure 30A). Additionally, consistent with the decrease in live stain, all 5 cell lines also demonstrated a marked increase in the presence of dead cells as indicated by ETHD staining intensity in our LD images (Figure 30A). Despite our observations with CAM and ETHD staining, CTB viability detection was unable to relate the presence of growth inhibition in 4 out of the 5 cell lines.

CTB viability detection revealed that in 2D all cell lines were affected by gefitinib, capable of producing a measurable GI<sub>50</sub> value in 4 out of 5 cell lines, with UM-22B inconsistently able to produce a growth inhibitory effects beyond 42% in our replicates

(Figure 30B-F). Interestingly, gefitinib sensitivity in 3D produced only modest growth inhibitory effects, with UM-22B, OSC-19 and BICR56 displaying sensitivity and BICR56 demonstrating the highest growth inhibitory effect of ~35% (Figure 30B-F). In contrast, the FaDu cell line was unable to demonstrate any effects with CTB (Figure 30B-F). Through image analysis of diameter and LD staining intensity we observed that at its highest concentration of 100 $\mu$ M, gefitinib was capable of producing cell kill sufficient to disrupt morphology, and shrink both the FaDu and OSC-19 cell lines, and both decrease live and increase dead staining intensity greater than the DMSO control across all cell lines (Figure 30G, H and Table 6). In particular, the UM-22B cell line seemed to produce the largest increase in dead stain vs control, followed by OSC-19 and BICR56, FaDu, and Cal 33 cell lines, respectfully (Figure 30A and H). These results demonstrate a similar

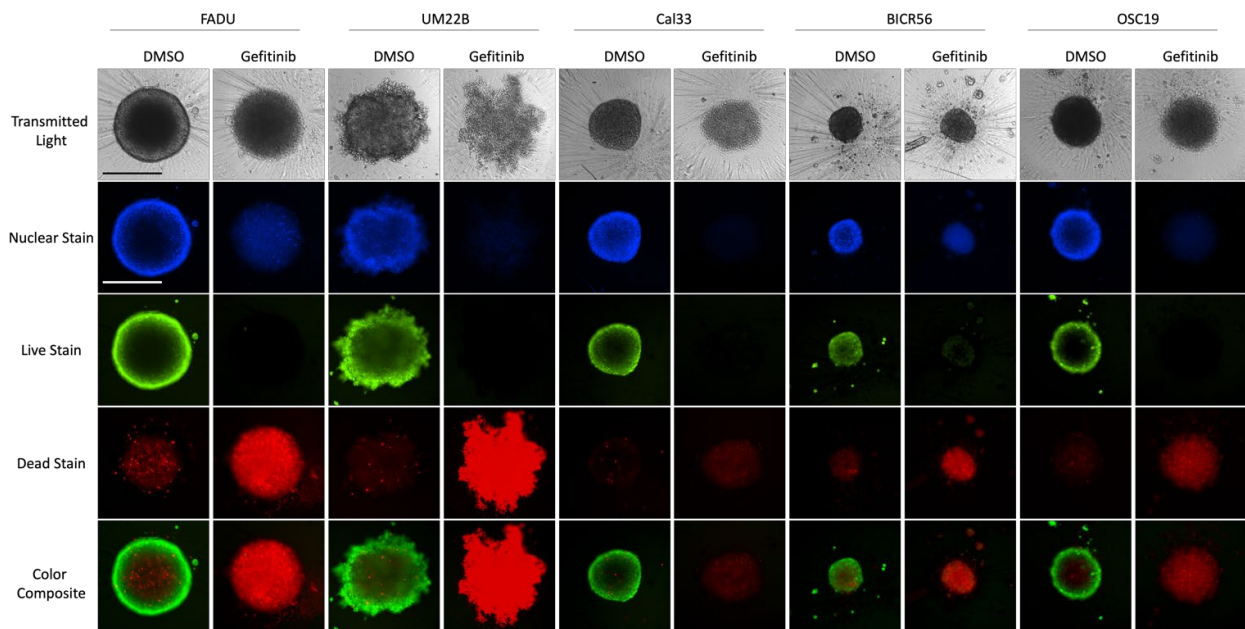
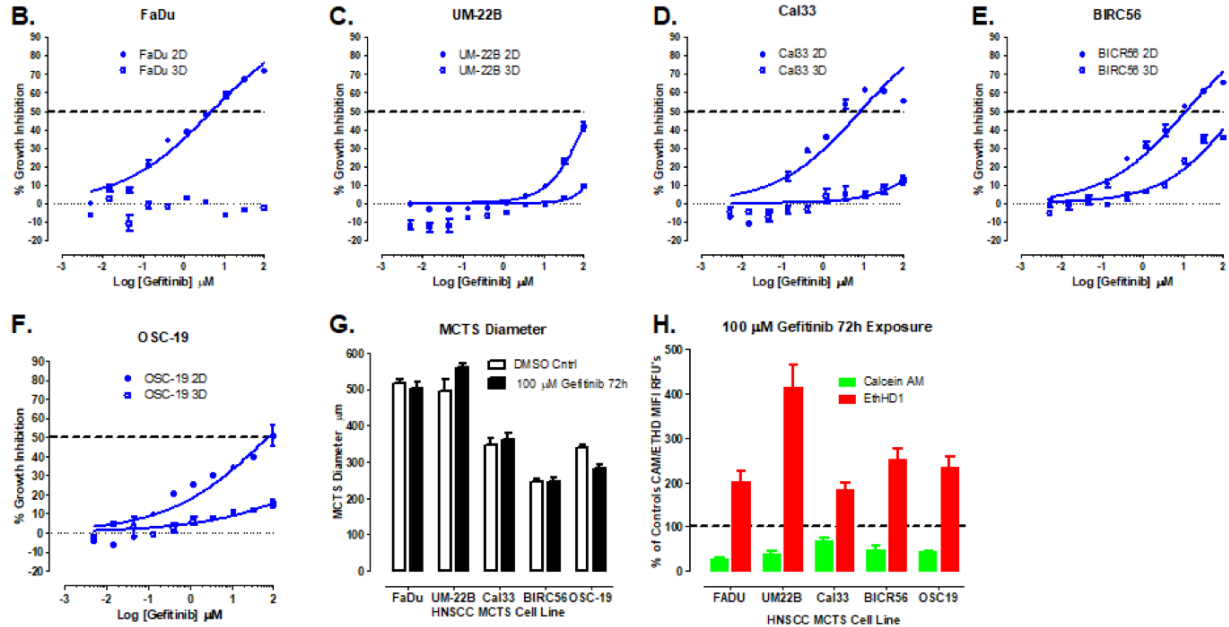


**Figure 30 Gefitinib sensitivity in HNSCC 3D multicellular tumor spheroids and 2D cell culture conditions**

**(A)** Representative images of 5 HNSCC cell lines seeded at 2,500 cells / well after 3 days of gefitinib treatment and 6 total days in culture, acquired at 4X on the IXM with the TL,

DAPI, FITC, and Texas Red channels. Greyscale TL images are presented along with, Hoechst nuclear stain in blue, and color composite fluorescent images of live cell CAM and dead cell EHD staining depicted as green and red, respectively.



Corresponding CTB viability measurements displayed as % growth inhibition were graphed as XY plots with symbols (●) and (■) representative of 2D and 3D culture conditions, respectively, across FaDU (B), UM-22B (C), Cal 33 (D), BICR56 (E), and OSC-19 (F) cell lines. (G) The line-scan tool of the MetaXpress image analysis software was used to measure the diameters and values were plotted in a bar graph where unfilled bars represent the DMSO control, and filled bars represent gefitinib treatment at its top concentration after 72hrs. (H) Live and dead staining intensity across all five HNSCC MCTSs after gefitinib treatment were obtained using the MetaXpress image analysis software, plotted as % of control live and dead staining intensity, with live stain represented as green filled bars and dead stain represented as red filled bars. Representative images from multiple independent experiments are presented. All scale bars represent 300  $\mu\text{m}$ . Data is representative of multiple independent experiments, and

at least triplicate (n=3) well measurements. All bar graphs are representative of triplicate (n=3) samples and error bars are indicative of mean  $\pm$  SD.

effect as observed in methotrexate, whereby, the effects present in imaging and image analysis did not correlate well with what was observed by CTB viability reagent. In terms of MCTS drug impact, gefitinib was able to produce a score of 4/5 across FaDu, UM-22B, and OSC-19 cell lines, a 3/5 in the Cal 33 cell line and a 2/5 in the BICR56 cell line, for an overall score of 17/25, making it the 6<sup>th</sup> most effective compound despite not producing GI<sub>50</sub> values (Table 7).

#### **5.3.11 HNSCC Sensitivity to Sunitinib**

The drug sunitinib represents a small molecule inhibitor of multiple receptor tyrosine kinases in particular with effects targeting VEGFRs and platelet-derived growth factors.<sup>95</sup> Through TL imaging we observed that 100 $\mu$ M sunitinib over 72hrs was capable of altering spheroid morphology in 3 of the 5 cell lines, and notably decreasing spheroid size in the two actively proliferating growth phenotypes, FaDu and UM-22B (Figure 31A). As seen in the TL light images of UM22B, Cal 33, and OSC-19, these cell lines no longer resembled organized, tight and compact spheroids but rather a diffuse aggregate of cells, in comparison the BICR56 cell line still resembled a compact spheroid, and FaDu became a looser but still rounded spheroid, with a marked reduction in size (Figure 31A). CAM live staining was decreased across all 5 cell lines, without a distinguishable presence of live cells visible in LD images, and both FaDu and UM-22B cell lines displaying the greatest decrease in staining intensity after 72hrs of compound exposure (Figure 31A).

ETHD dead stain was increased in all cell lines with similar trends observed as live stain, whereby, the rapid (FaDu) and moderate (UM-22B) growth phenotypes had the largest increase in dead staining intensity with distribution of ETHD throughout the aggregate of cells rather than focused to a specific region (Figure 31A and H).

We observed that sunitinib was capable of growth inhibitory effects greater than 50% inhibition in both 2D and 3D, with relatively close  $GI_{50}$  values across all cell lines with values in MCTSs of 21.7 in FaDu, 14.5 in UM-22B, 12.5 in Cal 33, 15.3 in BICR56, and 19.8 $\mu$ M in OSC-19 (Figure 31A-F and Table 3). In comparison to cisplatin (Figure 25) and doxorubicin in Chapter 4, the separation between  $GI_{50}$  values 3D to 2D was much closer, where FaDu was 4.01-fold less sensitive, UM-22B was 2.73-fold less sensitive, Cal 33 was 1.09-fold less sensitive, BICR56 was 2.59-fold less sensitive, and OSC-19 was 2.30-fold less sensitive (Table 3). We suspect that the observed close growth inhibitory relationship in 3D is due in part to the nature of these dose response relationships and their steep hillslopes. In particular, only the top two concentrations of sunitinib (100 and 33.3 $\mu$ M) seems to produce measurable growth inhibitory effects in 3D, and the top 3-4 producing measurable effects in the majority of cell lines in 2D (Figure 31B-H and Table 3).

In comparison to docetaxel and cisplatin, sunitinib treatment of MCTSs did not produce as robust of a dose-response relationship whereby drug effect was seen across several concentrations (Figure 25B-F, 26B-F, and 31B-F and Table 3). The effect produced in 2D seemed to be consistent across all cell lines, with a concentration dependent dose-response relationship observed in all 5 cell lines (Figure 31B-F). Additionally, sunitinib was able capable of decreasing spheroid diameter in the FaDu,

UM-22B, and BICR56 cell lines but only modestly affecting Cal 33, and increasing the diameter of OSC-19 slightly due to spheroid disruption (Figure 31G).

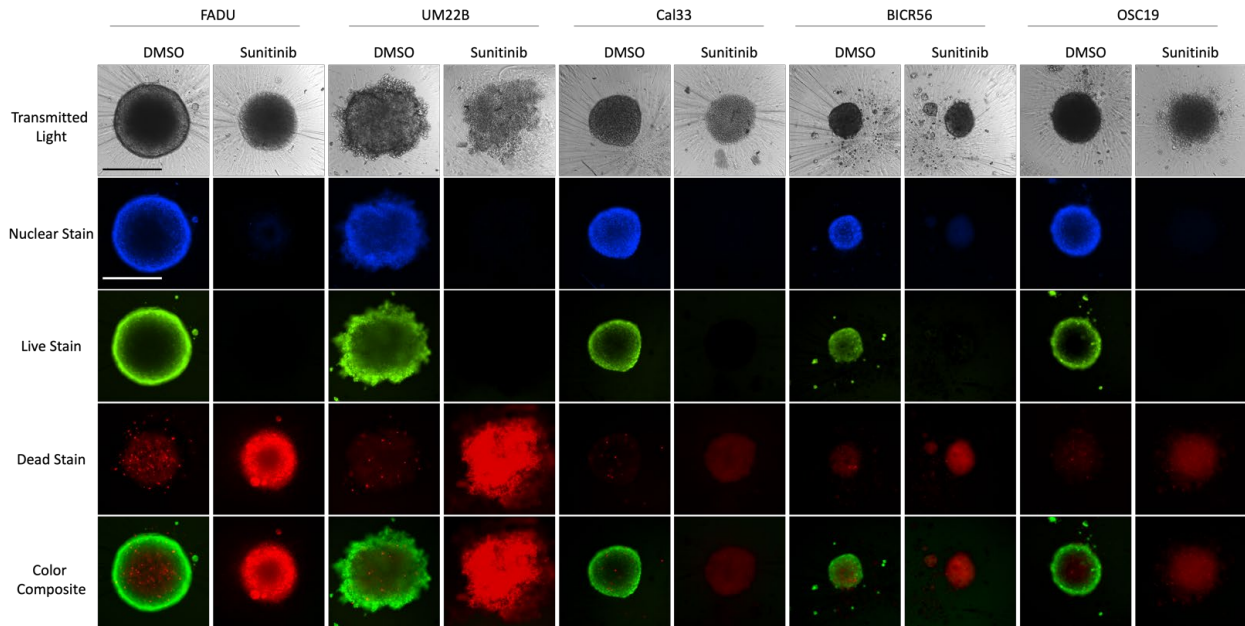
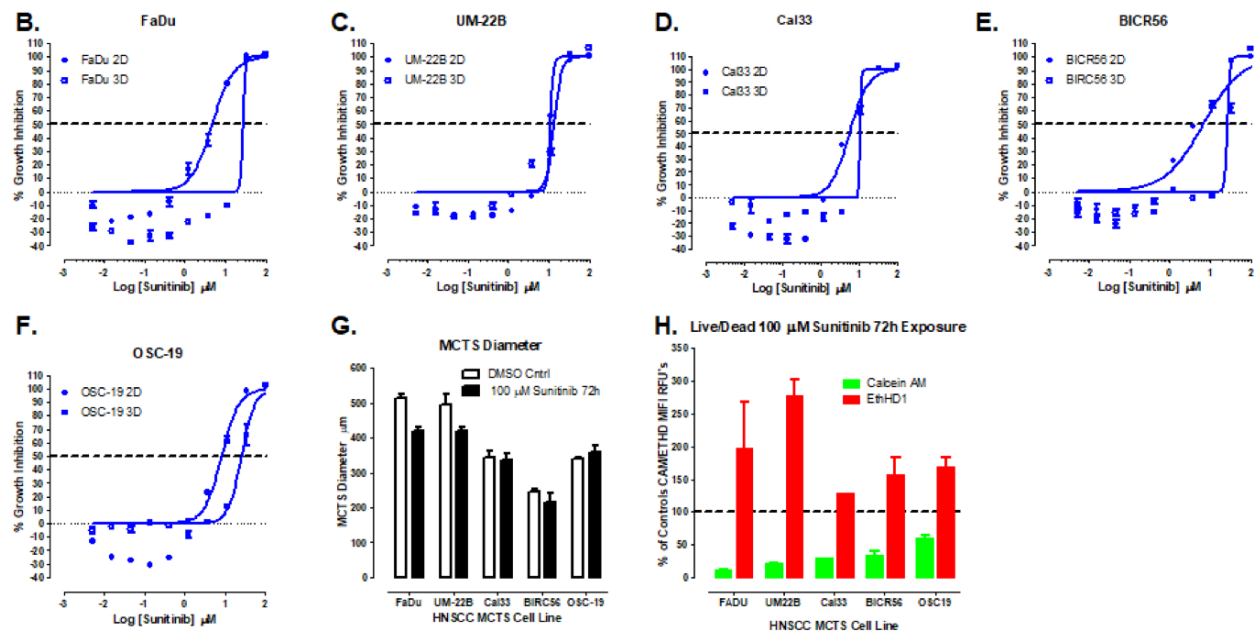


**Figure 31 Sunitinib sensitivity in HNSCC 3D multicellular tumor spheroids and 2D cell culture conditions**

**(A)** Representative images of 5 HNSCC cell lines seeded at 2,500 cells / well after 3 days of sunitinib treatment and 6 total days in culture, acquired at 4X on the IXM with the TL, DAPI, FITC, and Texas Red channels. Greyscale TL images are presented along with, Hoechst nuclear stain in blue, and color composite fluorescent images of live cell CAM and dead cell EHD staining depicted as green and red, respectively.



Corresponding CTB viability measurements displayed as % growth inhibition were graphed as XY plots with symbols (●) and (■) representative of 2D and 3D culture conditions, respectively, across FaDU (B), UM-22B (C), Cal 33 (D), BICR56 (E), and OSC-19 (F) cell lines. (G) The line-scan tool of the MetaXpress image analysis software was used to measure the diameters and values were plotted in a bar graph where unfilled bars represent the DMSO control, and filled bars represent sunitinib treatment at its top concentration after 72hrs. (H) Live and dead staining intensity across all five HNSCC MCTSs after sunitinib treatment were obtained using the MetaXpress image analysis software, plotted as % of control live and dead staining intensity, with live stain represented as green filled bars and dead stain represented as red filled bars. Representative images from multiple independent experiments are presented. All scale bars represent 300  $\mu\text{m}$ . Data is representative of multiple independent experiments, and at least triplicate (n=3) well measurements. All bar graphs are representative of triplicate (n=3) samples and error bars are indicative of mean  $\pm$  SD.

Sunitinib also both reduced the live and increased the dead staining intensities of all cell lines as MCTSs (Figure 31H). The increase in dead stain was determined to be

unimpactful in the FaDu cell line as established by our set thresholds. (Figure 31H, Table 6, and 7) In terms of drug impact, sunitinib was capable of producing a drug impact score in FaDu of 4/5, in UM-22B 5/5, in Cal33 3/5, in BICR56 4/5, and in OSC-19 3/5 for a total drug impact score of 19 (Table 7). These results indicate that at its highest concentration, sunitinib is capable of dramatically impacting the 5 HNSCC cell lines as MCTS.

### **5.3.12 HNSCC Sensitivity to Everolimus**

Everolimus represents an inhibitor of the mTOR pathway, a prominent player in mitogenic signaling.<sup>205</sup> Through TL we were able to identify that everolimus's effect at 100 $\mu$ M over 72hrs was capable of altering spheroid morphology in all cell lines as MCTSs, and furthermore, disrupting the spheroid structural integrity in the majority of cell lines (Figure 32A). As indicated by the change present in DMSO controls, we observed changes in morphology from compact or organized spheroids to cloudy, dispersed aggregates with undefined outer spheroid peripheries (Figure 32A). The BICR56 cell line, seemed to be the least affected morphologically, as it still retained some of its structure as a spheroid, but no longer resembled the rounded and compact structure present in its DMSO control (Figure 32A). Changes in observed CAM live staining intensity indicated that 4/5 HNSCC cell lines as spheroids contained few live cells capable of CAM metabolic conversion to its fluorescence metabolite, save for the BICR56 cell line which still contained a small aggregate of live cells (Figure 32A). Similarly, we observed an increase in ETHD dead staining intensity across all five cell lines, as demonstrated by a substantial increase in the presence of dead cells within the MCTSs (Figure 32A). Dead staining did

not seem to be focused to any particular region of the spheroids, but rather seemed evenly dispersed throughout the entire spheroid (Figure 32A).

Analysis of cell viability using CTB demonstrated that everolimus was capable of inhibiting growth in both 2D and 3D, whereby greater than 50% inhibition was achieved at the top concentration (Figure 32B-F and Table 3). Similar, to sunitinib, the GI<sub>50</sub> values of everolimus between 3D and 2D were much closer than what was observed with cisplatin, with changes in sensitivity in FaDu of 2.97-fold less sensitive, UM-22B of 1.13-fold less sensitive, Cal 33 of 1.41-fold less sensitive, BICR56 of 2.35-fold less sensitive, and OSC-19 of 2.25-fold less sensitive (Figure 32B-F). A clear dose-response relationship was not observed whereby, inhibitory effects were observed to decrease in a progressive manner as concentration decreased, this trend was absent in both 3D and 2D (Figure 32B-F). In particular, only the top 2 concentrations (100 and 33.33 $\mu$ M) of everolimus provided consistently measurable growth inhibitory effects beyond 50% in 2D across all cell lines (Figure 32B-F). Similar to what was observed with the cytotoxic drugs cisplatin and docetaxel, diameter measurements of MCTSs showed an increase, indicative of the loss of cell-cell interactions and overall spheroid architecture (Figure 32G). These observations were most pronounced in the UM-22B and OSC-19 cell lines, as morphologically, they showed the greatest level of disruption (Figure 32A and G). Of all the cell lines in 3D, it seemed that UM-22B was the most sensitive to everolimus, which produced a GI<sub>50</sub> value of 32.5 $\mu$ M, its morphology was completely disrupted as indicated in the TL images, and UM-22B had the largest increase in cell death with a fold-change of 10.4 in comparison to the control, as analyzed by image analysis of mean integrated intensity (Figure 32A-H and Table 3, 5, & 6). Image analysis of live staining integrated

intensity corroborated our observations in LD imaging of both the FaDu and OSC-19 cell lines, but through analysis of replicate well measurements, the observed decrease in live stain was less pronounced in UM-22B and Cal 33 cell lines (Figure 32H). In contrast, the image analysis of dead stain was able to corroborate our observations in the LD images, whereby, the presence of dead cells was increased in all cell lines as MCTSs after compound exposure with everolimus, and this increase was most pronounced in the UM-22B and Cal 33 cell lines vs their respective DMSO controls (Figure 32H). In terms of MCTS drug impact everolimus was scored as having 5/5 drug impact in FaDu, 4/5 in UM-22B, 4/5 in Cal 33, 4/5 in BICR56, and 5/5 in the OSC-19 cell lines, for a total score of 22/25, making it the second most impactful drug by our metrics.

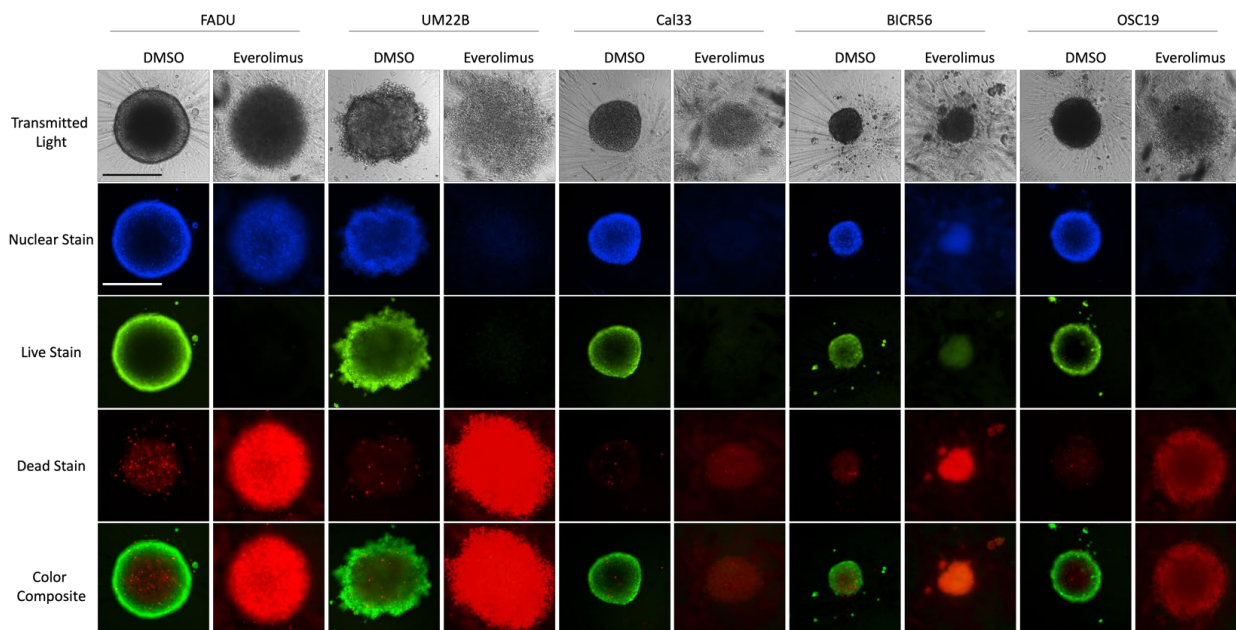
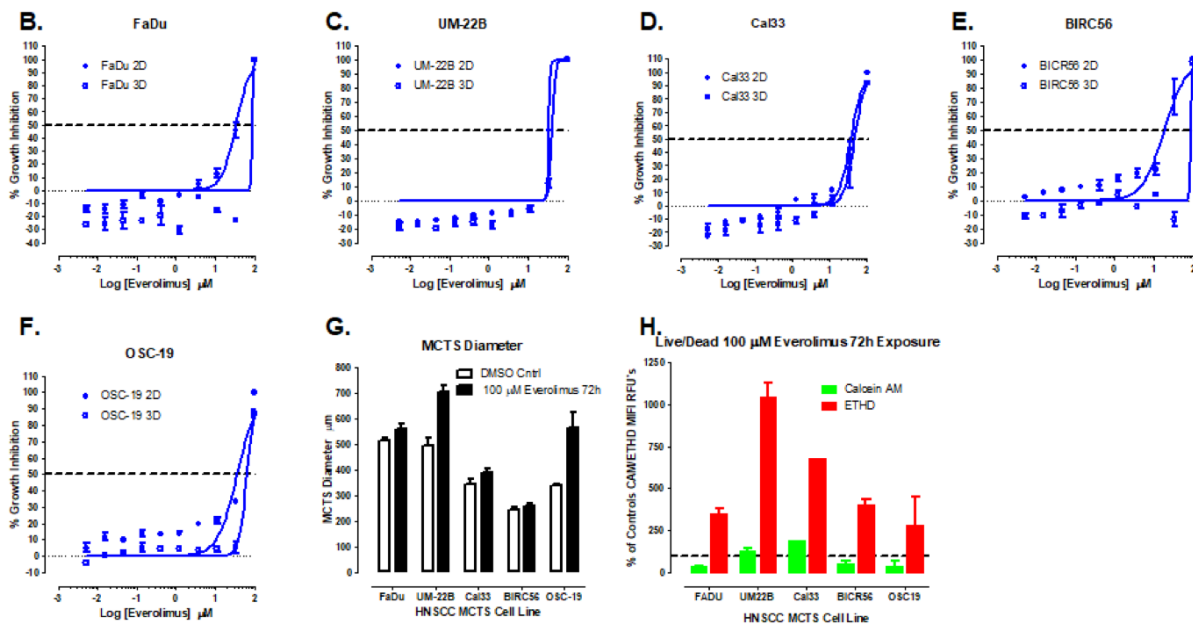


**Figure 32 Everolimus sensitivity in HNSCC 3D multicellular tumor spheroids and 2D cell culture conditions**

**(A)** Representative images of 5 HNSCC cell lines seeded at 2,500 cells / well after 3 days of everolimus treatment and 6 total days in culture, acquired at 4X on the IXM with the TL, DAPI, FITC, and Texas Red channels. Greyscale TL images are presented along

with, Hoechst nuclear stain in blue, and color composite fluorescent images of live cell CAM and dead cell EHD staining depicted as green and red, respectively.



Corresponding CTB viability measurements displayed as % growth inhibition were graphed as XY plots with symbols (●) and (■) representative of 2D and 3D culture conditions, across FaDU (B), UM-22B (C), Cal 33 (D), BICR56 (E), and OSC-19 (F) cell lines. (G) The line-scan tool of the MetaXpress image analysis software was used to measure the diameters and values were plotted in a bar graph where unfilled bars represent the DMSO control, and filled bars represent everolimus treatment at its top concentration after 72hrs. (H) Live and dead staining intensity across all five HNSCC MCTSs after everolimus treatment were obtained using the MetaXpress image analysis software, plotted as % of control live and dead staining intensity, with live stain represented as green filled bars and dead stain represented as red filled bars. Representative images from multiple independent experiments are presented. All scale bars represent 300  $\mu\text{m}$ . Data is representative of multiple independent experiments, and at least triplicate (n=3) well measurements. All bar graphs are representative of triplicate (n=3) samples and error bars are indicative of mean  $\pm$  SD.

#### **5.4 Discussion: The Necessity of Assessing Drug Impact on Multiple Fronts: Compound Sensitivity and Insensitivity in both 3D and 2D HNSCC Cell Lines**

Through our efforts we were able to identify a wide spectrum of drug responses across all 5 HNSCC cell lines with compounds capable of growth inhibition in both 3D and 2D such as, docetaxel, cisplatin, sunitinib, everolimus, and doxorubicin (Figures 25, 26, 31, 32 and Chapter 4. Figure 22 from Kochanek *et. al* 2019, Table 3).<sup>114</sup> Furthermore, effective drugs like docetaxel were capable of severely disrupting spheroid morphology, consistently producing a measurable GI<sub>50</sub> value, and especially decreasing live stain in the actively proliferating phenotypes, as well as increasing dead stain across all cell lines, which allowed them to score high in terms of MCTS impact (Figure 26A-H, Table 6, and Table 7). In contrast, we were able to observe that the effects produced by less effective drugs such as methotrexate in 3D, might indicate that the exertion of cytostatic effects, rather than cytotoxic. In methotrexate these effects seemed to be most impactful in the rapid (FaDu) and moderate (UM-22B) growth phenotypes, with cell death present on the cells of the outer spheroid periphery as indicated by the FaDu, and UM-22B cell lines which displayed this trend (Figure 27A). Both FaDu and UM-22B also had a marked decrease in spheroid diameter compared to controls, but interestingly, these effects were not enough to dampen the CTB viability signal and so even at its top concentration, no dose-dependent growth inhibitory response was observed in 3D (Figure 27A-H). Given our observations using both CTB as a proxy of viability, and live / dead imaging as another indicator of drug effect in 3D, we determined that it is necessary to have at least two different methods to quantify drug effect as CTB or imaging alone is insufficient to capture the full effects of compounds as seen in Table 3 and 5. Just because a compound does

not produce a measurable effect with CTB, does not mean that pharmacological effect is absent, which is why we found it necessary to determine other means of establishing drug effect especially the observation of changes in spheroid morphology as this demonstrates the presence of compound effects at the cellular level.

Another unique case where we found it absolutely necessary to use several metrics for drug impact and effect was in 5'FU, as LD images demonstrated that the FDA approved drug was sufficient to cause cell death, especially as seen in Cal 33 with the tremendous increase in staining intensity, it was insufficient in reducing the number of metabolically active live cells to a point where CTB viability reagent signal was affected (Figure 29A, D, and H). In contrast, the OSC-19 cell line showed a similar level of both live and dead staining intensity as the Cal 33 cell line, but detection of growth inhibition via CTB demonstrated that 5'FU was at least capable of detecting minor growth inhibitory effects reaching ~ 10% inhibition (Figure 29A, F, and H). As we illustrated previously, while both imaging and CTB are useful metrics for drug effect and impact, they are insufficient at conveying the whole picture when used individually.

Of the 19 compounds that we screened for growth inhibitory effect and overall drug impact, we observed that across 4 of the 5 cell lines 16 drugs demonstrated morphological effects that we qualified as distinct from their DMSO control treated morphologies (Table 5). In particular, one of the more effective drugs at producing morphological effects despite minimal CTB inhibitory effects was gefitinib, which was meant to mimic the EGFR inhibition of HNSCC approved drug cetuximab. Overall, gefitinib demonstrated a variety of responses in both 2D and 3D, whereby, effects produced in 3D were shown to be less sensitive than 2D and, in some circumstances, no measurable CTB effects were seen,

as indicated in the FaDu cell line (Figure 30B). However, 4 out of the 5 cell lines as MCTSs demonstrated morphological effects and 5/5 cell lines showed an increase in dead stain beyond our MCTS drug impact threshold, both of which would indicate a level of sensitivity in 3D, or level of dependence to EGFR that would explain the observed effects produced by gefitinib. We also assessed the effects of erlotinib as another mimetic of cetuximab's effects, but at its highest concentration, we observed issues with solubility, limiting the evaluation of drug effect (data not shown).

#### **5.4.1 Challenges of HNSCC Treatment in Patients and the Necessity of Physiologically Relevant Preclinical Models**

The pharmacological treatment of HNSCC has remained mostly the same with only seven drugs approved to date, and the current patient cure rates stagnating at approximately 50% for the past 30 years.<sup>130-132, 136, 138, 139</sup> Despite the introduction of cetuximab in 2006, and pembrolizumab in 2016, and the use of cisplatin, bleomycin, 5'FU, docetaxel and methotrexate as monotherapies, the remaining 5-year survival for patients with HNSCC remains poor.<sup>130, 131</sup> Our observation of drug sensitivity in HNSCC cell lines as MCTSs indicates that only 2 of the 5 included FDA approved drugs for HNSCC, cisplatin and docetaxel, were capable of producing sufficient growth inhibition and overall drug impact to be identified as hits preclinically (Figure 25 and 26). It was our expectation that drugs approved by the FDA for HNSCC would all rank the highest after *in vitro* evaluation of drug effect. What we observed, was that in 2D cell culture, this observation was true, whereby, drug sensitivity was observed across all 5 (Cisplatin, Docetaxel, Methotrexate, Bleomycin, and 5'FU) approved compounds and methotrexate

demonstrating cytostatic effects rather than highly cytotoxic (Figure 27B-F and Table 3). When we observed the effects produced by compounds from our screen in 3D however, we observed that only 2 of the 5 drugs were deemed “impactful” by our set standards, the other 3 were at the bottom of the ranks (Table 7). When we delved into the clinical responses evaluated in HNSCC, we observed why this might be the case. As reported in Brockstein 2011, patient response amongst the standard chemotherapeutic drugs was shown to be ~10-35%, with combination chemotherapy producing higher response rates but not higher survival rates vs single-agent therapy.<sup>206</sup> Patient response to FDA approved compounds included in our screen are as follows as reported by Brockstein 2011, with 35% in Docetaxel, 20-25 in Cisplatin, 13% in 5'FU, 20-25% in Methotrexate, and 30% in Bleomycin.<sup>206</sup>

Further analysis of other clinical trials indicated a similar result. Cisplatin monotherapy has not proven to be particularly effective against HNSCC. In a phase II clinical trial of 26 HNSCC patients published in 1977, only 2 had a full response, 6 showed partial responses, 10 had minor responses, with 8 exhibited no change in disease.<sup>207</sup> In a phase II clinical trial of HNSCC using only docetaxel IV at 100mg/m<sup>2</sup> for a period of 21 days, in patients with locoregionally advanced HNSCC of the 31 patients enrolled only 4 achieved complete response, 9 achieved partial response, 9 had stable disease and 7 experienced progression of the disease, overall the reported “major response rate” was 42%, with a median response of 5 months (range 2 to 14 months).<sup>208</sup> Of note, while combination therapy of chemotherapeutic drugs in HNSCC has not consistently shown a greater improvement in patient survival, as an addition to the standard induction chemotherapy treatment of 5'FU and cisplatin, docetaxel was

illustrated to improve both progression-free and overall survival by ~3 and 4 months respectively, albeit, with some greater incidences of grade 3 and 4 events like leukopenia and thrombocytopenia.<sup>209</sup> What we observed in 3D was a decrease in drug sensitivity across all FDA approved compounds, and through the development of our MCTS drug impact score we were better able to evaluate drug response across our compounds. What's more, we observed a similar trend as in many clinical studies of HNSCC response, whereby, drugs were not always capable of a total growth inhibitory response across all cell lines as MCTSs and rather just because a response was measurable did not indicate that a drug was affecting cell viability as assessed with CTB.

Our characterization of HNSCC cell lines as MCTSs have illustrated several key features of a solid tumor, namely, differential gradients of proliferation, the presence of a tumor microenvironment, and the ability of 3D to form a drug penetration barrier.<sup>64, 114</sup> These characteristics lend themselves to the decrease in sensitivity we have observed 2D to 3D. As several of these FDA approved chemotherapeutic drugs rely on targeting highly proliferative cells for maximum effect, it is not surprising that we see more selective effects in drugs such as methotrexate and 5'FU, whereby the most proliferative cell lines as MCTS displayed the greatest change vs DMSO controls (Figures 27 and 29). In Chapter 4, we identified that the outer layer of cells in the FaDu and UM-22B cell lines were actively proliferating via Click-it Edu incorporation, which indicate a population of cells of various microenvironments and phenotypic characteristics all present within a single spheroid, with most proliferative cells on the outside, followed by regions of quiescent, and necrotic cells as increasing size and compaction limit the exchange of gases, waste, and nutrients within the MCTSs. These observations were corroborated

by a study published by Laurent *et. al* 2013, who characterized MCTSs progression through the cell cycle and the differential zones of proliferation that exist within an MCTS, where cells closer to the center of the spheroid progress through the cell cycle more slowly than those in the outermost region.<sup>210</sup> In comparison to 2D, 3D represents a more physiologically-relevant cell culture model capable of demonstrating characteristics of an avascular solid tumor, and as such provided us with a more accurate depiction of drug response in HNSCC. Furthermore, the inclusion of our drug impact score, using multiple parameters to assess the effects produced in 3D by our screened compounds, allowed for a more complete picture of what was occurring at the cellular level and provided a metric more in line with clinical observations than using 2D cell culture. As this assessment is still in its nascence, it is not perfect and will potentially require additional avenues of evaluation to find the missing link between analysis of changes in CTB signal and analysis of live and dead staining intensity. Overall, we were able to use our optimized cell culture conditions to perform a more physiologically relevant drug screen using 2D as our comparator. We observed that with the majority of compounds, 2D was consistently more sensitive than 3D. Importantly, through our efforts, we established a method as the basis for evaluating overall compound impact and effectiveness on HNSCC spheroids, as an individual metric for evaluating compound effect is insufficient to convey the whole picture.

## 5.4.2 Clinical Translation with MCTS: Relationship of In Vitro Drug Concentrations to Patient Treatment

In a report published by Smith and Houghton, the authors outline the relevance of *in vitro* studies using 2D cell culture models of various cancers as they pertain to predicting clinically effective drug concentrations in patients.<sup>211</sup> In particular, the authors describe the interpretation of IC<sub>50</sub> results of various FDA approved cancer agents such as sorafenib. The reported opinion is that observed cell kill with sorafenib beyond the low to high nanomolar range approaching the micromolar range in cancer cell lines displays a relationship akin to cytotoxic agents. Essentially, off-target effects related to the inhibition of key cellular functions are incurred when cells reach the micromolar concentration of sorafenib inducing cell death in a global manner. Related to our observations of several of the targeted reagents specifically, gefitinib and sunitinib, we saw drug impact was achieved capable of altering spheroid morphology and viability. This observation was more impactful in sunitinib but at the top concentration of 100 $\mu$ M, capable of producing growth inhibitory effects beyond 50% inhibition. In an article published by Liston and Davis, the authors characterize the clinically relevant pharmacokinetic parameters obtained from patient data.<sup>212</sup> They report that for gefitinib and sunitinib the C<sub>max</sub> concentrations were 0.356 and 0.181 $\mu$ M/L, respectfully.<sup>212</sup> In our evaluation of growth inhibitory effects of both gefitinib and sunitinib, with only IC<sub>50</sub> values being achieved with sunitinib at 22 $\mu$ M, which far exceed the human C<sub>max</sub>, would indicate that the effects produced are the result of off-target inhibition leading to cell death rather than a result of specific inhibition of their higher affinity targets. Therefore, while these drugs have an

established clinical effect as indicated by their FDA approved status for other cancers, they were not capable of specific inhibition in HNSCC, and as such would not benefit follow-up in an *in vivo* model or clinical setting.

## **6.0 Implications, Limitations, and Future Directions**

### **6.1 Data-Driven Strategies for Drug Discovery and Screening**

Through our efforts our laboratory has been able to highlight the design and characterization of several data-driven approaches in Chapters 2 Synergism Confirmation, 4 HNSCC MCTS Characterization, and 5 HNSCC Drug Sensitivity 2D vs 3D, covering both high content and high throughput screening methodologies. The goal of such strategies is to rationalize the data and derive testable hypotheses to advance the findings for potential pre-clinical and clinical translation. As described in chapter 2, we were able to identify and confirm the synergistic relationship of 4 drug combinations across several cancer cell lines highlighted by our laboratories high throughput screening campaign contracted by the NCI. With both data from the scientific community and data obtained through our own experimentation we developed a suitable hypothesis to propose a mechanism of synergistic action amongst the drug combinations observed to be synergistic within our confirmation studies. We proposed that drug efflux was being inhibited at the transporter level which increased overall exposure of chemotherapeutic substrates to the cells. With a little ingenuity, we were able to design a simple, reliable, and economical high content screening strategy that was able to determine Hoechst fluorescent substrate accumulation in MDCKII cell lines. Furthermore, we were able to quantify changes in fluorescent substrate accumulation in the presence of inhibitors of the ABCG2 efflux transporter identified in our 4 drug combinations. What we observed was the ability of raloxifene and gefitinib, two drugs that appeared consistently in many

of our pilot screen combinations, to increase fluorescence accumulation through either direct competition of ABCG2, or by inhibition of a different mechanism such as allosteric modulation and these results were previously corroborated by other laboratories as cited in chapter 2.

We were able to generate a testable hypothesis in our study and carry out the necessary experiments to test it *in vitro*, but without the appropriate facilities to carry out animal studies it would be up to collaboration to advance our findings to *in vivo* and eventually the clinical settings. Of note, the NCI has been able to illustrate the ability to translate the results of such data-driven strategies from *in vitro* to *in vivo*. As indicated in Chapter 2, the NCI ALMANAC represents a compendium of data acquired through *in vitro* experimentation of pairwise combinations of drugs and the observed activity of drug combinations across 60 different cell lines and 9 distinct tumor types.<sup>55</sup> Through their efforts the NCI was able to take two drug combinations into phase I clinical trials. By following a logical progression from *in vitro*, to *in vivo*, and culminating in treatment of patients. In addition, their study was able to identify a possible synergistic mechanism of action between clofarabine and bortezomib which relates to reduction of survivin levels dependent of or independent of p53.<sup>55</sup>

It is our hope that through the development of our synergism confirmation and MOA imaging strategy that we can accomplish similar translation in the future, perhaps with collaboration of a laboratory that focuses on *in vivo* experimentation. Additionally, given the dire state of drug discovery in oncology and the need to provide better therapeutic strategies, developing a screen through drug repurposing of FDA approved compounds paired with our screening, confirmation, and imaging strategy may provide a

potential avenue to overcome both the economic and innovative challenges stagnating the preclinical stage of drug discovery.<sup>213</sup> Furthermore, inclusion of drugs traditionally not identified as having antineoplastic effects may demonstrate potentiation or synergism through alternative mechanisms of action when paired with an approved antineoplastic agent with cytotoxic or cytostatic effects, which would make them ideal as candidates using our screening strategy.

### **6.1.1 3D Application of Data-Driven Strategies**

To provide a more physiologically relevant and translatable model of a tumor, we employed 3D MCTSs, as they have been illustrated to demonstrate the characteristics of a solid, avascular tumor despite being an *in vitro* model. As a screening tool, current 3D models have been adapted for both throughput and convenience in comparison to using animal models. Through our efforts we have characterized the morphological, growth, and cellular phenotypes of 11 different HNSCC cell lines derived from various patient samples in chapter 4. Our goal was to establish a more accurate baseline of 3D for the purpose of screening FDA approved antineoplastic agents and other compounds in a more physiologically relevant model. We observed several phenotypes echoic of the diversity and heterogeneity observed in patient tumors. Upon further inspection, we were able to discern the development of key tumor microenvironmental characteristics, inherent to what is observed in both animals and patients; in particular, we observed the development of a necrotic core in both the FaDu and OSC-19 cell lines, differential zones of proliferation in FaDu and UM-22B with Click-it EDU and limited penetration of doxorubicin across the spheroid boundary across the majority of cell lines. These

observations indicate that we are capable of replicating physiological characteristics and as such, that 3D MCTSs embody a more complex and representative model for drug discovery if the goal is animal and eventually patient translation.

Through our efforts to determine drug sensitivity across our 5 characterized HNSCC cell lines in both 2D and 3D with 19 FDA approved antineoplastic compounds we observed that drug impact could not be solely determined via CTB signal but rather through determination of changes in morphology, diameter, and with changes in live / dead staining intensity via image acquisition and analysis. We developed a drug impact score to determine the overall effectiveness of a compound across each the above qualifiers. By scoring drug impact we were able to observe that not all drugs were capable of providing an impact to CTB metabolic viability, but that consistently morphology and diameter were influenced by 16 compounds in FaDu and UM-22B cell lines, 13 compounds in OSC-19, 7 compounds in Cal 33, and 6 compounds in BICR56. It seemed that the most observable trend was seen in the rapid and moderate growth phenotypes versus any other phenotype.

3D represents a stepping stone in preclinical drug discovery, whereby, logical selection of putative drug candidates can occur working from simpler models like 2D cell culture and biochemical assays to more complex models such as 3D and eventually including patient xenografts as a means of predicting drug effect for prioritization and selection of drug candidates for clinical trials. In addition, use of 3D paired with patient samples as indicated in introductory chapter 3, represents a precision medicine application whereby 3D organoids are derived from patient samples and can model

potential drug efficacy on a personalized level.<sup>129</sup> These methods truly illustrate the utility and translational ability that 3D has to offer.

## **6.2 Limitations**

### **6.2.1 Challenges in Cancer Drug Screening**

The primary goal of a cancer drug screen is to identify potential hits, for follow up, and eventually, translation to a more clinically relevant model and culminating in the treatment of patients. The physiological relevance of a model will dictate the feasibility of translation, and classically the ideology of drug screening has been to start with a less complex model and triage hits progressing through models of greater complexity and physiological relevance. With our drug screening campaign and confirmation studies, we utilized 2D cell cultures of the NCI 60 cell line panel as our main source of cancer heterogeneity. While it does represent a diverse collection of cell lines and tumor types, its use has been dated since the 1980's; given the adaptive nature of cancer cell cultures, especially in an environment that is only a reduced representation of *in vivo* conditions, it is a distinct inevitability that the phenotype and genetic profile of these cell lines has changed.<sup>20, 25</sup> As such, it may become necessary to assess any impactful genetic changes over time within these cell lines, as the results of a drug screen may depend on alterations of key genetic pathways that changed from previous reports years prior. While this does represent a limitation of the model itself, it does not mean that the information cannot be of use in drug screening, especially when we consider the trends obtained from

such a large and diverse panel of cell lines and the ability of the NCI to clinically translate the results during the ALMANAC campaign.<sup>55</sup> Furthermore, Ling and colleagues have outlined that one advantage of using a larger and more diverse panel of cell lines with a smaller set of compounds, is that the trends present will provide a stronger potential relationship between drug effect and any related genetic susceptibilities.<sup>214</sup>

### **6.2.2 Challenges with MCTS**

Multicellular tumor spheroids, represent a more complex in vitro model that is capable of recapitulating tumor architecture and microenvironmental characteristics.<sup>96, 104, 196</sup> These characteristics allow for more physiologically relevant drug screening and analyses of cancer cell lines or patient tumor samples, but they aren't perfect. As it stands, our use of 3D has been limited given that neither an adequate stromal cell population including tumor associate cells, fibroblasts, and immune cells are present in our models. The presence of these different cells associated as stroma and crosstalk between the tumor have been linked with changes to the tumor microenvironment as well as drug resistance.<sup>215, 216</sup> Furthermore, no vascularization within our MCTSs exist, which also contributes to the tumor microenvironment and characteristics of the surrounding cells as well as tumor aggression as indicated in the microfluidic models section of chapter 3.<sup>118, 120-123</sup> Both the absence of stroma, and microvasculature prevent our MCTSs from being more complete representations of *in vivo* conditions.

One of the biggest challenges faced in trying to characterize the HNSCC spheroids is the inability to more adequately analyze the internal cellular population beyond image analysis of intact whole spheroids. Through imaging of whole spheroids, we have been

able to look several molecular characteristics, namely, active proliferation, mitochondrial activity, the presence of dead and viable cells and lastly drug penetration. However, when trying to assay the presence of hypoxia at the innermost region of the spheroids we were unable to detect the presence of any hypoxic regions in the spheroid and posit several potential issues: the possibility that there is limited penetration of larger molecules such as antibodies into the deeper regions of the spheroid could prevent us from detecting hypoxic regions despite harsher permeabilization protocols; with a lack of either a hypoxic chamber or chemical induction of hypoxia, we were unable to provide a control to determine if hypoxic detection is limited to the quality of the antibody or our inability to achieve hypoxic conditions. Several other laboratories have illustrated their success of detecting hypoxia through using paraffin embedded spheroid sections to determine regions within the spheroid that hypoxia develops, especially in larger spheroids where size-dependent diffusion of oxygen occurs.<sup>217</sup> It is a limitation with the equipment available in our laboratory that we could not perform similar sectioning and hypoxia detection.

In addition, trying to assay the entire cellular population of a spheroid has also been a challenge when determining drug effect using CellTiter-Blue homogenous assay. In Chapter 5, we determined the impact and effectiveness of 19 different FDA approved cancer drugs, only 5 of which are approved for HNSCC, and determined the ability of these drugs to impact morphology, cell viability, and metabolic activity. What we observed was that only using CellTiter-Blue alone was insufficient to qualify drug effectiveness in 3D. CellTiter-Blue represents a reagent that requires metabolic redox conversion from resazurin to resorufin, whereby the less viable a cell is the lower the

amount of metabolic conversion. Given that spheroids have been illustrated as having differential zones of proliferation, with proliferative, quiescent and necrotic regions sequentially, the further cells are from the surface, each having theoretically reduced metabolic function dependent on spheroid size. As such, we would expect that if the outermost region of the spheroid was compromised by drug effects, that metabolic viability would be reduced vis-à-vis CellTiter-Blue signal. What we have observed is that similar to understanding a patient's tumor population, the cellular population of a spheroid is complex and does not respond as we might predict and as such, requires additional analytical methods to adequately observe and assess. This is why we selected several different methods to determine the level of effect that cancer drugs have on HNSCC spheroids.

### **6.3 Future Directions**

Given our experience with screening drug combinations for synergism and performing confirmation studies for the identification of favorable drug-drug interactions between drug pairs, it would be prudent to conduct a drug combination screen using a more physiologically relevant model, namely, 3D MCTSs. We could use 3D MCTSs to analyze synergism amongst both FDA approved antineoplastic agents as well as any synthetic or natural product compounds of interest capable of producing a growth-inhibitory effect. In order to appropriately perform such a drug combination screen, we would need to characterize the growth phenotype, morphology, and viability over time of any cancer cell lines that we plan on using, to both establish a baseline and identify which

cell lines would provide an adequate recapitulation of physiological conditions of an avascular solid tumor, similarly to our published research in Kochanek *et. al* 2019.<sup>114</sup> Furthermore, this screen would follow in suit with our previous work and would be performed in an unbiased manner, set on screening drugs in pairwise combinations across a representation of several cancer cell lines and tumor types as characterized 3D MCTSs. We would also seek to confirm any hits flagged as synergistic, as our laboratory has a published strategy for this as indicated in more detail in chapter 2.

Additionally, we could expand our pilot screen of 19 FDA approved antineoplastic agents in HNSCC from chapter 5, 2D vs 3D drug sensitivity comparison, to encompass a wider range of compounds, perhaps including a set of FDA approved compounds repurposed from other applications to determine if antineoplastic effects are present. In addition, we would like to perform an unbiased pilot screen of the already used 19 FDA approved compounds in pairwise combinations to determine if any favorable drug-drug interactions exist that could increase the effectiveness of compounds beyond their individual use. As we have already obtained information about the effectiveness of the 19 compounds and their appropriate top concentrations this avenue seems most likely. Furthermore, given our experiences with analysis of drug impact on 3D MCTSs, we would seek to find or compare alternative methods of determining cellular viability vs CTB, for determination of changes in viability for whole spheroid.

## Bibliography

1. Bayat Mokhtari, R.; Homayouni, T. S.; Baluch, N.; et al. Combination therapy in combating cancer. *Oncotarget* **2017**, *8*, 38022-38043.
2. DeVita, V. T., Jr.; Young, R. C.; Canellos, G. P. Combination versus single agent chemotherapy: a review of the basis for selection of drug treatment of cancer. *Cancer* **1975**, *35*, 98-110.
3. Farber, S. Some observations on the effect of folic acid antagonists on acute leukemia and other forms of incurable cancer. *Blood* **1949**, *4*, 160-7.
4. Huggins, C.; Hodges, C. V. Studies on prostatic cancer. I. The effect of castration, of estrogen and androgen injection on serum phosphatases in metastatic carcinoma of the prostate. *CA Cancer J Clin* **1972**, *22*, 232-40.
5. Goodman, L. S.; Wintrobe, M. M.; et al. Nitrogen mustard therapy; use of methyl-bis (beta-chloroethyl) amine hydrochloride and tris (beta-chloroethyl) amine hydrochloride for Hodgkin's disease, lymphosarcoma, leukemia and certain allied and miscellaneous disorders. *J Am Med Assoc* **1946**, *132*, 126-32.
6. Burchenal, J. H.; Murphy, M. L.; Ellison, R. R.; et al. Clinical evaluation of a new antimetabolite, 6-mercaptopurine, in the treatment of leukemia and allied diseases. *Blood* **1953**, *8*, 965-99.
7. Skipper, H. E. A review: on the mechanism of action of certain temporary anti-cancer agents. *Cancer Res* **1953**, *13*, 545-51.
8. Law, L. W. Effects of combinations of antileukemic agents on an acute lymphocytic leukemia of mice. *Cancer Res* **1952**, *12*, 871-8.
9. Skipper, H. W., Thompson, J. H., and Ball, M. Attempts at dual blocking of biochemical events in cancer chemotherapy. *Cancer Res* **1954**, *14*, 503-508.
10. Goldin, A.; Humphreys, S. R.; Mantel, N.; et al. Combined treatment of advanced leukemia (L1210) in mice with amethopterin and 6-mercaptopurine. *J Natl Cancer Inst* **1956**, *17*, 631-8.
11. Frei, E., 3rd; Holland, J. F.; Schneiderman, M. A.; et al. A comparative study of two regimens of combination chemotherapy in acute leukemia. *Blood* **1958**, *13*, 1126-48.
12. Sartorelli, A. C. Some approaches to the therapeutic exploitation of metabolic sites of vulnerability of neoplastic cells. *Cancer Res* **1969**, *29*, 2292-9.
13. Young, R. C.; DeVita, V. T. Cell cycle characteristics of human solid tumors in vivo. *Cell Tissue Kinet* **1970**, *3*, 285-90.
14. Freireich, E. J., Karon, M., Frei, E III. . Quadruple combination therapy (VAMP) for acute lymphocytic leukemia of childhood. *Proc Am Assoc Cancer Res* **1964**, *5*, 20.
15. DeVita, V. T., Jr.; Chu, E. A history of cancer chemotherapy. *Cancer Res* **2008**, *68*, 8643-53.
16. Devita, V. T., Jr.; Serpick, A. A.; Carbone, P. P. Combination chemotherapy in the treatment of advanced Hodgkin's disease. *Ann Intern Med* **1970**, *73*, 881-95.
17. Einhorn, L. H.; Donohue, J. Cis-diamminedichloroplatinum, vinblastine, and bleomycin combination chemotherapy in disseminated testicular cancer. *Ann Intern Med* **1977**, *87*, 293-8.

18. Law, L. W.; Dunn, T. B.; et al. Observations on the effect of a folic-acid antagonist on transplantable lymphoid leukemias in mice. *J Natl Cancer Inst* **1949**, *10*, 179-92.
19. Hanka, L. J.; Martin, D. G.; Neil, G. L. A new antitumor antimetabolite, (alphaS,5S)-alpha-amino-3-chloro-4,5-dihydro-5-isoxazoleacetic acid (NSC-163501): antimicrobial reversal studies and preliminary evaluation against L1210 mouse leukemia in vivo. *Cancer Chemother Rep* **1973**, *57*, 141-8.
20. Goldin, A.; Venditti, J. M. The new NCI screen and its implications for clinical evaluation. *Recent Results Cancer Res* **1980**, *70*, 5-20.
21. Shoemaker, R. H. The NCI60 human tumour cell line anticancer drug screen. *Nat Rev Cancer* **2006**, *6*, 813-23.
22. Skehan, P.; Storeng, R.; Scudiero, D.; et al. New colorimetric cytotoxicity assay for anticancer-drug screening. *J Natl Cancer Inst* **1990**, *82*, 1107-12.
23. Rubinstein, L. V.; Shoemaker, R. H.; Paull, K. D.; et al. Comparison of in vitro anticancer-drug-screening data generated with a tetrazolium assay versus a protein assay against a diverse panel of human tumor cell lines. *J Natl Cancer Inst* **1990**, *82*, 1113-8.
24. Monks, A.; Scudiero, D.; Skehan, P.; et al. Feasibility of a high-flux anticancer drug screen using a diverse panel of cultured human tumor cell lines. *J Natl Cancer Inst* **1991**, *83*, 757-66.
25. Boyd, M. R. *The NCI In Vitro Anticancer Drug Discovery Screen*. *Cancer Drug Discovery and Development* [Online]; Humana Press, Totowa, NJ: 1997.
26. Acton, E. M.; Narayanan, V. L.; Risbood, P. A.; et al. Anticancer specificity of some ellipticinium salts against human brain tumors in vitro. *J Med Chem* **1994**, *37*, 2185-9.
27. Shoemaker, R.; Balaschak, M.; Alexander, M.; et al. Therapeutic activity of 9-chloro-2-methylellipticinium acetate in an orthotopic model of human brain cancer. *Oncol Rep* **1995**, *2*, 663-7.
28. Pettit, G. R., Inoue, M., Karnano, Y., Herald, D.L., Arn, C., Dufresne, C., Christie, N.D., Schmidt, J.M., Doubek, D.L., Krupa, T.S. Isolation and structure of the powerful cell growth inhibitor cephalostatin 1. *J Am Chem Soc* **1988**, *110*, 2006-2007.
29. Pettit, G. R., Karnano, Y., Inoue, M., Dufresne, C., Boyd, M.R., Herald, C.L., Schmidt, J.M., Dubek, D.L., Christie, N.D.. Antineoplastic agents 214. Isolation and structure of cephalostatins 7-9. *J Org Chem* **1992**, *57*, 429-431.
30. Thompson, I.; Hall, T. C.; Moloney, W. C. Combination therapy of adult acute myelogenous leukemia: experience with the simultaneous use of vincristine, amethopterin, 6-mercaptopurine and prednisone. *N Engl J Med* **1965**, *273*, 1302-7.
31. Dancy, J. E.; Chen, H. X. Strategies for optimizing combinations of molecularly targeted anticancer agents. *Nat Rev Drug Discov* **2006**, *5*, 649-59.
32. Druker, B. J.; Tamura, S.; Buchdunger, E.; et al. Effects of a selective inhibitor of the Abl tyrosine kinase on the growth of Bcr-Abl positive cells. *Nat Med* **1996**, *2*, 561-6.
33. Druker, B. J.; Guilhot, F.; O'Brien, S. G.; et al. Five-year follow-up of patients receiving imatinib for chronic myeloid leukemia. *N Engl J Med* **2006**, *355*, 2408-17.
34. Joensuu, H.; Roberts, P. J.; Sarlomo-Rikala, M.; et al. Effect of the tyrosine kinase inhibitor STI571 in a patient with a metastatic gastrointestinal stromal tumor. *N Engl J Med* **2001**, *344*, 1052-6.
35. Shah, N. P.; Tran, C.; Lee, F. Y.; et al. Overriding imatinib resistance with a novel ABL kinase inhibitor. *Science* **2004**, *305*, 399-401.

36. Yap, E.; Tumian, N. R.; Azma, R. Z.; et al. Primary imatinib resistance in chronic myeloid leukemia patients in a developing country: BCR-ABL kinase domain mutations or BCR-ABL independent mechanisms? *Malays J Pathol* **2017**, *39*, 107-113.
37. Slamon, D. J.; Leyland-Jones, B.; Shak, S.; et al. Use of chemotherapy plus a monoclonal antibody against HER2 for metastatic breast cancer that overexpresses HER2. *N Engl J Med* **2001**, *344*, 783-92.
38. Hurwitz, H.; Fehrenbacher, L.; Novotny, W.; et al. Bevacizumab plus irinotecan, fluorouracil, and leucovorin for metastatic colorectal cancer. *N Engl J Med* **2004**, *350*, 2335-42.
39. Sandler, A. B. e. a. Randomized phase II/III Trial of paclitaxel (P) plus carboplatin (C) with or without bevacizumab (NSC # 704865) in patients with advanced non-squamous non-small cell lung cancer (NSCLC). *J. Clin. Oncol.* **2005**, *24*.
40. Peifer, M.; Weiss, J.; Sos, M. L.; et al. Analysis of compound synergy in high-throughput cellular screens by population-based lifetime modeling. *PLoS One* **2010**, *5*, e8919.
41. Axelrod, M.; Gordon, V. L.; Conaway, M.; et al. Combinatorial drug screening identifies compensatory pathway interactions and adaptive resistance mechanisms. *Oncotarget* **2013**, *4*, 622-35.
42. Mathews Griner, L. A.; Guha, R.; Shinn, P.; et al. High-throughput combinatorial screening identifies drugs that cooperate with ibrutinib to kill activated B-cell-like diffuse large B-cell lymphoma cells. *Proc Natl Acad Sci U S A* **2014**, *111*, 2349-54.
43. Chou, T. C. Theoretical basis, experimental design, and computerized simulation of synergism and antagonism in drug combination studies. *Pharmacol Rev* **2006**, *58*, 621-81.
44. Chan, G. K.; Wilson, S.; Schmidt, S.; et al. Unlocking the Potential of High-Throughput Drug Combination Assays Using Acoustic Dispensing. *J Lab Autom* **2016**, *21*, 125-32.
45. Ocana, A.; Pandiella, A. Personalized therapies in the cancer "omics" era. *Mol Cancer* **2010**, *9*, 202.
46. Wood, L. D.; Parsons, D. W.; Jones, S.; et al. The genomic landscapes of human breast and colorectal cancers. *Science* **2007**, *318*, 1108-13.
47. Stommel, J. M.; Kimmelman, A. C.; Ying, H.; et al. Coactivation of receptor tyrosine kinases affects the response of tumor cells to targeted therapies. *Science* **2007**, *318*, 287-90.
48. Benvenuti, S.; Sartore-Bianchi, A.; Di Nicolantonio, F.; et al. Oncogenic activation of the RAS/RAF signaling pathway impairs the response of metastatic colorectal cancers to anti-epidermal growth factor receptor antibody therapies. *Cancer Res* **2007**, *67*, 2643-8.
49. Junttila, T. T.; Akita, R. W.; Parsons, K.; et al. Ligand-independent HER2/HER3/PI3K complex is disrupted by trastuzumab and is effectively inhibited by the PI3K inhibitor GDC-0941. *Cancer Cell* **2009**, *15*, 429-40.
50. Cancer Genome Atlas Research, N.; Weinstein, J. N.; Collisson, E. A.; et al. The Cancer Genome Atlas Pan-Cancer analysis project. *Nat Genet* **2013**, *45*, 1113-20.
51. Barretina, J.; Caponigro, G.; Stransky, N.; et al. The Cancer Cell Line Encyclopedia enables predictive modelling of anticancer drug sensitivity. *Nature* **2012**, *483*, 603-7.
52. Bamford, S.; Dawson, E.; Forbes, S.; et al. The COSMIC (Catalogue of Somatic Mutations in Cancer) database and website. *Br J Cancer* **2004**, *91*, 355-8.
53. Feng, Z.; Kochanek, S.; Close, D.; et al. Design and activity of AP endonuclease-1 inhibitors. *J Chem Biol* **2015**, *8*, 79-93.

54. Close, D. A.; Wang, A. X.; Kochanek, S. J.; et al. Implementation of the NCI-60 Human Tumor Cell Line Panel to Screen 2260 Cancer Drug Combinations to Generate >3 Million Data Points Used to Populate a Large Matrix of Anti-Neoplastic Agent Combinations (ALMANAC) Database. *SLAS Discov* **2018**, 2472555218812429.
55. Holbeck, S. L.; Camalier, R.; Crowell, J. A.; et al. The National Cancer Institute ALMANAC: A Comprehensive Screening Resource for the Detection of Anticancer Drug Pairs with Enhanced Therapeutic Activity. *Cancer Res* **2017**, 77, 3564-3576.
56. Close, D. A.; Wang, A. X.; Kochanek, S. J.; et al. Implementation of the NCI-60 Human Tumor Cell Line Panel to Screen 2260 Cancer Drug Combinations to Generate >3 Million Data Points Used to Populate a Large Matrix of Anti-Neoplastic Agent Combinations (ALMANAC) Database. *SLAS Discov* **2019**, 24, 242-263.
57. Szakács, G., Annereau, JP, Lababidi, S, Shankavaram, U, Arciello, A, Bussey, KJ, Reinhold, W, Guo, Y, Kruh, GD, Reimers, M, Weinstein, JN, Gottesman, MM. Predicting drug sensitivity and resistance: profiling ABC transporter genes in cancer cells. *Cancer Cell*. **2004**, 6, 129-137.
58. Wang, L.; Leggas, M.; Empey, P. E.; et al. Stereoselective interaction of pantoprazole with ABCG2. II. In vitro flux analysis. *Drug Metab Dispos* **2012**, 40, 1024-31.
59. Wang, L.; Leggas, M.; Goswami, M.; et al. N-(4-[2-(1,2,3,4-tetrahydro-6,7-dimethoxy-2-isoquinolinyl)ethyl]-phenyl)-9,10-dihydro-5-methoxy-9-oxo-4-acridine carboxamide (GF120918) as a chemical ATP-binding cassette transporter family G member 2 (Abcg2) knockout model to study nitrofurantoin transfer into milk. *Drug Metab Dispos* **2008**, 36, 2591-6.
60. Chou, T., Talalay, P. Quantitative analysis of dose-effect relationships: the combined effects of multiple drugs or enzyme inhibitors. *Adv Enzyme Regul.* **1984**, 22, 27-55.
61. Chou, T. Drug combination studies and their synergy quantification using the Chou-Talalay method. *Cancer Res.* **2010**, 70, 440-446.
62. Tallarida, R. J. Drug synergism: its detection and applications. . *J Pharmacol. Exp. Ther.* **2001**, 298, 865-872.
63. Greco, W., Bravo, G, Parsons, JC. The search for synergy: A critical review from a response surface perspective. . *Pharmacol. Rev.* **1995**, 47, 331-385.
64. Shan, F.; Close, D. A.; Camarco, D. P.; et al. High-Content Screening Comparison of Cancer Drug Accumulation and Distribution in Two-Dimensional and Three-Dimensional Culture Models of Head and Neck Cancer. *Assay Drug Dev Technol* **2018**, 16, 27-50.
65. Leggas, M., Panetta, JC, Zhuang, Y, Schuetz, JD, Johnston, B, Bai, F, Sorrentino, B, Zhou, S, Houghton, PJ, Stewart, CF. Gefitinib modulates the function of multiple ATP-binding cassette transporters in vivo. *Cancer Res.* **2006**, 66, 4802-4807.
66. Nakamura, Y.; Oka, M.; Soda, H.; et al. Gefitinib ("Iressa", ZD1839), an epidermal growth factor receptor tyrosine kinase inhibitor, reverses breast cancer resistance protein/ABCG2-mediated drug resistance. *Cancer Res* **2005**, 65, 1541-6.
67. Abaan, O., Polley, EC, Davis, SR, Zhu, YJ, Bilke, S, Walker, RL, Pineda, M, Gindin, Y, Jiang, Y, Reinhold, WC, Holbeck, SL, Simon, RM, Doroshow, JH, Pommier, Y, Meltzer, PS. The exomes of the NCI-60 panel: a genomic resource for cancer biology and systems pharmacology. *Cancer Res.* **2013**, 73, 4372-82. .

68. Holbeck, S., Collins, JM, and Doroshow, JH. Analysis of Food and Drug Administration-Approved Anticancer Agents in the NCI-60 Panel of Human Tumor cell Lines. *Mol. Cancer Ther.* **2010**, *9*, 1451-1460.
69. Shoemaker, R. The NCI60 human tumour cell line anticancer drug screen. *Nat Rev Cancer.* **2006**, *6*, 813-823.
70. Liu, H., Cheng, D, Weichel, AK, Osipo, C, Wing, LK, Chen, B, Louis, TE, Jordan, VC. Cooperative effect of gefitinib and fumitremorgin c on cell growth and chemosensitivity in estrogen receptor alpha negative fulvestrant-resistant MCF-7 cells. *Int J Oncol.* **2006**, *29*, 1237-1246.
71. Mimeault, M., Mehta, PP, Hauke, R, Henichart, JP, Depreux, P, Lin, MF, Batra, SK. Improvement of cytotoxic effects induced by mitoxantrone on hormone-refractory metastatic prostate cancer cells by co-targeting epidermal growth factor receptor and hedgehog signaling cascades. *Growth Factors.* **2007**, *25*, 400-416.
72. Chu, Q., Amano, O, Kanda, Y, Kunii, S, Wang, Q, Sakagami, H. Tumor-specific cytotoxicity and type of cell death induced by gefitinib in oral squamous cell carcinoma cell lines. *Anticancer Res.* **2009**, *29*, 5023-5031.
73. Perry, W. r., Shepard, RL, Sampath, J, Yaden, B, Chin, WW, Iversen, PW, Jin, S, Lesoon, A, O'Brien, KA, Peek, VL, Rolfe, M, Shyjan, A, Tighe, M, Williamson, M, Krishnan, V, Moore, RE, Dantzig, AH. Human splicing factor SPF45 (RBM17) confers broad multidrug resistance to anticancer drugs when overexpressed--a phenotype partially reversed by selective estrogen receptor modulators. *Cancer Res.* **2005**, *65*, 6593-6600.
74. Bao, W., Chen, BA, Gao, F, Ding, JH, Xu, WL, Sheng, HL, Gao, C, Sun, YY, Chen, J, Wang, J, Zhao, G, Ma, Y. Effect of cyclosporine A, raloxifene and their combination on the reversion of multidrug resistance of K562/A02 line. *Zhongguo Shi Yan Xue Ye Xue Za Zhi.* **2006**, *14*, 895-899.
75. Erjala, K., Raitanen, M, Kulmala, J, Grénman, R. Concurrent use of vinorelbine and gefitinib induces supra-additive effect in head and neck squamous cell carcinoma cell lines. *J Cancer Res Clin Oncol.* **2007**, *133*, 169-176.
76. Tsai, C., Chiu, CH, Chang, KT, Chen, JT, Lai, CL, Chen, YM, Hsiao, SY. Gefitinib enhances cytotoxicities of antimicrotubule agents in non-small-cell lung cancer cells exhibiting no sensitizing epidermal growth factor receptor mutation. *J Thorac Oncol.* **2012**, *7*, 1218-1227.
77. Szakaacs, G.; Annereau, J. P.; Lababidi, S.; et al. Predicting drug sensitivity and resistance: profiling ABC transporter genes in cancer cells. *Cancer Cell* **2004**, *6*, 129-37.
78. Fletcher, J., Haber, M, Henderson, MJ, Norris, MD. ABC transporters in cancer: more than just drug efflux pumps. *Nat Rev Cancer.* **2010**, *10*, 147-156.
79. Kitazaki, T., Oka, M, Nakamura, Y, Tsurutani, J, Doi, S, Yasunaga, M, Takemura, M, Yabuuchi, H, Soda, H, Kohno, S. Gefitinib, an EGFR tyrosine kinase inhibitor, directly inhibits the function of P-glycoprotein in multidrug resistant cancer cells. *Lung Cancer.* **2005 Sep**; *49(3):337-43.* **2005**, *49*, 337-343.
80. Yanase, K., Tsukahara, S, Mitsuhashi, J, Sugimoto, Y. Functional SNPs of the breast cancer resistance protein-therapeutic effects and inhibitor development. *Cancer Lett.* **2006**, *234*, 73-80.
81. Yanase, K.; Tsukahara, S.; Asada, S.; et al. Gefitinib reverses breast cancer resistance protein-mediated drug resistance. *Mol Cancer Ther* **2004**, *3*, 1119-25.

82. Yang, C., Huang, CJ, Yang, CS, Chu, YC, Cheng, AL, Whang-Peng, J, Yang, PC. Gefitinib reverses chemotherapy resistance in gefitinib-insensitive multidrug resistant cancer cells expressing ATP-binding cassette family protein. *Cancer Res.* **2005**, *65*, 6943-6949.
83. Boumendjel, A., Baubichon-Cortay, H, Trompier, D, Perrotton, T, Di Pietro, A. Anticancer multidrug resistance mediated by MRP1: recent advances in the discovery of reversal agents. *Med Res Rev.* **2005**, *25*, 453-472.
84. Cheong, J., Halladay, JS, Plise, E, Sodhi, JK, Salphati, L. The Effects of Drug Metabolizing Enzyme Inhibitors on Hepatic Efflux and Uptake Transporters. *Drug Metab Lett.* **2017**, *11*, 111-118.
85. Wempe, M., Wright, C, Little, JL, Lightner, JW, Large, SE, Caflisch, GB, Buchanan, CM, Rice, PJ, Wachter, VJ, Ruble, KM, Edgar, KJ. Inhibiting efflux with novel non-ionic surfactants: Rational design based on vitamin E TPGS. *Int J Pharm.* **2009**, *370*, 93-102.
86. Huang, W., Hsieh, YL, Hung, CM, Chien, PH, Chien, YF, Chen, LC, Tu, CY, Chen, CH, Hsu, SC, Lin, YM, Chen, YJ. BCRP/ABCG2 inhibition sensitizes hepatocellular carcinoma cells to sorafenib. *PLoS One.* **2013**, *8*, e83627.
87. Siegel, R. L.; Miller, K. D.; Jemal, A. Cancer statistics, 2019. *CA Cancer J Clin* **2019**, *69*, 7-34.
88. Wong, C. H.; Siah, K. W.; Lo, A. W. Estimation of clinical trial success rates and related parameters. *Biostatistics* **2018**.
89. Hay, M.; Thomas, D. W.; Craighead, J. L.; et al. Clinical development success rates for investigational drugs. *Nat Biotechnol* **2014**, *32*, 40-51.
90. Kunz-Schughart, L. A.; Freyer, J. P.; Hofstaedter, F.; et al. The use of 3-D cultures for high-throughput screening: the multicellular spheroid model. *J Biomol Screen* **2004**, *9*, 273-85.
91. Martin, D. S.; Balis, M. E.; Fisher, B.; et al. Role of murine tumor models in cancer treatment research. *Cancer Res* **1986**, *46*, 2189-92.
92. Thoma, C. R.; Zimmermann, M.; Agarkova, I.; et al. 3D cell culture systems modeling tumor growth determinants in cancer target discovery. *Adv Drug Deliv Rev* **2014**, *69-70*, 29-41.
93. Tannock, I. F. Tumor physiology and drug resistance. *Cancer Metastasis Rev* **2001**, *20*, 123-32.
94. Rodrigues, T.; Kundu, B.; Silva-Correia, J.; et al. Emerging tumor spheroids technologies for 3D in vitro cancer modeling. *Pharmacol Ther* **2018**, *184*, 201-211.
95. Chabner, B.; Longo, D. *Cancer Chemotherapy and Biotherapy: Principles and Practice*. Fifth ed.; 2011.
96. Hirschhaeuser, F.; Menne, H.; Dittfeld, C.; et al. Multicellular tumor spheroids: an underestimated tool is catching up again. *J Biotechnol* **2010**, *148*, 3-15.
97. Wartenberg, M.; Hescheler, J.; Acker, H.; et al. Doxorubicin distribution in multicellular prostate cancer spheroids evaluated by confocal laser scanning microscopy and the "optical probe technique". *Cytometry* **1998**, *31*, 137-45.
98. Sant, S.; Johnston, P. A. The production of 3D tumor spheroids for cancer drug discovery. *Drug Discov Today Technol* **2017**, *23*, 27-36.
99. Lovitt, C. J.; Shelper, T. B.; Avery, V. M. Advanced cell culture techniques for cancer drug discovery. *Biology (Basel)* **2014**, *3*, 345-67.

100. Fischbach, C.; Chen, R.; Matsumoto, T.; et al. Engineering tumors with 3D scaffolds. *Nat Methods* **2007**, *4*, 855-60.
101. Tibbitt, M. W.; Anseth, K. S. Hydrogels as extracellular matrix mimics for 3D cell culture. *Biotechnol Bioeng* **2009**, *103*, 655-63.
102. Borowicz, S.; Van Scoyk, M.; Avasarala, S.; et al. The soft agar colony formation assay. *J Vis Exp* **2014**, e51998.
103. Friedrich, J.; Seidel, C.; Ebner, R.; et al. Spheroid-based drug screen: considerations and practical approach. *Nat Protoc* **2009**, *4*, 309-24.
104. Vinci, M.; Gowan, S.; Boxall, F.; et al. Advances in establishment and analysis of three-dimensional tumor spheroid-based functional assays for target validation and drug evaluation. *BMC Biol* **2012**, *10*, 29.
105. Lama, R.; Zhang, L.; Naim, J. M.; et al. Development, validation and pilot screening of an in vitro multi-cellular three-dimensional cancer spheroid assay for anti-cancer drug testing. *Bioorg Med Chem* **2013**, *21*, 922-31.
106. Pickl, M.; Ries, C. H. Comparison of 3D and 2D tumor models reveals enhanced HER2 activation in 3D associated with an increased response to trastuzumab. *Oncogene* **2009**, *28*, 461-8.
107. Wenzel, C.; Riefke, B.; Grundemann, S.; et al. 3D high-content screening for the identification of compounds that target cells in dormant tumor spheroid regions. *Exp Cell Res* **2014**, *323*, 131-43.
108. Wang, C.; Tang, Z.; Zhao, Y.; et al. Three-dimensional in vitro cancer models: a short review. *Biofabrication* **2014**, *6*, 022001.
109. Smith, S. J.; Wilson, M.; Ward, J. H.; et al. Recapitulation of tumor heterogeneity and molecular signatures in a 3D brain cancer model with decreased sensitivity to histone deacetylase inhibition. *PLoS One* **2012**, *7*, e52335.
110. Costa, E. C.; de Melo-Diogo, D.; Moreira, A. F.; et al. Spheroids Formation on Non-Adhesive Surfaces by Liquid Overlay Technique: Considerations and Practical Approaches. *Biotechnol J* **2018**, *13*.
111. Souza, G. R.; Molina, J. R.; Raphael, R. M.; et al. Three-dimensional tissue culture based on magnetic cell levitation. *Nat Nanotechnol* **2010**, *5*, 291-6.
112. Haisler, W. L.; Timm, D. M.; Gage, J. A.; et al. Three-dimensional cell culturing by magnetic levitation. *Nat Protoc* **2013**, *8*, 1940-9.
113. Selby, M.; Delosh, R.; Laudeman, J.; et al. 3D Models of the NCI60 Cell Lines for Screening Oncology Compounds. *SLAS Discov* **2017**, *22*, 473-483.
114. Kochanek, S. J.; Close, D. A.; Johnston, P. A. High Content Screening Characterization of Head and Neck Squamous Cell Carcinoma Multicellular Tumor Spheroid Cultures Generated in 384-Well Ultra-Low Attachment Plates to Screen for Better Cancer Drug Leads. *Assay Drug Dev Technol* **2019**, *17*, 17-36.
115. Ivascu, A.; Kubbies, M. Diversity of cell-mediated adhesions in breast cancer spheroids. *Int J Oncol* **2007**, *31*, 1403-13.
116. Klein, J. D.; Grandis, J. R. The molecular pathogenesis of head and neck cancer. *Cancer biology & therapy* **2010**, *9*, 1-7.
117. Stransky, N.; Egloff, A. M.; Tward, A. D.; et al. The mutational landscape of head and neck squamous cell carcinoma. *Science* **2011**, *333*, 1157-60.
118. Aw Yong, K. M.; Li, Z.; Merajver, S. D.; et al. Tracking the tumor invasion front using long-term fluidic tumoroid culture. *Sci Rep* **2017**, *7*, 10784.

119. Sung, K. E.; Beebe, D. J. Microfluidic 3D models of cancer. *Adv Drug Deliv Rev* **2014**, *79-80*, 68-78.
120. Garcia-Cardena, G.; Comander, J.; Anderson, K. R.; et al. Biomechanical activation of vascular endothelium as a determinant of its functional phenotype. *Proc Natl Acad Sci U S A* **2001**, *98*, 4478-85.
121. Price, G. M.; Wong, K. H.; Truslow, J. G.; et al. Effect of mechanical factors on the function of engineered human blood microvessels in microfluidic collagen gels. *Biomaterials* **2010**, *31*, 6182-9.
122. Lin, K.; Hsu, P. P.; Chen, B. P.; et al. Molecular mechanism of endothelial growth arrest by laminar shear stress. *Proc Natl Acad Sci U S A* **2000**, *97*, 9385-9.
123. Ito, K.; Sakamoto, N.; Ohashi, T.; et al. Effects of frequency of pulsatile flow on morphology and integrin expression of vascular endothelial cells. *Technol Health Care* **2007**, *15*, 91-101.
124. Blackman, B. R.; Garcia-Cardena, G.; Gimbrone, M. A., Jr. A new in vitro model to evaluate differential responses of endothelial cells to simulated arterial shear stress waveforms. *J Biomech Eng* **2002**, *124*, 397-407.
125. Lazzari, G.; Nicolas, V.; Matsusaki, M.; et al. Multicellular spheroid based on a triple co-culture: A novel 3D model to mimic pancreatic tumor complexity. *Acta Biomater* **2018**, *78*, 296-307.
126. Sherman, H.; Gitschier, H. J.; Rossi, A. E. A Novel Three-Dimensional Immune Oncology Model for High-Throughput Testing of Tumoricidal Activity. *Front Immunol* **2018**, *9*, 857.
127. Courau, T.; Bonnereau, J.; Chicoteau, J.; et al. Cocultures of human colorectal tumor spheroids with immune cells reveal the therapeutic potential of MICA/B and NKG2A targeting for cancer treatment. *J Immunother Cancer* **2019**, *7*, 74.
128. Aberle, M. R.; Burkhart, R. A.; Tiriach, H.; et al. Patient-derived organoid models help define personalized management of gastrointestinal cancer. *Br J Surg* **2018**, *105*, e48-e60.
129. Pauli, C.; Hopkins, B. D.; Prandi, D.; et al. Personalized In Vitro and In Vivo Cancer Models to Guide Precision Medicine. *Cancer Discov* **2017**, *7*, 462-477.
130. Brockstein, B. Management of recurrent head and neck cancer: recent progress and future directions. *Drugs* **2011**, *71*, 1551-1559.
131. Goerner, M.; Seiwert, TY, Sudhoff, H. Molecular targeted therapies in head and neck cancer--an update of recent developments. *Head Neck Oncol.* **2010**, *2*, 8-12.
132. Stransky, N., Egloff, AM, Tward, AD, Kostic, AD, Cibulskis, K, Sivachenko, A, Kryukov, GV, Lawrence, MS, Sougnez, C, McKenna, A, Shefler, E, Ramos, AH, Stojanov, P, Carter, SL, Voet, D, Cortés, ML, Auclair, D, Berger, MF, Saksena, G, Guiducci, C, Onofrio, RC, Parkin, M, Romkes, M, Weissfeld, JL, Seethala, RR, Wang, L, Rangel-Escareño, C, Fernandez-Lopez, JC, Hidalgo-Miranda, A, Melendez-Zajgla, J, Winckler, W, Ardlie, K, Gabriel, SB, Meyerson, M, Lander, ES, Getz, G, Golub, TR, Garraway, LA, Grandis, JR. The mutational landscape of head and neck squamous cell carcinoma. *Science* **2011**, *333*, 1157-1160.
133. Ramqvist, T., Dalianis, T. Oropharyngeal cancer epidemic and human papillomavirus. *Emerg Infect Dis.* **2010**, *16*, 1671-1677.
134. Cattley, R., Radinsky, RR. Cancer therapeutics: understanding the mechanism of action. *Toxicol Pathol.* **2004**, *32*, 116-121.

135. Johnston, P., Sen, M, Hua, Y, Camarco, D, Shun, TY, Lazo, JS, Grandis, JR. High-content pSTAT3/1 imaging assays to screen for selective inhibitors of STAT3 pathway activation in head and neck cancer cell lines. *Assay Drug Dev Technol.* **2014**, *12*, 55-79.
136. Li, H., Wawrose, JS, Gooding, WE, Garraway, LA, Lui, VW, Peyser, ND, Grandis, JR. Genomic analysis of head and neck squamous cell carcinoma cell lines and human tumors: a rational approach to preclinical model selection. *Mol Cancer Res.* **2014**, *12*, 571-582.
137. Ocana, A., Pandiella, A, Siu, LL, Tannock, IF. Preclinical development of molecular-targeted agents for cancer. *Nat Rev Clin Oncol.* **2011**, *8*, 200-209.
138. Denaro, N., Russi, EG, Adamo, V, Colantonio, I, Merlano, MC. Postoperative therapy in head and neck cancer: state of the art, risk subset, prognosis and unsolved questions. *Oncology* **2011**, *81*, 21-29.
139. Perez-Ordóñez, B., Beauchemin, M, Jordan, RCK. Molecular biology of squamous cell carcinoma of the head and neck. *J. Clin. Pathol.* **2006**, *59*, 445-453.
140. Addeo, R., Caraglia, M, Iuliano, G. Pembrolizumab: the value of PDL1 biomarker in head and neck cancer. *Expert Opin Biol Ther.* **2016**, *16*, 1075-1078.
141. Chow, L., Haddad, R, Gupta, S, Mahipal, A, Mehra, R, Tahara, M, Berger, R, Eder, JP, Burtneß, B, Lee, SH, Keam, B, Kang, H, Muro, K, Weiss, J, Geva, R, Lin, CC, Chung, HC, Meister, A, Dolled-Filhart, M, Pathiraja, K, Cheng, JD, Seiwert, TY. Antitumor Activity of Pembrolizumab in Biomarker-Unselected Patients With Recurrent and/or Metastatic Head and Neck Squamous Cell Carcinoma: Results From the Phase Ib KEYNOTE-012 Expansion Cohort. *J Clin Oncol.* **2016**, *34*, 3838-3845.
142. Seiwert, T., Burtneß, B, Mehra, R, Weiss, J, Berger, R, Eder, JP, Heath, K, McClanahan, T, Lunceford, J, Gause, C, Cheng, JD, Chow, LQ. Safety and clinical activity of pembrolizumab for treatment of recurrent or metastatic squamous cell carcinoma of the head and neck (KEYNOTE-012): an open-label, multicentre, phase 1b trial. *Lancet Oncol.* **2016**, *17*, 956-965.
143. Toniatti, C.; Jones, P.; Graham, H.; et al. Oncology drug discovery: planning a turnaround. *Cancer Discov* **2014**, *4*, 397-404.
144. Hait, W. Anticancer Drug Development: the grand challenges. *Nat. Rev. Drug Discovery* **2010**, *9*, 253-254.
145. Hutchinson, L., Kirk, R. High drug attrition rates--where are we going wrong? *Nat Rev Clin Oncol.* **2011**, *8*, 189-190.
146. Kamb, A., Wee, S, Lengauer, C. Why is cancer drug discovery so difficult? *Nat Rev Drug Discov.* **2007**, *6*, 115-120.
147. Barretina, J., Caponigro, G, Stransky, N, Venkatesan, K, Margolin, AA, Kim, S, Wilson, CJ, Lehár, J, Kryukov, GV, Sonkin, D, Reddy, A, Liu, M, Murray, L, Berger, MF, Monahan, JE, Morais, P, Meltzer, J, Korejwa, A, Jané-Valbuena, J, Mapa, FA, Thibault, J, Bric-Furlong, E, Raman, P, Shipway, A, Engels, IH, Cheng, J, Yu, GK, Yu, J, Aspesi, P Jr, de Silva, M, Jagtap, K, Jones, MD, Wang, L, Hatton, C, Palesscandolo, E, Gupta, S, Mahan, S, Sougnez, C, Onofrio, RC, Liefeld, T, MacConaill, L, Winckler, W, Reich, M, Li, N, Mesirov, JP, Gabriel, SB, Getz, G, Ardlie, K, Chan, V, Myer, VE, Weber, BL, Porter, J, Warmuth, M, Finan, P, Harris, JL, Meyerson, M, Golub, TR, Morrissey, MP, Sellers, WR, Schlegel, R, Garraway, LA. The Cancer Cell Line Encyclopedia enables predictive modelling of anticancer drug sensitivity. *Nature* **2012**, *483*, 603-7.

148. Kim, N., He, N, Yoon, S. Cell line modeling for systems medicine in cancers. *Int J Oncol.* **2014**, *44*, 371-6.
149. Shoemaker, R. The NCI60 human tumour cell line anticancer drug screen. *Nat Rev Cancer.* **2006**, *6*, 813-823.
150. Johnston, P., Sen, M, Hua, Y, Camarco, DP, Shun, TY, Lazo, JS, Wilson, GM, Resnick, LO, LaPorte, MG, Wipf, P, Hury, DM, Grandis, JR. HCS Campaign to Identify Selective Inhibitors of IL-6-Induced STAT3 Pathway Activation in Head and Neck Cancer Cell Lines. *Assay Drug Dev Technol.* **2015**, *13*, 356-76.
151. Baker, B., Chen, CS. Deconstructing the third dimension: how 3D culture microenvironments alter cellular cues. *J Cell Sci.* **2012**, *125*, 3015-3024.
152. Ekert, J., Johnson, K, Strake, B, Pardin, J, Jarantow, S, Perkinson, R, Colter, DC. Three-dimensional lung tumor microenvironment modulates therapeutic compound responsiveness in vitro--implication for drug development. *PLoS One.* **2014**, *9*.
153. Friedrich, J., Seidel, C, Ebner, R, Kunz-Schughart, LA. Spheroid-based drug screen: considerations and practical approach. *Nature Protocols* **2009**, *4*, 309-324.
154. Härmä, V., Virtanen, J, Mäkelä, R, Happonen, A, Mpindi, JP, Knuutila, M, Kohonen, P, Lötjönen, J, Kallioniemi, O, Nees, M. A comprehensive panel of three-dimensional models for studies of prostate cancer growth, invasion and drug responses. *PLoS One.* **2010**, *5*.
155. Hongisto, V., Jernström, S, Fey, V, Mpindi, JP, Kleivi Sahlberg, K, Kallioniemi, O, Perälä, M. High-throughput 3D screening reveals differences in drug sensitivities between culture models of JIMT1 breast cancer cells. *PLoS One.* **2013**, *8*.
156. Abbot, A. Biology's new dimension. *Nature* **2003**, *424*, 870-872.
157. Close, D. A.; Camarco, D. P.; Shan, F.; et al. The Generation of Three-Dimensional Head and Neck Cancer Models for Drug Discovery in 384-Well Ultra-Low Attachment Microplates. *Methods Mol Biol* **2018**, *1683*, 355-369.
158. Fang, Y., Eglen, RM. Three-Dimensional Cell Cultures in Drug Discovery and Development. *SLAS Discov.* **2017**, *22*, 456-472.
159. Lovitt, C., Shelper, TB, Avery, VM. Advanced cell culture techniques for cancer drug discovery. *Biology* **2014**, *3*, 345-367.
160. Pampaloni, F.; Reynaud, E. G.; Stelzer, E. H. The third dimension bridges the gap between cell culture and live tissue. *Nat Rev Mol Cell Biol* **2007**, *8*, 839-45.
161. Selby, M., Delosh, R, Laudeman, J, Ogle, C, Reinhart, R, Silvers, T, Lawrence, S, Kinders, R, Parchment, R, Teicher, BA, Evans, DM. 3D Models of the NCI60 Cell Lines for Screening Oncology Compounds. *SLAS Discov.* **2017**, *22*, 473-483.
162. Howes, A., Richardson, RD, Finlay, D, Vuori, K. 3-Dimensional culture systems for anti-cancer compound profiling and high-throughput screening reveal increases in EGFR inhibitor-mediated cytotoxicity compared to monolayer culture systems. *PLoS One.* **2014**, *9*.
163. Lovitt, C., Shelper, TB, Avery, VM. Miniaturized Three-dimensional Cancer Model for Drug Evaluation. *Assay Drug Dev Technol* **2013**, *11*, 435-448.
164. Madoux, F., Tanner, A, Vessels, M, Willetts, L, Hou, S, Scampavia, L, Spicer, TP. A 1536-Well 3D Viability Assay to Assess the Cytotoxic Effect of Drugs on Spheroids. *SLAS Discov.* **2017**, *22*, 516-524.

165. Onozato, Y., Kaida, A, Harada, H, Miura, M. Radiosensitivity of quiescent and proliferating cells grown as multicellular tumor spheroids. *Cancer Sci.* **2017**, *108*, 704-712.
166. Ryan, S., Baird, AM, Vaz, G, Urquhart, AJ, Senge, M, Richard, DJ, O'Byrne, KJ, Davies, AM. Drug Discovery Approaches Utilizing Three-Dimensional Cell Culture. *Assay Drug Dev Technol.* **2016**, *14* 19-28.
167. Vinci, M., Gowan, S, Boxall, F, Patterson, L, Zimmermann, M, Court, W, Lomas, C, Mendiola, M, Hardisson, D, Eccles, SA. Advances in establishment and analysis of three-dimensional tumor spheroid-based functional assays for target validation and drug evaluation. *BMC Biol.* **2012**, *10*, 29-49.
168. Wenzel, C., Riefke, B, Gründemann, S, Krebs, A, Christian, S, Prinz, F, Osterland, M, Golfier, S, Räse, S, Ansari, N, Esner, M, Bickle, M, Pampaloni, F, Mattheyer, C, Stelzer, EH, Parczyk, K, Prechtel, S, Steigemann, P. 3D high-content screening for the identification of compounds that target cells in dormant tumor spheroid regions. *Exp Cell Res.* **2014**, *323*, 131-143.
169. Singh, M., Close, DA, Mukundan, S, Johnston, PA, Sant, S. Production of Uniform 3D Microtumors in Hydrogel Microwell Arrays for Measurement of Viability, Morphology, and Signaling Pathway Activation. *Assay Drug Dev Technol.* **2015**, *13*, 570-583.
170. Ahrens, T., Timme, S, Hoepfner, J, Ostendorp, J, Hembach, S, Follo, M, Hopt, UT, Werner, M, Busch, H, Boerries, M, Lassmann, S. Selective inhibition of esophageal cancer cells by combination of HDAC inhibitors and Azacytidine. *Epigenetics.* **2015**, *10*, 431-445.
171. Ahrens, T., Timme, S, Ostendorp, J, Bogatyreva, L, Hoepfner, J, Hopt, UT, Hauschke, D, Werner, M, Lassmann, S. Response of esophageal cancer cells to epigenetic inhibitors is mediated via altered thioredoxin activity. *Lab Invest.* **2015**.
172. Fichter, C., Gudernatsch, V, Przepadlo, CM, Follo, M, Schmidt, G, Werner, M, Lassmann, S. ErbB targeting inhibitors repress cell migration of esophageal squamous cell carcinoma and adenocarcinoma cells by distinct signaling pathways. *J Mol Med (Berl).* **2014**, *92*, 1209-1223.
173. Stoner, G., Kaighn, ME, Reddel, RR, Resau, JH, Bowman, D, Naito, Z, Matsukura, N, You, M, Galati, AJ, Harris, CC. Establishment and characterization of SV40 T-antigen immortalized human esophageal epithelial cells. *Cancer Res.* **1991**, *51*, 365-371.
174. Kholmukhamedov, A., Schwartz, JM, and Lemasters, JJ. MitoTracker Probes and Mitochondrial Membrane Potential. *Shock.* **2013**, *39* 543., 543.
175. Scaduto, R. J., and Grotyohann, LW. Measurement of Mitochondrial Membrane Potential Using Fluorescent Rhodamine Derivatives. *Biophysical Journal* **1999**, *76* 469–477.
176. Das, V.; Bruzzese, F.; Konecny, P.; et al. Pathophysiologically relevant in vitro tumor models for drug screening. *Drug Discov Today* **2015**, *20*, 848-55.
177. Schmidt, M., Scholz, CJ, Polednik, C, Roller, J. Spheroid-based 3-dimensional culture models: Gene expression and functionality in head and neck cancer. *Oncology Reports* **2016**, *35*, 2431-2440.
178. Rotem, A., Janzer, A, Izar, B, Ji, Z, Doench, JG, Garraway, LA, Struhl, K. Alternative to the soft-agar assay that permits high-throughput drug and genetic screens for cellular transformation. *Proc Natl Acad Sci U S A.* **2015**, *112*, 5708-5713.
179. Kang, H., Kiess, A, Chung, CH. Emerging biomarkers in head and neck cancer in the era of genomics. *Nat Rev Clin Oncol.* **2015**, *12*, 11-26.

180. Network, T. C. G. A. Comprehensive genomic characterization of head and neck squamous cell carcinomas. *Nature* **2015**, *517*, 576–582.
181. Sun, W., Califano, JA. Sequencing the head and neck cancer genome: implications for therapy. *Ann N Y Acad Sci.* **2014**, *1333*, 33-42.
182. Walter, V., Yin, X, Wilkerson, MD, Cabanski, CR, Zhao, N, Du, Y, Ang, MK, Hayward, MC, Salazar, AH, Hoadley, KA, Fritchie, K, Sailey, CJ, Weissler, MC, Shockley, WW, Zanation, AM, Hackman, T, Thorne, LB, Funkhouser, WD, Muldrew, KL, Olshan, AF, Randell, SH, Wright, FA, Shores, CG, Hayes, DN. Molecular subtypes in head and neck cancer exhibit distinct patterns of chromosomal gain and loss of canonical cancer genes. *Plos One* **2013**, *8*, e56823.
183. Hagemann, J., Jacobi, C, Hahn, M, Schmid, V, Welz, C, Schwenk-Zieger, S, Stauber, R, Baumeister, P, Becker, S. Spheroid-based 3D Cell Cultures Enable Personalized Therapy Testing and Drug Discovery in Head and Neck Cancer. *Anticancer Res.* **2017**, *37*, 2201-2210.
184. Kerr, D., Kaye, SB. Aspects of cytotoxic drug penetration, with particular reference to anthracyclines. *Cancer Chemother Pharmacol.* **1987**, *19*, 1-5.
185. Minchinton, A., Tannock, IF. Drug penetration in solid tumours. *Nat Rev Cancer.* **2006**, *6*, 583-592.
186. Tannock, I., Lee, CM, Tunggal, JK, Cowan, DS, Egorin, MJ. Limited penetration of anticancer drugs through tumor tissue: a potential cause of resistance of solid tumors to chemotherapy. *Clin Cancer Res.* **2002**, *8*, 878-884.
187. Grantab, R., Sivananthan, S, Tannock, IF. The penetration of anticancer drugs through tumor tissue as a function of cellular adhesion and packing density of tumor cells. *Cancer Res.* **2006**, *66*, 1033-1039.
188. Grantab, R., Tannock, IF. Penetration of anticancer drugs through tumour tissue as a function of cellular packing density and interstitial fluid pressure and its modification by bortezomib. *BMC Cancer* **2012**, *12*.
189. Tredan, O.; Galmarini, C. M.; Patel, K.; et al. Drug resistance and the solid tumor microenvironment. *J Natl Cancer Inst* **2007**, *99*, 1441-54.
190. Rothenberg, S. M.; Ellisen, L. W. The molecular pathogenesis of head and neck squamous cell carcinoma. *J Clin Invest* **2012**, *122*, 1951-7.
191. Suh, Y.; Amelio, I.; Guerrero Urbano, T.; et al. Clinical update on cancer: molecular oncology of head and neck cancer. *Cell Death Dis* **2014**, *5*, e1018.
192. Cancer Genome Atlas, N. Comprehensive genomic characterization of head and neck squamous cell carcinomas. *Nature* **2015**, *517*, 576-82.
193. Le Tourneau, C.; Faivre, S.; Siu, L. L. Molecular targeted therapy of head and neck cancer: review and clinical development challenges. *Eur J Cancer* **2007**, *43*, 2457-66.
194. Vermorken, J. B.; Trigo, J.; Hitt, R.; et al. Open-label, uncontrolled, multicenter phase II study to evaluate the efficacy and toxicity of cetuximab as a single agent in patients with recurrent and/or metastatic squamous cell carcinoma of the head and neck who failed to respond to platinum-based therapy. *J Clin Oncol* **2007**, *25*, 2171-7.
195. Gamerith, G.; Rainer, J.; Huber, J. M.; et al. 3D-cultivation of NSCLC cell lines induce gene expression alterations of key cancer-associated pathways and mimic in-vivo conditions. *Oncotarget* **2017**, *8*, 112647-112661.
196. Benien, P.; Swami, A. 3D tumor models: history, advances and future perspectives. *Future Oncol* **2014**, *10*, 1311-27.

197. Zhang, Q.; Thomas, S. M.; Xi, S.; et al. SRC family kinases mediate epidermal growth factor receptor ligand cleavage, proliferation, and invasion of head and neck cancer cells. *Cancer Res* **2004**, *64*, 6166-73.
198. Lalla, R. V.; Boisoneau, D. S.; Spiro, J. D.; et al. Expression of vascular endothelial growth factor receptors on tumor cells in head and neck squamous cell carcinoma. *Arch Otolaryngol Head Neck Surg* **2003**, *129*, 882-8.
199. Feldman, R.; Gatalica, Z.; Knezetic, J.; et al. Molecular profiling of head and neck squamous cell carcinoma. *Head Neck* **2016**, *38 Suppl 1*, E1625-38.
200. Li, C.; Li, R.; Grandis, J. R.; et al. Bortezomib induces apoptosis via Bim and Bik up-regulation and synergizes with cisplatin in the killing of head and neck squamous cell carcinoma cells. *Mol Cancer Ther* **2008**, *7*, 1647-55.
201. Iglesias-Bartolome, R.; Martin, D.; Gutkind, J. S. Exploiting the head and neck cancer oncogenome: widespread PI3K-mTOR pathway alterations and novel molecular targets. *Cancer Discov* **2013**, *3*, 722-5.
202. Yin, X.; Zhang, H.; Lundgren, K.; et al. BIIB021, a novel Hsp90 inhibitor, sensitizes head and neck squamous cell carcinoma to radiotherapy. *Int J Cancer* **2010**, *126*, 1216-25.
203. He, S.; Smith, D. L.; Sequeira, M.; et al. The HSP90 inhibitor ganetespib has chemosensitizer and radiosensitizer activity in colorectal cancer. *Invest New Drugs* **2014**, *32*, 577-86.
204. Umezawa, H.; Maeda, K.; Takeuchi, T.; et al. New antibiotics, bleomycin A and B. *J Antibiot (Tokyo)* **1966**, *19*, 200-9.
205. Dunlop, E. A.; Tee, A. R. Mammalian target of rapamycin complex 1: signalling inputs, substrates and feedback mechanisms. *Cell Signal* **2009**, *21*, 827-35.
206. Brockstein, B. E. Management of recurrent head and neck cancer: recent progress and future directions. *Drugs* **2011**, *71*, 1551-9.
207. Wittes, R. E.; Cvitkovic, E.; Shah, J.; et al. CIS-Dichlorodiammineplatinum(II) in the treatment of epidermoid carcinoma of the head and neck. *Cancer Treat Rep* **1977**, *61*, 359-66.
208. Dreyfuss, A. I.; Clark, J. R.; Norris, C. M.; et al. Docetaxel: an active drug for squamous cell carcinoma of the head and neck. *J Clin Oncol* **1996**, *14*, 1672-8.
209. Vermorken, J. B.; Remenar, E.; van Herpen, C.; et al. Cisplatin, fluorouracil, and docetaxel in unresectable head and neck cancer. *N Engl J Med* **2007**, *357*, 1695-704.
210. Laurent, J.; Frongia, C.; Cazales, M.; et al. Multicellular tumor spheroid models to explore cell cycle checkpoints in 3D. *BMC Cancer* **2013**, *13*, 73.
211. Smith, M. A.; Houghton, P. A proposal regarding reporting of in vitro testing results. *Clin Cancer Res* **2013**, *19*, 2828-33.
212. Liston, D. R.; Davis, M. Clinically Relevant Concentrations of Anticancer Drugs: A Guide for Nonclinical Studies. *Clin Cancer Res* **2017**, *23*, 3489-3498.
213. Pantziarka, P.; Bouche, G.; Meheus, L.; et al. The Repurposing Drugs in Oncology (ReDO) Project. *Ecancermedalscience* **2014**, *8*, 442.
214. Ling, A.; Gruener, R. F.; Fessler, J.; et al. More than fishing for a cure: The promises and pitfalls of high throughput cancer cell line screens. *Pharmacol Ther* **2018**, *191*, 178-189.
215. Criscitiello, C.; Esposito, A.; Curigliano, G. Tumor-stroma crosstalk: targeting stroma in breast cancer. *Curr Opin Oncol* **2014**, *26*, 551-5.

216. Wang, W.; Li, Q.; Yamada, T.; et al. Crosstalk to stromal fibroblasts induces resistance of lung cancer to epidermal growth factor receptor tyrosine kinase inhibitors. *Clin Cancer Res* **2009**, *15*, 6630-8.
217. Leek, R.; Grimes, D. R.; Harris, A. L.; et al. Methods: Using Three-Dimensional Culture (Spheroids) as an In Vitro Model of Tumour Hypoxia. *Adv Exp Med Biol* **2016**, *899*, 167-96.